Doctoral Dissertation
博士論文

Highly granular scintillator-strip electromagnetic calorimeter for precision physics at future Higgs factories

(次世代ヒッグスファクトリーにおける精密物理研究のための高精細シンチレータストリップ電磁カロリメータ)

A Dissertation Submitted for the Degree of Doctor of Philosophy
December 2021
令和 3 年 12 月博士（理学）申請

Department of Physics, Graduate School of Science,
The University of Tokyo
東京大学大学院理学系研究科物理学専攻

Naoki Tsuji
辻 直希

Abstract

Several future Higgs factories based on the electron-positron collider are planned for precision Higgs physics to search for the new physics beyond the Standard Model. The calorimeters play a crucial role on the precision Higgs measurement, and especially an electromagnetic calorimeter with a quite high granularity is required. The Scintillator Electromagnetic CALorimeter (Sc-ECAL) is one of the technology options for the ECAL at the future Higgs factories. In order to demonstrate the performance of the Sc-ECAL and the scalability to the full-scale detector, the technological prototype has been developed with the full 30 layers. The performances of the Sc-ECAL such as the stability, position resolution, and the shower properties are demonstrated using the prototype. In addition, a new method to measure the saturation of the SiPM by the scintillation light excited by the UV light is developed. Finally, using the current configuration of the Sc-ECAL, it is demonstrated by the simulation that an excellent jet energy resolution is achievable. In conclusion, the Sc-ECAL is found to be a promising and mature technology for the highly granular calorimeter to achieve the precision physics at the future Higgs factories.

Contents

Preface

Background

The discovery of the Higgs boson has opened a new era in high energy physics. The precision measurements of the properties of the Higgs boson is quite important to search for the new physics beyond the Standard Model. Several future Higgs factories based on the electron-positron collider are planned for precision Higgs physics. The precision Higgs measurement demands the precise measurement of the hadron jet with the jet energy resolution of 3–4%. The calorimeters play a crucial role to achieve this requirement. Especially an ECAL with the high granularity of the 5 mm $\times$ 5 mm cell size is required. The scintillator electromagnetic calorimeter (Sc-ECAL) is one of the technology options at the future Higgs factories. It is based on a scintillator strip readout by a silicon photomultiplier (SiPM), and realizes the 5 mm $\times$ 5 mm cell size by aligning the strips orthogonally in x-y configuration.

Structure of this thesis

This thesis focuses on a highly granular Scintillator Electromagnetic CALorimeter (Sc-ECAL) for the precision physics at future Higgs factories. Chapter 1 gives a physics background for the Higgs factories. Chapter 2 explains the International Linear Collider (ILC) on behalf of the Higgs factories. The concept of the Particle Flow Algorithm (PFA) and physics contribution of the ECAL is also introduced. Chapter 3 gives a detail of the Sc-ECAL and the preliminary study. Chapter 4 gives a detail of a new technological prototype for the Sc-ECAL. Chapter 5 explains a status of commissioning tests of the prototype, and Chapter 6 and 7 show the results of the tests. Chapter 6 shows results of the calibrations of key parameters, and Chapter 7 shows the results of the performance evaluation and the comparison with the Monte Carlo simulation. Chapter 8 gives a development of a new method for a saturation correction. Finally, Chapter 9 shows an evaluation of the jet energy resolution. This thesis is concluded in Chapter 10

Author’s contribution

The Sc-ECAL involving the technological prototype has been developed in the ILC-ILD group and the CEPC-ECAL group. The prototype is developed as a joint effort of the these groups. Although the author was not able to participate directly in the construction due to the COVID-19, but jointly checked the data quality of the commissioning tests. The schemes of the calibration and reconstruction written in Chapter 5 are mainly developed by the author. The calibration and performance evaluation written in Chapter 6 and 7 are done by the author. In addition, the new method of the saturation correction written in Chapter 8 is developed by the author, and the evaluation of the jet energy resolution written in Chapter 9 is also done by the author.

Chapter 1

Introduction

1.1 Standard Model

The Standard Model is a widely accepted framework in the particle physics. In July 2012, the ATLAS and CMS experiments at the Large Hadron Collider (LHC) discovered the Higgs boson [1][2], the only particle predicted by the Standard Model but not found. Although the Higgs boson completes the Standard Model, there are many physics phenomena that cannot be explained by the Standard Model, such as the existence of dark matter. In order to comprehensively understand these physics phenomena, a new theory beyond the Standard Model is required. Many new theories beyond the Standard Model have been proposed, and among them, the super-symmetry theory and extra-dimensional theory are considered to be the most promising. It is expected that the new phenomena predicted by the new theories can be searched for by observing the Higgs boson. In addition, the Higgs boson itself has not yet been studied in details, and this is also one of the most important issues. The Higgs factories are planned to make precise measurements of the Higgs boson and to search for the new physics.

This chapter gives the outline of the Higgs factories.

1.1.1 Elementary particles

The Standard Model has been established as the fundamental theory of the particle physics, and experimental results on the properties and interactions of elementary particles are explained by the Standard Model. Fig. 1.1 shows the list of elementary particles included in the Standard Model. The Standard Model in particle physics consists of a group of particles called quarks and leptons, which are the smallest elements of matter, gauge bosons, which mediate the interactions between quarks and leptons, and the Higgs boson, which is associated with the Higgs field.

Quarks are the spin-1/2 particles with the strong interaction, and leptons are spin-1/2 particles with the weak interaction. Quarks are classified into six types according to their charge and generation: up, charm, and top, with charge $+2/3$; down, strange, and bottom, with charge $-1/3$. Leptons are also classified into six types: electron, muon, and tau, with charge -1; electron neutrino, muon neutrino, and tau neutrino, with no charge. The main differences between generations are mass, but the reason for the existence of generations and whether there are more than three generations is still unknown. Each quark also has three degrees of freedom depending on the quantum number called the color charge. The asymptotic freedom is associated with strong interactions, and quarks can only exist in combinations which is colorless, i.e., in bound states such as mesons and baryons.

Gauge bosons are spin-1 boson particles, which are exchanged between elementary particles. For example,

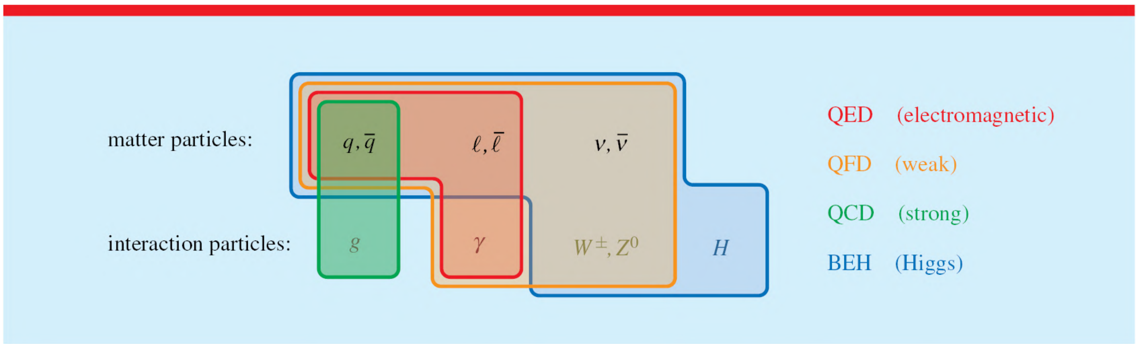

Figure1.1 Elementary particles of the Standard Model [3]

charged particles undergo the electroweak interaction by exchanging photons, particles with color charge undergo the strong interaction by exchanging gluons, and particles with weak charge undergo the weak interaction by exchanging Z bosons and $W^{\pm}$ bosons. The strength of the interaction is expressed by the magnitude of the coupling constant with the gauge boson, and there is a correspondence between the lifetime of the gauge boson and the distance reached by the interaction.

In the Standard Model, the mass term of the gauge boson is forbidden under the $\mathrm{SU}(2)_{\mathrm{L}} \otimes \mathrm{U}(1)_{\mathrm{Y}}$ gauge symmetry, and the large mass of Z and $W^{\pm}$ bosons cannot be explained. In order to explain this, the Higgs mechanism was proposed in 1964 [4]. Under the Higgs mechanism, the spontaneous breaking of the gauge symmetry is achieved by requesting the Higgs field, and the mass term of the gauge boson appears. In 2012, the Higgs boson was discovered by the Large Hadron Collider (LHC) at CERN [1][2], and the Standard Model is completed.

1.1.2 Gauge theory

The interactions between elementary particles are explained by the gauge theory. In the quantum field theory, a quantum field ϕ is associated with each fundamental particle, and its properties are described by the Lagrangian $L(\partial_{\mu}\phi_{\mu}, \phi_{\mu})$. By solving the Euler equation for the Lagrangian, the equation of the quantum field can be derived.

Assuming the Lagrangian is invariant under the local gauge symmetry of the quantum field, the vector field called the gauge field appears. The product of the gauge field and the quantum field represents the interaction and defines the form of the Lagrangian. The idea that the local gauge symmetry determines the Lagrangian and describes the interaction is called the gauge theory.

Among the four types of interactions, the electromagnetic interaction is described by the quantum electrodynamics, the strong interaction is described by the quantum chromodynamics, and the weak interaction is unified with the electromagnetic interaction by the Glashow-Weinberg-Salam theory (GWS theory) [5][6][7]. The gravitational interaction is extremely weak compared to the other interactions, so it does not have observable effects at sub-atomic scales and is not described in the Standard Model.

1.1.3 Higgs mechanism

The creation of the mass is explained by the Higgs mechanism in the Standard Model. According to the GWS theory, the electroweak interaction is derived by $\mathrm{SU}(2)_{\mathrm{L}} \otimes \mathrm{U}(1)_{\mathrm{Y}}$, but the mass term of the gauge boson is forbidden which cannot explain the large masses of Z and $W^{\pm}$. In order to explain the gauge boson mass while preserving the gauge symmetry of the Lagrangian, the spontaneous symmetry breaking is adopted. The scalar field that interacts with the gauge boson, the complex two-dimensional Higgs field: Φ, is introduced, and the potential of the Higgs field is written by:

$$V(\Phi) = \mu^2 \Phi^\dagger \Phi + \lambda(\Phi^\dagger \Phi)^2 \tag{1.1}$$

where,

$$V(\Phi) = \frac{1}{\sqrt{2}} \begin{pmatrix} \phi^+ \\ \phi^0 \end{pmatrix} = \frac{1}{\sqrt{2}} \begin{pmatrix} \phi_1 + i\phi_2 \\ \phi_3 + i\phi_4 \end{pmatrix} \tag{1.2}$$

The point where the potential is minimized is considered to be the stable point of the vacuum. Here, $\lambda \geq 0$ is required to prevent the negative divergence of the potential. In the early universe, $\mu^2 \geq 0$, the stable point of the vacuum is $\Phi = 0$. However, as the universe cools down, $\mu^2 < 0$, the shape of the potential changes as shown in Fig. 1.2.

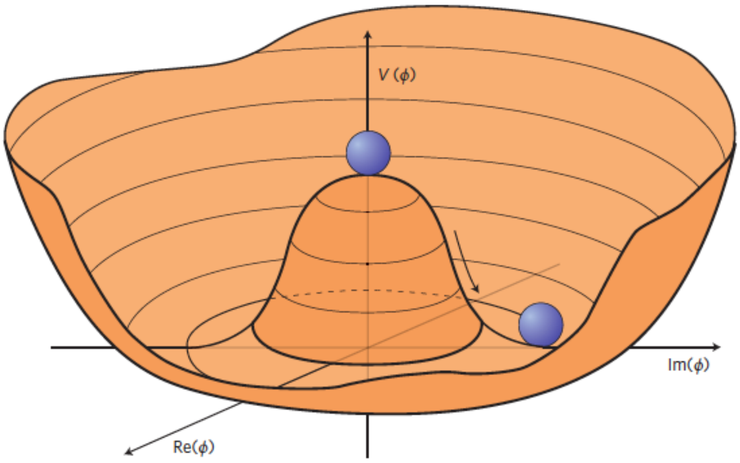

Figure1.2 The symmetry-breaking Higgs potential[8]

There are countless stable points in the vacuum, and the phase rotation symmetry of the Higgs field is broken at the moment when one point is chosen. The minimum point of the potential $V(\Phi)$ is moved from the origin ($\phi_1 = \phi_2 = \phi_3 = \phi_4 = 0$) to the point that satisfies:

$$\Phi^\dagger \Phi = \frac{1}{2}(\phi_1^2 + \phi_2^2 + \phi_3^2 + \phi_4^2) = -\frac{\mu^2}{2\lambda} \tag{1.3}$$

In this point, the vacuum has a finite expectation value of the Higgs field $\langle \Phi \rangle$, and this can be interpreted as the condensation of the Higgs field in the vacuum.

$$V(\Phi) = \mu^2 \Phi^\dagger \Phi + \lambda(\Phi^\dagger \Phi)^2 \tag{1.4}$$

The field is expanded as $\phi^0(x) = v + h(x)$ around this point. The gauge is chosen so that h is real. On the other hand, the interaction between the Higgs field and the gauge boson is determined by the gauge principle and is derived from the Lagrangian of the scalar particle, where ∂_μ is replaced by D_μ:

$$L_{\text{Higgs}} = (D_\mu \Phi)^\dagger (D^\mu \Phi) - V(\Phi) \tag{1.5}$$

where $D_\mu = \partial_\mu + ig\sigma^a W_\mu^a/2 + ig'YB_\mu/2$, W_μ and B_μ are the gauge fields associated with the $SU(2)_L$ and $U(1)_Y$ symmetry with g and g' couplings, σ^a with $a = 1, 2, 3$ are the Pauli matrices and $Y = 1/2$ is the hyper-charge of the Higgs doublet. It allows Z and $W^\pm$ bosons to acquire the masses written by:

$$m_W = \frac{g}{2}v, m_Z = \frac{\sqrt{g^2 + g'^2}}{2}v \tag{1.6}$$

Since the Higgs field is defined as the complex scalar doublet, it has four degrees of freedom. Three of these degrees of freedom are consumed by the phase rotation at the stable point of the vacuum, and the remaining degrees of freedom become the Higgs boson with mass. The mass of the Higgs boson can be written by:

$$m_h = \sqrt{2\lambda v^2} = \sqrt{2|\mu^2|} \tag{1.7}$$

The mass of the Higgs boson is one of the most important parameters in the Standard Model. The mass of the Higgs boson is $m_h = \sqrt{2\lambda v^2}$, where v is the vacuum expectation value, and λ is the Higgs self-coupling parameter. While v is determined by one parameter, the Fermi coupling as $v = (\sqrt{2}G_F)^{1/2}$, λ is unknown. Therefore, the Higgs boson mass is a degree of freedom in the Standard Model. After the discovery of the Higgs boson at the ATLAS and CMS experiments in 2012, the ATLAS and CMS experiments continued the combined measurements of the Higgs boson mass. It results in $125.09 \pm 0.21 \pm 0.11$ GeV [9]. It is said that the ATLAS and CMS experiments can be able to determine the Higgs boson mass with an uncertainty of about 0.1 GeV.

The coupling of the Higgs boson to the other elementary particles of the Standard Model can be proportional to the mass of the particle and the vacuum expectation value. The couplings are written by:

$$\begin{aligned} g_{Hf\bar{f}} &= \frac{M_f}{v} \\ g_{HVV} &= \frac{2M_V^2}{v} \\ g_{HHVV} &= \frac{2M_V^2}{v^2} \\ g_{HHH} &= \frac{3M_H^2}{v} \\ g_{HHHH} &= \frac{3M_H^2}{v^2} \end{aligned} \tag{1.8}$$

where M_f is the mass of the fermion, V means the vector bosons (Z, $W^{\pm}$) and M_V is the mass of the vector boson.

The Higgs couplings to fermions and bosons are linearly proportional to the masses of the fermions and bosons, so more massive particles have larger Higgs branching ratio. The branching ratio is largest for the bottom quarks, $BR(H \to b\bar{b}) = 57.8\%$. However, this channel has a poor signal-to-noise ratio and poor resolution due to the $b\bar{b}$ pair production backgrounds via the strong interaction at the hadron colliders like the LHC, so this channel can not be useful for precise measurement of the Higgs boson mass and coupling.

Over the years, there have been many attempts to estimate the ultimate sensitivity of the LHC experiments to the Higgs boson couplings. The results are shown in Fig. 1.3. The LHC experiments will be able to simultaneously determine the Higgs couplings to the Standard Model particle in a way that, if not completely model independent, at least depends only on minimal theoretical assumptions. These determinations should be accurate enough to confirm or disprove the hypothesis that the recently observed particle has the profile of the Higgs boson.

1.1.4 Motivation of precision Higgs measurements

Many parameters of the Standard Model have been measured in a number of experiments. Since there are correlations between the parameters, it is possible to predict the values of other parameters based on some of the measurements. In other words, precise measurements of the observables of the Standard Model are very important because they can verify the self-consistency of the Standard Model itself, and they can also provide information that indirectly suggests the existence of new physics beyond the Standard Model.

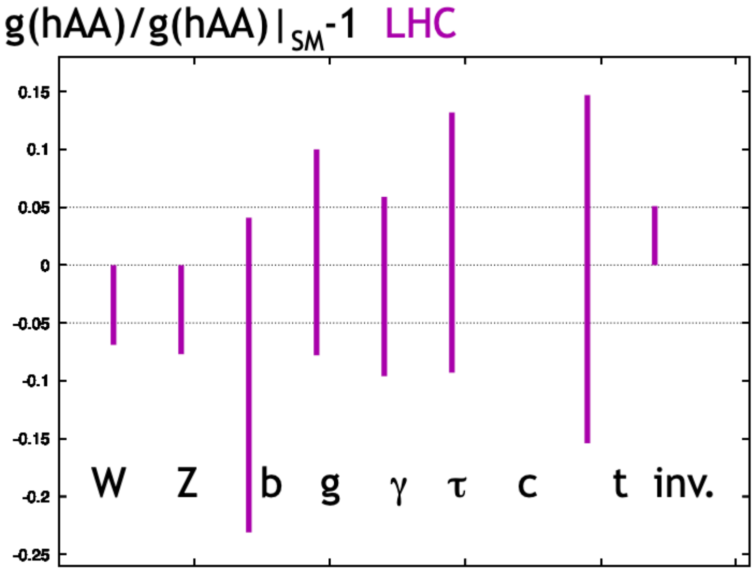

Figure1.3 Estimate of the sensitivity of the LHC experiments to Higgs boson couplings in a model-independent analysis. The plot shows the 1 σ intervals for LHC at 14 TeV with 300 fb^{-1}. [10]

The properties of the Higgs boson that we need to investigate is the mass, the decay width, the spin/parity/charge conjugate (JPC), and its gauge and Yukawa couplings. The key is the mass-coupling constant relation. If the Higgs boson is the only source of mass for all Standard Model particles, then the coupling constant should be proportional to the mass, as shown in Fig. 1.4. Therefore, any deviation from the straight line is a signal of physics beyond the standard theory. In other words, the Higgs boson would open a new window to for new physics.

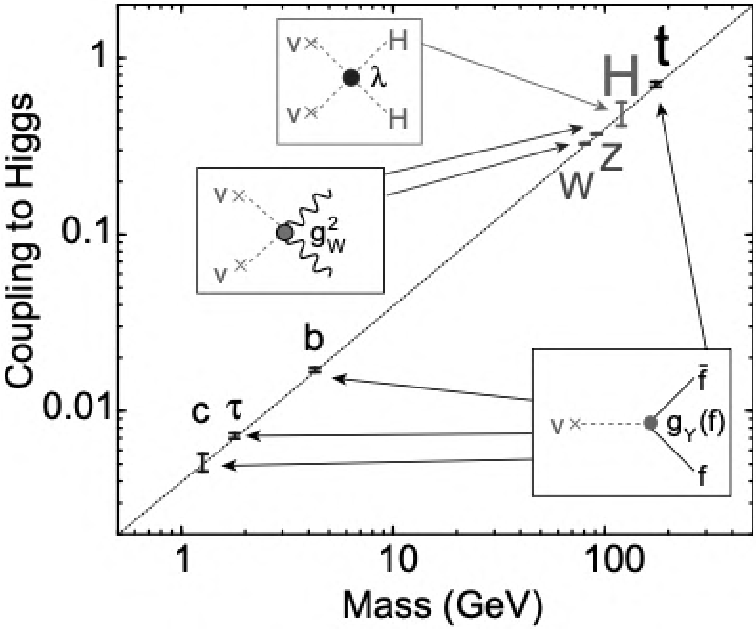

Figure1.4 mass-coupling constant relation[11]

The magnitude of the deviation generally follows the decoupling theorem:

$$\frac{\Delta g}{g} = O(\frac{v^2}{M^2}) \tag{1.9}$$

Here, M is the mass scale of the new physics. Since there is no sign of new physics at the LHC so far, M is considered to be quite large. This means that the deviation from the Standard Model is a few percent to at most 10%. In order to detect these small deviations from the Standard Model and to match new physics beyond the Standard Model by the pattern of deviations, accuracy at the % level is necessary. To achieve this accuracy, the future Higgs factories and a high performance instrument to maximize physics opportunities at the Higgs factories are necessary.

The lepton colliders realize a clean environment because the kinematics of the initial state is clear. The $H \to b\bar{b}$ channel can be used for precise measurements of the Higgs boson mass, and realize the model-independent measurements of the Higgs couplings decaying to the other elementary particles. Nevertheless, there are inherent complexities in measuring hadronic final states.

1.2 Higgs factories

The Higgs factories are the colliders that produces large quantities of the Higgs bosons. The purpose of the Higgs factories is to investigate the nature of the Higgs bosons, which still remains a mystery, and to verify physics beyond the Standard Model. The Higgs factories basically uses electron-positron collisions because the kinematics of the initial state must be clear in order to precisely measure the cross section and total decay width of the Higgs bosons through the Higgs-associated production process. There are two types of accelerators: a linear accelerator and a circular accelerator. The center of mass energy of the linear accelerator can be extended to a TeV scale by extending the linear part of the accelerator and/or by improving the performance of the accelerating gradient through technological development. On the other hand, the circular accelerator can be operated as a Z/W factories, and the tunnel can be reused to expand to a hadron collider with a beam energy of several tens of TeV. An overview of the two Higgs factories that are currently planned for construction around the world will be introduced.

1.2.1 International Linear Collider (ILC)

The International Linear Collider (ILC) project[12] is a future energy-frontier electron-positron linear collider. The project is being considered for construction in the Kitakami Mountains in Japan, stretching from Iwate to Miyagi prefectures. Fig. 1.5 shows the schematic diagram of the ILC accelerator. The operation at $\sqrt{s} = 250$ GeV is planned, and upgrades are planned for 350 GeV, 500 GeV, and 1 TeV. The superconducting RF is used for the accelerator, and the linear accelerator part can be extended and/or upgraded to update the center-of-mass energy. The linearity of the accelerator makes it easy to control the polarization of electrons and positrons to promote or inhibit specific reactions.

1.2.2 Circular Electron Positron Collider (CEPC)

The Circular Electron Positron Collider (CEPC) [13] is the electron-positron circular collider with the circumference of 100 km that is planned to be built in China. After the operation of the CEPC, the proton-proton collider (Super Proton Proton Collider, SppC) will replace the accelerator in the tunnel. The configuration of the CEPC accelerator is shown in Fig. 1.6. The accelerator consists of the linear accelerator section, the booster, the main

Figure1.5 Schematic layout of the ILC at $\sqrt{s} = 250$ GeV. ©Rey.Hori/KEK

ring, and two collision sites, each of which is equipped with the detector. The main ring is a double ring consisting of an electron ring and a positron ring.

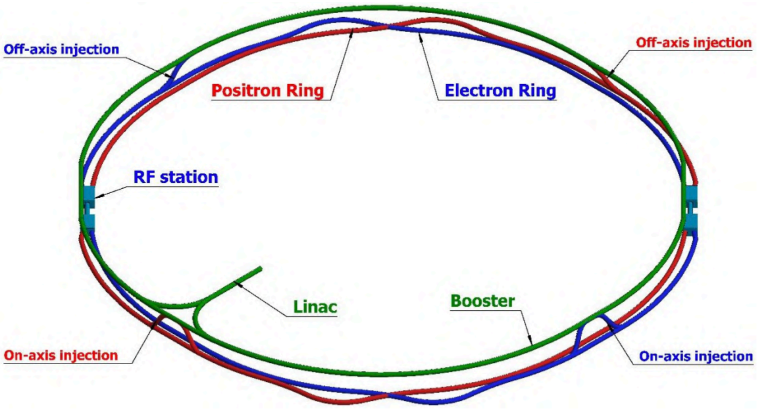

Figure1.6 Configuration for the CEPC accerelator [13]

1.3 Physics at Higgs factories

In the Higgs factories, the Higgs bosons are produced in large quantities, and the Higgs coupling constant is measured to verify the deviation from the Standard Model with very high accuracy. The key is to measure the cross section and decay width of the Higgs boson independent of the physics model. It is also possible to search for new particles by taking advantage of the clean environment of electron-positron collisions, and the search range can be extended by upgrading the center-of-mass energy. The following is a list of typical targets for each center-of-mass energy.

1.3.1 $\sqrt{s} = 250$ GeV

In the Higgs factories, the key is to operate the collider at the center-of-mass energy around 250 GeV. This is because the Higgs production cross section by the Higgs-associated production process ($e^- e^+ \to Zh$: Fig. 1.7 left) is the largest at 250 GeV (see Fig. 1.8). The mass and production cross section of the Higgs boson can be measured precisely without depending on the decay mode of the Higgs boson, taking advantage of the fixed energy of the initial state due to electron-positron collisions and the simplicity of the reaction.

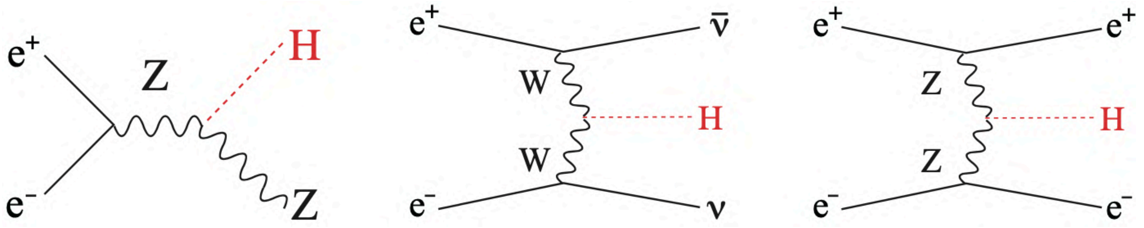

Figure1.7 Feynman diagrams for the three major Higgs production processes at the ILC[10]

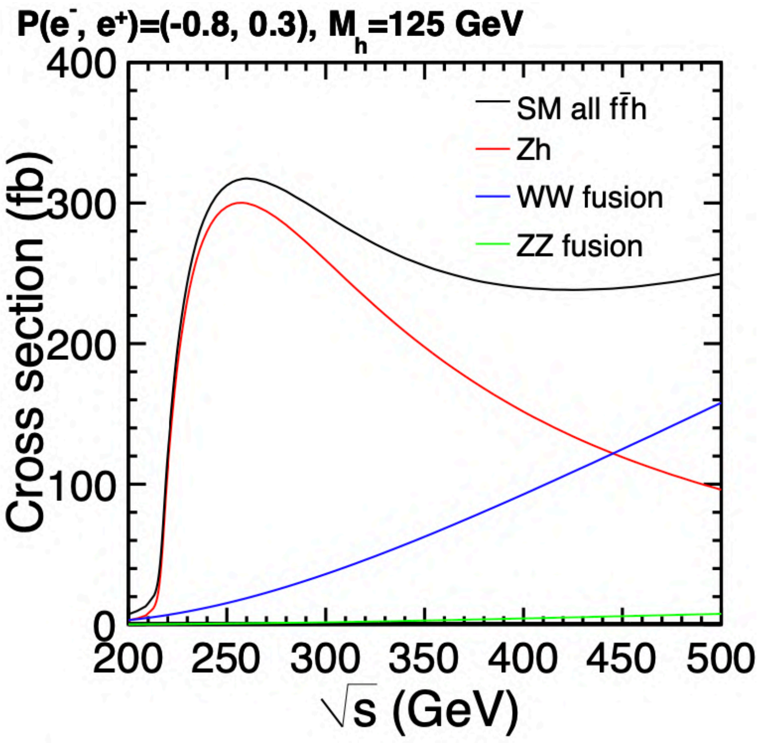

Figure1.8 Production cross section for the process[10]

Higgs couplings

The goal of the ILC program at $\sqrt{s} = 250$ GeV is to determine the various Higgs couplings with high precision in model-independent way. In the Standard Model, all Higgs boson couplings are predicted by the value of the Higgs boson mass, which is known at the LHC to an accuracy of 0.2% [9]. Any deviation from these predictions would imply new physics beyond the Standard Model. The expected value of the deviations is small in a typical

BSM scenario. Therefore, one of the main goals of future e^+e^- colliders is to achieve an accuracy of $O(1\%)$ in the measurement of the Higgs boson coupling.

The clean environment of the ILC allows us to measure the major decay modes in a high accuracy such as $h \to b\bar{b}$, $h \to WW^*(W^{(*)} \to q\bar{q})$, and so on. In addition, with the use of high performance detectors, we can see $h \to c\bar{c}$ and $h \to gg$, decays. This is very difficult at the LHC. Fig. 1.9 shows Lego plots of the distributions of the b-like and c-like variables against Monte Carlo data, various Higgs decays, and a template of the Standard Model background for the fit. The different decay modes and backgrounds of the Higgs boson show distinct distributions and can be separated from each other. It should be noted that in the $\sigma \times BR$ measurement, the main decay modes, $Z \to q\bar{q}$ and $Z \to \nu\bar{\nu}$ decays, can be used to increase the statistics. This is also realized by the clean environment of the ILC.

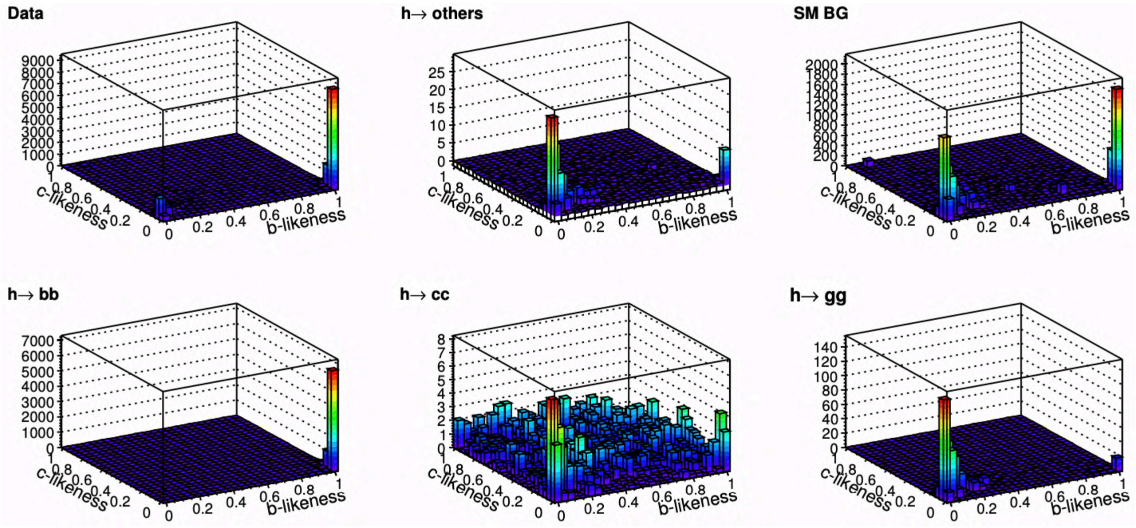

Figure1.9 Two-dimensional images of the three-dimensional template samples as a function of b-likeness v.s. c-likeness. The bottom row shows Higgs decays, left to right, to $b\bar{b}$, $b\bar{b}$, and gg. The top row shows, left to right, the full Monte Carlo Higgs sample, the Higgs decays to non-2-jet modes, and the Standard Model background.[10]

Effective Field Theory (EFT)

The coupling strength of the Higgs boson to $A\bar{A}$ is obtained from the partial width $\Gamma(h \to A\bar{A})$:

$$BR(h \to A\bar{A}) = \Gamma(h \to A\bar{A})/\Gamma_h \tag{1.10}$$

where Γ is the total width of the Higgs boson. The SM width of the Higgs boson at 125 GeV is 4.1 MeV, which is too small to be measured directly. Therefore, the width of the Higgs boson has to be determined indirectly, which requires a model formulation.

The width is usually determined using the κ parametrization. Assuming that the Higgs couplings for each species A are modified by the multiplication factor κ_A, the parameterization can be written by:

$$\frac{\Gamma(h \to ZZ^*)}{SM} = \kappa_Z^2, \frac{\sigma(e^+e^- \to Zh)}{SM} = \kappa_Z^2 \tag{1.11}$$

where SM means the prediction in the Standard Model. A sufficient number of measurements are available in the e^+e^- collider experiment to determine all the κ_A. The ratio $\sigma(e^+e^- \to Zh)/BR(h \to ZZ^*)$ is independent of κ_Z

and can be directly used to determine the Higgs width. However, at 250 GeV ILC with 2 ab^{-1} data, the statistics to measure $BR(h \to ZZ^*)$ is limited, and the accuracy of the width determination is compromised.

The κ formalism is not exactly model independent. In case of the Higgs coupling to ZZ, the Higgs boson has two different structures:

$$\delta L = \frac{m_z^2}{v}(1+\eta_Z)hZ_\mu Z^\mu + \zeta_Z \frac{1}{v} hZ_{\mu\nu}Z^{\mu\nu} \tag{1.12}$$

where the coefficients η_Z and ζ_Z mean independent parameters derived from the new physics. The coupling to WW has a similar structure with parameters η_W and ζ_W. The parameters η_Z and ζ_W are expected to be zero in the κ formalism. The effect of the term with the ζ_Z depends on the momentum configuration of the vector boson because the ζ_Z depends on the momentum:

$$\frac{\Gamma(h \to ZZ^*)}{SM} = (1 + 2\eta_Z - 0.50\zeta_Z) \tag{1.13}$$

$$\frac{\sigma(e^+e^- \to Zh)}{SM} = (1 + 2\eta_Z + 5.7\zeta_Z) \tag{1.14}$$

for a 125 GeV Higgs boson and $\sqrt{s} = 250$ GeV. Then, the Higgs width cannot be uniquely determined by the ratio in Equation 1.10.

This problem is solved by the Effective Field Theory (EFT) formalism. The new particles derived from the new physics are expected to be heavy because the LHC experiment has not discovered them yet. If the new particles are sufficiently heavy, the physics of the 125 GeV Higgs boson can be described by integrating these particles out of the Lagrangian and replacing their effects with an extension of the Standard Model operator. The gauge-invariant Lagrangian in the Standard Model consists of the operators up to four dimensions. The additional operators in six or more dimensions corrects the Standard Model. If the minimum mass of the new particle is M, the six-dimensional operators have coefficients proportional to m_h^2/M^2, which is the first order of an expansion in m_h^2/M^2. The operators in 8 or more dimensions is expected to be a further factor of m_h^2/M^2. Therefore, it is proposed to parametrize the effects of the new physics on the Higgs boson by writing an effective Lagrangian with $SU(3) \times SU(2) \times U(1)$-invariant operators with 6 dimensions. This is called the Standard Model Effective Field Theory (EFT) formalism.

Expected precision for Higgs boson couplings

The process $e^+e^- \to Zh$ has the maximum cross section at $\sqrt{s} = 250$ GeV, and about half a million Zh events were obtained from an integrated luminosity of 2 ab^{-1}. This makes it possible to precisely measure the inclusive cross section σ_{Zh} and the decay rates $\sigma_{Zh} \times BR$ for various decay modes using the recoil mass method. The $\sigma_{Zh} \times BR$ is measured to be 1.0% at $\sqrt{s} = 250$ GeV [14]. Fig. 1.11 shows the distribution of the recoil mass.

Table 1.1 shows the expected precisions for Higgs boson couplings in the κ formalism. All of the Higgs boson couplings can be calculated via a global fit in the κ formalism using the basic observables of σ and $\sigma \times BR$. The total width of the Higgs boson is written by:

$$\Gamma_h = \frac{\Gamma_{ZZ}}{BR_{ZZ}} = \frac{\Gamma_{WW}}{BR_{WW}} \tag{1.15}$$

where Γ_{ZZ} (Γ_{WW}) is the partial decay width to ZZ^* (WW^*). In the κ formalism, Γ_{ZZ} (Γ_{WW}) is proportional to the square of the $\kappa_Z(\kappa_W)$, which is proportional to the $\sigma_{Zh}(\sigma_{\nu\nu h})$:

$$\Gamma_{ZZ} \propto \kappa_Z^2 \propto \sigma_{Zh}(\Gamma_{WW} \propto \kappa_W^2 \propto \sigma_{\nu\nu h}) \tag{1.16}$$

The other couplings κ_A and partial decay widths Γ_{AA}, where $A = b, c, g, \tau, \mu, \gamma$, are written by:

$$\kappa_A^2 \propto \Gamma_{AA} = \Gamma_h \times BR_{AA} \tag{1.17}$$

κ_Z can be determined precisely with accuracy of 0.38% at $\sqrt{s} = 250$ GeV, while the other couplings κ_A are determined to better than $\sim 2\%$.

Table 1.1 also shows the expected precisions of Higgs boson couplings in the EFT formalism. Fig. 1.10 shows the illustration and comparison with the predictions of the uncertainties of the Higgs couplings at the HL-LHC. In the EFT formalism, a larger global fit to the Higgs boson couplings can be used. This fit includes the basic observables of σ and $\sigma \times BR$, additional observables from the $e^+e^- \to Zh$ reaction, and observables from the electroweak precision physics and $e^+e^- \to W^+W^-$ reaction. The EFT greatly improves the measurement of the Higgs boson couplings. The details is written in [14][15].

Table1.1 Projected relative errors for Higgs boson couplings and other Higgs observables, in %, for fits in the κ and EFT formalisms. The ILC250 columns assume a total integrated luminosity of 2 ab^{-1} at $\sqrt{s} = 250$ GeV. The ILC500 columns assume a total integrated luminosity of 200 fb^{-1} at $\sqrt{s} = 350$ GeV, and a total integrated luminosity of 4 ab^{-1} at $\sqrt{s} = 500$ GeV. Three observables at the HL-LHC, $BR_{\gamma\gamma}/BR_{ZZ}$, $BR_{\gamma Z}/BR_{\gamma\gamma}$ and $BR_{\mu\mu}/BR_{\gamma\gamma}$, are included in all of the fits. The effective couplings $g(hWW)$ and $g(hZZ)$ are defined as proportional to the square root of the corresponding partial widths. The last two lines give 95% confidence upper limits on the exotic branching ratios. [16]

	ILC250		+ILC500	
	κ fit	EFT fit	κ fit	EFT fit
$g(hbb)$	1.8	1.1	0.60	0.58
$g(hcc)$	2.4	1.9	1.2	1.2
$g(hgg)$	2.2	1.7	0.97	0.95
$g(hWW)$	1.8	0.67	0.40	0.34
$g(h\tau\tau)$	1.9	1.2	0.80	0.74
$g(hZZ)$	0.38	0.68	0.30	0.35
$g(h\gamma\gamma)$	1.1	1.2	1.0	1.0
$g(h\mu\mu)$	5.6	5.6	5.1	5.1
$g(h\gamma Z)$	16	6.6	16	2.6
$g(hbb)/g(hWW)$	0.88	0.86	0.47	0.46
$g(h\tau\tau)/g(hWW)$	1.0	1.0	0.65	0.65
$g(hWW)/g(hZZ)$	1.7	0.07	0.26	0.05
Γ_h	3.9	2.5	1.7	1.6
$BR(h \to inv)$	0.32	0.32	0.29	0.29
$BR(h \to other)$	1.6	1.6	1.3	1.2

Precision measurement for Higgs mass

In the mass measurement, the decay mode of $e^-e^+ \to Zh$, $Z \to l^-l^+ (l = e, \mu)$ is used (recoil mass method), which is not affected by the decay mode of the Higgs boson because only the leptons produced in the Z decay are used. The the recoil mass in the Higgs-associated production process is calculated by:

$$m_h = \sqrt{(\sqrt{s} - (E_{l^-} + E_{l^+}))^2 - |\vec{p}_{l^-} + \vec{p}_{l^+}|^2} \tag{1.18}$$

The uncertainty in the mass of the Higgs boson (δm_h) is a source of systematic error in predicting the Higgs boson couplings. In most cases, the uncertainties in the Higgs boson mass, δm_h, is sufficient in 0.2%, except the

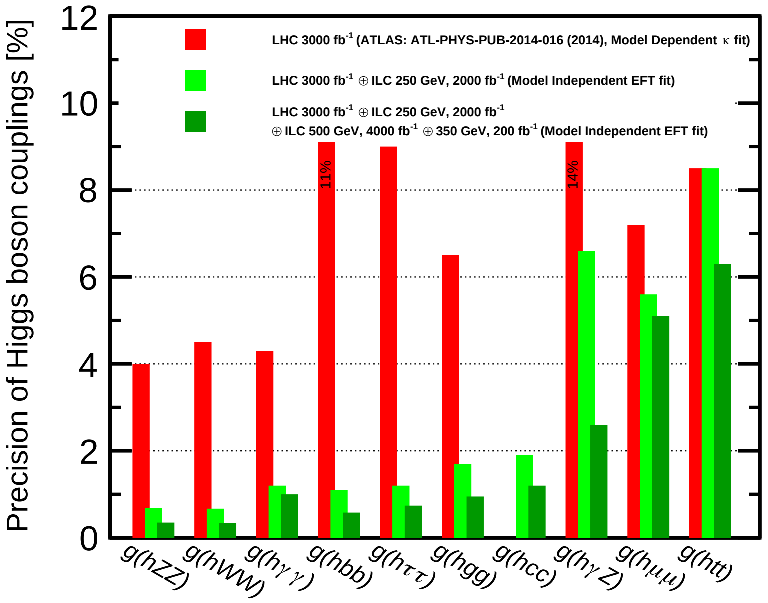

Figure1.10 Illustration of the Higgs boson coupling uncertainties in the EFT formalism, and comparison of these projections to the results of model-dependent estimates for HL-LHC uncertainties. [16]

processes of $h \to ZZ^*$ and $h \to WW^*$. It was pointed out in [17] that:

$$\delta_W = 6.9 \times \delta m_h, \delta_Z = 7.7 \times \delta m_h \tag{1.19}$$

where δ_W and δ_Z are the relative errors for $g(hWW)$ and $g(hZZ)$ respectively. The mass of the Higgs boson can be measured very precisely at the 250 GeV ILC. Fig. 1.11 shows the spectrum of the recoil mass using the leptonic recoil channel. A very clean Higgs signal protruding as a sharp peak above the background can be seen. The key point is that we can capture the production of the Higgs boson without seeing the decay of the Higgs boson at all. This allows us to measure the Higgs mass with an accuracy of 14 MeV. This results in systematic errors for δ_W and δ_Z of 0.1%.

1.3.2 $\sqrt{s} = 500$ GeV

Direct measurement for triple Higgs coupling

The triple Higgs coupling can be measured by the $e^-e^+ \to Zhh$ and $e^-e^+ \to \nu\bar{\nu}hh$ process shown in Fig. 1.12. The cross section reaches the maximum at around $\sqrt{s} = 500$ GeV. Combining the three channels corresponding to the different Z decay modes $Z \to l^+l^-$, $\nu\bar{\nu}$, and $q\bar{q}$, the process can be detected with a 5σ excess significance at beam polarization $(P_{e^-}, P_{e^+}) = (-0, 8, +0.3)$ and integrated luminosity 2 ab^{-1}, and the cross section can be measured as $\Delta\sigma/\sigma = 0.27$. However, there is a large contribution from the background diagram without self-coupling, and the relative error in self-coupling λ is $\Delta\lambda/\lambda = 0.44$ with appropriate event weighting to increase the contribution from the self-coupling diagram.

Direct measurement for top quark Yukawa coupling

Since the production threshold of the $e^-e^+ \to t\bar{t}h$ process is $\sqrt{s} = 470$ GeV, as shown in Figure 1.13, the top Yukawa coupling can be directly measured. Since the contribution from the irrelevant h-off-Z diagram can be neglected at $\sqrt{s} = 500$ GeV, the top Yukawa coupling g_t can be extracted by simply counting the number of signal events.

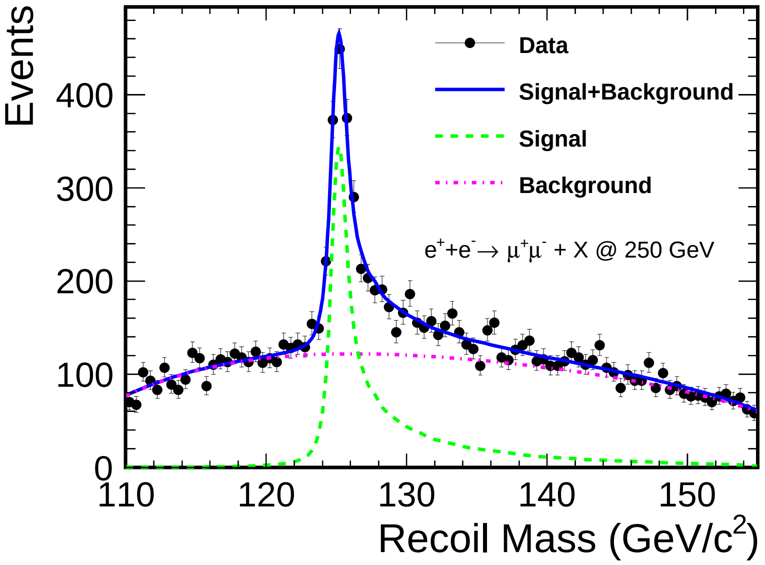

Figure1.11 Higgs recoil mass distribution in the Higgsstrahlung process $e^- e^+ \to Zh$. [18]

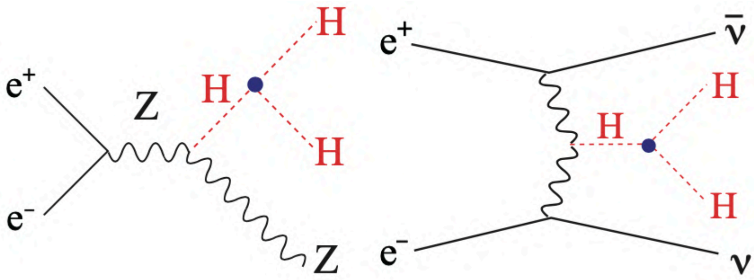

Figure1.12 Relevant diagrams containing the triple Higgs coupling[10]

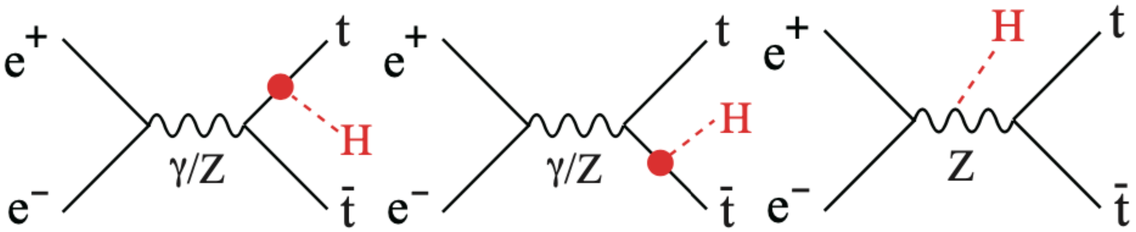

Figure1.13 Three diagrams contributing to the $e^- e^+ \to t\bar{t}h$ process[10]

WW fusion and the hWW coupling

The WW fusion process takes over the Higgs-strahlung process around $\sqrt{s} = 450$ GeV. The cross section of the WW fusion process is about 160 fb at $\sqrt{s} = 500$ GeV. This large cross section and the larger luminosity allows the hWW coupling to be directly measured with high precision. In terms of the Higgs cross section and branching ratio, the quantities to be measured are described

$$\sigma(\nu\bar{\nu}h) \cdot BR(h \to b\bar{b}) \sim \Lambda(h \to WW^*) \cdot BR(h \to b\bar{b}) \tag{1.20}$$

Combining this with the direct measurement of the branching ratio at $\sqrt{s} = 250$ GeV allows us to determine the cross section $\sigma(\nu\bar{\nu})$ with an accuracy of 2.7%, which corresponds to an expected error in the hWW coupling of $\Delta g_{hWW}/g_{hWW} = 1.4\%$. A large data sample of the fusion process is also useful to improve the accuracy of the

$h \to WW^*$ branching ratio. Replacing ZZ with WW, we obtain the full width of the Higgs $\Delta\Lambda_h/\Lambda_h \sim 6\%$.

1.3.3 $\sqrt{s} > 1$ TeV

In the energy region above 1 TeV, more precise measurements of the Higgs self-coupling and total decay width will be possible. In addition, it is possible to search for the direct production of unknown heavy new particles from the single photon production process in the initial state, and to search for new particles indirectly by precisely measuring the coupling between the Higgs boson and other particles and verifying the deviation from the value predicted by the Standard Model.

The results of the ILC can also be described as a precise test of the Standard Model relationship that the Higgs coupling for each particle is exactly proportional to the mass of that particle. The uncertainty of these tests is shown in Fig. 1.14. The ILC provides the understanding of the nature of the newly discovered bosons and their impact on the puzzle of electroweak symmetry breaking.

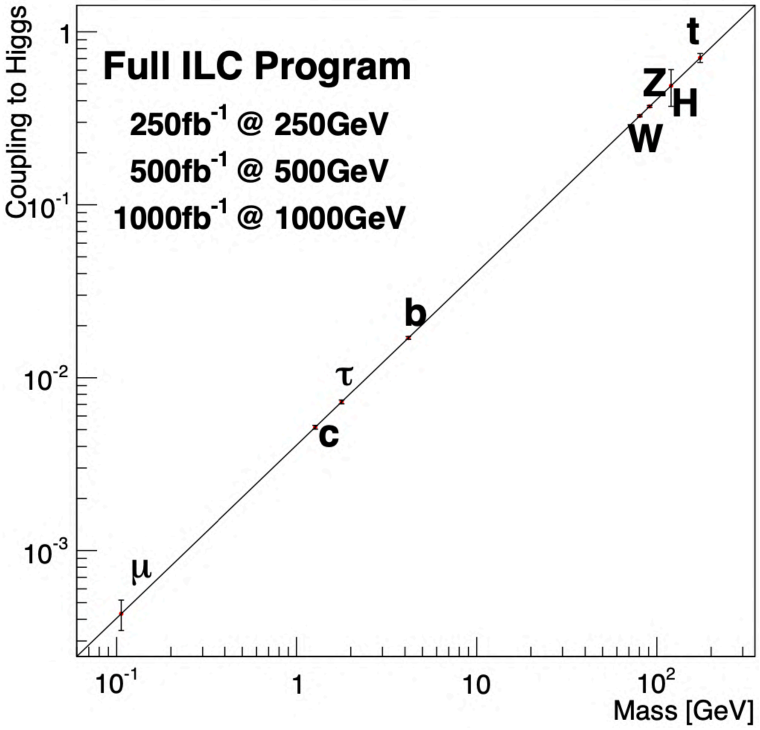

Figure1.14 Expected precision from the full ILC program of tests of the Standard Model prediction that the Higgs coupling to each particle is proportional to its mass. The normalization is different from each particle.[10]

Chapter 2

International Linear Collider (ILC)

This chapter describes the components and details of the ILC accelerator and detector as an example of the Higgs factory. However, the method of the beam generation and the design of the accelerator varies from accelerator to another. On the other hand, the detectors are quite similar in all the Higgs factories because the physics to be measured is the same. In the Higgs factory, the high-precision detector is required for the precise measurement of the Higgs boson.

2.1 Accelerator

The ILC beam has a bunch-train structure consisting of multiple bunches; a train of 1312 bunches collide at a frequency of 5 Hz. Since it is a linear accelerator, it is easy to control the spin polarization of the particles in the beam, and in the current design, the electron and positron polarization will be controlled to $(P_-, P_+) = (\mp 0.8, \pm 0.3)$, respectively. The spin polarization is defined by N_R and N_L, where N_R and N_L are the number of right- and left-polarized particles, respectively.

$$P = \frac{N_R - N_L}{N_R + N_L} \tag{2.1}$$

At the high energy physics, the ability to control the polarization can, for example, increase the fraction of reactions involving W bosons (e.g., $e^-e^+ \to \nu\bar{\nu}h$) where only left-handed electrons are involved when P_- is negative compared to the unpolarized case. Alternatively, when P_- is positive, it is possible to suppress the background events involving W bosons in the $e^-e^+ \to Zh$, $Z \to ll$ processes.

In the ILC, the process from the beam generation to collision is carried out by the following four elements.

- Electron and positron source
- Dampling rings
- Main linear accelerator
- Beam-delivery system

2.1.1 Electron and positron source

Electron source

In the electron source, a polarized laser is used to generate polarized electrons. Fig. 2.1 shows the configuration of the electron source. When GaAs is irradiated by a polarized laser using the DC gun, polarized electrons of 140-160 keV are emitted due to the photoelectric effect. Depending on the polarization scenario of the ILC, the target electron polarization ratio is ±80%. The polarized electrons are first placed in the normal-conducting acceleration cavity, where they are accelerated to 76 MeV while forming a bunch of about 3 × 1010 electrons. Then, the energy and incident direction of the polarized electrons are uniformly aligned by the energy collimator, and the electrons are further accelerated to 5 GeV in the superconducting acceleration cavity. Before being injected into the damping ring, the spins are also vertically aligned by the superconducting solenoid.

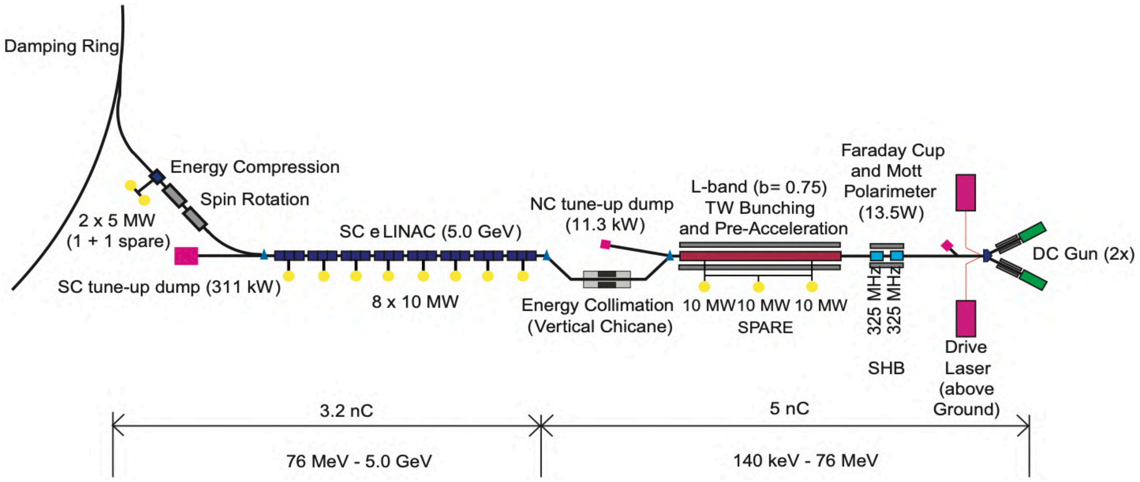

Figure2.1 Schematic view of the polarised electron source[19]

Positron source

The positron source utilizes polarized electrons generated by the electron source. The electrons are finally accelerated to 150 GeV in the main linear accelerator, as described below. Here, the electrons pass through a spiral device called an undulator. The undulator is located at the position shown in Fig. 2.2.

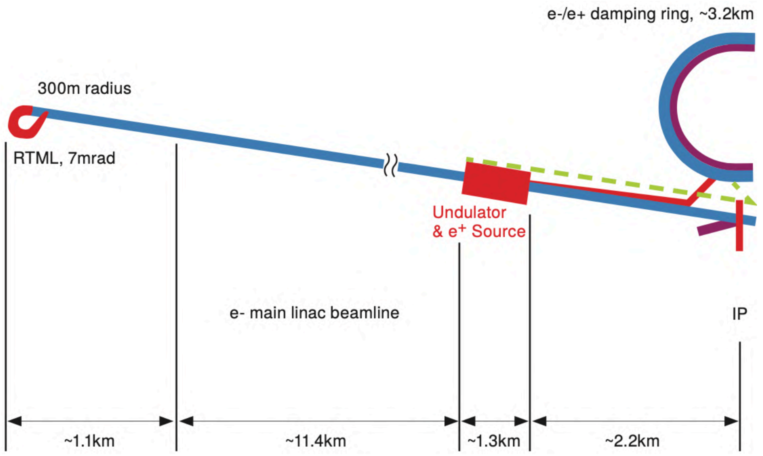

Figure2.2 Layout of positron system[19]

Fig. 2.3 shows an overview of the positron source. In the undulator, the direction of the magnetic field alternates, and meandering electrons emit energetic photons (10-30 MeV) due to the bremsstrahlung. By injecting these photons to a 1.4 cm-thick titanium alloy disk, an electromagnetic shower is generated, which can produce a large number of electron-positron pairs. After acceleration to 125 MeV, the electrons and positrons are separated by applying a magnetic field to produce a positron beam. The resulting positrons are accelerated to 400 MeV in the normal conduction acceleration cavity, as are the electrons, and further accelerated to 5 GeV in the superconducting acceleration cavity, where their spin direction and energy are aligned. The accelerated positrons are injected into the damping ring by the kicker system that generates an instantaneous magnetic field.

It is said to be capable of ±30% positron polarization at the basic design stage, but with space for additional undulators. It is expected that up to ±60% polarization will be possible after the upgrade. In that case, however, a photon collimator will be required in front of the titanium target.

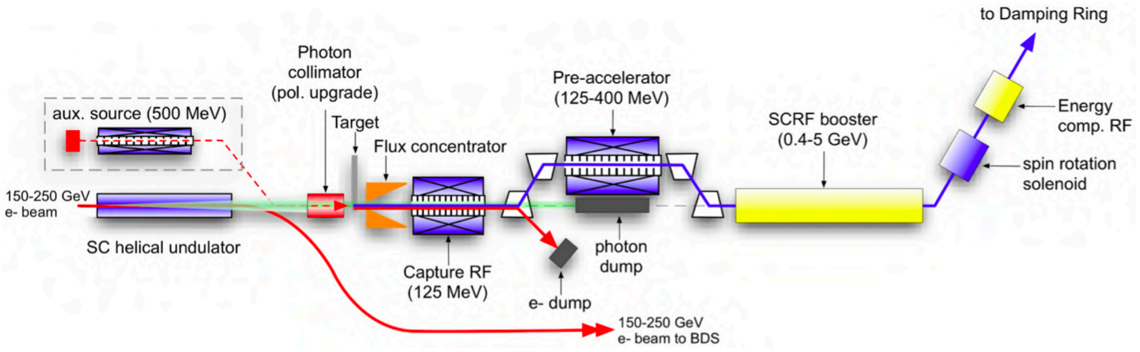

Figure2.3 Overall layout of the positron source[19]

2.1.2 Damping ring

The electrons and positrons accelerated up to 5 GeV are injected into the damping ring. The purpose of the damping ring is to reduce the emittance. The emittance is a parameter of the dispersion of particles in the beam, and is defined as the area of the beam in phase space.

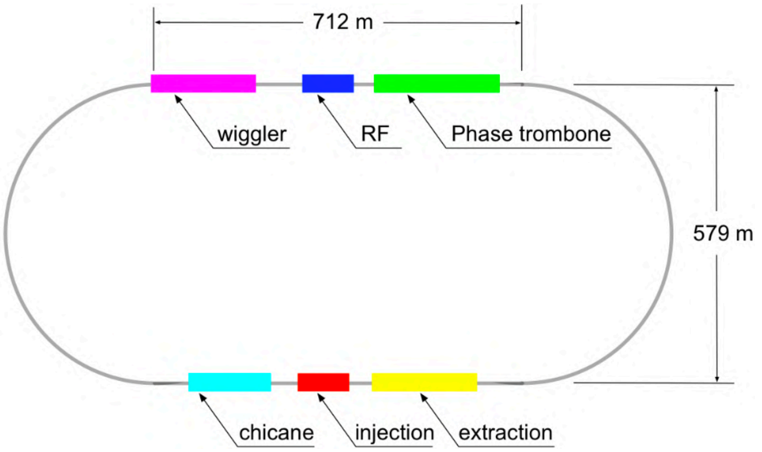

Figure2.4 Schematic of the damping-ring layout[19]

Fig. 2.4 shows an overview of the damping ring. The electron or positron beam entering the damping ring travels around the ring, which is about 6.7 km in circumference, for about 200 ms. During this time, the beam undergoes the bremsstrahlung in the curved part of the ring and is accelerated in the straight part. The beam, whose momentum is reduced by the bremsstrahlung, recovers only the momentum in the direction of the reference orbit in the acceleration part, resulting in a decrease in emittance. By repeating this process, the position and momentum of the particles in the beam are adjusted, and a low-emittance beam can be realized. The bunch is then ejected by the kicker again and transported to the main linear accelerator.

2.1.3 Main linear accelerator

As shown in Fig. 2.5, the beam from the damping ring is transported to the end of the accelerator (ELTL) and the direction of travel is reversed (ETURN). The 5 GeV beam is accelerated to 15 GeV by compressing the bunch length from several mm to several hundred μm in EBC1 and EBC2. The beam is then accelerated to its maximum energy using the superconducting acceleration cavity of the Main Linear Accelerator (Main Linac).

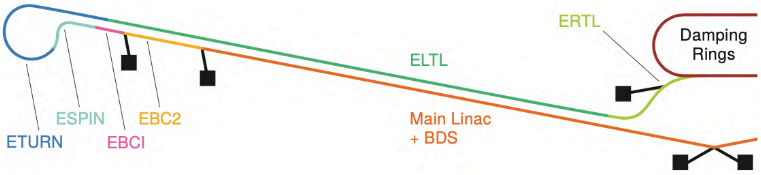

Figure2.5 Schematic of the main linac layout [19]

A 1 m long niobium superconducting acceleration cavity (Fig. 2.6) is used as the acceleration cavity. About 800 cryomodules consisting of nine acceleration cavities and the superconducting cooling system are connected and installed in the tunnel, and the cavity is operated at an ultra-low temperature of 2 K with high frequency. The design value of the acceleration gradient is 31.5 MV/m on average.

Figure2.6 A superconducting nine-cell 1.3 GHz resonator (cavity) [20]

2.1.4 Beam-delivery system

In the beam-delivery system, the accelerated beam is narrowed down and transported to the interaction point for collision, and the remaining particles are stopped by the beam dump. An overview of the delivery system is shown in Fig. 2.7. During the beam delivery, the beam energy and spread are measured, and the information is fed back to the final convergence system for fine adjustment. In the final beam convergence system, the beam is focused on by a quadrupole magnet to the rms of beam size of 516 nm and 7.66 nm in x and y axis respectively. The electrons and positrons collide at an angle of 14 mrad at the interaction point (Fig. 2.8). The beam is crossed at an angle to facilitate the collection of non-collided particles.

2.2 Detector

Two detector concepts are proposed: the International Large Detector (ILD) (Fig. 2.9), which is mainly developed in Japan and Europe, and the Silicon Detector (SiD), which is mainly developed in the U.S. The ILD is larger than the SiD and can acquire more spatial information by using gas TPC. When the ILC is in operation, the two detectors are placed alternately on the beamline by the push-pull system, and the results from both detectors are used for complementary verification. The DAQ of the ILC is designed to reduce power consumption by transferring data

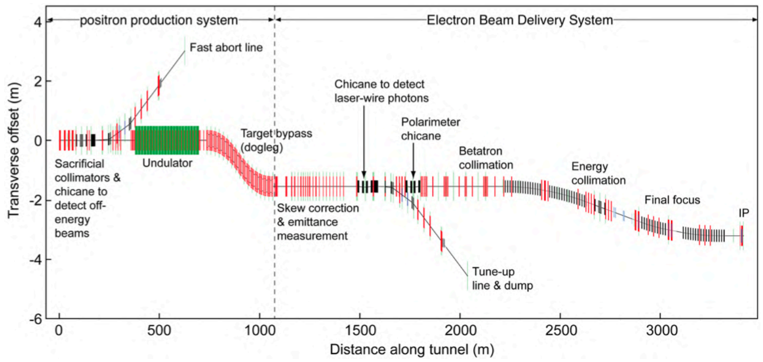

Figure2.7 Schematic of the beam-delivery system layout [19]

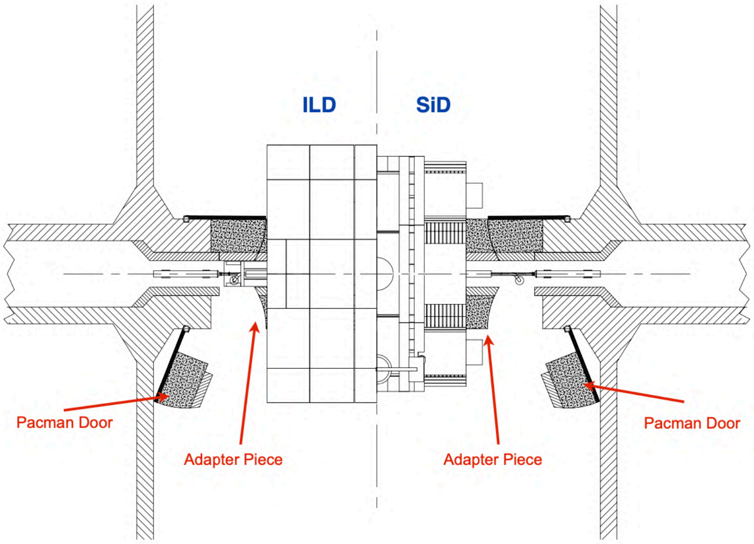

Figure2.8 Design of the interaction point, detector, and shielding [19]

during the 5 Hz bunch train. The length of the bunch train is 1 ms out of 200 ms, so the electric power is turned on only for about 1% during the operation, called power pulsing, which reduces power consumption. In particular, the components of the ILD will be discussed.

The structure of the ILD is shown in Fig. 2.10. From the decay point (IP) to the outside of the detector, the structure is as follows.

- Vertex detector
- Silicon tracking system; Silicon detector and Time Projection Chamber (TPC)
- Calorimeter; Electromagnetic calorimeter (ECAL) and Hadron calorimeter (HCAL)
- Solenoid coil
- Muon detector

2.2.1 Vertex detector

The vertex detector is a semiconductor detector used to measure the production points of primary particles and the decay points of short-lived particles produced by beam collisions. The decay point is reconstructed by

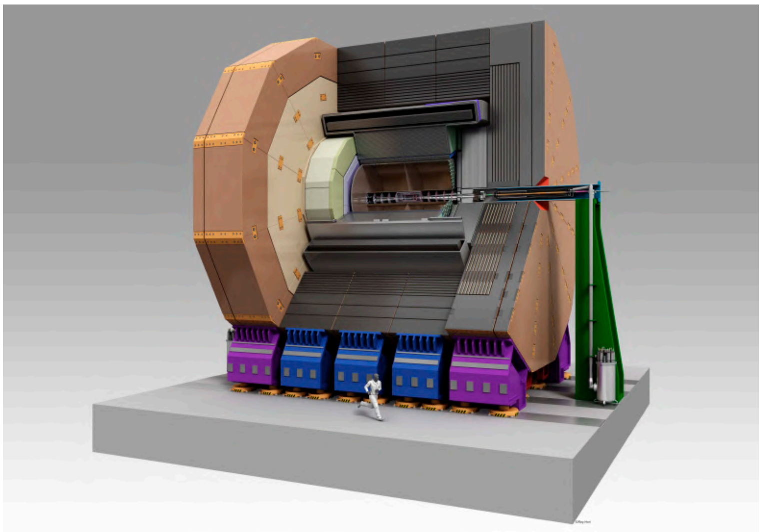

Figure2.9 View of the ILD detector concept [21]

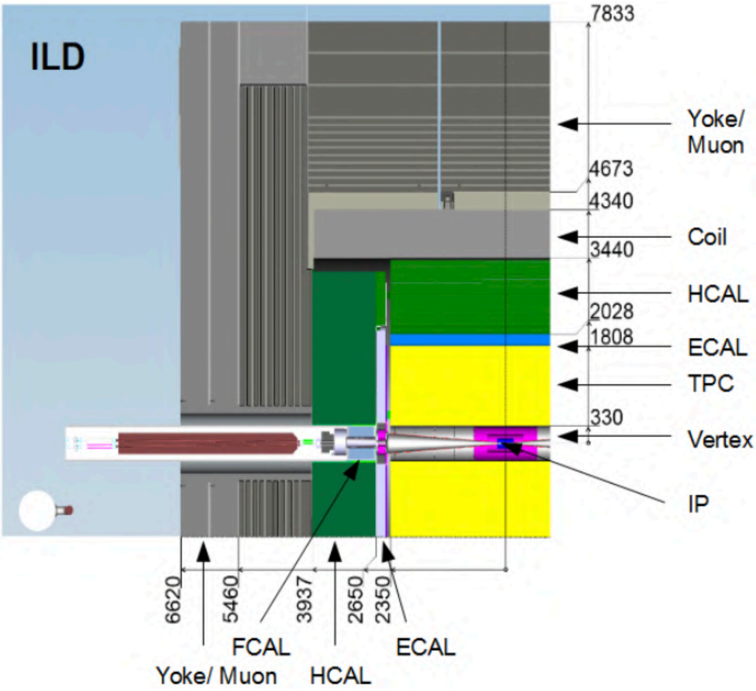

Figure2.10 Quadrant view of the ILD detector concept [21]

connecting the points where the particles pass as the track. It consists of three ladder layers in a cylindrical concentric shape, and each ladder has a two-layer structure with pixel sensor layers placed 2 mm apart on both sides (Fig. 2.11). In this way, six positions are detected for each charged particle track. The ladder of the first ladder layer has half the length of the other two ladders to reduce the background. Three types of pixel sensors are being investigated.

- CMOS Pixel Sensors (CMOS)
- Fine Pixel CCD (FPCCD)

- Depleted Field Effect Transistors (DEPFETs)

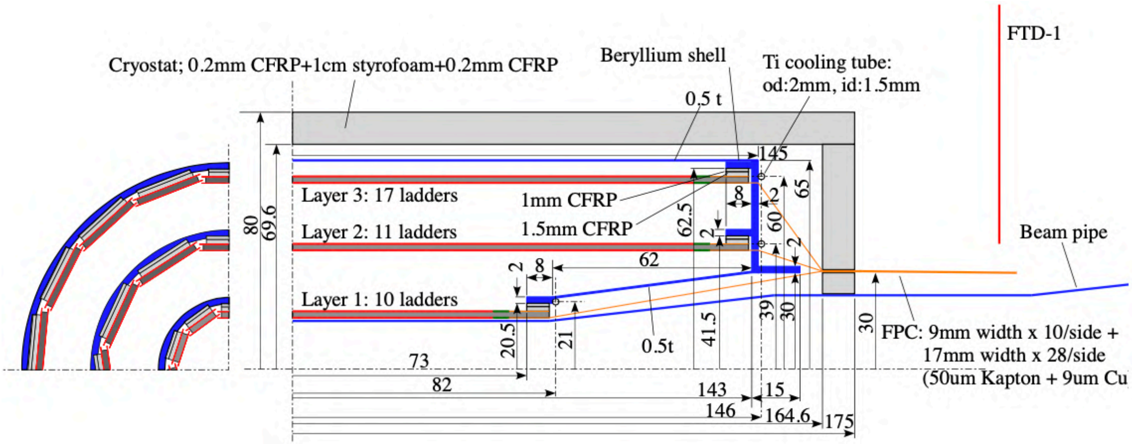

Figure2.11 Mechanical support structure of the ILD vertex detector [21]

2.2.2 Silicon tracking system

The silicon tracking detector is designed to obtain the passage point and time of flights for the track reconstruction. The layout of each detector is shown in Fig. 2.12. By taking advantage of the high position resolution and time stamp of the silicon detector and combining it with the hit information of the TPC, it is possible to obtain a high-definition time stamp of the track.

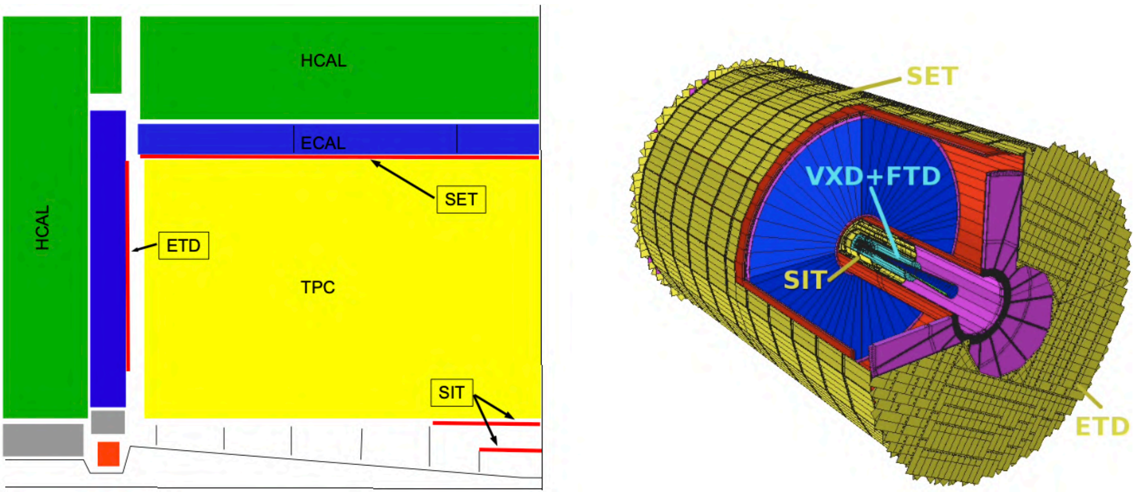

Figure2.12 Layout of the tracking sysytem [21]

2.2.3 Time Projection Chamber (TPC)

The ILD main tracking detector uses a large gas TPC, because the tracking detector must have a low mass in order to accurately measure the energy in the calorimeter. It provides a large number of 3D spatial points and a more continuous track than a silicon detector, thus increasing the position resolution. Fig. 2.13 shows the structure of the TPC. There is a cathode in the center, and electron amplification and detection layers are placed on the plates at both ends. The Micro Pattern Gas Detector (MPGD) such as a Gas Electron Multipliers (GEM) and Micromegas are being investigated for the electron amplification.

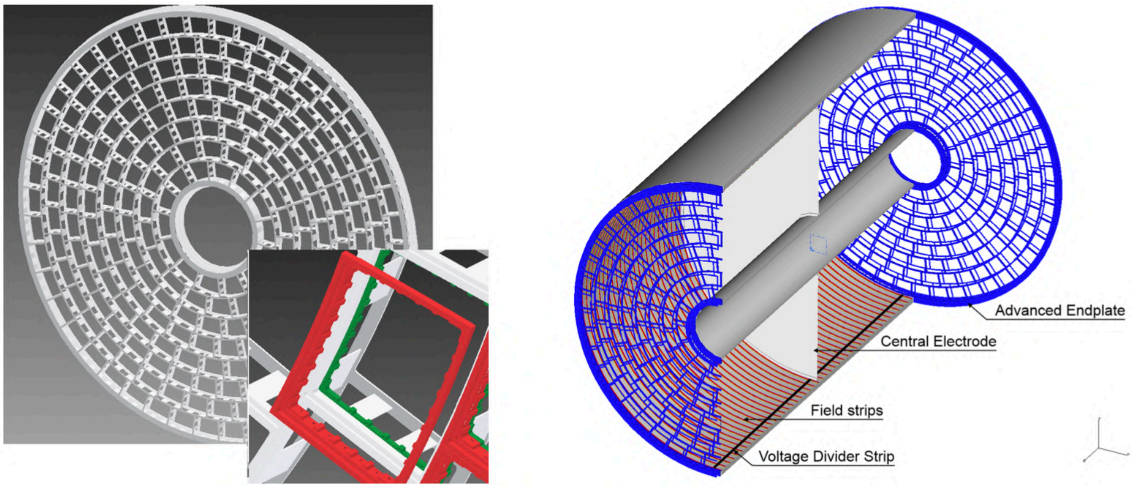

Figure2.13 Structure of the TPC [21]

The inside of the TPC is filled with T2K gas [22], which is a mixture of Ar, CF_4, and isobutane. The ionized electrons generated when charged particles pass through the TPC are drifted by the electric field applied in the direction of the beam axis and detected as signals by the MPGD. This makes it possible to reconstruct the charged particle trajectory in three dimensions using the drift time of the ionized electrons and the two-dimensional signal. In addition, the $\frac{dE}{dx}$ can be calculated by the magnitude of the signal, and the particle can be identified.

2.2.4 Calorimeter

A calorimeter is a detector that measures the energy of a particle. Because of the reconstruction algorithm of the Particle Flow Algorithm (PFA) described in the next section, the ILD calorimeter is divided into an electromagnetic calorimeter, which measures the energy of photons, and a hadron calorimeter, which measures the energy of neutral hadrons. Both calorimeters are sampling calorimeters, with an alternating arrangement of absorber layers that generate showers and detection layers that detect particles in the showers. Incident high-energy particles interact with the absorber layers to create a shower, and the energy of the particles in the shower is measured in the detection layers. The energy of the incident particles is reconstructed from the energy of the shower and its shape. Photons and electrons have a short interaction length due to their electromagnetic interaction, and form a dense shower with a short length and narrow width. On the other hand, hadrons have a small cross section due to their strong interaction, and their showers spread out due to recoil, resulting in large, wide, low-density showers.

The layout of the Electromagnetic CALorimeter (ECAL) within the ILD detectors is shown in Fig. 2.14. The ECAL identifies photons and measures their energies. Tungsten works as an absorber layer. The density of tungsten is larger than that of iron, and its Molière radius is smaller, so it can efficiently generate electromagnetic showers and allows the ECAL to be compact. Several technology options for the detection layer are investigated: one using pixelated silicon detectors (Si-ECAL), one using strips of plastic scintillators and SiPMs (Sc-ECAL), and a hybrid design mixing the two. All of them have a cell size of $5\ \mathrm{mm} \times 5\ \mathrm{mm}$ to measure high-density electromagnetic showers, and can realize a very highly granular calorimeter.

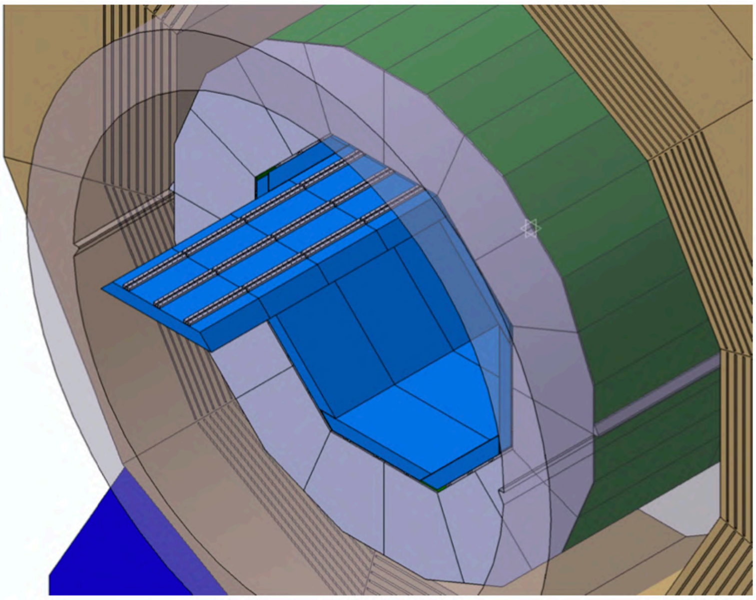

Figure2.14 The electromagnetic calorimeter within the ILD detectors [21]

The layout of the Hadron CALorimeter (HCAL) is shown in Fig. 2.15. The absorber layer is made of iron, which is also suitable for measuring the energy of electromagnetic showers generated by hadronic interactions, and the calorimeter is large enough to capture the hadronic showers. Two technology options of detection layers are considered: a semi-digital type (SDHCAL) that uses a gas RPC with semi-digital readout (2bit) with a $10\ \mathrm{mm} \times 10\ \mathrm{mm}$ cell, and an analogue type (AHCAL) that uses a 30 mm × 30 mm scintillator tile readout by a SiPM.

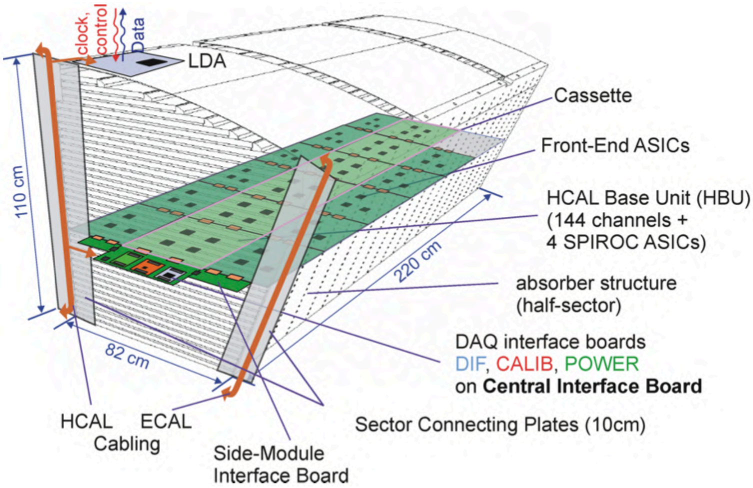

Figure2.15 Arrangement of AHCAL layers [21]

2.2.5 Solenoid coil

3.5 T magnetic field is applied to the entire detector by a superconducting solenoid coil. The momentum is measured by bending the charged particle track. The arrangement of the coils is shown in Fig. 2.16. Unlike conventional detectors, the calorimeters are placed inside the coils for the PFA. In addition, there is an anti-Detector-Integrated-Dipole (anti-DID) on the outside of the coil. It generates a magnetic field to protect the vertex detector and the tracking system from the electron-positron pair background created by the gamma-ray reaction caused by the beam effect.

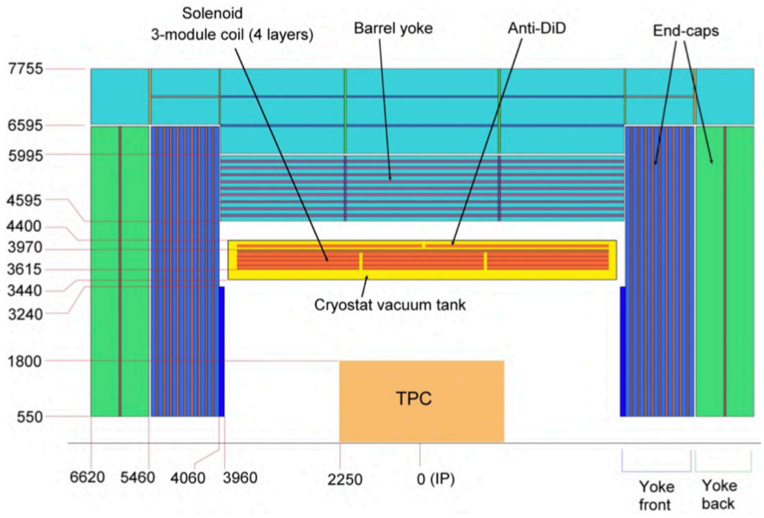

Figure2.16 ILD magnet cross section [21]

2.2.6 Muon detector

The iron yoke and the detection layers are used to measure muons. It is also used as the tail catcher to measure the energy of particles that have passed through the calorimeters. Two technology options of detection layers are being investigated: using a scintillator strip equipped with a wavelength shifting fiber and a SiPM, and using an RPC. As shown in Fig. 2.17, 14 detection layers are inserted between the iron yokes in the cylindrical direction and 12 layers in the beam axis direction. The inner part of the detector, where the detection layers are crowded, is designed as the tail catcher, while the outer part, where the detection layers are separated from each other, is designed for muon detection. The iron yoke serves not only to detect muons and generate hadron showers, but also to confine the magnetic field of the solenoid.

2.3 Particle Flow Algorithm (PFA)

An unprecedented jet energy resolution is required at the ILC to cleanly separate H, W, and Z hadronic decays. Their final states consisting of multiple jets are formed after many interaction processes. Since the invariant masses of the jets are used to identify and reconstruct the particles, the accurate reconstruction of them is very important for precise measurements. The invariant mass of the di-jet is given by

$$M^2 = 2E_1E_2(1 - \cos\theta_{12}) \tag{2.2}$$

where E_1 and E_2 are the jet energies, and θ_{12} is the angle between them. If the angular uncertainty can be neglected, the jet energy resolution σ_E/E can be converted into the mass resolution:

$$\frac{\sigma_M}{M} = \frac{1}{\sqrt{2}}\frac{\sigma_E}{E} \tag{2.3}$$

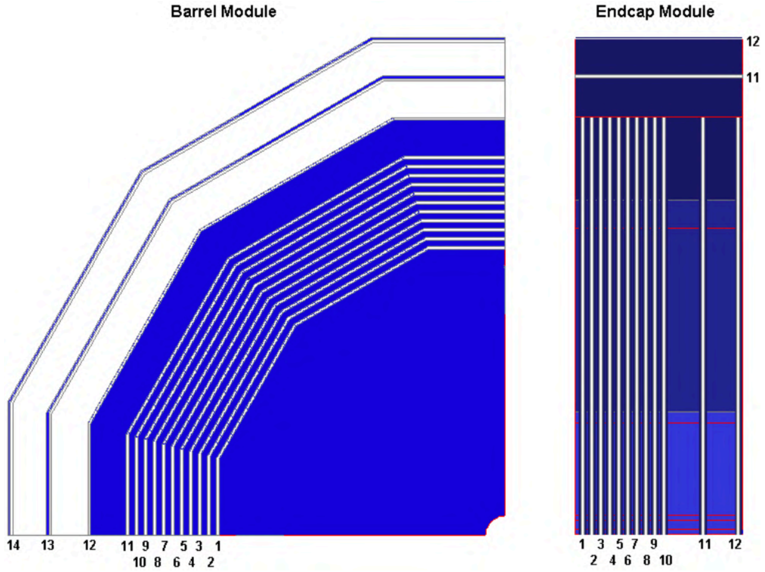

Figure2.17 Sensitive layers of the muon detector [21]

An invariant mass resolution comparable to the gauge boson width:

$$\frac{\sigma_m}{m} = 2.7\% \approx \frac{\Gamma_Z}{m_W} \approx \frac{\Gamma_Z}{m_Z} \tag{2.4}$$

leads to an effective 3.6σ separation of the hadronic decay of the W/Z boson. In the traditional method, the jet energy resolution is written by:

$$\frac{\sigma_E}{E} = \frac{\alpha}{\sqrt{E(\mathrm{GeV})}} \oplus \beta \tag{2.5}$$

where α is the stochastic term and usually greater than 60%, and β is the constant term and usually a few $\%$. To achieve the target of $\sigma_m/m = 2.7\%$, the stochastic term have to be $< 30\%/\sqrt{E(\mathrm{GeV})}$.

Therefore, the ILC is aiming at a jet energy resolution of $\sigma_E/E = 30 - 40\%/\sqrt{E(\mathrm{GeV})}$ so that the decay of the Higgs, and Z/W bosons can be distinguished by reconstructing the invariant masses of the two jets. The requirements for the jet energy resolution are beyond what can be achieved with the current state-of-the-art detectors. An alternative to the classical reconstruction method is developed, the Particle Flow Algorithm (PFA), which provides a significant improvement in the jet energy resolution. The particle flow reconstruction requires a highly granular calorimeter.

2.3.1 Jets

Through a process of the hadronization, quarks are transformed into colorless hadrons, which are observed by detectors. At the hadronization energy scale, the QCD couplings become large. Therefore, these processes cannot be calculated by the perturbation theory. However, a number of phenomenological models have been developed. Although each model has many free parameters and is far from a concrete theoretical description, the experimental data can be described reasonably well by these models.

According to the color confinement, the only state that can exist as a free particle is the colorless state. Therefore, all bound states of quarks and antiquarks are colorless. When quarks and antiquarks are produced in a process such as $e^+e^- \to q\bar{q}$, they separate with equal and opposite momentum in the center-of-mass frame. At distances as short as 1 fm, they can move as quasi-free particles due to the asymptotic degrees of freedom of QCD. As the distance increases, each particle undergoes a hadronization process and materializes as a collimated spray of colorless particles called a jet. Gluons are similarly hadronized.

The mechanism of the jet production can be explained in two steps. In the first step, quarks accelerated over short distances of less than 1 fm in the production process emit gluons. Similar to the bremsstrahlung process, colored particles can also emit gluons. Since the gluons have a color charge, they can also emit additional radiation. This process causes a cascade of particles known as a parton shower.

In the second step, as the produced quarks are further separated, a gluonic flux tube is constructed between each pair, confining the two objects. At distances as large as 1 fm, the energy stored in the color field between the two objects increases to enough energy to produce a new $q\bar{q}$ pair. This causes the color field to split into smaller fields with lower energy, a favorable condition. This process continues until the quark and antiquark energies are sufficiently low to produce a chain of $q\bar{q}$ pairs, which combine into colorless hadrons. The unstable hadrons produced in the hadronization process decay into more stable particles, which are observed by the detector.

2.3.2 Concept of PFA

In order to achieve the jet energy resolution of 3–4%, a method called the Particle Flow Algorithm (PFA) has been devised [23]. As shown in Fig. 2.18 (left), the jet energy was conventionally obtained as the sum of the measured energies in ECAL and HCAL. In a typical jet, about 72% of the energy (62% charged hadrons and 10% neutral hadrons) is measured by HCAL, and the typical resolution of HCAL of $55\%/\sqrt{E(\mathrm{GeV})}$ makes it difficult to achieve the target jet energy resolution. On the other hand, the PFA identifies each particle in the jet and determines its energy and momentum with the most appropriate detector, as shown in Figure 2.18 (right). In the HCAL, only long-lived neutral hadrons (about 10% of the jet energy) are measured. This allows the jet energy resolution to be significantly improved by measuring each particle with a detector having the optimum resolution.

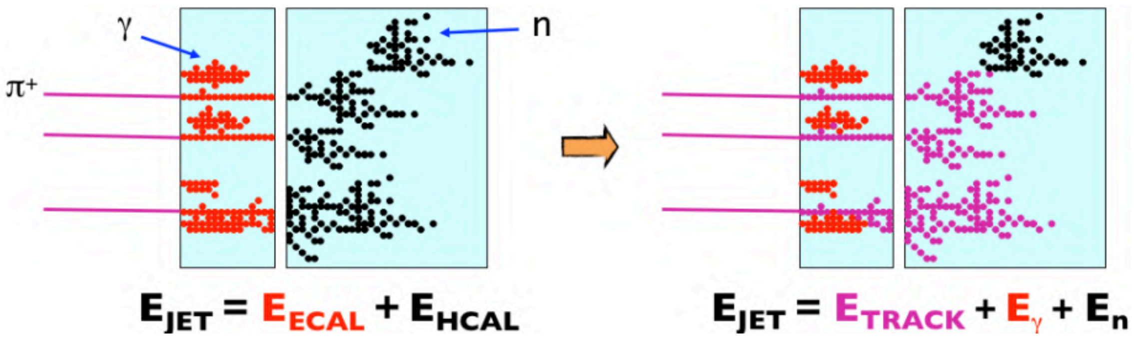

Figure2.18 The concept of the PFA. Charged particles (purple) are reconstructed and measured by the internal tracker, photons (red) by the ECAL, and neutral hadrons (black) by the HCAL. [23]

The PFA reconstructs the particles in the jet from the charged particle tracks obtained by the tracking detector and the shower information obtained by the calorimeter. Particles bent by the magnetic field are reconstructed as charged particles by the internal tracker, and particles unaffected by the magnetic field are reconstructed as neutral particles by the calorimeter. Therefore, it is important to separate the charged particle showers from the neutral particle showers with high accuracy, and a highly granular calorimeter is required for this purpose.

Fig. 2.19 shows the possible errors in the reconstruction using the PFA, which are called confusion. As shown in the left and center figures, when a charged hadron shower and a photon or neutral hadron shower occur near each other, the latter may be recognized as the charged hadron shower. In addition, as shown in the right figure, the tail of a charged hadron shower may be recognized as a separate neutral hadron shower. In order to eliminate these errors, the high-granular calorimeter and the reconstruction algorithm that optimally integrates the information from the tracking detector and calorimeter are required.

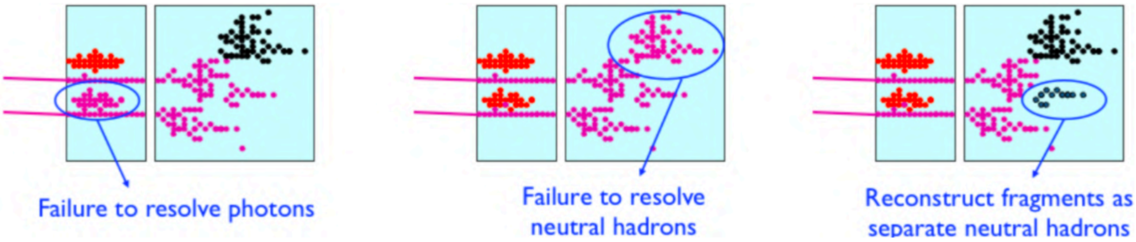

Figure2.19 Possible errors during the reconstruction using the PFA. [23]

The PandoraPFA [23][24] is the typical reconstruction program that incorporates PFA based on the ILD. It uses Monte Carlo simulations to reconstruct jets and verify the performance of the ILD model. Fig. 2.20 shows the event display, which is color-coded by energy and particle type, indicating that the PandoraPFA is able to separate charged particles from neutral particles by integrating the information from the tracking detector and the high-granular calorimeters.

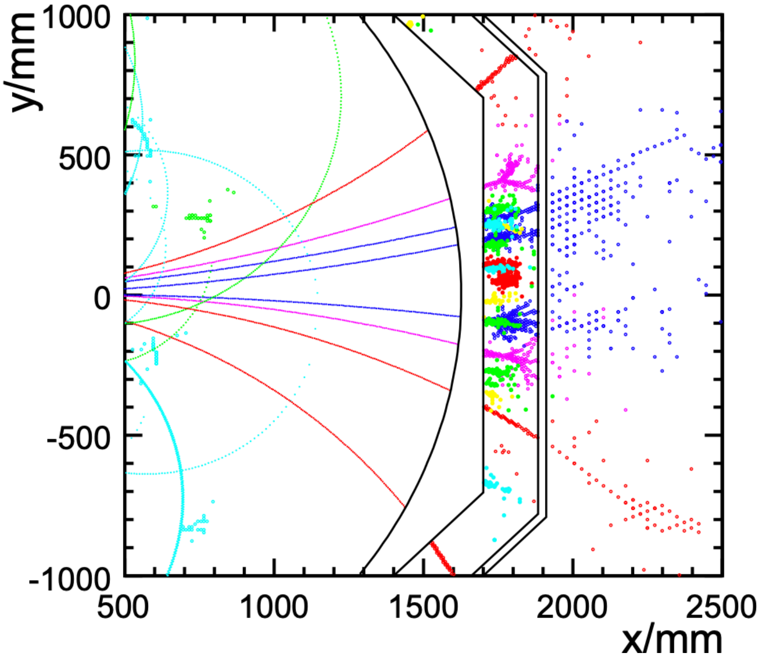

Figure2.20 Event display for the PandoraPFA simulation with 100 GeV jets. [24]

The PandoraPFA development is guided by a detailed understanding of the relative roles played by resolution and confusion effects in different energy regimes, as well as detector characteristics that affect performance. In order to use the energy-momentum match, PFA calorimeters with their emphasis on imaging must also have high energy resolution. In addition, the energy uncertainty of particles within the jet contributes significantly to the resolution of the jet at low energies where the particles are well separated, but at higher energies the effect of confusion becomes significant. The transition is around 100 GeV as shown in the Fig. 2.21. This performance is compared to the resolution obtained with the conventional approach, which is based on calorimeter information only. At jets as high as 500 GeV, confusion dominates, as shown separately, but is greatly improved by the particle flow. Note that the degradation at high energies is also due to leakage, which has a significant impact on pure calorimeter.

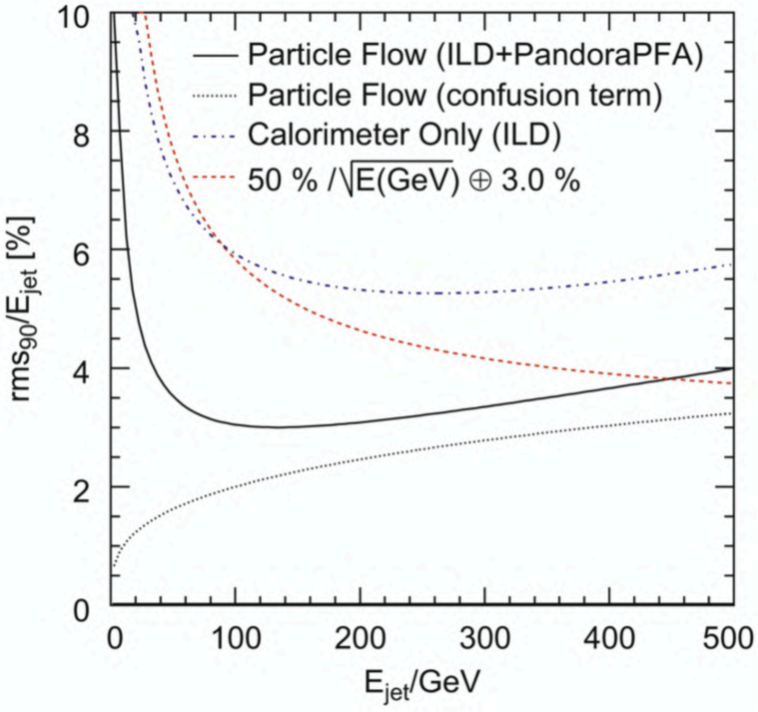

Figure2.21 Jet energy resolution simulation using the ILD as a function of energy, where rms_{90} is the RMS at the range containing 90% of the events. The contribution from confusion, and the resolution obtained from the calorimeters alone for comparison, and that of an ideal calorimeter with given parameters are also shown. [24]

2.3.3 Physics contribution of PFA calrimeter

The Highly-granular calorimeters required by the PFA will greatly contribute to the precise Higgs physics at the future Higgs factories such as the ILC. The PFA realizes the ultra high jet energy resolution of 3–4%, which realizes the precise measurement of the hadronic decay of $H/W/Z$, and then realizes the precise measurement of the Higgs boson couplings. The ILD has initiated a systematic benchmarking effort to study the performance of the latest ILD concept, and to determine the correlations between science objectives and detector performance [25]. The list of benchmark analyses is shown in Table 2.1, and the precise jet measurement is crucial in many important physics. The PFA calorimeter is the critical system to achieve the ultra high jet energy resolution.

In order to measure the branching ratio and coupling of the Higgs boson, the jet tagging is necessary, because the Higgs decay process of $h \to WW^*/ZZ^*/q\bar{q}/gg$ produces di-jets, and the decay mode can be determined only by the invariant mass of the jets. The cross-section of each decay process can be calculated by the events after the jet tagging, then the branching ratio can be calculated.

Since the invariant masses of the jets are used to tag the jets and measure the Higgs boson couplings accurately, the accurate reconstruction of jets is very important for the precision Higgs physics. Jets contain a number of particles involving charged particles of 64%, gamma-ray of 26%, neutral hadrons of 10%, and they inject into a

Table2.1 Table of benchmark reactions which are used by ILD to optimize the detector performance. The analyses are mostly conducted at 500 GeV centre-of-mass energy, to optimally study the detector sensitivty. The channel, the physics motivation, and the main detector performance parameters are given. [25]

Measurement	**Main physics question**	**main issue addressed**
Higgs mass in $H \to b\bar{b}$	Precision Higgs mass determination	Flavour tag, jet energy resolution, lepton momentum resolution
Branching ratio $H \to \mu^+\mu^-$	Rare decay, Higgs Yukawa coupling to muons	High-momentum p_t resolution, μ identification
Limit on $H \to$ invisible	Hidden sector / Higgs portal	Jet energy resolution, Z or recoil mass resolution, hermeticity
Coupling between Z and left-handed τ	Contact interactions, new physics related to 3rd generation	Highly boosted topologies, τ reconstruction, π^0 reconstruction
Cross section of $e^+e^- \to \nu\nu qqqq$	Vector Bosons Scattering, test validity of SM at high energies	W/Z separation, jet energy resolution, hermeticity
Left-Right asymmetry in $e^+e^- \to \gamma Z$	Full dim-6 EFT interpretation of Higgs measurements	Jet energy scale calibration, lepton and photon reconstruction
Hadronic branching ratios for $H \to b\bar{b}$ and $c\bar{c}$	New physics modifying the Higgs couplings	Flavour tag, jet energy resolution
A_{FB}, A_{LR} from $e^+e^- \to b\bar{b}$ and $t\bar{t} \to b\bar{b}qqqq/b\bar{b}qql\nu$	Form factors, electroweak coupling	Flavour tag, PID, (multi-)jet final states with jet and vertex charge
Discovery range for low ΔM Higgsinos	Testing SUSY in an area inaccessible for the LHC	Tracks with very low p_t, ISR photon identification, finding multiple vertices
Discovery range for WIMP's in mono-photon channel	Invisible particles, Dark sector	Photon detection at all angles, tagging power in the very forward calorimeters
Discovery range for extra Higgs bosons in $e^+e^- \to Zh$	Additional scalars with reduced couplings to the Z	Isolated muon finding, ISR photon identification.

specific area. In order to measure the invariant mass of the jets accurately, an ultra high jet energy resolution is essential. The PFA calorimeters realize the high performance of the particle identification and separation of the contribution of each particle, hence, significantly improved the jet energy resolution.

Since the PFA ECAL measures the energy of the gamma-rays, which make up 24% of the jets, it has the large contribution of the measurements of the jet energy. In addition, not only electrons and gamma-rays, but also charged hadrons and muons are injected to the ECAL. The PFA ECAL needs to extract only gamma-rays from a large number of particles in a specific area and measure their energy, which requires a very high granularity. For example, when an electron and a gamma-ray are incident on a nearby location at the same time and their showers are overlapped, the energy contribution of the electron is subtracted from that of the gamma-ray, then the gamma-ray energy is measured accurately. When a charged hadron and a gamma-ray are incident and the gamma-ray shower and charged hadron track are overlapped, not only the energy contribution from the charged hadrons is separated from the reconstructed energy, but also the information of the particle track should be sent to the HCAL. The particle tracks and showers must be accurately measured and the contribution of each particle must be separated, requiring 3D reconstruction with highly-granular cells.

2.3.4 Requirement for PFA ECAL

In order to separate the particles using the very compact ECAL, the material with small Molière radius is required, and the granularity of the calorimeter must be higher than the conventional calorimeters with a $O(m)$ granularity. In order to separate the photons and elucidate the substructure of the hadronic shower, the transverse and longitudinal cell sizes of ECAL and HCAL must be on the order of the radiation length X_0, resulting in a channel number of 10^7–10^8. Both ECAL and HCAL must be contained within the magnetic coil in order to keep as little material as possible in between when integrating the tracking and calorimeter information.

The requirement of the granularity at the PFA ECAL is the cell size of $5\ \mathrm{mm} \times 5\ \mathrm{mm}$. Fig. 2.22 shows the configuration with the cell size less than $10 \times 10\ \mathrm{mm}^2$ meets the ILC jet energy requirement of 3–4%. For 45 GeV jets, this dependence is relatively weak because the confusion term does not significantly affect the resolution. For higher energy jets, the performance drops significantly with increasing cell size mainly due to the confusion. The cell size for the PFA ECAL has to be at least $10\ \mathrm{mm} \times 10\ \mathrm{mm}$ to meet the jet energy requirement, but If aiming for higher accuracy and higher energy measurements, the $5\ \mathrm{mm} \times 5\ \mathrm{mm}$ segmentation is preferred.

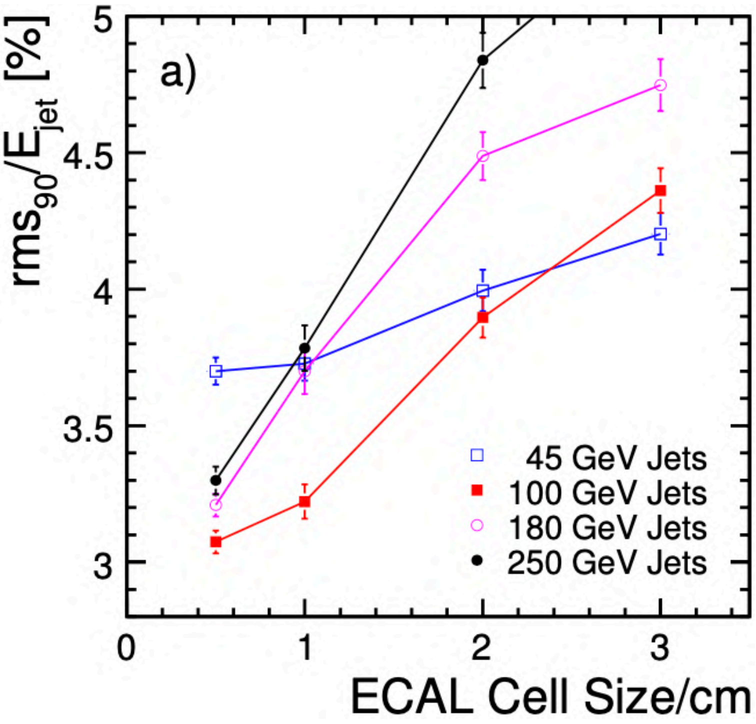

Figure2.22 The dependence of the jet energy resolution (rms_{90}) on the ECAL transverse segmentation at the Si-ECAL. [21]

The highly-granular PFA ECAL with a cell size of $5\ \mathrm{mm} \times 5\ \mathrm{mm}$ make a significant contribution to the precise measurement of the Higgs boson in the ILC.

Chapter 3

Scintillator Electromagnetic CALorimeter (Sc-ECAL)

In the PFA, particle tracks are identified one by one by mapping the track information of the tracking system to the hit information of the calorimeter. The electromagnetic calorimeter is required to have a transverse segmentation of $5\,\mathrm{mm} \times 5\,\mathrm{mm}$, which is much higher than that of the typical electromagnetic calorimeter in the collider experiments. This chapter describes the details of the electromagnetic calorimeter options (Fig. 3.1), especially the scintillator ECAL.

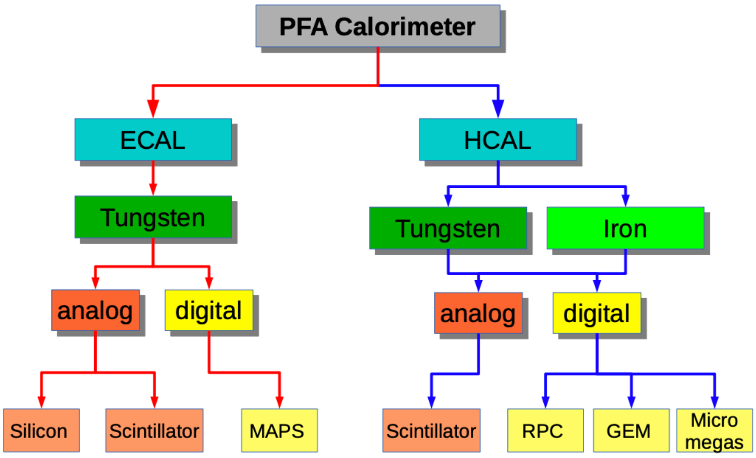

Figure3.1 Technology options of the ECAL (left) and HCAL (right). [21]

3.1 Calorimeter

3.1.1 Shower

When high-energy electrons are injected into a material, they cause bremsstrahlung and emit γ-rays. The generated γ-rays undergo pair production and emit electron-positron pairs. These two processes are repeated until the energy of the produced particles becomes lower than the critical energy below which the ionization energy loss dominates and the bremsstrahlung is no longer emitted. This phenomenon, in which incident electrons interact with matter and develop in time like a shower, is called an electromagnetic shower. The length of the shower in the direction of the incident axis is proportional to $\log E_0$ (where E_0 is the energy of the incident particle), and the shower radius is defined as the Molière radius R_M:

$$R_M[\mathrm{g/cm^2}] \approx \frac{216[\mathrm{MeV}]X_0}{E_c[\mathrm{MeV}]} \tag{3.1}$$

where E_c is the critical energy of the material and X_0 is the radiation length:

$$X_0[\mathrm{g/cm^2}] \approx \frac{716[\mathrm{g/cm^{-2}}]A}{Z(Z+1)In(287/\sqrt{Z})} \tag{3.2}$$

where the A is the mass number and the Z is the atomic number of the material. ~90% of the particle energy is contained within the Molière radius.

On the other hand, when high-energy hadrons are injected into a material, spallation reactions occur and many particles are produced due to the strong interaction. As a parameter of the shower, the nuclear interaction length $\lambda_0 \sim 35A^{1/3}[\mathrm{g/cm^2}]$ is used, which is generally much larger than the radiation length. Therefore, a thick layer of high-density material is required to capture the entire shower. Because the cross section of the hadron shower is smaller than that of the electromagnetic shower and much of the energy is used for nuclear decomposition, the measurement of the hadron shower results in poor energy resolution.

3.1.2 Total absorption calorimeter and sampling calorimeter

In the total absorption calorimeter, the absorber itself is used as a detector, and particles are detected using scintillation light or Cherenkov light. This type of calorimeter has good energy resolution because it can absorb and detect the energy of the entire shower, but it requires a larger calorimeter to absorb all the energy, especially for hadron showers, and the cost is high.

The sampling calorimeter has a sandwich structure of absorber and detector. A plastic scintillator, silicon detector, or gas detector is used in the detection layer. Since most of the energy of the shower falls in the absorber layer and only a part of the energy can be measured in the detection layer, the energy resolution is low. However, it is possible to build a large-scale calorimeter that can cover the entire shower length at low cost. In addition, it is easy to make the highly-granular detection layer, making it suitable for the ILD detectors using the PFA. Therefore, the ILD adopts sampling type calorimeters.

3.2 Scintillator ECAL (Sc-ECAL)

There are two technology options of the analogue ECAL for the PFA ECAL for the ILD. Both options are the sampling calorimeters. This section mainly gives the overview of the scintillator ECAL (Sc-ECAL).

3.2.1 Silicon ECAL (Si-ECAL)

Si-ECAL is one of the technology options for the ILD ECAL. The structure of the Si-ECAL is shown in Fig. 3.2. The Si-ECAL uses a silicon semiconductor detector as the detection layer. It has the advantage of better signal-to-noise ratio and higher readout accuracy than the Sc-ECAL, while it requires a large number of readout channels of about 10^8. A silicon pad sensor with $5\ \mathrm{mm} \times 5\ \mathrm{mm}$ silicon cells is placed on a tungsten plate to form the orthogonal structure of the detection layer and absorber layer. Since the detection layer can be thinner than the scintillator, the entire ECAL layer can be made thinner.

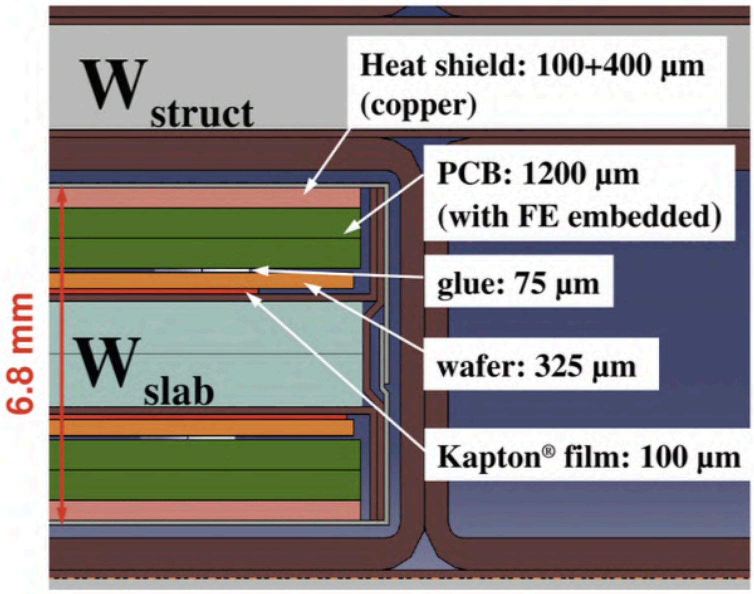

Figure3.2 Cross section of the electromagnetic calorimeter layers for the silicon option. [21]

3.2.2 Scintillator ECAL (Sc-ECAL)

The Sc-ECAL consists of three parts: a cylindrical barrel around the beam axis, an end cap that covers both ends of the barrel, and a ring that fills the gap between the barrel and the end cap. The Sc-ECAL is capable of covering almost all particles produced by collisions at the center of the ILD. The DAQ mechanism and cabling are all integrated into the space between the barrel and the end cap to reduce dead space as much as possible. The blue area in Fig. 3.3 is the barrel of the Sc-ECAL. The barrel has two rings in the beam axis direction, each divided into 8 sections in the azimuthal direction. The Si-ECAL also has the same mechanical structure.

The layer structure is shown in Fig. 3.4. In order to capture electromagnetic showers, 30 layers of absorber layers and detection layers are arranged alternately. The thickness is designed to be ~2 mm for the absorber layer and ~3.5 mm for the detector layer.

The Sc-ECAL uses scintillator strips readout by silicon photomultipliers (SiPMs) in the detection layer. The use of plastic scintillators makes the calorimeter less expensive than silicon detectors. The scintillator strips are arranged orthogonally in a direct line between the front and back layers to create pseudo $5\ \mathrm{mm} \times 5\ \mathrm{mm}$ pixels, as shown in the bottom of Fig. 3.4. In the current design, the strip has a dimension of 5 mm wide, 45 mm long, and 2 mm thick, and a SiPM is attached to the surface. It is possible to reduce the number of readout channels to about 1/10 compared to Si-ECAL. On the other hand, Sc-ECAL has a problem of false hits (ghost hits) when two particles enter the ECAL at the same time at a close distance by crossing the strips (Fig. 3.5), so the length of the strip should be optimized to reduce ghost hits, as discussed in Section 4.2.

The Sc-ECAL uses tungsten ($X_0 = 3.5\ \mathrm{mm}, R_M = 9.3\ \mathrm{mm}$) in the absorber layer. Tungsten forms the narrow showers, and is suitable for the compact detector to achieve the better separation of particles in a limited space.

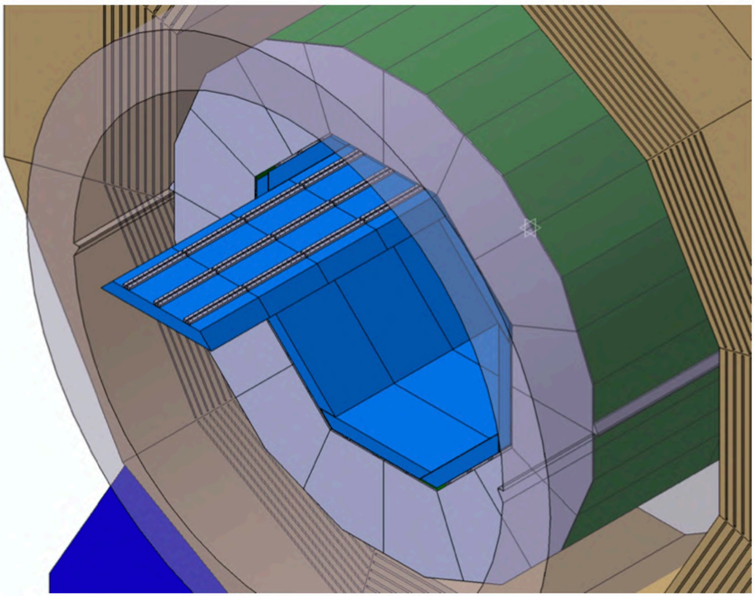

Figure3.3 The electromagnetic calorimeter (in blue) within the ILD Detector. The cylindrical (in green) object outside the ECAL is hadron calorimeter. [21]

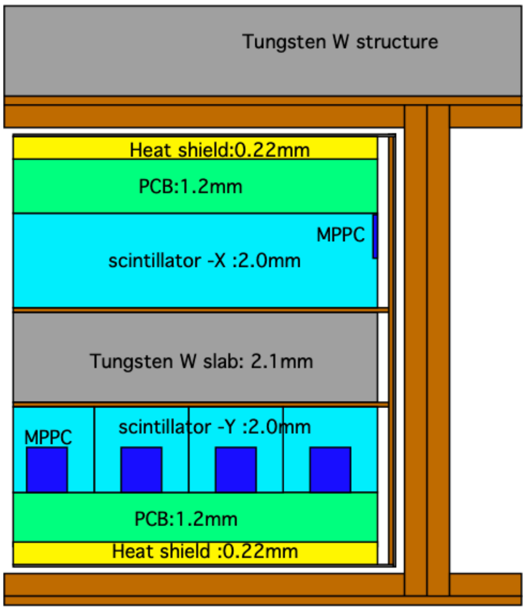

Figure3.4 Structure of the Sc-ECAL. ScintillatorX and ScintillatorY are positioned orthogonally. [21]

3.3 Physics prototype

The concept of Sc-ECAL has been already validated using a physics prototype [26]. This section summarizes the structure and performance evaluation of the physics prototype.

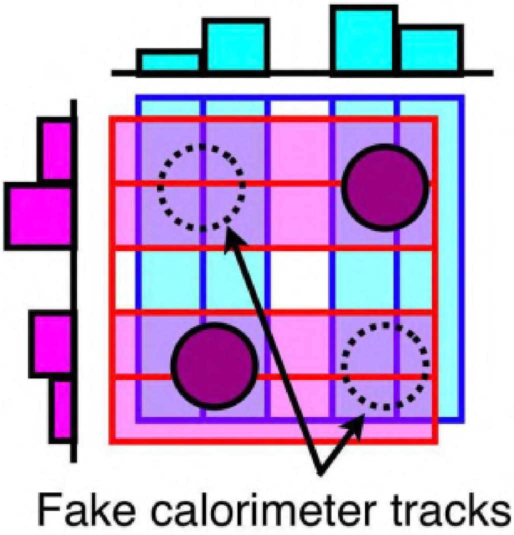

Figure3.5 Ghost hits in the ScECAL. In addition to the true hit pair, a false hit pair is generated, and it is not possible to determine which is the correct hit pair or combination.

3.3.1 Detector

The physics prototype for the Sc-ECAL shown in Fig. 3.6 was constructed and tested. The prototype consisted of 30 pairs of alternating tungsten absorber and scintillator layers, with the total thickness of 266 mm. Fig. 3.7 shows the design of a detection layer, consisting of four rows of 18 scintillator strips. Fig. 3.8 shows the design of a single polystyrene-based scintillator strip with the central hole for the wavelength shifting (WLS) fiber. The size of the strip was $9.85 \times 44.71 \times 3.02\ \mathrm{mm}^3$, and a notch with a depth of 1.40 mm and a width of 4.46 mm to accommodate the SiPM. A double clad 1 mm diameter Y-11 WLS fiber produced by Kuraray [27] with a length of 43.6 mm was inserted into the hole of each strip. Each strip was wrapped with a 57 μm-thick reflective foil produced by Kimoto [28]. A multi-pixel photon counter (MPPC), from Hamamatsu Photonics K.K. [29], was used as the photosensor. The size of the MPPC package was $1.3 \times 4.2 \times 3.2\ \mathrm{mm}^3$. The four long sides of each strip were polished to precisely control the strip size and to ensure reflection of the surfaces.

The signal lines from the MPPCs and their power supply lines were grouped together on a flat cable, and these cables were connected to a single base board outside the prototype as shown in Fig. 3.6. It contained six analogue boards with a readout ASIC [30]. Each ASIC controlled 18 MPPCs, and one base board controlled 108 MPPCs.

3.3.2 Test beam at FNAL

The prototype was exposed to particle beams of varying type and energy at the Meson Test Beam Facility number 6 (MT6) at the Fermilab: electron beams from 1 to 32 GeV to study the electromagnetic response of the detector; muons from 32 GeV to calibrate the detector; and charged pions from 1 to 32 GeV to study the hadronic response.

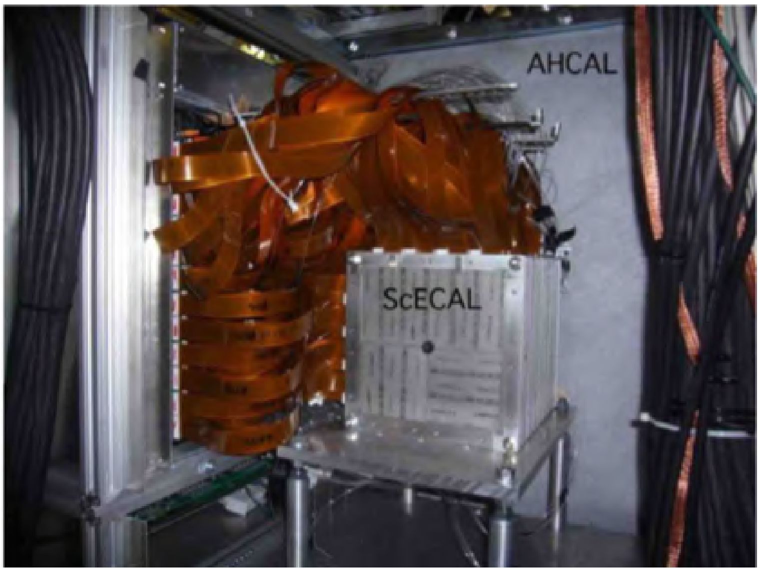

Figure3.6 The Sc-ECAL prototype in front of the CALICE AHCAL [26]

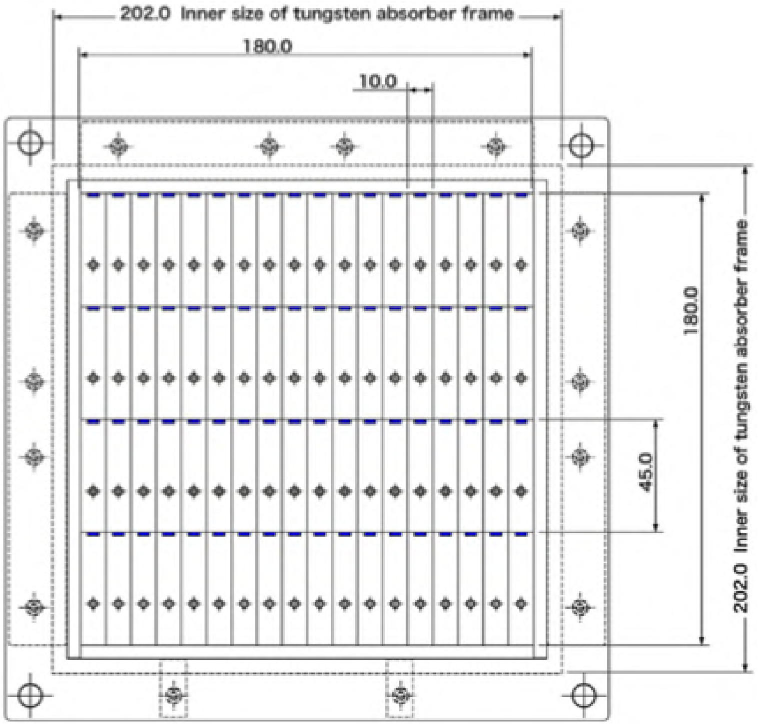

Figure3.7 The arrangement of 72 strips in a scintillator layer [26]

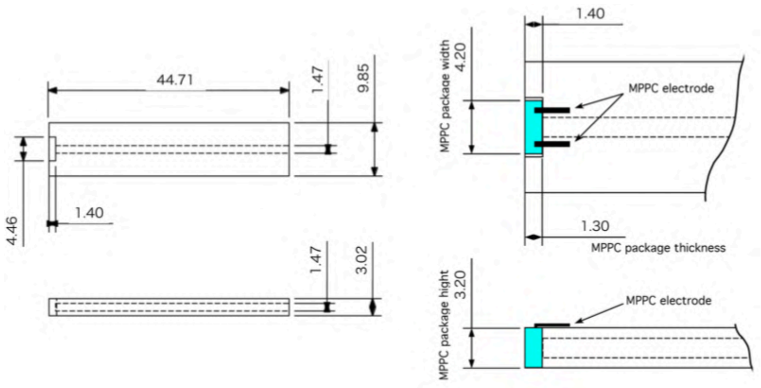

Figure3.8 Top and side views of a scintillator strip (left) and the notches cut into the strips to accommodate the MPPC packages (right). All dimensions are given in mm. [26]

3.3.3 Performance of the prototype

Fig. 3.9 shows the mean reconstructed energy as a function of the injected electron beam energy. The slope and offset at the linear fit shown as the solid line are (130.22 ± 0.26) MIP/GeV and (23.2 ± 1.6) MIP, respectively, where the MIP is the detector response to the minimum ionized particle. The maximum deviation from linearity at each beam energy is $(1.1 \pm 0.4)\%$, at 8 GeV.

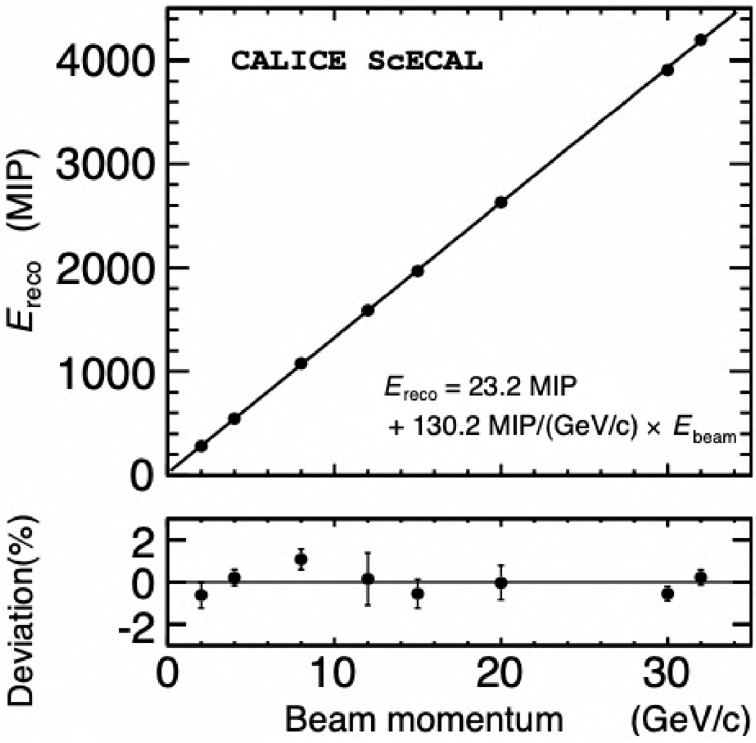

Figure3.9 Response of the ScECAL prototype to 2–32GeV electrons (top), deviation from the result of a linear fit (bottom). The error bars show the statistical and systematic uncertainties. [26]

Figure 3.10 shows the energy resolution as a function of the inverse of the square root of the beam energy. The curves show the results of fitting the data with the two-component parameter for energy resolution:

$$\frac{\sigma_E}{E_{\mathrm{reco}}} = \frac{C_{\mathrm{stoch}}}{\sqrt{E_{\mathrm{beam}}[\mathrm{GeV}]}} \oplus C_{\mathrm{const}} \tag{3.3}$$

where C_{stoch} and C_{const} are the fit parameters and determined to be $(12.5 \pm 0.4)\%$ and $(1.2 \pm 0.4)\%$, respectively. The uncertainties include both systematic and statistical contributions.

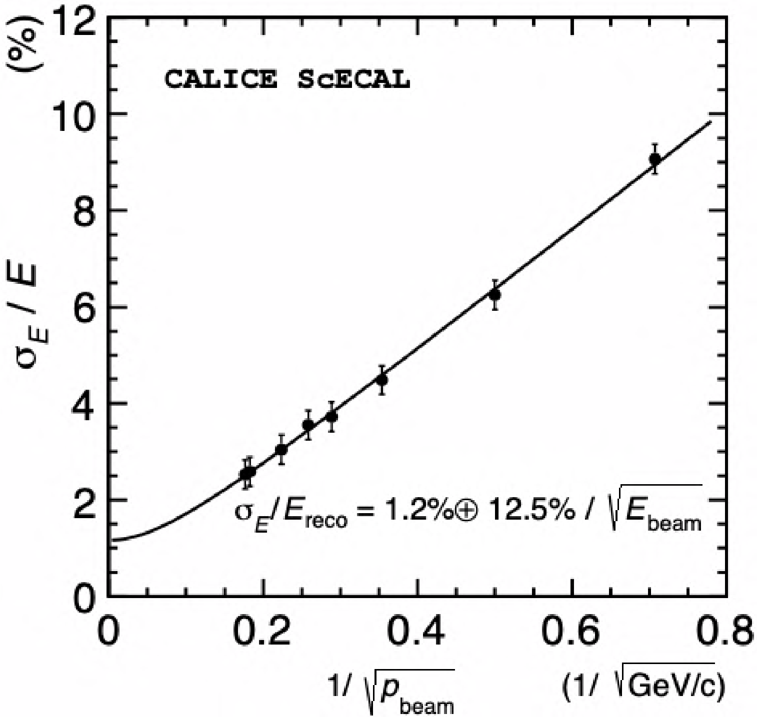

Figure3.10 Energy resolution of the Sc-ECAL as a function of the inverse square root of the beam energy. The error bars show the statistical and systematic uncertainties. [26]

The left figure in Fig. 3.11 compares the simulated response of the prototype to electrons with the data. The slope of $dE_{\mathrm{reco}}/dE_{\mathrm{beam}} = 130.27 \pm 0.06\ \mathrm{MIP/GeV}$ observed in the simulation is consistent with the data of $130.03 \pm 0.24\ \mathrm{MIP/GeV}$, but the offset is -3.0 ± 0.1 MIP, which is 27 MIP less than the data. This observation is clearly illustrated by the ratio of the simulation to the data in Fig. 3.11, left, bottom, suggesting that there is a constant difference at all energies. This can be attributed to a small amount of background contamination remaining in the data, even though the detector noise is determined by overlaying random trigger events on top of the simulated events.

Fig. 3.11 right shows the energy resolution of the data and simulations under several different conditions modeled by the simulations. The simulations agree with the data within the uncertainty range; the discrepancy persists when applying the beam energy spread from higher beam energies to the data recorded at 2 GeV and 4 GeV $(2.3 \pm 0.3\%)$.

3.3.4 Issues of physics prototype

The concept of the Sc-ECAL was validated using the physics prototype, but it remains some issues. First, the pixel size of $10 \times 10\ \mathrm{mm}^2$ doesn't meet the requirement of $5 \times 5\ \mathrm{mm}^2$ at the PFA ECAL. At the time of the physics prototype, the cell size of $10 \times 10\ \mathrm{mm}^2$ was considered to be sufficient, but due to the progress of simulation studies

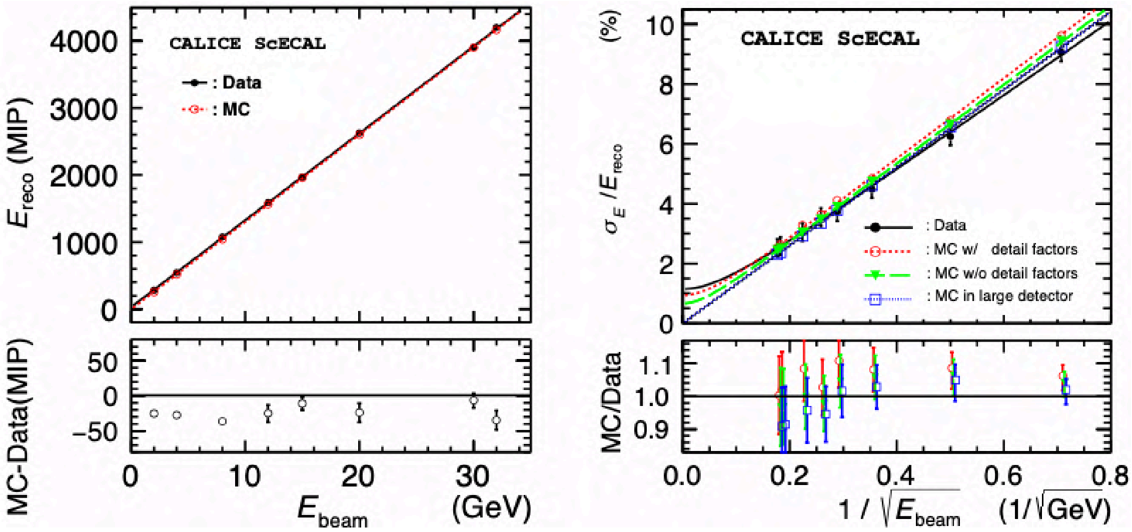

Figure3.11 The response (left) and the energy resolution (right) of data and the simulated prototype to the electron beams. [26]

and updates of the ILD design, the pixel size requirement is now $5 \times 5\ \mathrm{mm}^2$.

Second, the strip design was complex and not suitable for mass production towards the construction of the full detector. The machining of the notch and hole for a WLS fiber took a lot of work at the cast moulding, and the production of the mould with the complex design was difficult at the injection moulding. Furthermore, the MPPC was located at the side of the strip, so the soldering the MPPC to the board also took a lot of work and the area at the MPPC itself became an inactive space. Therefore, an improved strip design is required.

Third, a fully integrated electronics (ECAL Base Unit, EBU) has been developed after the physics prototype. The EBU is equipped with a readout ASIC, SPIROC2E. The EBU can control a large number of MPPCs, and calibrate them using LED. The temperature is monitored using temperature sensors on the EBU.

In order to overcome these issues, the technological prototype of the Sc-ECAL is proposed to demonstrate the performance of the Sc-ECAL using the full-scale prototype, and to prepare for the construction of the actual detector.

Chapter 4

Large technological prototype

The concept of the Sc-ECAL was already validated using a physics prototype. Now we focus on demonstrating the performance of Sc-ECAL with a technological prototype with fully integrated detection layers.

4.1 Technological prototype

The technological prototype has been constructed as a joint effort by the ILC-ILD group and the CEPC-ECAL group. Fig. 4.1 shows the layout of the sandwich structure (top) and an exploded view of the Sc-ECAL prototype (bottom). The absorber layers and alternating detection layers form a sandwich structure. The technological prototype consists of 15 super-layers. Each super-layer contains two sets of detection layers and a single tungsten-copper alloy absorber plate inserted in the center of the sandwich structure (Fig. 4.1). The detection layer and the readout electronics are integrated into the ECAL Base Unit (EBU) board. Thirty EBU boards are used in total. One EBU detection layer contains 210 scintillator strips coupled with a SiPM; the readout of the SiPM is done by the SPIROC2E chip [31] with 36 integrated channels. There are 6300 SiPM channels in total for the whole system readout by 180 SPIROC2E chips.

The technological prototype has been constructed with full 30 layers and fully integrated detection layers using the same technology as foreseen in the actual detector to demonstrate the performance of the Sc-ECAL and the scalability. The technology options for the PFA HCAL such the Analogue Hadron CALorimeter (AHCAL) and Semi-Digital Hadron CALorimeter (SDHCAL) have completed the performance demonstration of a large technological prototype, while the PFA ECAL is not yet at that stage, and the performance demonstration with a large technological prototype is urgently needed. The possibility of the construction of the Sc-ECAL can be shown by constructing the full-scale prototype using the same technology as for the actual detector and establishing the system for the mass production. The high performance and feasible technology of the Sc-ECAL can be shown by the performance evaluation of the technological prototype with cosmic-ray test, LED test, and test beam experiment.

The development of a highly granular calorimeter is of great significance because it is an indispensable technology for realizing precise physics at the future Higgs factories. The construction and performance demonstration of the Sc-ECAL technological prototype is an important research that will greatly contribute to the precision measurement of Higgs bosons with the PFA calorimeter. This will be the first ever demonstration for the PFA-ECAL concept with a technological prototype among the technology options.

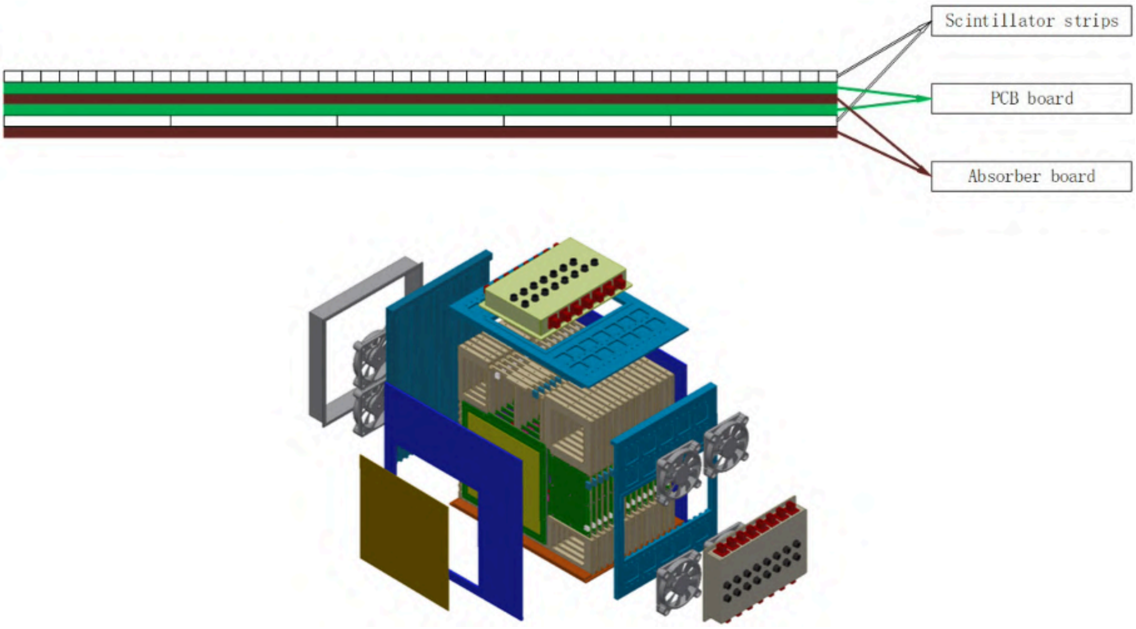

Figure4.1 The layout of sandwich structure (top) and exploded view of the full-scale Sc-ECAL technological prototype (bottom)[32]

4.2 Strip Splitting Algorithm (SSA)

This section describes the principle of a novel reconstruction algorithm for the Sc-ECAL called Strip Splitting Algorithm (SSA), and the simulation study using the SSA to optimize the strip length.

4.2.1 Strip Splitting Algorithm

In order to achieve the cell size of 5 mm × 5 mm with the scintillator strips aligned alternately in orthogonal orientations, a method called the Strip Splitting Algorithm (SSA) is used [33]. As shown in Fig. 4.2 (left), a scintillator strip layer consisting of n strips is arranged orthogonally in the upper and lower layers, and a particle passes through this layer. The central strip layer is divided into n virtual cells according to the projections from the upper and lower strips, as shown in Fig. 4.2 right. For the k-th virtual cell ($k = 1, \ldots, 9$), the weighting factor w_k is obtained by:

$$w_k = \sum_i E_i \tag{4.1}$$

where $\sum_i$ is the sum over the strips with the same index at upper and lower layers, and E_i is the energy deposit in strip i. The energy deposit in the virtual cell k is defined by weighting the energy deposit E_{strip} of the strip in the middle layer:

$$E_k = E_{strip} \frac{w_k}{\sum_j w_j} \tag{4.2}$$

where, $\sum_j$ represents the sum over all strips at upper and lower layers.

The SSA is applied to all layers and strips to realize the $5 \times 5 \mathrm{mm}^2$ cell segmentation. This is the first implementation of the SSA to the real detector.

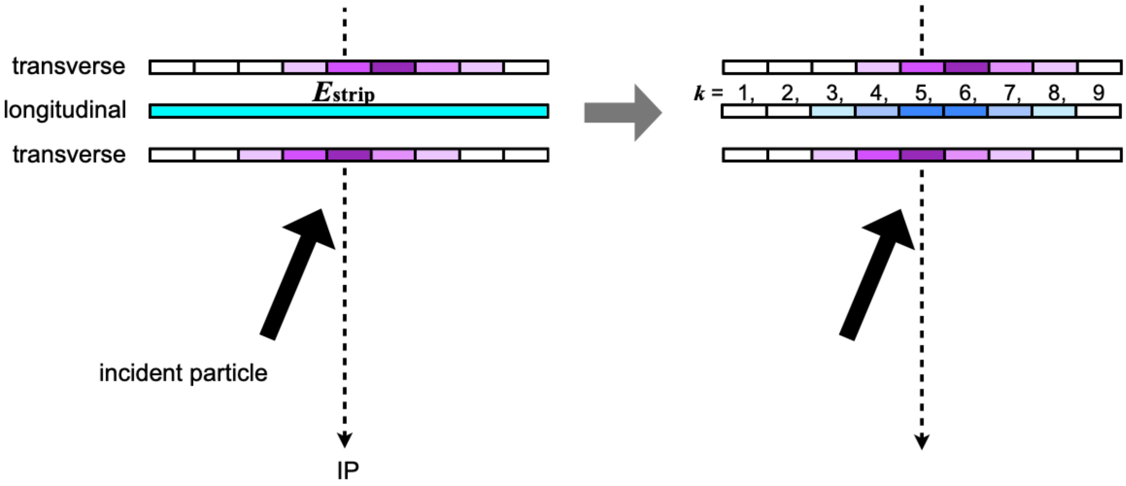

Figure4.2 A cartoon illustrating the SSA procedure. The energy, E_{strip} reconstructed in the central, "longitudinal", strip is split among virtual cells ($k = 1, \ldots, 9$) by considering the energy in the orthogonally aligned "transverse" strips in neighboring layers. [33]

4.2.2 Optimization of the strip length

Two jet events with center-of-mass energy of 200 GeV were simulated with the ILD including the Sc-ECAL using different strip lengths, and analyzed using the PandoraPFA. Figure 4.3 shows the jet energy resolution for different strip lengths. In order to resolve the ambiguity caused by intersecting strips of 5 mm width and different lengths, the SSA was implemented in the PandoraPFA. The results with and without SSA show that there is no strong degradation with the application of SSA or with increasing the length of the strip. A strip length of 45 mm as with the physics prototype is chosen as the baseline

4.3 Prototype design

This section focuses on the design of the detection layer and the readout electronics.

4.3.1 Design of detection layer

The technological prototype consists of 30 alternating detection layers and absorber layers, one detection layer is also called Ecal Basic Unit (EBU) with an integrated readout electronics. Each detection layer consists of an integrated sensitive unit and readout electronics, with the scintillator strip and SiPM forming the sensitive detection unit and the readout electronics PCB also serving as the mechanical structure for the sensitive unit. The total thickness of a detection layer is less than 6 mm, including the thickness of the sensitive unit, the PCB and the electronics, where the thickness of the scintillator strip plus the reflective film package is less than 3 mm, and the thickness of the PCB is only 1.2 mm.

Fig. 4.4 shows the layout of the detection layer. The technological prototype uses a 5 mm × 45 mm × 2 mm scintillator strip. The detection layer consists of 210 channels divided into 5 rows and 42 columns, with a total sensitive area of 222.3 mm × 226.6 mm, which can contain the lateral spread of the electromagnetic showers and reduce energy leakage. Each scintillator is wrapped with 65 μm 3M ESR reflective film, leaving 300 μm gaps

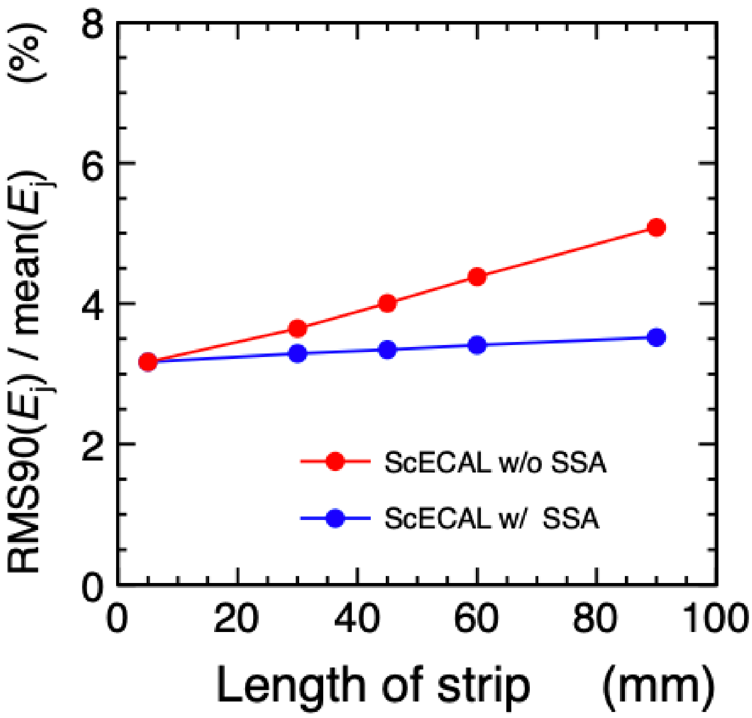

Figure4.3 Jet energy resolution as a function of strip length for the ScECAL option, shown without (red) and with (blue) the strip splitting algorithm [21]

between adjacent strips in the shorter side and 400 μmgaps in the longer side to cover the scintillator processing errors and assembly accuracy. The fraction of the dead area caused by the gap between scintillators is about 6.5%. The prototype uses two types of SiPMs from Hamamatsu, both with a package size of 1.9 mm × 2.4 mm. The 24 layers use Hamamatsu MPPC S12571-010P with 10,000 pixels at 10 μm pitch and the other 6 layers use Hamamatsu MPPC S12571-015P with 4,489 pixels cells at 15 μm pitch. In order to calibrate the SiPM gain, a LED is installed for each strip on the front-end board.

4.3.2 Design of absorber layer

The photon energy of physical interests at the ILC ranges from 100 MeV to 100 GeV, so the prototype has to have sufficient amount of material in the longitudinal direction to avoid energy leakage. The radiation length of tungsten is 0.35 cm, and the the Molière radius is 18 $\mathrm{g/cm^2}$. These are the smallest among the common materials, and tungsten can absorb more energy of electromagnetic particles with the same thickness. So it is ideal to choose tungsten as the absorber material.

However, the pure tungsten material itself is very hard and brittle, not easily machined, and prone to breakage during transportation and assembly. The tungsten alloy with copper increases the radiation length, which is not desirable to the electromagnetic shower absorption, so a lower percentage of copper is desired. The tungsten-copper alloy with a mass ratio of 85:15 is chosen based on industrial production experience, with an equivalent radiation length of 0.44 cm. The prototype adopts a 30 × 3.2 mm absorber layer design, and the total longitudinal thickness of the absorber is about 22 X_0. In this configuration, more than 99% of the energy of the electromagnetic shower from 100 GeV gamma is deposited in the prototype.

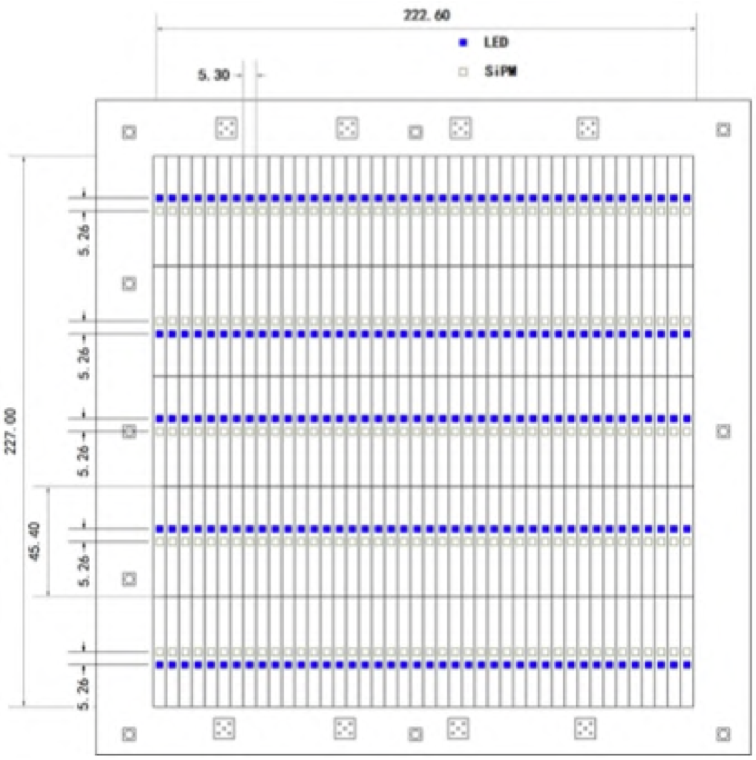

Figure4.4 Layout of detection layer, scintillator strips, and LED distribution

4.3.3 Design of mechanical structure

For a more flexible and secure assembly of the prototype, two sets of the detection and absorption layers are alternately arranged mechanically to form a super-layer, where the strips are aligned in orthogonal orientations for the two detection layers, as shown in Fig. 4.5. The bottom layer is an absorber layer, followed by a detection layer with the scintillator unit side down. A 1.8 mm high through-hole polyimide spacer is placed in the middle of the electronics plate where the mechanical holes are located, followed by a second absorber layer to avoid damaging the electronics by direct contact between the absorber layer and the electronics. The top layer is another detection layer with the scintillator unit upward to keep the entire super-layer surface flat, and similarly a 1.8 mm polyimide spacer is placed at the location of the mechanical hole between the absorber layer and the electronics. The final absorber and the detection layer are assembled as a super-layer by screwing them to the support structure. The edges of the support structure are hollowed to reduce the weight and to facilitate assembly and handling, and to provide ventilation holes for heat dissipation in the front panel. The prototype consists of 15 super layers with 30 alternating detection and absorption layers, plus two detection layers with SiPM double-side readout.

The prototype also needs to have an overall prototype mechanical structure with specific requirements including the followings:

- Each super-layer can be flexibly assembled and disassembled as an independent unit
- The longitudinal spacing between super-layers should be less than 2 mm
- Independent heat dissipation system, to ensure the normal temperature of the working environment
- It provides some protection from light

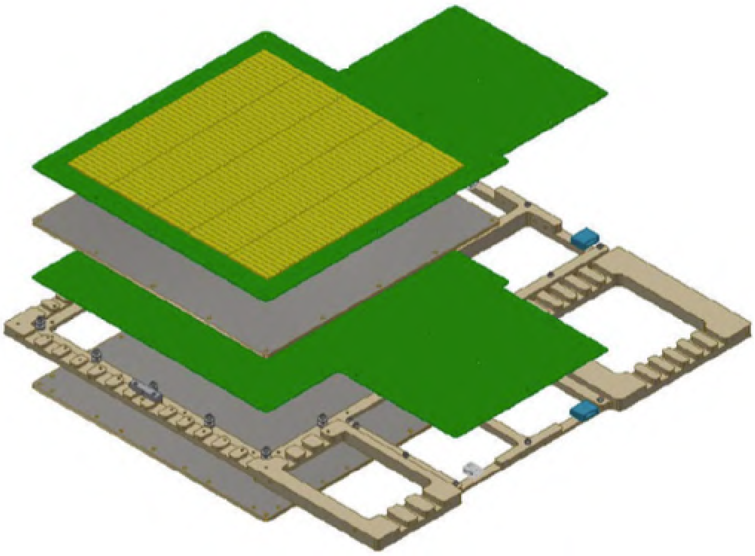

Figure4.5 Schematic diagram of the super-layer structure, with two consecutive detection layers rotated by 90 degree arranged vertically, and the absorber and detection layers assembled together by a support frame

- Capable of supporting the entire gauge for easy transport for the test beam experiment.

In order to meet all the requirements, the mechanical structure of the prototype is designed as shown in Fig. 4.6. Each side panel of the mechanical structure is milled and processed with a whole aluminum plate, ensuring the overall mechanical strength and the light weight. There are 18 sets of card slots designed inside the upper and lower panels, each card slot can support a super-layer, and 1.5 mm space is reserved between two super layers for contingency. The left and right side panels can be disassembled separately, and the super-layer can be assembled and disassembled from both sides by plugging and unplugging. After assembling, the super-layer can be fixed by 12 screws at the corresponding positions on the left and right sides and the upper side to ensure the stability of the super-layer. Each front panel has one power cable and one signal cable, and all the wirings are connected through an interface on the mechanical structure, which is designed for effective light avoidance. There are 18 HDMI ports on the upper side panel and 18 HDMI ports on the right side panel for the signal cable connection of the front panel, and two 16-wire connectors for the power supply of the front panel. There is a set of six fans on the left and right side panels, with a total power of 120 W and the same direction of airflow, which can be used to cool the front panel during operation. In addition, the front and rear panels are made of separate 1 mm aluminum plates at the corresponding positions in the detection layer, and the marker lines are drawn according to the actual size and position of the detection layer to facilitate the positioning of the prototype for subsequent beam testing and to reduce the amount of material in front of the detection layer.

4.4 Scintillator strip

The detection layer of the technological prototype consists of $5\ \mathrm{mm} \times 45\ \mathrm{mm}$ scintillator strips on the EBU board. The scintillation light is detected by the Silicon PhotoMultiplier (SiPM) mounted on the EBU.

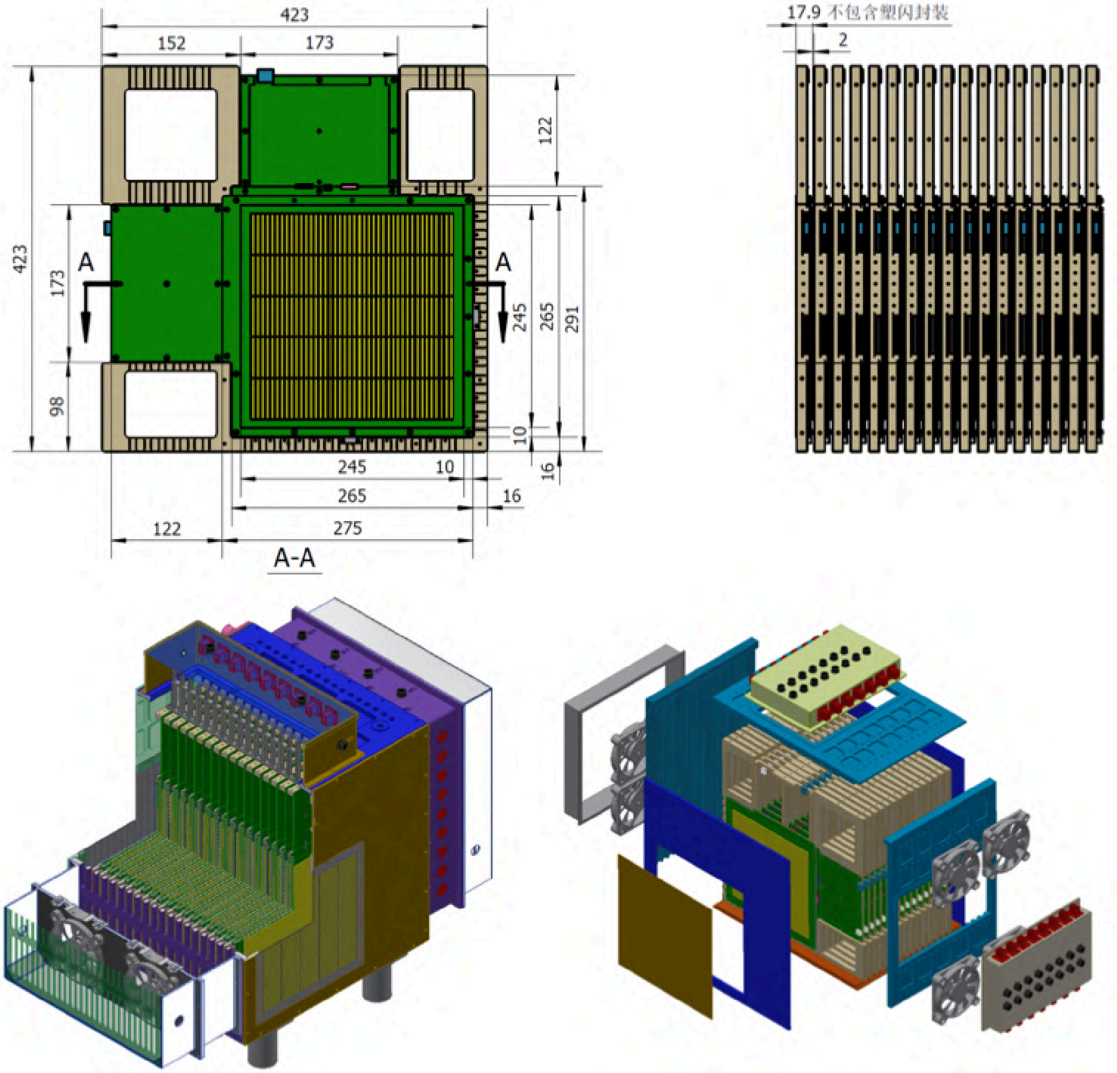

Figure4.6 Design of the mechanical structure of the prototype, the schematic diagrams of super layer structure (top left), super layer arrangement (top right), the internal section of the prototype (bottom left), and the exploded view of the prototype (bottom right)

4.4.1 Scintillator material

A plastic scintillator is a transparent light-emitting organic material, consisting of a base material and a light-emitting substance (e.g., PPO, biphenyl, etc.). The light-emitting substance is called the first solvent and the light yield of the scintillator can be increased by adjusting the light-emitting substance. In addition to the luminescent substance, a wavelength-shifting agent, also known as a secondary solvent, is usually added to the scintillator. The wavelength shifter absorbs the fluorescence of the light-emitting substance and emits fluorescence at different wavelengths. The use of wavelength-shifting agents can reduce the self-absorption effect of scintillators, and can optimize the scintillator fluorescence spectrum to match the spectral response of the photodetector.

There are two major methods for producing scintillators: cast moulding and injection moulding. In the cast moulding method, the scintillator material is moulded at low temperature. The scintillator produced by the cast moulding has high light yield, but it is expensive because it takes a long time to mould. Also, since it is basically moulded as a large plate, it must be machined into the desired shape. The injection moulding is a method where the scintillator material at high temperature is injected to a mould. Although the amount of light yield is smaller than that of the cast moulding, it is suitable for a large scale production such as scintillators for collider experiments because it can produce any shape at low cost.

The technological prototype uses BC-408 made by Saint-Gobain [34], a plastic scintillator based on polyvinyl toluene (PVT) produced by the cast moulding, with the performance parameters shown in Table 4.1. It emits about 10,000 scintillation photons per 1 MeV electron energy deposit. The emission spectrum is in the visible light range, and a photodetector with sensitivity to visible light can be used. It has a time response performance on the ns scale. The scintillator strip is wrapped in the Enhanced Specular Reflector (ESR) film from 3M [35], as shown in Fig. 4.7. The ESR film has a reflectance of 98% or higher in the visible light range.

Table4.1 Performance parameters of BC-408 [34]

Light output, %Anthracene	64%
Rise time	0.9 ns
Decay time	2.1 ns
Wavelength of maximum emission	425 nm
Light Attenuation length	210 cm

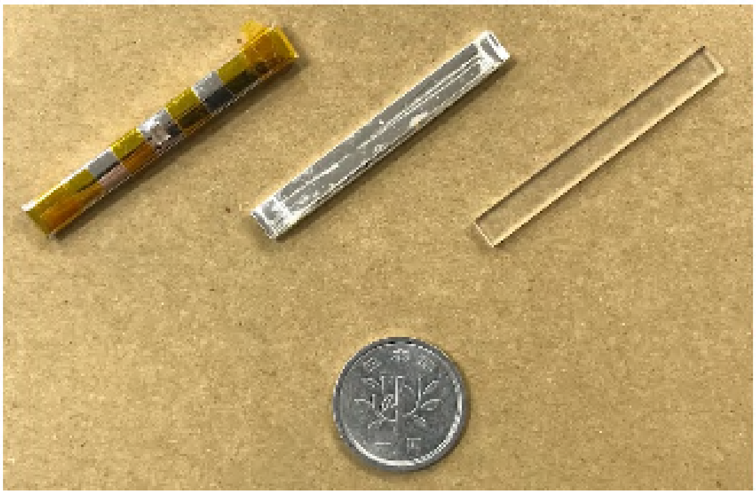

Figure4.7 Scintillator strip. The photo shows a scintillator strip 5 mm wide, 45 mm long, and 2 mm thick, with the ESR film.[36]

The dedicated plastic scintillator material with low cost and high light yield is also developed for the Sc-ECAL. The focus of the development is on polystyrene-based scintillators using the injection moulding, which is suitable for a large scale production. By optimizing the manufacturing parameters, moderately high light yields of 65–70% have been achieved over commercial PVT-based scintillators. The details of the scintillator strip produced by the injection moulding is discussed in Appendix A.

4.4.2 Scintillator design

The scintillator strip is coupled by the SiPM, and three coupling models are investigated: side-end coupling, bottom-end coupling, and bottom-center coupling. The uniformity of light yield along the strip is important to the ECAL energy resolution. The results of the performance test with three coupling models are shown in Fig. 4.8. The bottom-center coupling gives the best uniformity with additional advantages: avoiding the dead area between scintillators introducing by SiPMs, simplifying the detection layer assembly, and allowing for a large-size SiPM. The bottom center coupling is adopted as the default design of the detection layer. Fig. 4.9 shows the design of scintillator strip for the prototype.

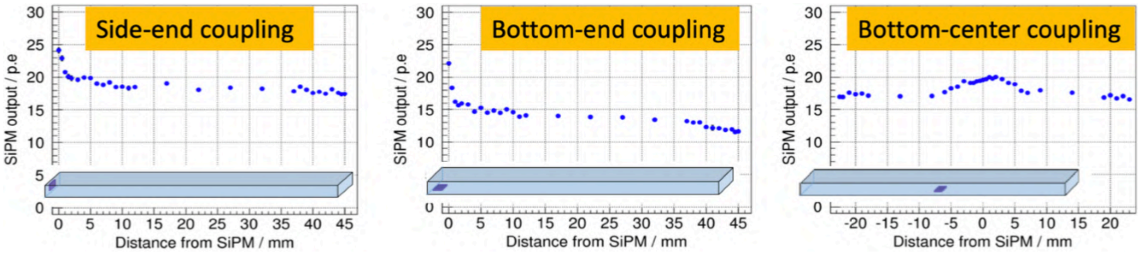

Figure4.8 Light yield measurement at different SiPM coupling: side-end coupling (left), bottom-end coupling (center), and bottom-center coupling (right). Commercial PVT scintillator coupled with MPPC S12571-015P is used.

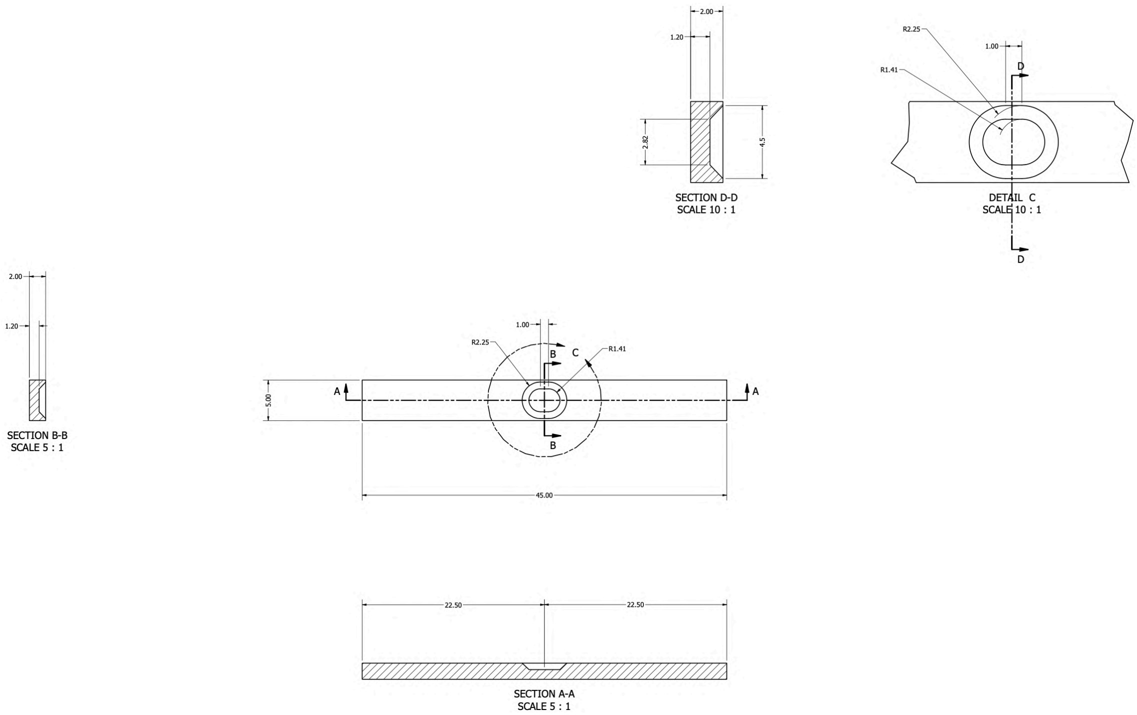

Figure4.9 Design of the scintillator strip. Unit is mm.

The SiPM double-side readout is being developed, and discussed in Appendix A.

4.5 Silicon PhotoMultiplier (SiPM)

As mentioned above, the Silicon PhotoMultiplier (SiPM) is used to read out the scintillation light. The SiPM consists of Avalanche PhotoDiodes (APDs) aligned on pixels. Compared to the conventional PhotoMultiplier Tube (PMT), the SiPM has the following advantages:

- Compact size
- Low cost
- Low operation voltage
- Magnetic field resistance
- Photon counting

The Multi-Pixel Photon Counter (MPPC) manufactured by Hamamatsu Photonics is used in the Sc-ECAL. The Sc-ECAL uses a surface-mount type with an active area of $1.0\ \mathrm{mm} \times 1.0\ \mathrm{mm}$ and $10/15\ \mu\mathrm{m}$ pixel pitch (Fig. 4.10 left). The details of the MPPC are described below.

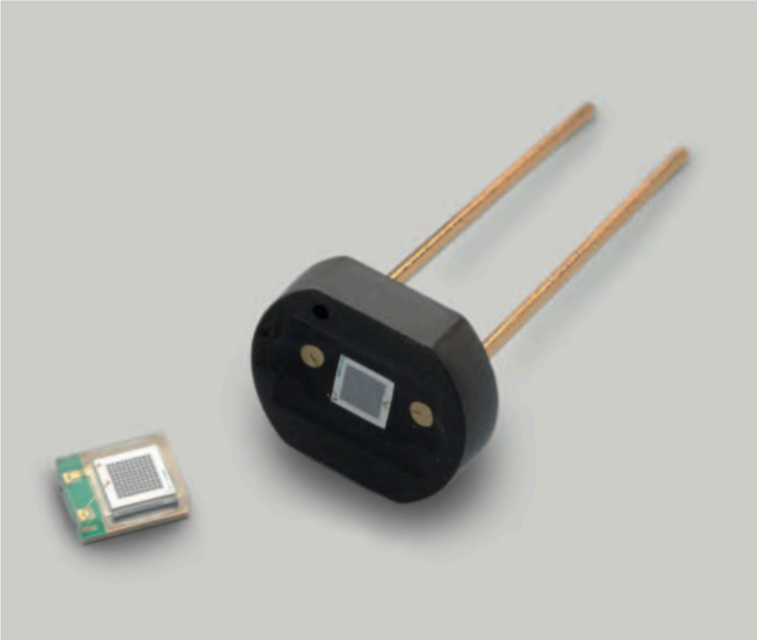

Figure4.10 Hamamatsu MPPC S12571[37]

4.5.1 Principle

The MPPC consists of a number of Geiger-mode APD pixels spread on a $1\ \mathrm{mm} \times 1\ \mathrm{mm}$ to $3\ \mathrm{mm} \times 3\ \mathrm{mm}$ silicon chip as shown in Fig. 4.11 left and Fig. 4.12. The cross section of the pixel is shown in Fig. 4.11 right. By applying a reverse voltage slightly higher than the threshold (breakdown voltage) for the APD to operate in the Geiger mode, the photoelectrons produced by the incident photons are avalanche amplified in the amplification region. A current through the fired pixel causes a voltage drop in the quenching resistor connected to the pixel. The output charge Q_{pix} from a pixel is proportional to the pixel capacitance C_{pix} and the overvoltage ΔV (the difference between the operation voltage V_{op} and the breakdown voltage V_{bd}):

$$Q_{pix} = C_{pix}(V_{op} - V_{bd}) \tag{4.3}$$

If the C_{pix} and ΔV are constant, the output is constant regardless of the incident photons. By lowering the potential difference across the amplification region, the avalanche converges and can respond to the next incoming photon.

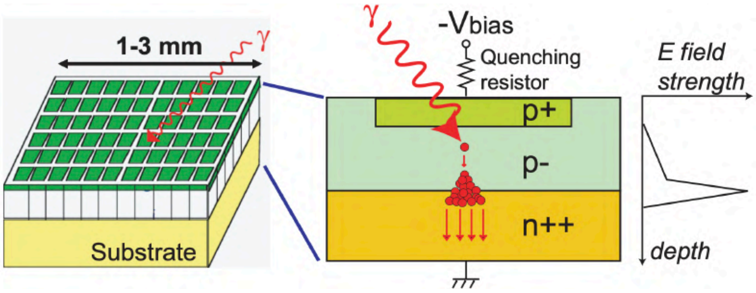

Figure4.11 Structure and operating principle of MPPC. [38] Red circles are electrons. In reality, holes generated by the electron avalanche also cause the avalanche.

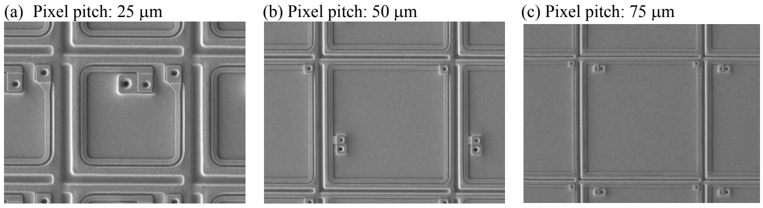
(a) Pixel pitch: 25 μm
(b) Pixel pitch: 50 μm
(c) Pixel pitch: 75 μm

Figure4.12 Magnified images of MPPCs with 25 μm, 50 μm, and 75 μm pixel pitches [39]

A single pixel is saturated by an electron avalanche from a single photoelectron, so it is impossible to observe more than one photoelectron. The MPPC with many tiny pixels outputs the sum of the charges of all pixels. As shown in Fig. 4.13, the number of incident photons can be measured one by one and the number of incident photons at a time can be determined. This is one of the main features of MPPC. Fig. 4.14 shows an example of the MPPC output waveform. The peaks corresponding to the number of photoelectrons can be clearly seen, and because the amplified layer is thin, the signal rises quickly and the MPPC can have an excellent time resolution.

4.5.2 Gain, breakdown voltage

The electron avalanche terminates when the applied voltage drops below the breakdown voltage, so the MPPC gain is proportional to the overvoltage, and is obtained by dividing the charge from Eq. 4.3 by the elementary charge ($1.602 \times 10^{-19} C$). Therefore, the MPPC gain can be obtained from the difference of the peaks between the pedestal and one photoelectron charge in the ADC distribution shown in Fig. 4.15.

There is a linear relation between the applied voltage and the single photoelectron gain. The breakdown voltage can be measured as the voltage with zero gain. It is known that the breakdown voltage has relatively large temperature dependence. This has been confirmed for devices of various pixel sizes and temperatures ranging from room temperature to liquid nitrogen temperature, and the temperature coefficient has been measured to be approximately $50\ \mathrm{mV/K}$ [41].

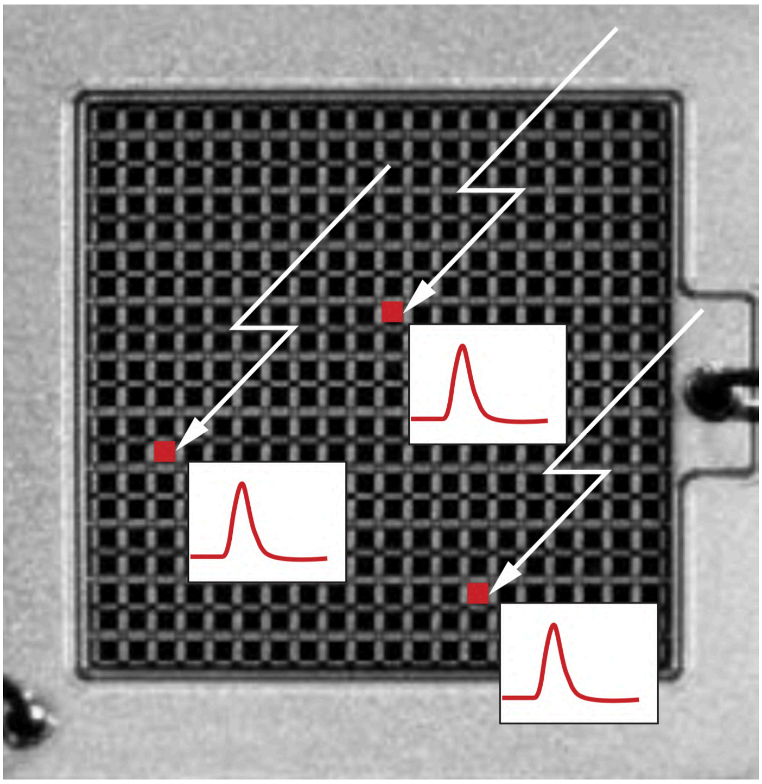

Figure4.13 Image of photon counting by MPPC [40]

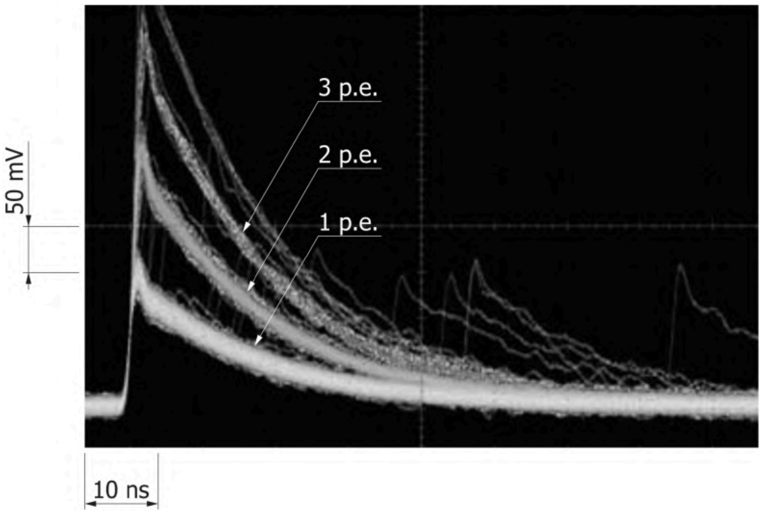

Figure4.14 Example of the MPPC waveform[40]

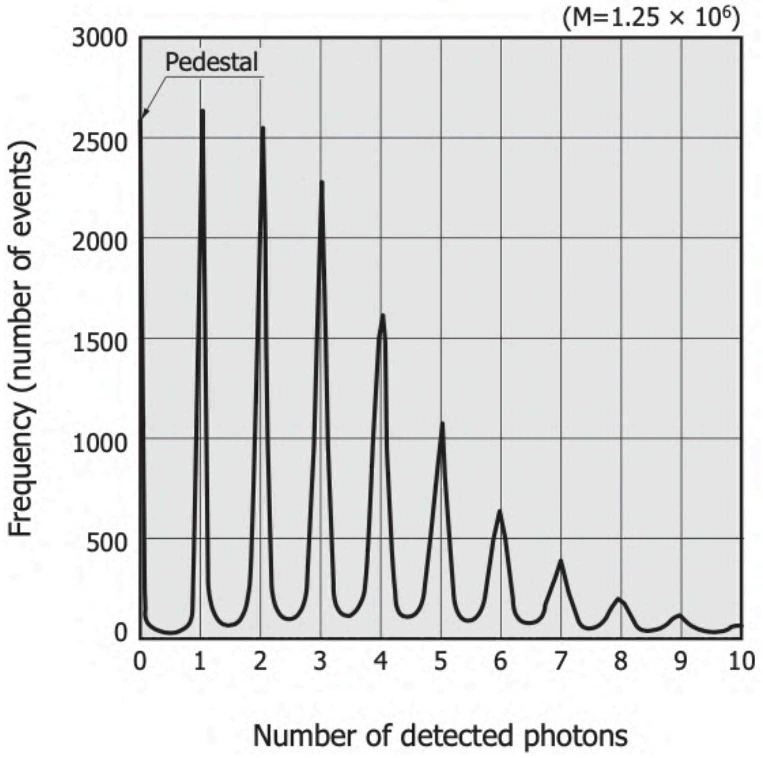

Figure4.15 Pulse height spectrum of MPPC [40]

4.5.3 Photon detection efficiency, dark noise

One of the important properties of a photodetector is its Photon Detection Efficiency (PDE). The PDE of the MPPC is determined by three factors: quantum efficiency (QE), fill factor (ratio of photosensitive area to sensor area), and probability of electron avalanche. MPPC has a higher QE than PMT due to the structure of the APD, but the fill factor is 50–70% due to the presence of insensitive regions around each pixel. The probability of an electron avalanche depends on the overvoltage, so the PDE also depends on the overvoltage.

Even in the absence of photon incidence, dark noise is generated by an avalanche of electrons due to thermal excitation. The size of the noise is identical to one photoelectron, but events equivalent to two or more photoelectrons may appear due to the effect of the cross-talk after-pulse described below.

4.5.4 Cross-talk, after-pulse

When an electron avalanche occurs in one pixel, photons with infrared wavelengths are generated, and they may enter an adjacent pixel and trigger another electron avalanche. This is called a cross-talk. This results in the measurement of more photoelectrons than actual incident photons. A trench structure between adjacent pixels filled with tungsten can reduce the cross-talk.

The electrons in the electron avalanche are trapped in the lattice defects of the crystal in the amplified region, and are re-emitted after a certain period of time, which can cause another avalanche. This is called an after-pulse. The capture probability of electrons and the time constant of re-emission change depending on the depth of the potential of the lattice defect. The understanding of this phenomenon is still in progress, but it can be reduced by using a silicon wafer with a better quality.

4.5.5 Saturation

As the number of photons entering the MPPC increases, more than two photons enter one pixel. However, even if more than two photons are injected into one pixel, the electron avalanche occurs only once. Therefore, as shown in Fig. 4.16, as the number of incident photons increases, the linearity with the number of excited pixels (number of detected photons) becomes worse. Furthermore, if more photons than the number of pixels are incident, the photons above the number of pixels cannot be detected, resulting in a constant output. Therefore, the number of excited pixels can be expressed by the following equation.

$$N_{fired} = N_{total} \times \{1 - exp(\frac{-N_{photons} \times PDE}{N_{total}})\} \tag{4.4}$$

To avoid the saturation, it is necessary to use MPPCs that have a sufficient number of pixels with a smaller pixel pitch for simultaneously incident photons. The details in the saturation is discussed in Chapter 8.

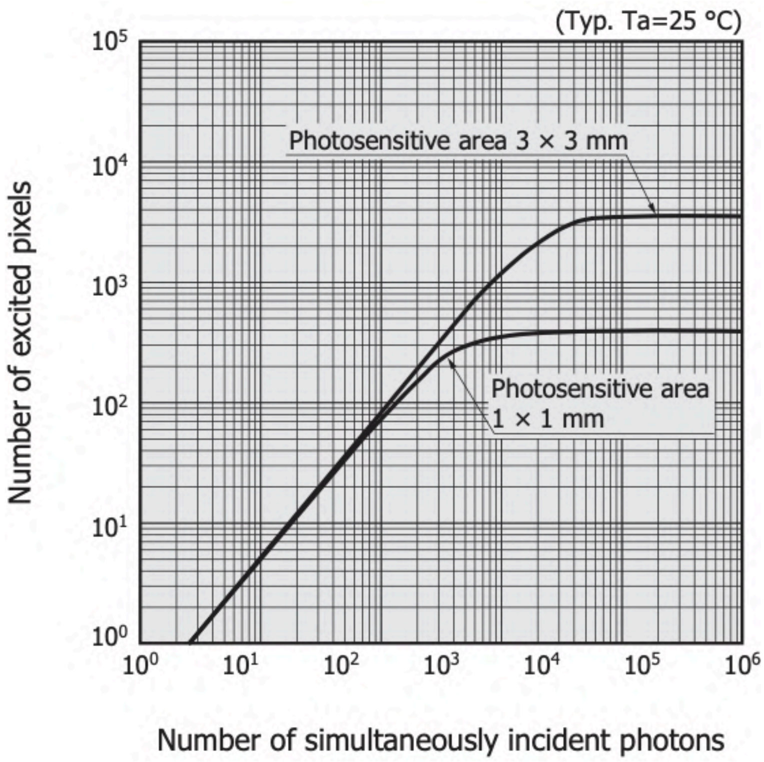

Figure4.16 Saturation of MPPC [40]

4.5.6 Small-pixel SiPM

The Sc-ECAL requires a large dynamic range because an electromagnetic shower forms the dense and thin shower and the BhaBha scattering causes the many shower in a close region. A large number of MIPs up to about 1,000 can be injected to one strip at a time, so a SiPM with a large dynamic range is required.

There has been an important development in the SiPM for the Sc-ECAL. Hamamatsu Photonics K.K. has developed an MPPC with a reduced pixel pitch down to 10 or 15 μm, which is quite useful to achieve the larger dynamic range required for the Sc-ECAL. The technological prototype uses both types of a pixel pitch of 10 and 15 μm (S12571-010P, S12571-015P[37]).

The latest small-pixel MPPCs have been further improved with trench structures between pixels. They reduce a crosstalk and dark noise, and improved photon detection efficiency [42]. The properties of small-pixel MPPCs are shown in Table 4.2.

Table4.2 Properties of small-pixel MPPCs by Hamamatsu Photonics K.K. [37][42]

Model	S12571-010P	S12571-015P	S14160-1310PS	S14160-1315PS
Photosensitive area	1×1 mm^2	1×1 mm^2	1.3×1.3 mm^2	1.3×1.3 mm^2
Pixel size	10 μm	15 μm	10 μm	15 μm
Number of pixels	10000	4489	16675	7296
Photon detection efficiency	10%	25%	18%	32%
Amplification rate	1.35×10^5	2.3×10^5	1.8×10^5	3.6×10^5
Cross-talk probability	$\sim 5\%$	$\sim 15\%$	$< 1\%$	$< 1\%$
Fill facror	33%	53%	31%	49%

4.6 ECAL Base Unit (EBU)

The electronics system of the technological prototype includes the front-end readout electronics and back-end Data AcQuisition system (DAQ) [43]. Each front-end board has a corresponding Data InterFace board (DIF), which is responsible for powering the front-end board, distributing commands, and collecting data. All DIF boards are connected to the back-end DAQ board, and all front-end boards are synchronized for triggering and data collection. The back-end part is responsible for sending clock, trigger, configuration commands, and uplink data collection to the front-end boards. The front-end board also integrates temperature monitoring, charge scaling, and LED scaling systems for a series of monitoring and scaling of the prototype system.

4.6.1 Front-end readout electronics

The SPIROC chip [44] is a dedicated chip for the SiPM multi-channel readout designed and developed by OMEGA [31]. The latest version SPIROC2E is used in the technological prototype. SPIROC2E supports 36 channels of input, mixed analog and digital parts. Fig. 4.17 and 4.18 illustrate the structure of one analog channel and the digital section of the SPIROC chip respectively. The analog section is responsible for input analog signal amplification, shaping and filtering, and charge and time sampling. The ADC part uses a 12-bit Wilkinson ADC to convert the shaped and amplified signal. The DAC is mainly responsible for adjusting the SiPM bias voltage for SiPM temperature compensation, and setting the trigger threshold and gain automatic switching threshold. The digital section is responsible for data packing and caching, generating the necessary flag bits, and writing the chip configuration registers and data transfer and communication.

Table 4.3 shows the main parameters of the SPIROC2E chip. SPIROC2E features large dynamic range, low noise, low power consumption, high accuracy, and a large number of readout channels. The SPIROC2E chip has self-triggering and forced-triggering modes. The latter mode can further reduce power consumption because of the long interval between ILC collisions, so that the analog part of the readout electronics can be powered down during the analog-to-digital conversion and data transfer until the next bunch train. In addition, the 16 instance

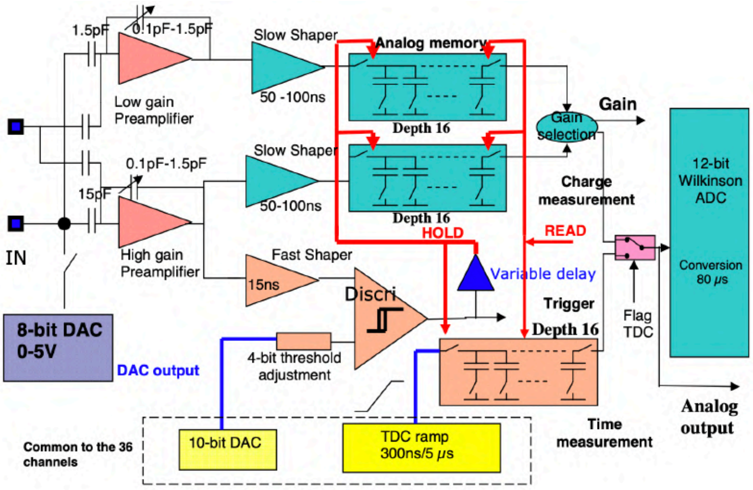

Figure4.17 One analog channel structure of the SPIROC chip [44]

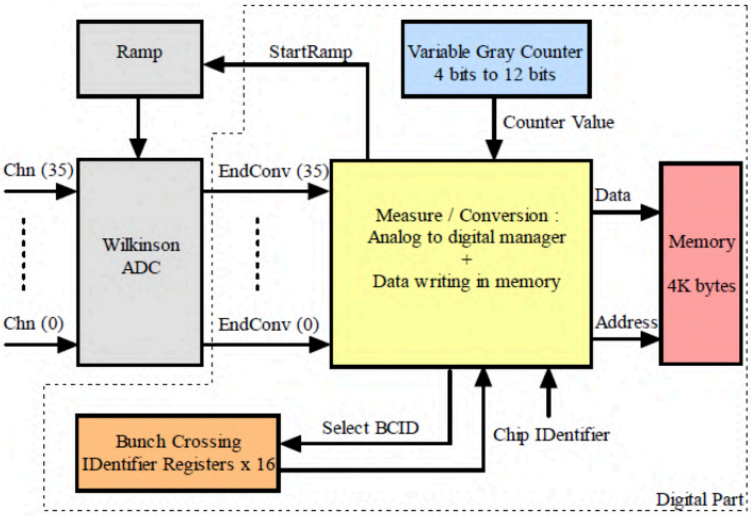

Figure4.18 Digital section structure of the SPIROC chip [44]

buffer depth per channel are specifically designed for the ILC collision mode.

Each detection layer has 210 SiPMs, and all SiPMs are readout by a cascade of 6 SPIROC2E chips, with the last chip's 6 channels left idle. Each chip readouts the SiPM at the corresponding location according to the principle of the shortest alignment, and Fig. 4.19 shows the distribution of the readout channels for each chip. The power module of the front-end board is placed on the DIF board, including the power supply for SPIROC2E and SiPM high voltage. This design can reduce the power consumption and thickness on the front-end board, and the design of independent modules of the front-end board and data readout board is convenient for maintenance and operation.

4.6.2 Temperature monitoring system

The temperature variation affects the properties of the SiPM such as the carrier mobility and the breakdown voltage V_{br}. The overvoltage V_{over} of SiPM is equal to the difference between the operation voltage V_{op} and the breakdown voltage V_{br}. When V_{br} increases with increasing temperature and V_{op} is kept constant, V_{over} decreases.

Table4.3 Performance parameters of SPIROC2E [44]

Input signal polarity	+
Trigger	Self-triggering and forced-triggering
Number of channels	36
Dynamic range	2000 times
Shaping time	25–200 ns
Signal output	Charge and time
Bias voltage adjustment	0–4.5 V (8 bit)
ADC bit widths	12 bit
Power consumption	$\sim$8 mW per channel (continuous operation mode)
Incident buffer depth	16

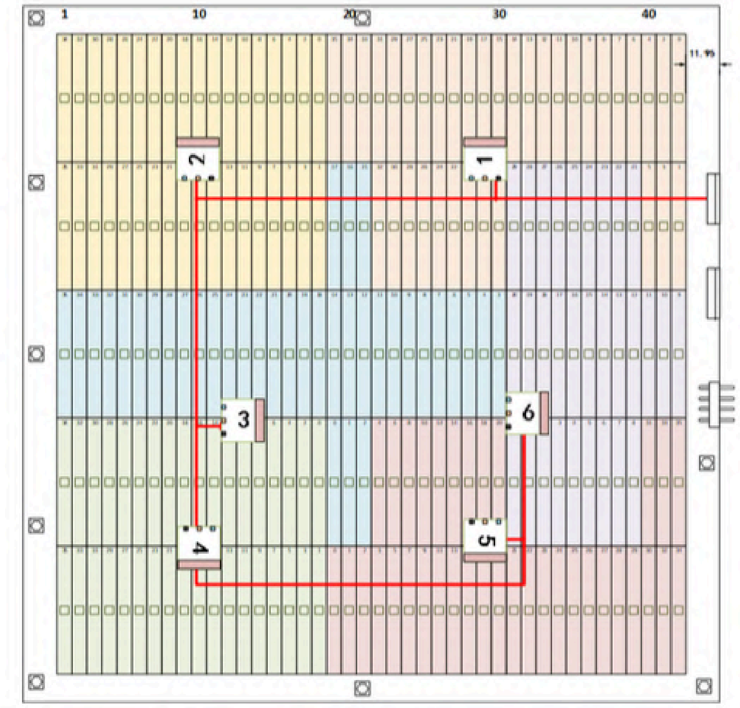

Figure4.19 Distribution of ASIC readout channels

The gain and PDE of SiPMs are proportional to V_{over}. It is necessary to control the operating temperature of SiPMs within a certain range and monitor the temperature for the correction of the temperature dependence of the gain and the energy response of SiPMs.

The overall power consumption of the front-end readout electronics is $\sim$60 W/h. The two major sources of the heat dissipation in the front-end electronics are the SPIROC2E chip on the EBU board and the high-voltage chip on the DIF board. The temperature distribution of the front-end board is related to the location of the chips, and the SiPMs are soldered at different locations on the front-end board, so it would be too much to install a temperature sensor for each SiPM location. It is possible to measure the temperature at several locations and calculate the temperature at each SiPM location by a special reconstruction algorithm [45]. Then the SiPM gain can be corrected offline or be compensated online by adjusting the operating voltage. Each EBU is equipped with 16 temperature probing chips soldered at several locations, as shown in Fig. 4.20, covering mainly around the devices with large heat generation and the edges of the whole EBU. Each temperature probing chip can measure from 0 °C to 85 °C with an accuracy of $\pm 0.1°$C.

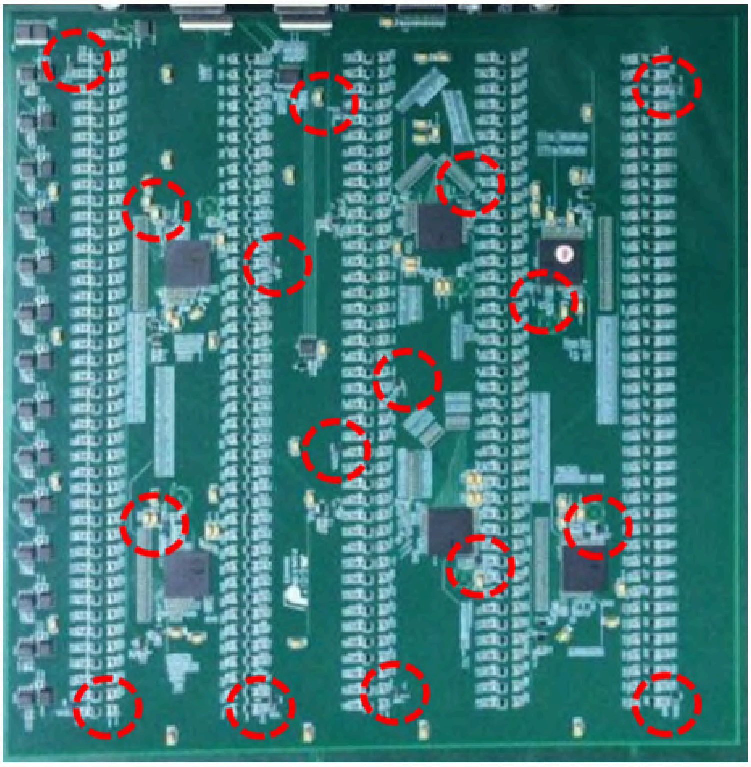

Figure4.20 Distribution of 16 temperature probe chips on EBU

4.6.3 Electric scaling system

The SPIROC2E has both high and low gain modes. The high gain mode is used when the input signal is small and the low gain mode is used when the input signal is large. Each SPIROC2E chip has a probe pin that can be connected to an external input signal, and the chip's internal configuration allows to achieve scaling of all electronics readout channels. The step voltage signal ΔV is converted to a charge $Q = C_t \times \Delta V$ on the series capacitor C_t, allowing the front-end electronics readout system to be scaled by the analog signal input, commonly referred to as electrical scaling. The equivalent input capacitance of the preamp is about 16.5 pF and the external resistance to ground is typically 100 Ω. The corresponding choice of capacitance of 18 pF yields a decay time $\tau \sim 3.5$ ns of the scaled signal, which basically matches the signal waveform characteristics of a SiPM. The digital-to-analog converter (DAC) provides an output voltage of 0–2.5 V to six amplifiers, which is then converted by 18 pF capacitors to a charge similar to that of the SiPM signal waveform.

4.6.4 LED scaling system

Each strip is equipped with an LED for gain calibration and monitoring. Fig. 4.21 shows the circuit schematic of the LED scaling system. Because not all channels can be covered by a single driver, the 210 channels are divided into 14 groups and the scale of each group is selected by a selector switch. By adjusting the signal strength of the driver circuit, the bias voltage on the LEDs can be controlled. The LEDs can be turned on and off by using two NMOS onsets at the ends of each LED to generate light pulses with a width of less than 10 ns.

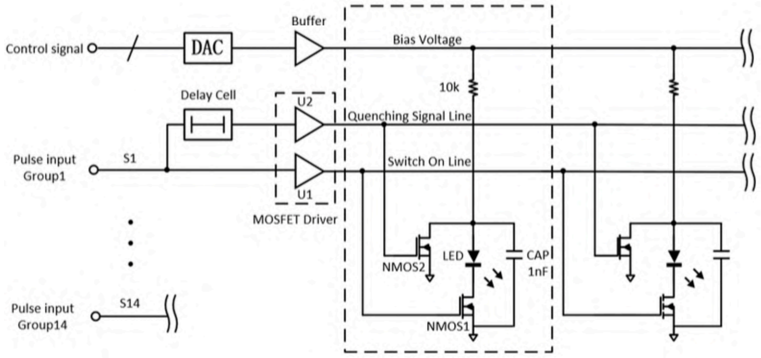

Figure4.21 Circuit schematic of LED narrow pulse scale system

The LED is located at a distance of 5.26 mm from the SiPM in a hole punched on the PCB board as shown in Fig. 4.22. The LED is inverted and welded to the back of the PCB board, and the ESR has also made a hole in the corresponding position. The light from the LED is transmitted in the scintillator to the SiPM surface. The wavelength of LED is ~400 nm, which matches with the peak wavelength of the SiPM measurement spectrum.

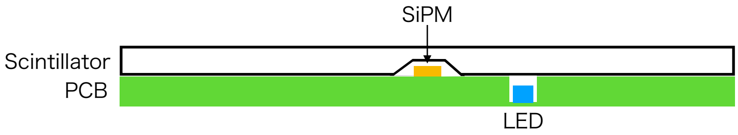

Figure4.22 LED position for one channel

4.6.5 Data Acquisition System

The back-end data acquisition system of the technological prototype includes a DAQ board, FELIX acquisition card and server. Fig. 4.23 shows the schematic diagram of the electronic readout system of the prototype, including the main functions of each module and the upstream and downstream logic. The DAQ board is connected to the 30 front-end DIF boards via HDMI cable. Its main functions are: (1) aggregating transmission data from the DIFs; (2) distributing clocks and commands synchronously to the DIFs; (3) receiving external trigger information and fan-out to the DIFs after logical processing; and (4) communicating with the back-end FELIX and uploading data. FELIX is a data acquisition system designed for ATLAS upgrade [46] with high bandwidth and high throughput scalability to meet the needs of back-end data acquisition systems for complex detector systems in next-generation high-energy physics experiments. The FELIX acquisition card and the DAQ board are connected by two optical fibers, and their functions are: (1) DAQ link processing; (2) data routing; and (3) data exchange with the server.

4.7 Construction

This section gives the fabrication and assembly of the detection layer, and the assembly and commissioning of the complete technological prototype in conjunction with the data acquisition system.

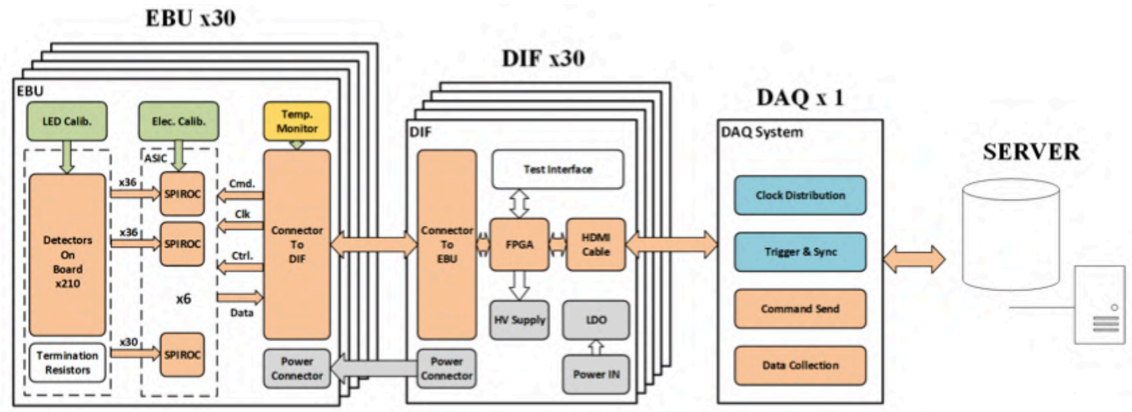

Figure4.23 Schematic diagram of the readout system

4.7.1 Production of detection layer

The detection layer consists of the following components: scintillator strip, reflective film, SiPM, and electronics. Fig. 4.24 shows the flow of the detection layer fabrication. After the production of the electronics board and the soldering of the SiPMs, the electronics test and the SiPM and LED test are performed to ensure that all devices are working properly. In addition, all front-end boards are tested in a temperature-controlled room for 48 hours at 50 ° to ensure the long-term stability of all front-end boards. The left in Fig. 4.24 shows the strips wrapped with the ESR film. All strips are made of several large 2 mm thick BC-408 plastic scintillator plates cut into 5 mm × 45 mm × 2 mm scintillator strip and a dimple for coupling to the SiPM is machined on the bottom of the strip. The reflective film required to package the strip is made from 3M ESR film, cut to the size of the strip with the corresponding perforation for the SiPM and LED. After the strip is wrapped with the ESR film, 10% of each batch is randomly selected for the light yield test to ensure that the strips produced in each batch meet the light yield requirements of the prototype. The strips are assembled and adhered to the EBU board using an epoxy resin adhesive. The right in Fig. 4.24 shows the complete detection layer. A total of 30 detection layers re fabricated for the prototype, and 2 additional layers with the SiPM double-side readout are also fabricated, discussed in Appendix A.

Fig. 4.25 shows the components of a super-layer and Fig. 4.26 shows the assembled super-layer. The two detection and absorber layers are assembled into a super-layer. All detection layers are assembled in a clean room. A total of 15 super-layers were produced, and the contents of the super-layers are shown in Table 4.4. An additional super-layer with the SiPM double-side readout was also produced, and the details are discussed in Appendix A.

Table4.4 Items of super-layers

Super-layer	Number of modules (EBU)	SiPM	Strip length	Strip material (process)
Bottom-side readout 1	12 (24)	S12571-010P	45 mm	BC-408 (casting)
Bottom-side readout 2	3 (6)	S12571-015P	45 mm	BC-408 (casting)
Double-side readout	1 (2)	S12571-015P	90 mm	Polystyrene (injection)

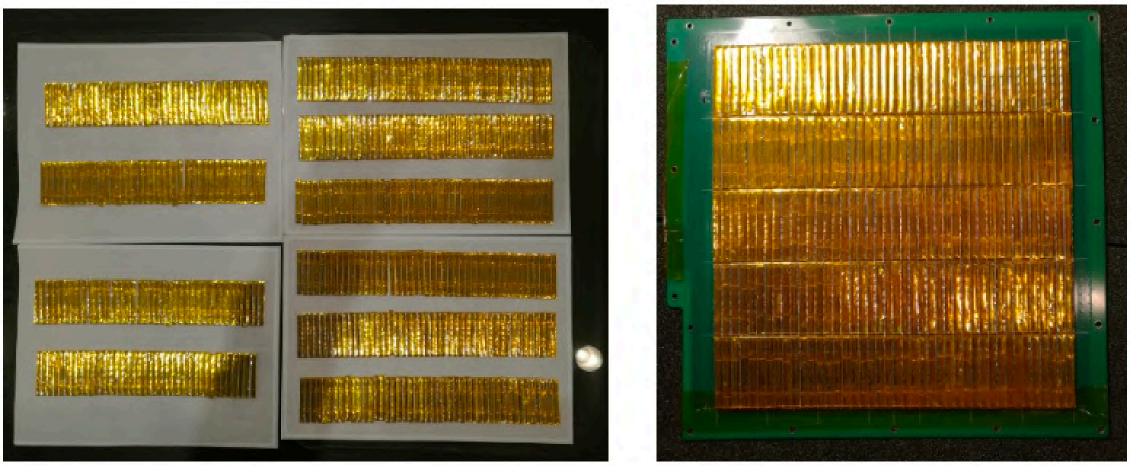

Figure4.24 Plastic scintillator strips wrapped with the ESR reflective, the outside of ESR is sealed with 3M insulation tape (left). Single-layer board after assembling scintillator strips (right)

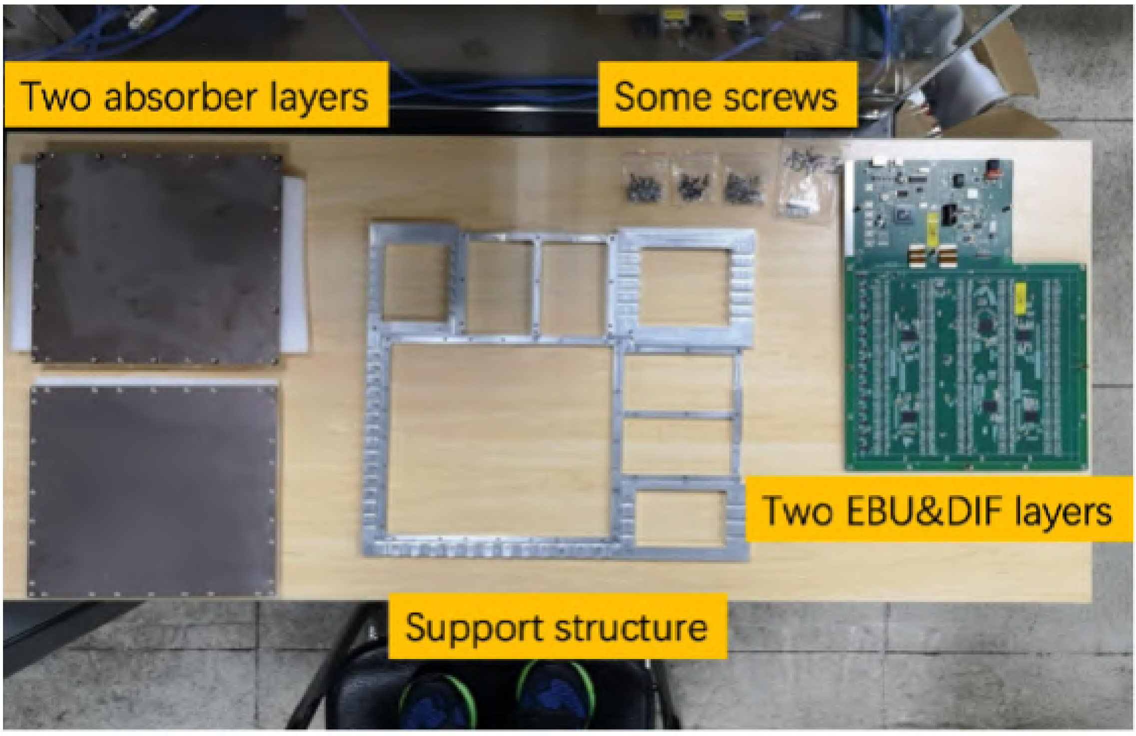

Figure4.25 Components of a super-layer

4.7.2 Assembly and integration of prototype systems

The super-layer is the basic unit of the prototype and each super-layer can be individually assembled and disassembled in a very flexible way to facilitate different tests. After the fabrication, each super-layer is inserted one by one into the corresponding slot and screwed to the a mechanical frame. Fig. 4.27 shows the arrangement of the detection layers for each type of SiPM. The 15 μm-pitch SiPM (S12571-015P) has lower dynamic range compared to the 10 μm-pitch SiPM (S12571-010P), so the detection layers with S12571-015P are placed on the

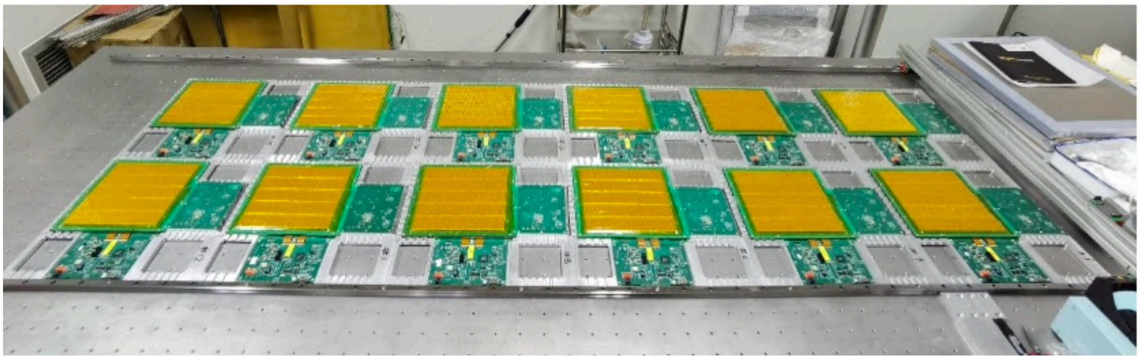

Figure4.26 Assembled super-layer units

first and last layers of the prototype where the saturation effect is small. The fan cooling system is assembled on the outermost side of the mechanical structure, with a set of 120 W cooling systems on the left and right sides emitting air in the same direction. The overall dimensions are about 796 mm × 428 mm × 538 mm, weighing more than 200 kg as shown in Fig. 4.28.

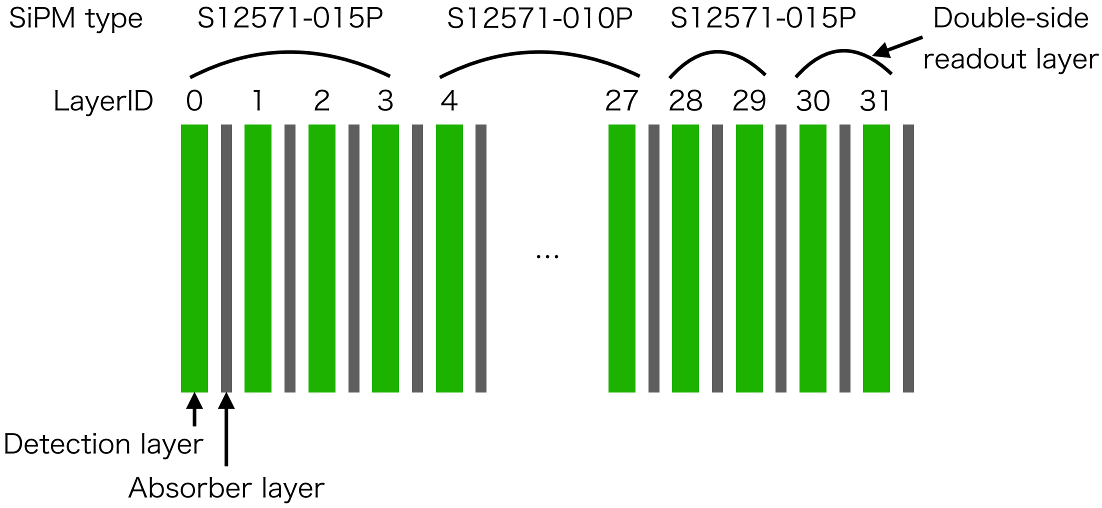

Figure4.27 Layout of the detection layers corresponding to the SiPM types of S12571-015P (15 μm-pitch) and S12571-010P (10 μm-pitch)

The main body of the technological prototype can be separated, and the front-end board is powered by connecting a power source outside the prototype, and the DAQ board is connected to the server. Fig. 4.29 shows the joint commissioning of the prototype with the data acquisition system. All parts of the prototype are functioning properly, and more tests to evaluate the key performance of the technological prototype are presented from the next chapter.

4.8 Commissioning

The purpose of this study is to demonstrate the performance of the Sc-ECAL. This Sc-ECAL technological prototype is the first large-scale technological prototype for the PFA ECAL, and the demonstration of its performance is crucial toward the construction of the actual detector. By calibrating the key parameters of the prototype and

Figure4.28 The internal structure and the appearance of the main part of the assembled prototype

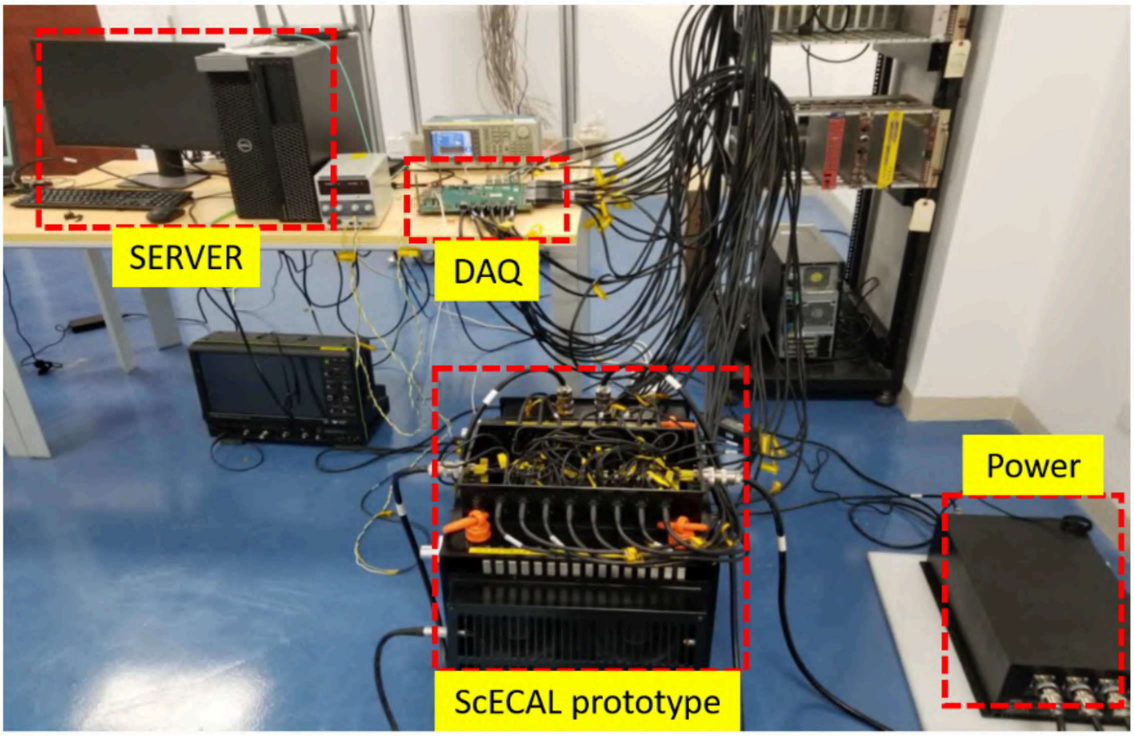

Figure4.29 Joint commissioning of the prototype and data acquisition system

checking their stability, it can be verified that the Sc-ECAL can be operated stably in the actual detector. By demonstrating the performance such as the position resolution, shower scalability, and jet energy resolution, it can be confirmed that the Sc-ECAL meets the requirements for the PFA ECAL required for the precision physics at the future Higgs factory.

To achieve these objectives, a four-step study is conducted:

- Calibration and stability check of the key parameters of the technological prototype
- Performance evaluation of the technological prototype
- New method for the saturation correction

- Evaluation of the jet energy resolution

Please note that the analysis uses 30 standard detection layers, and does not use the two detection layers with the SiPM double-side readout due to the different configuration.

At the first step, the key parameters such as the SiPM gain and MIP response are calibrated channel by channel using the LED and cosmic-ray. The stabilities of these parameters are also checked by taking the long-term calibration run. By looking at the stability of each channel and each layer, it can be verified whether the actual detector can be operated stably.

At the second step, the performance of the technological prototype is evaluated. The position resolution is evaluated by the straight track of cosmic-ray events, and make sure it meets the requirement of the 5 mm $\times$ 5 mm cell size for the PFA ECAL. Because the test beam experiment was cancelled due to the COVID-19, the performance using the electromagnetic shower is evaluated by the cosmic-ray induced showers. The performance is compared with the Monte Carlo simulation, and it is verified that the prototype is working as expected.

At the third step, a new method for the saturation correction is developed. The saturation is an issue at the Sc-ECAL because the Sc-ECAL has many pile-up hits from the dense EM shower. A novel measurement method and modeling of the SiPM saturation is developed for more accurate correction of the saturation for the use of the scintillator and SiPM. This method makes an impact on the saturation correction for not only the Sc-ECAL, but also other detectors using the scintillators and SiPMs.

At the final step, the jet energy resolution is evaluated using the full simulation of the ILD detectors. The parameters of the Sc-ECAL obtained by the technological prototype, and the saturation behavior based on the new method are used in the evaluation. It is confirmed that the jet energy resolution of $3 - -4\%/\sqrt{E(\mathrm{GeV})}$ required for the precision Higgs physics is achievable with the Sc-ECAL. We will also discuss the usefulness of the new saturation model and the comparison of SiPM types to contribute to the design decision of the actual detector.

Chapter 5

Commissioning and Reconstruction

The Sc-ECAL technological prototype has been constructed, then is commissioning. The commissioning includes the LED test and cosmic-ray test, which can be used to calibrate the key parameters of the prototype and evaluate the performance of the Sc-ECAL. The calibrations for the key parameters of the Sc-ECAL such as the SiPM gain and MIP response should be performed to make sure the detector is working property and establish how to operate the actual detector. The algorithm for the reconstruction is developed and applied to the analysis of the cosmic-ray data.

This chapter shows the flow of the commissioning, calibration procedure, and the reconstruction for the cosmic-ray test. The procedures of the calibration and the algorithm of the reconstruction can be applied to the actual detector as well. The results of the calibration and performance evaluation are shown from the next chapter.

5.1 Calibration and commissioning test

The completed technological prototype needs the detector calibration and performance test. The calibrations for several parameters are necessary to reconstruct the physics event. After the calibrations, the performance of the prototype should be checked. This section gives the calibration procedure and the tests for the calibrations and performance evaluation.

5.1.1 Calibration procedure

The raw signal from the prototype is based on the ADC count. The signal ADC count should be converted to the energy using several calibration factors. The calibration for the prototype is performed in 5 steps:

- Gain calibration
- Inter-calibration
- Cross-talk and after-pulse calibration
- Pedestal calibration
- MIP response calibration

As the first step, the per-channel response is converted to the number of photoelectrons using the single photoelectron gain of the SiPM. The ADC-photoelectron conversion factor, c^{gain}, is determined by the single photoelectron charge measured by the LED light. After the calibration, the non-linear response of the large signal can be corrected. The saturation of the SiPM, discussed in Chapter 8, is a function of the number of photoelectrons, so the signal converted by the c^{gain} can be used to the correction of the SiPM saturation.

As the second step, the charge injection of the electronics is performed. The c^{gain} is measured using a high gain amplifier to sufficiently separate the photoelectron peaks, whereas the physics data acquisition uses a low gain amplifier due to the wide dynamic range required. The inter-calibration factor, c^{inter}, is used to convert the low gain signal to the unit of high gain. The c^{inter} is measured as the ratio of the amplitudes of the response to LED light with the high gain to the low gain settings.

As the third step, the probability of the cross-talk and after-pulse P_{CTAP} is measured. The SiPM saturation contains the effect of the cross-talk and after-pulse. By determining the CTAP probability in each channel using the LED light, the SiPM saturation can be corrected more accurately.

As the forth step, the pedestal is subtracted from the signal ADC counts. The pedestal, $c^{pedstal}$, can be obtained by the mean of the distribution of the events without signal.

As the fifth step, the per-channel response is normalized using the response to the minimum ionized particle (MIP) in the cosmic-ray data. The calibration factor, c^{MIP}, is expected as the most probable value (MPV) of the Landau distribution obtained by the cosmic-ray. The injection angle of the cosmic-ray is corrected to the vertical incidence. After this calibration, the detected energy of the detector is expressed in units of MIP.

Using these calibration factors, a signal in channel i for the physics event can be written by:

$$A_i^{corr}[\mathrm{MIP}] = F^{-1}_{P_{CTAP}}\big((A_i[\mathrm{ADC}](T) - c^{pedestal})\frac{c_i^{inter}}{c_i^{gain}(T)}\big)\frac{c_i^{gain}(T)}{c_i^{inter}c_i^{MIP}(T)} \tag{5.1}$$

where $A_i[\mathrm{ADC}](T)$ is the uncorrected signal of the cell in ADC counts at temperature T, and F^{-1} with a parameter P_{CTAP} is the function for the saturation correction. Some calibration factors are determined as a function of temperature. The $(A_i[\mathrm{ADC}](T) - c^{pedestal})\frac{c_i^{inter}}{c_i^{gain}(T)}$ converts the uncorrected signal in ADC counts to the signal in units of the number of photoelectrons. The $F^{-1}_{P_{CTAP}}$ corrects the saturation of the SiPM. The $\frac{c_i^{gain}(T)}{c_i^{inter}c_i^{MIP}(T)}$ converts the signal in the number of p.e. after the saturation correction to the corrected signal in units of the number of MIPs.

The sum of these signals is the energy of the physics event in units of MIP, which is written by

$$E_{reco}[\mathrm{MIP}] = \Sigma_{strip}A_i^{corr}[\mathrm{MIP}] \tag{5.2}$$

The average value of E_{reco} as a function of incident beam energy represents the calibration of the energy scale in GeV.

5.1.2 LED test

For the first to third calibration steps, c^{gain}, c^{inter}, and P_{CTAP} are determined using the LED test. The gain and CTAP calibration need the LED light with low intensity in order to separate the photoelectron peaks, while the inter-calibration needs some runs with several light intensities in order to obtain the ratio of the low gain and high gain. The LED scan from low light intensities to high intensities is performed.

The LED test is performed in laboratory. The LED driver gives the bias voltage to the LED, then the LED outputs a narrow blue light pulse. The SiPM detects the LED light coming through the strip. The data is taken by the forced-triggering from the driver. The scan with several light intensities can be done by changing the bias voltage from the driver. The LED test is performed once a day over a month to check the stability of each parameter.

5.1.3 Cosmic-ray test

For the forth and fifth calibration steps, $c^{pedstal}$ and c^{MIP} are determined by the calibration using cosmic-ray muons. In order to determine these factors and check the their stabilities, the long-term cosmic-ray test over 3 months is performed.

The longterm cosmic-ray test is performed in laboratory. The prototype is rotated by $90°$ as shown in Fig. 5.1. The cosmic-ray data is taken by the coincidence of Layer 1 and Layer 29, whose layers are located at the top and bottom of the prototype.

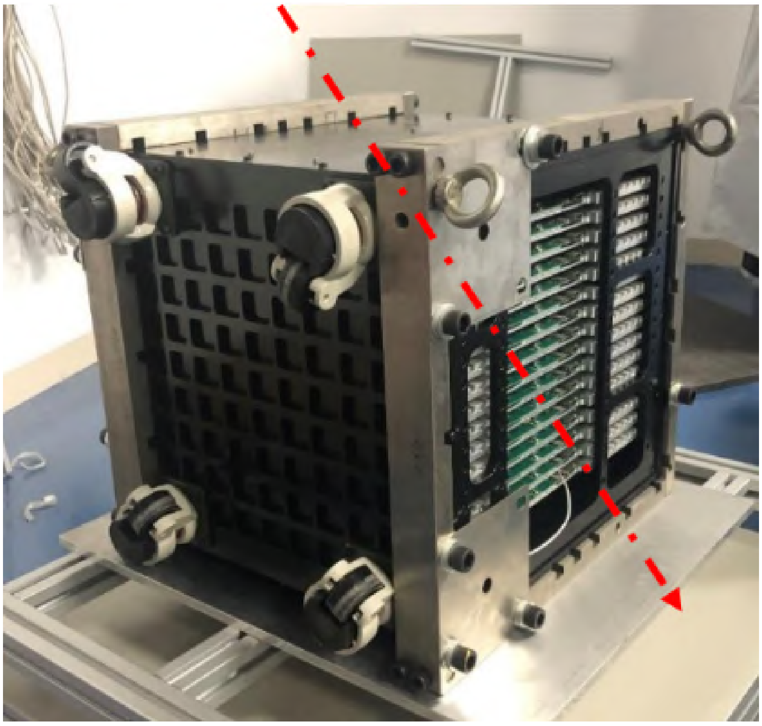

Figure5.1 Prototype is rotated by 90° for cosmic-ray test

The threshold is set for each SPIROC2E chip as ∼0.5 MIP ADC counts. When a channel exceeds the threshold, the data of 36 channels belonging to the same chip are stored in one memory cell. Usually, if the 16 memory cells equipped in a SPIROC2E chip are full, the data is extracted from the chip and sent to the PC. However, the rate of cosmic-ray events is very low ~ 0.25 Hz, so the memory cells are refreshed every 4 ms. The master clock sends the time origin and clock to each layer. If there are hits beyond the threshold at the trigger layers of Layer 1 and 29 in 4 ms refresh period, the data stored at the memory cell at that time are extracted from all chips with the hits beyond the threshold. The data includes the bunch-crossing ID, ADC counts in the high gain and low gain mode, TDC counts, temperature, and so on.

The cosmic-ray tests are carried out over 3 months. The event rate is $\sim$ 16 events per minute. ~ 2000 hits are collected at each channel. The temperature is monitored during the cosmic-ray tests by the temperature sensors equipped on the EBU.

5.1.4 Test beam experiment

The detailed calibration and performance of the prototype must be evaluated by the test beam experiment. The MIP calibration is also performed using the muon beam, and the conversion from the signal in units of MIP to absolute energy scale can be calibrated using the electromagnetic shower. The energy linearity can be evaluated by the electron beam with several energies, and the energy resolution is evaluated by the deviation of the detected energy with high-energy electron.

The test beam experiment for the Sc-ECAL prototype was planned in August 2020 at Deutsches Elektronen-Synchkrotron (DESY), but postponed to February 2021 due to the COVID-19 pandemic, and the test beam in February 2021 was also canceled due to the pandemic. The test beam experiment is currently planned using the electron beam at the Beijing Synchrotron Radiation Facilities (BSRF) [47], but the schedule and beam quality are not clear.

The performance is evaluated using the electromagnetic showers induced by the cosmic-rays. The shower events are searched for in the cosmic-ray data, and some properties of the showers such as the profile and the total energies are compared with the Monte Carlo simulation.

5.2 Reconstruction for straight track

The reconstruction algorithm for the straight track is developed. The straight track can be used to eliminate the noise hits and calibrate the MIP response. The straight-track reconstruction for the cosmic-ray is performed in four steps:

- Pre-selection
- Strip Splitting Algorithm (SSA)
- Cone clustering
- Track fit

This section describes each step in detail. After the reconstruction, the signal ADC counts are corrected using the angular information of the track.

5.2.1 Pre-selection

At the pre-selection step, the cuts for the total number of layers and channels with his are performed. Fig. 5.2 shows the cut of the noise events and the cosmic-ray events. The peak around 3 layers is caused by the dark noise of the SiPM and the accidental trigger. The events with more than 22 layers with hits are selected, because the events, whose total hit layers is small, may not come from the cosmic-ray events, but the dark noise from the SiPMs or the accidental triggered events. The events with more than 64 channels with hits are eliminated, because the events with many hits more than 3 hits per layer have too many noise hits.

5.2.2 SSA

As discussed in Section 4.2.1, the SSA is used for the analysis of the prototype data. The pitch of each channel is 5.3 mm × 5.3 mm, which is slightly larger than the size of the strip, due to the gap between the strips for machining

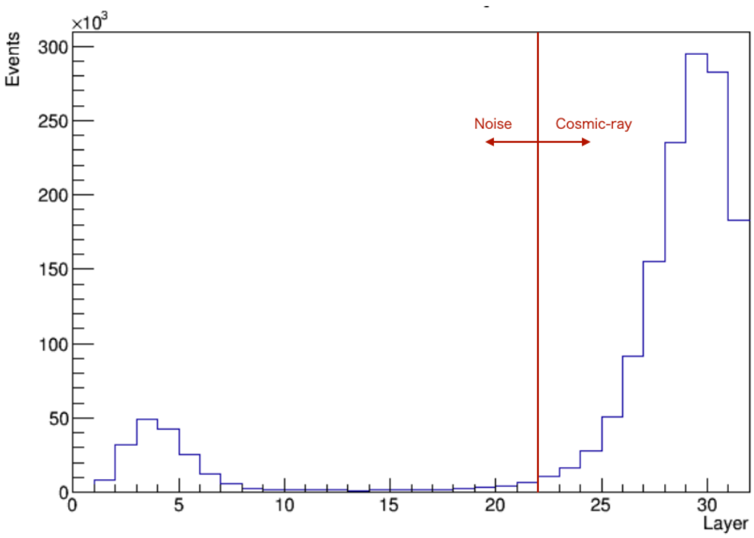

Figure5.2 Distribution of the total number of the hit layers

accuracy and reflector. The edge pop off due to $5.3 \times 9 = 47.7 > 45.4$, and the strip cannot be split by just 9 cells. Then the edge processing is implemented.

As shown in Fig. 5.3, the orthogonally aligned strips have partially overlapped area at the strip edge. This area is split as one independent cell. The position of the cell is set as the center of the overlapped area, and the energy weight from the upper or lower layer is weighted according the overlapped length. The strip is split by 10 cells including the edge, and the implementation of the SSA to the prototype is done.

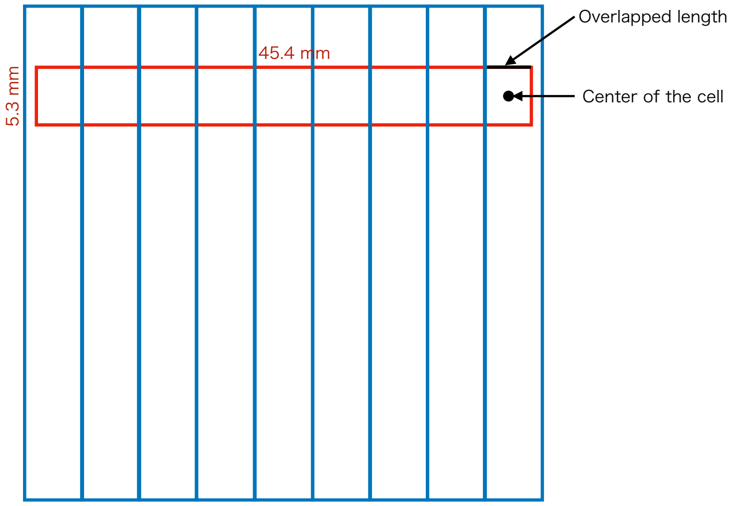

Figure5.3 Edge processing of the SSA

5.2.3 Cone clustering

The cone-based clustering algorithm is used to find the cosmic-ray hits and eliminate the noise. The overview of the cone clustering is shown in Fig. 5.4. The clustering starts from the top layer, and the cone is spread from the initial hit to the next layer or the layer after that. The cone is spread in the initial direction of the injection particle.

If the hits lie within the cone, the hits are added to the cluster. The next cone is spread from new cluster hits to the next layer or the layer after that, then find the next cluster hits within the cone. The cone algorithm repeats this process. The isolated hits due to the random noise are eliminated by this algorithm.

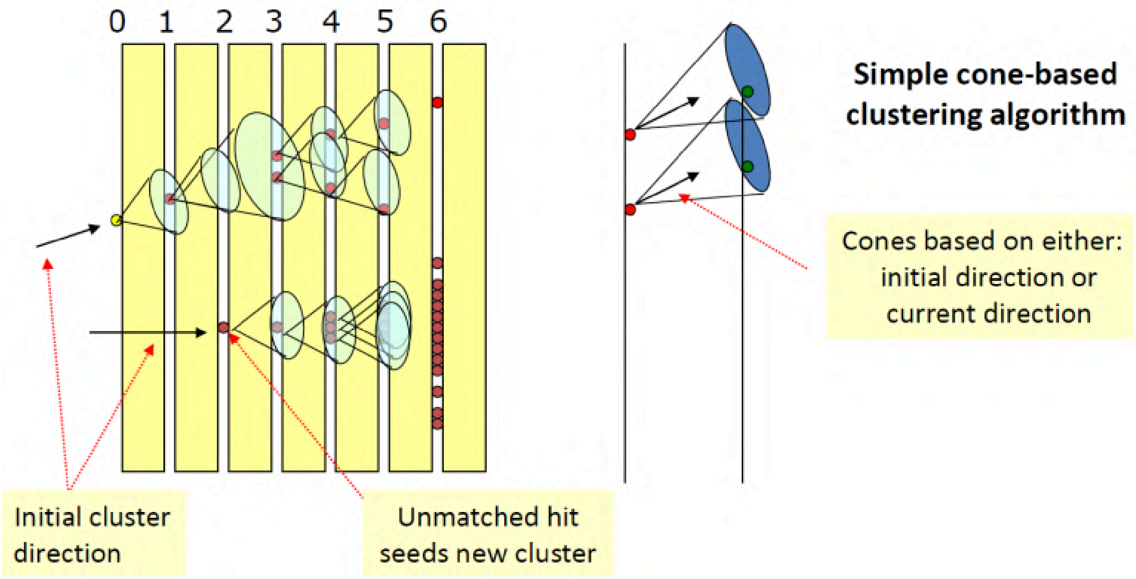

Figure5.4 Overview of the cone algorithm [48]

5.2.4 Track fit

A track fitting is performed for the hits after the SSA and the clustering in x and y axis using TMinuit, and the track information such as the slope and intercept is obtained. The clustering hits still have noise hits, so the track fit is performed iteratively. First, the all hits are fitted linearly, and the track is obtained. If the residual of the hit, the difference between the hit position and the track, is smaller than the threshold, the hit is regarded as the cosmic-ray hit. If the residual is larger than the threshold, the hit is regarded as the noise. Then, the fit is performed using the hits regarded as the cosmic-ray hit, and the procedure is repeated lowering the threshold step-by-step. The threshold is changed from 47.5 mm to 7.5 mm in 5 mm pitch.

Fig. 5.5–5.7 show the event display of the cosmic-ray after the pre-selection, after the SSA, after the clustering and track fit, respectively. The SSA works properly and the strip is split by the small cells. The noise hits still remain after the SSA, while the noise hits are subtracted after the clustering and track fit. The hits belonging the cosmic-ray track are successfully clustered and the track is obtained.

5.2.5 Angular correction

For the MIP response calibration, the signal ADC count at each hit is corrected by the injection angle using the track information. When the cosmic-ray is incident on the strip with an angle, the energy deposit increases compared to the case of perpendicular incidence. The path length in the strip can be calculated with the track angle, and the ADC count is corrected by the path length to the strip thickness (2 mm). Fig. 5.8 shows the distributions of the signal ADC counts with and without the angular correction. The peaks of the distribution are shifted to lower ADC counts, and the spreads become smaller after the correction. The angular correction is applied at each

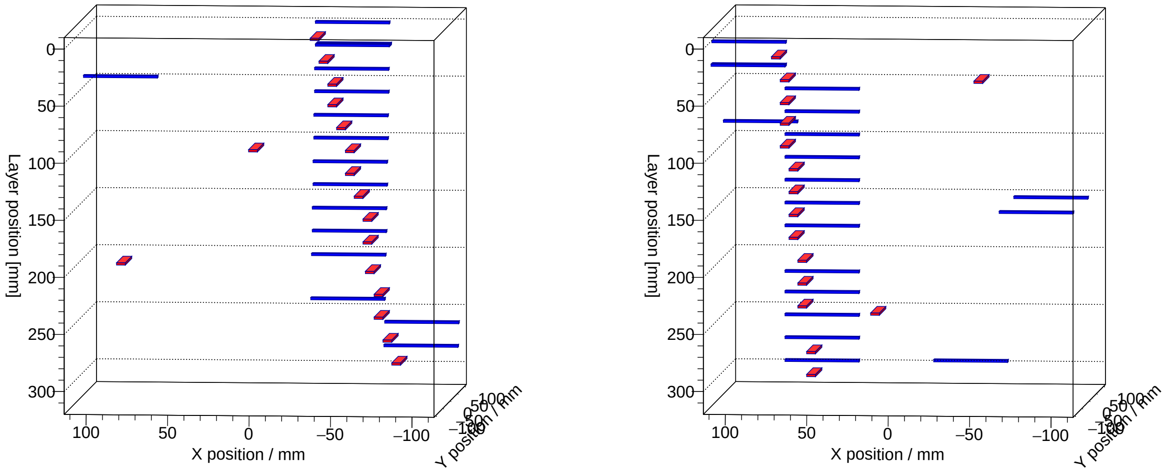

Figure5.5 Event display of the cosmic-ray after the pre-selection

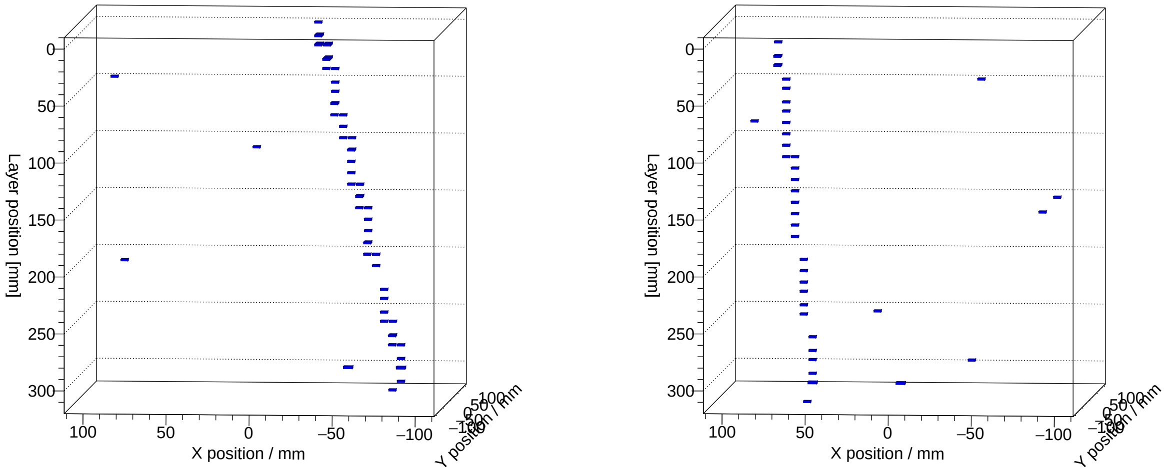

Figure5.6 Event display of the cosmic-ray after the SSA

hit and each event.

5.3 Reconstruction for shower event

The test beam experiment was cancelled, so the performance of the Sc-ECAL for the electromagnetic showers is evaluated using the cosmic-ray showers. The reconstruction for shower events is performed in three steps:

- Calibration
- SSA
- Shower search

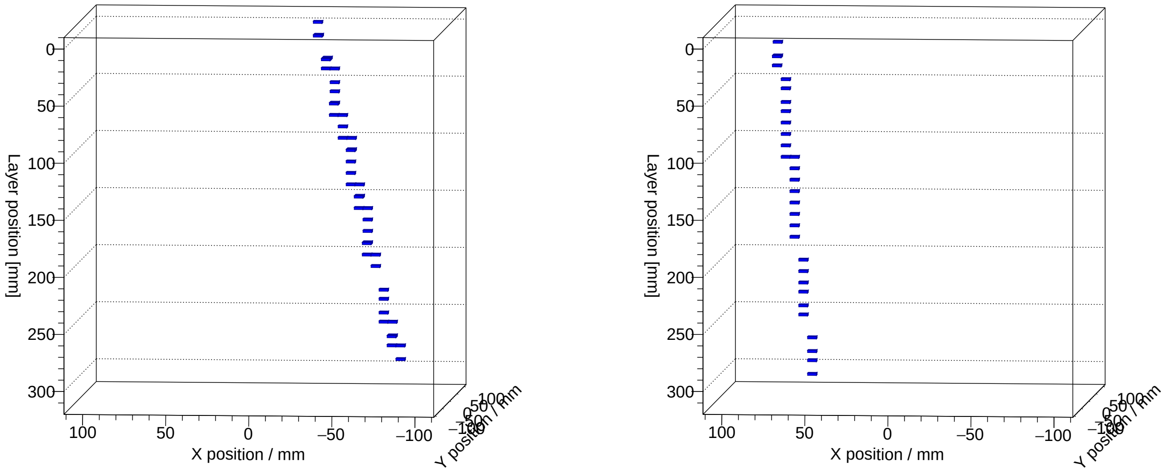

Figure5.7 Event display of the cosmic-ray after the clustering and track fit

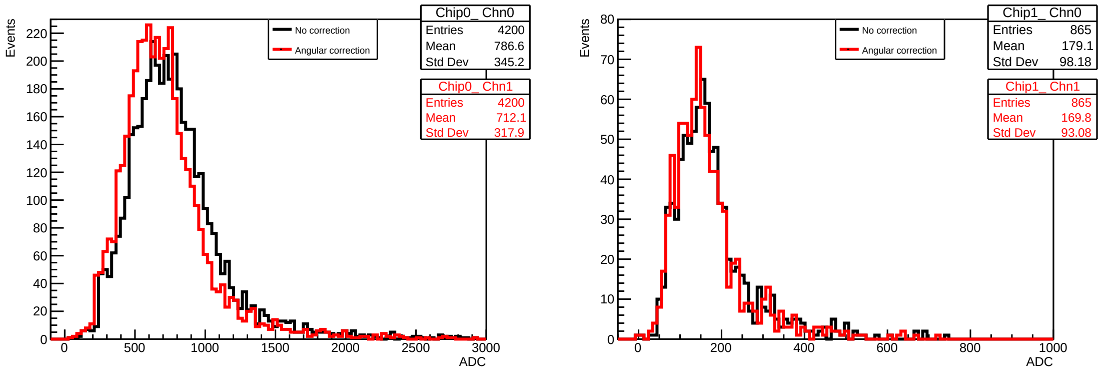

Figure5.8 The distribution of the signal ADC counts at one channel of 15 μm-pitch SiPM (right) and 10 μm-pitch SiPM (left). The black shows the distribution without any correction, and the red shows the distribution after the angular correction.

5.3.1 Calibration

The calibration procedure follows Section 5.1.1, but in case of the cosmic-ray shower, the saturation correction of the SiPM is not implemented because the light yield is too low to be affected by the saturation. The temperature correction is implemented in each hit, and the calibration is performed as:

$$A_i^{corr}[\text{MIP}] = \left(A_i[\text{ADC}](T) - c^{pedestal}\right)\frac{1}{c_i^{inter}c_i^{MIP}(T)} \tag{5.3}$$

$$A_i^{temp\ corr}[\text{MIP}] = (1 + (T_i - T_{ref})d^{MIP})A_i^{corr}[\text{MIP}](T) \tag{5.4}$$

where the temperature correction described in the second line is discussed in Section 6.6.3.

The SSA is the same as the track finding discussed in 5.2.2.

5.3.2 Shower search

The shower search is performed by combining the cone clustering and applying cuts to the cluster hits. The angle of the incident particle is important to search for the shower event, so the first few layers are used to calculate the incident angle. The procedure of the shower search is as follows:

- Cone clustering with no incident angle
- Shower identification
- Linear fit before the shower start
- Cone clustering with incident angle
- Shower identification

Fig. 5.9 shows the scheme of the shower identification. At first, the cone clustering with no injection angle (the zenith angle is 0 degree, vertical to Prototype) is performed. Using the cluster hits, the number of hits and the energies are summed by each layer. If 9 or more hits and 1.5 MIP or more energy are detected in three consecutive layers, the event is recognized as the shower event. The shower start layer is set as the one layer before the cut of the three consecutive layers.

After the first shower identification, the linear fit is performed using the hits before the shower start. In order to calculate the incident angle, the events that the first 6 layers are always linear (the sum of hits is less than 9) are selected and fitted by the TMinuit. Then, the cone clustering with the incident angle is performed using the angle of the fitted linear track. The shower identification is performed again, then the shower events are extracted.

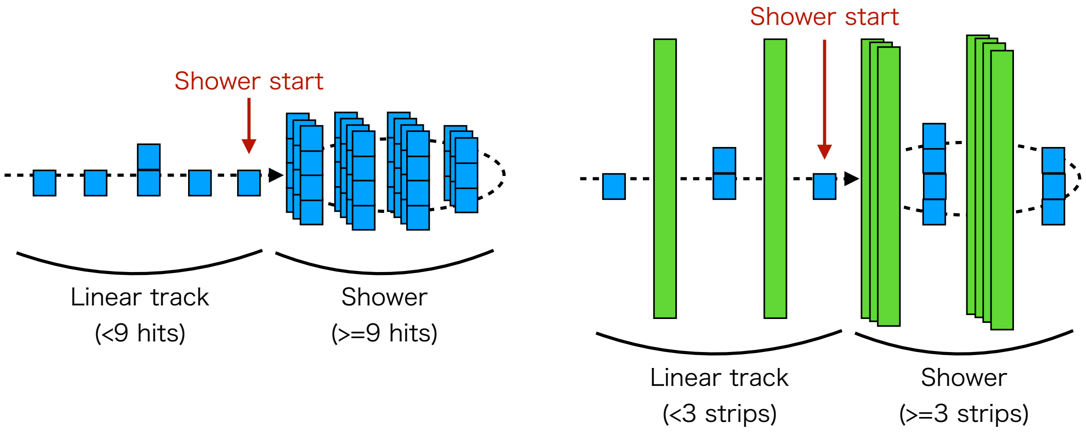

Figure5.9 Scheme of the shower search after the SSA (left), and before the SSA (right) for comparison.

Fig. 5.10 shows the event display of the shower events found by the shower search algorithm. The same shower search is performed by the simulation with the same setup of cosmic-ray test. Fig. 5.11 shows the the event display of the shower events by the simulation. About 5 thousand shower events are obtained in the cosmic-ray data, and about 13 thousand events are obtained in the simulation. The performance evaluation using the cosmic-ray shower is discussed in Sec. 7.4

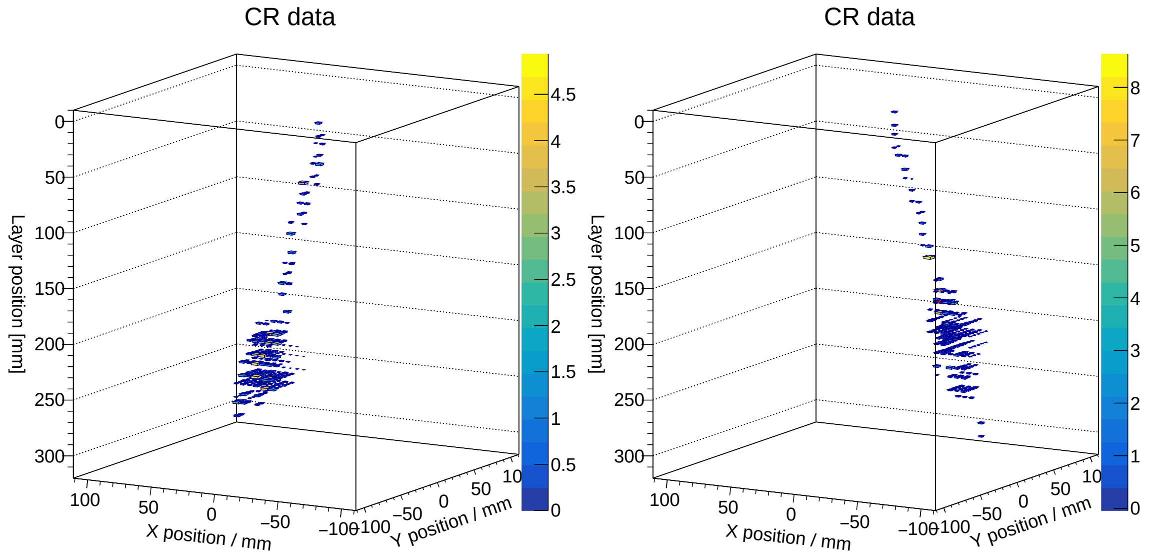

CR data

CR data

Figure5.10 Event displays of the shower events in the cosmic-ray data. The color bar shows the number of MIPs.

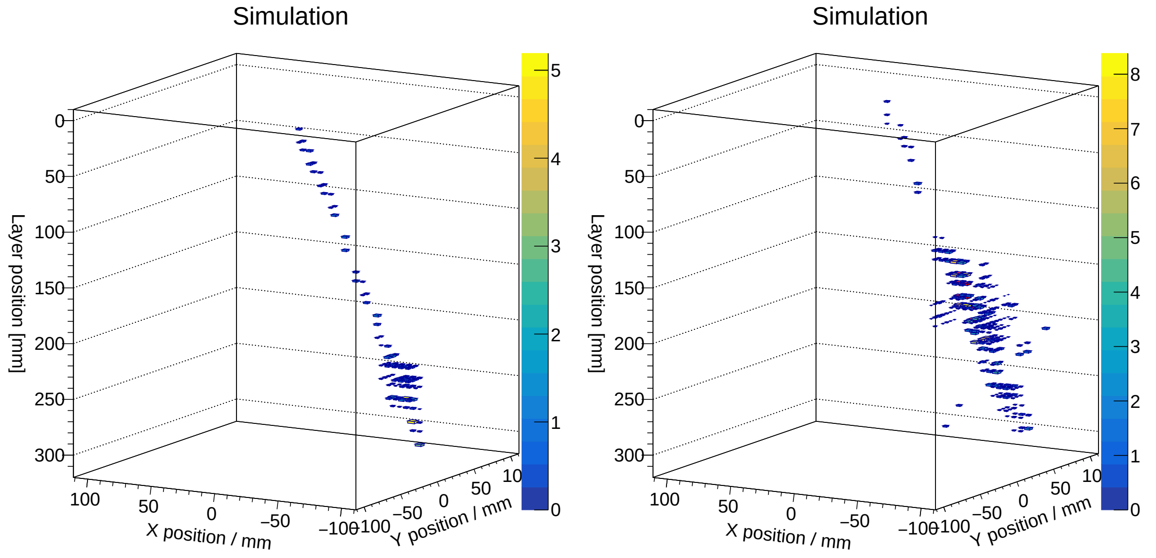

Simulation

Simulation

Figure5.11 Event displays of the shower events in the simulation. The color bar shows the number of MIPs.

Chapter 6

Calibration

According to the calibration procedure discussed in section 5.1, the key parameters for the Sc-ECAL are calibrated in the LED test and cosmic-ray test. The calibrations in the LED test are as follows:

- Gain calibration for SiPMs
- Inter-calibration for electronics
- Cross-talk and after-pulse calibration for SiPMs

The calibrations in the cosmic-ray test are as follows:

- Pedestal calibration
- MIP calibration

The temperature is monitored during the LED test and cosmic-ray test using the temperature sensors on the EBU. The temperature correction for the MIP calibration is performed to eliminate the effect of the temperature dependence of the SiPM.

This chapter gives the results of the calibrations and temperature monitoring.

6.1 Gain

The signal ADC count is converted to the number of photoelectrons using the single photoelectron gain of the SiPM. The ADC-photoelectron conversion factor, c^{gain}, is determined by the gap of peaks of the ADC spectrums at several photoelectrons using the LED light. After the calibration, the SiPM saturation at the large signal can be corrected. The SiPM saturation, discussed in Chapter 8, is a function of the number of photoelectrons, so the signal converted by the c^{gain} can be used to the correction of the saturation.

6.1.1 Gain calibration

Fig. 6.1 and 6.2 show the typical ADC distributions with low LED intensity for 15 μm-pitch and 10 μm-pitch SiPM respectively. The peaks of pedestal, one photoelectron, two photoelectrons are clearly separated, and fitted by the multi-gaussian. The gain calibration factor, c^{gain}, is the interval of the peaks of the gaussians.

Fig. 6.3 shows the distributions of all channels for 15 μm-pitch (left) and 10 μm-pitch (right) SiPM. The difference of the pixel capacitance of the SiPM causes the difference of the gain between 15 μm-pitch and 10 μm-pitch SiPM. The ratio of the gain ($c^{gain}_{15\mu\mathrm{m}}/c^{gain}_{10\mu\mathrm{m}} = 25.4/15.36 = 1.65$) is consistent with the catalogue value

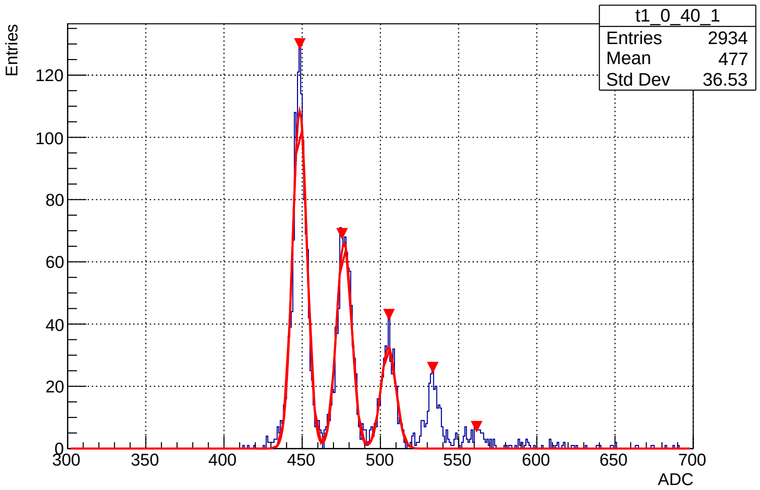

Figure6.1 ADC distribution with low LED intensity for 15 μm-pitch SiPM. The red line is the fit function with the multi-gaussian.

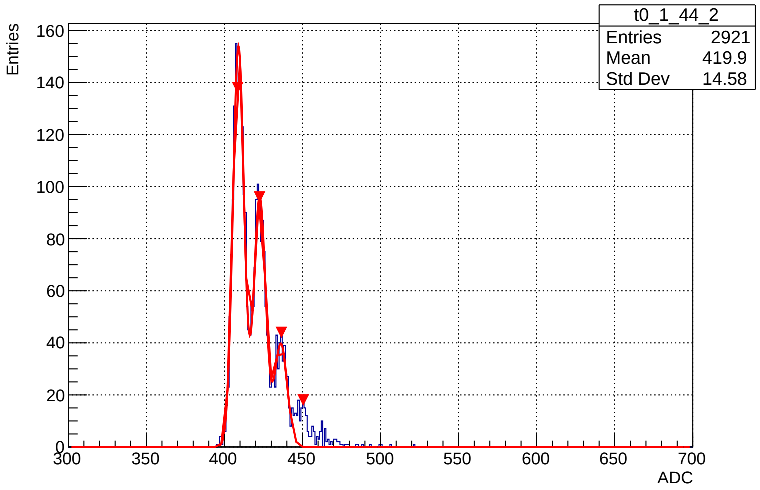

Figure6.2 ADC distribution with low LED intensity for 10 μm-pitch SiPM. The red line is the fit function with the multi-gaussian.

$(2.30/1.35 = 1.70)$, so the per-channel c^{gain} calibration is succeeded. The signal ADC counts can be converted to the number of photoelectrons, and the correction of the SiPM saturation at high light yields can be applied.

6.2 Inter-calibration

The high-gain signal is necessary to measure the c^{gain} using the well separated photoelectron peaks, whereas physics data acquisition uses a low-gain signal due to the wide dynamic range required. The inter-calibration factor, c^{inter}, is used to convert the low-gain signal to the unit of high-gain. The c^{inter} is measured for each channel as the ratio of the amplitudes of the response to the signal with the high-gain to the low-gain settings.

The inter-calibration is performed with the three methods:

- LED: LED scan with several light intensities
- Cosmic-ray: Cosmic-ray data recording both the low gain and high gain

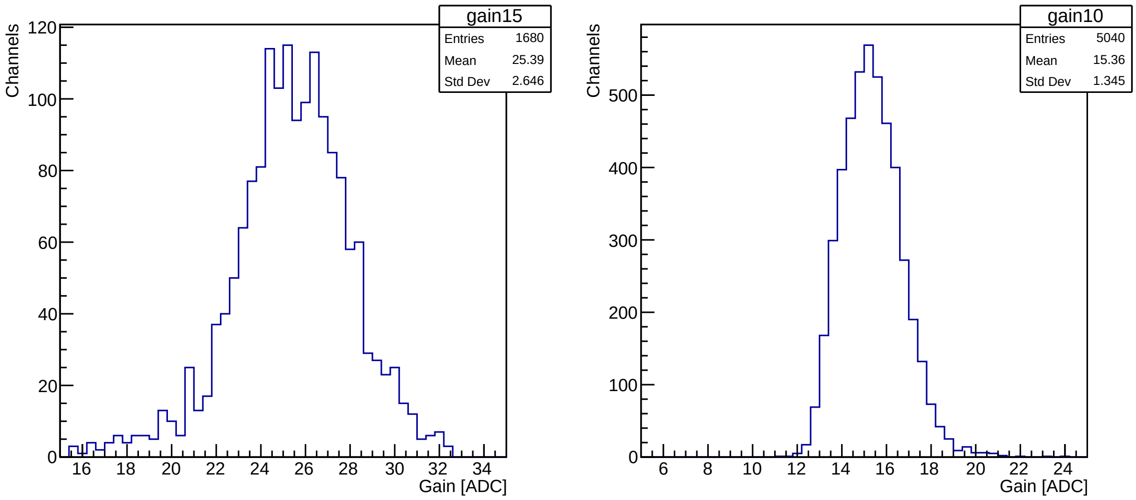

Figure6.3 Distribution with the gains for 15 μm-pitch (left) and 10 μm-pitch (right) SiPM.

- DAC: Directly injecting the test charge from the digital-to-analogue converter (DAC) to the SPIROC2E

This section gives the results of the inter-calibration with the three methods and the comparison between three methods.

6.2.1 Inter-calibration for high-gain and low-gain

LED

The LED data is taken with varying the intensities of the LED light. The data with each intensity stores the ADC counts with high-gain and low-gain settings. The inter-calibration factor, c^{inter}, can be obtained by the ratio of the ADC counts of high-gain to low-gain. Fig. 6.4 shows the typical 2D plot of the ratio of high-gain to low-gain. Each point shows the mean of the gaussian of the ADC distribution for high-gain and low-gain at each LED intensity. The high-gain preamplifier saturates over 3500 ADC counts, so the linear fir is taken below 3500 ADC counts. The slope of the linear function is the c^{inter}.

Fig. 6.5 shows the distribution of the inter-calibration factors for all the channels. The per-channel c^{inter} is obtained. The pitch of the LED light intensity is set as the finest setting, but the fitting error is large due to few fitting points. 5 points can be used for the fitting at Fig. 6.4, but some channels have fewer fitting points. This problem can be solved by updating the LED system with finer pitch.

Cosmic-ray

In the cosmic-ray data, both the signal with high-gain and low-gain settings are recorded, and Fig. 6.6 shows the typical plot of the ratio of high-gain to low-gain. The c^{inter} is obtained in the same way as the LED method. Fig. 6.7 shows the distribution of the inter-calibration factors for all the channels with cosmic-ray method. The per-channel c^{inter} is also obtained.

DAC

At the DAC method, the test charge from the DAC is directly injected into the SPIROC2E, and both the data with high-gain and low-gain are recorded. Fig. 6.8 shows the typical plot of the ratio of high-gain to low-gain. The c^{inter} is obtained in the same way as the LED method. Fig. 6.9 shows the distribution of the inter-calibration factors for all the channels with DAC method. The per-channel c^{inter} is also obtained.

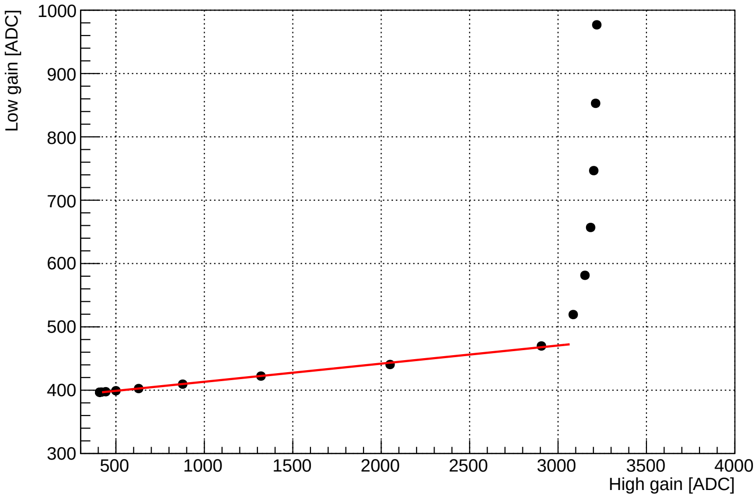

Figure6.4 Typical 2D plot for ADC counts of high gain vs. low gain at one channel. The red line shows the linear function fitted until the ADC counts of high gain saturate.

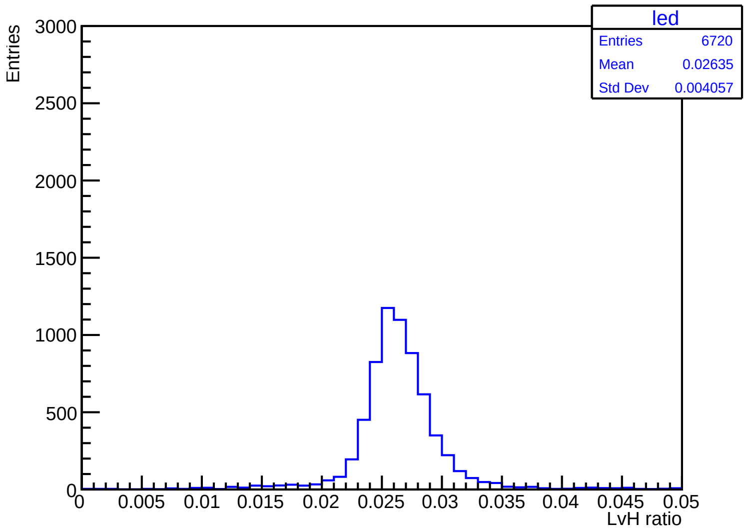

Figure6.5 Distribution of the inter-calibration factors for all channels with LED method.

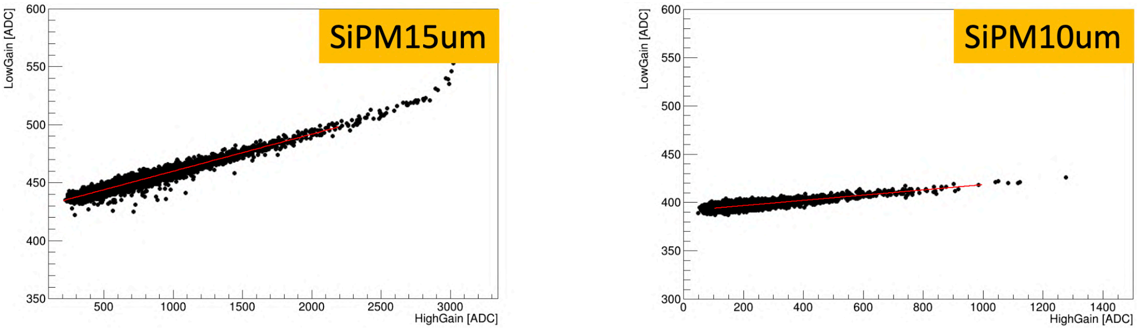

Figure6.6 Typical 2D plot for ADC counts of high gain vs. low gain with the cosmic-ray method.

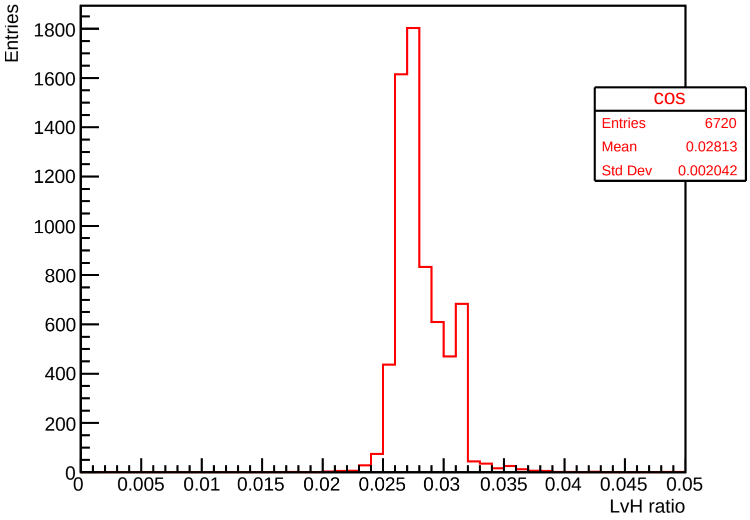

Figure6.7 Distribution of the inter-calibration factors with cosmic-ray method.

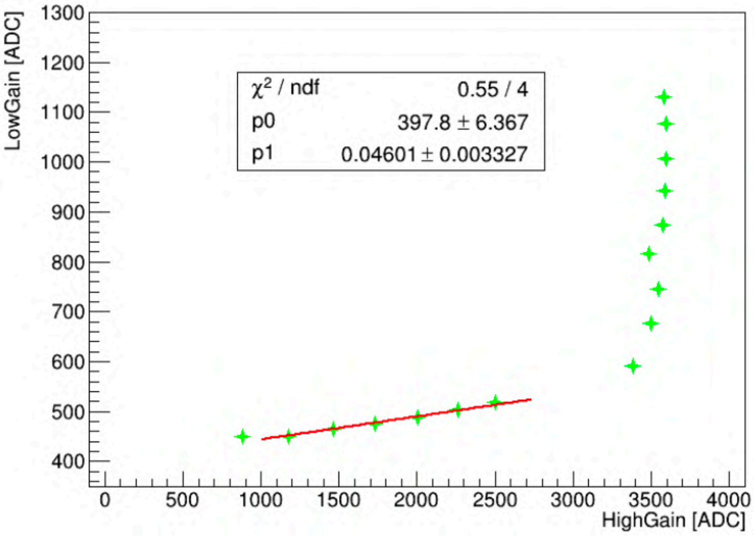

Figure6.8 Typical 2D plot for ADC counts of high gain vs. low gain with the DAC method.

6.2.2 Comparison with three methods

Fig. 6.10 shows the c^{inter} distributions with three methods. The mean values of the distributions with the LED and cosmic-ray methods almost match, but the mean of the DAC method is apart from the others. The waveform of the test charge injecting from the DAC to the SPIROC2E is different from the SiPM waveform, and the bandwidth of the high-gain circuit depends on the waveform. These differences lead to a difference in the amplification factor. The spread of the distribution of LED method is larger than that of the cosmic-ray method, because some of the channels have only few points in the linear region. Therefore, the results with the cosmic-ray method is suitable, but the improvement of the LED system and the waveform calibration for the DAC method is necessary toward the operation at the actual detector.

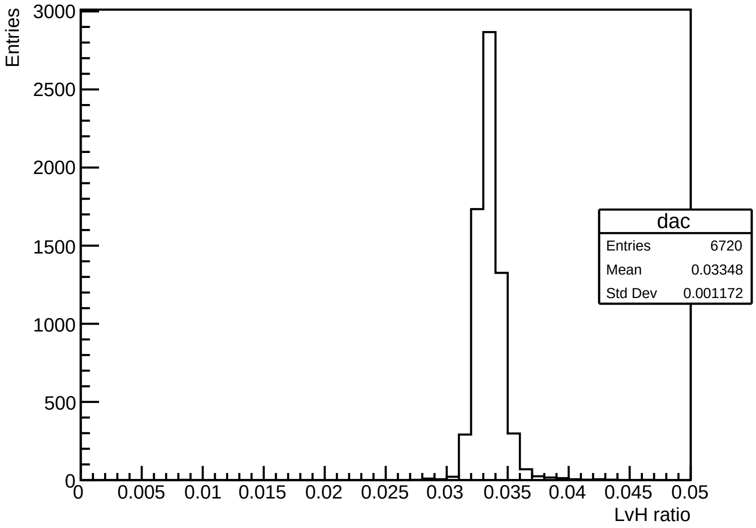

Figure6.9 Distribution of the inter-calibration factors with DAC method.

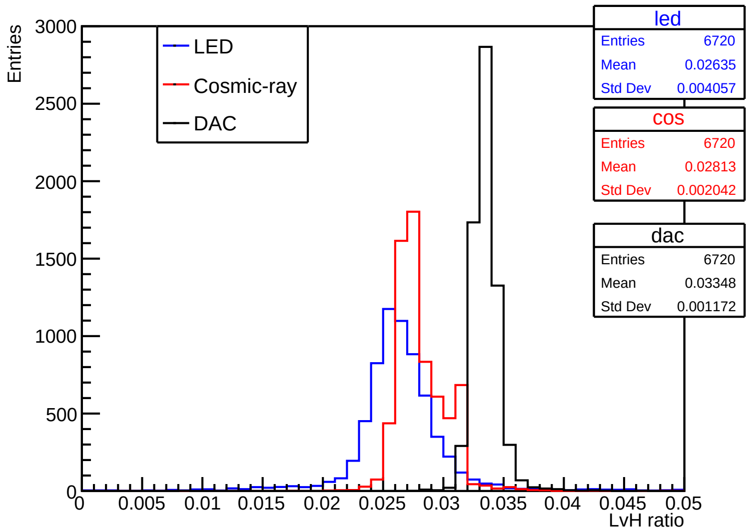

Figure6.10 Distributions of the inter calibration factor with the LED method (blue), cosmic-ray method (red), and DAC method (black).

6.3 Cross-talk and after-pulse

The combined probability of cross-talk and after-pulse, P_{CTAP}, is measured using the LED data. The SiPM saturation is affected by some SiPM properties including the cross-talk and after-pulse. By determining the CTAP probability in each channel using the LED light, the correction for the saturation can be made more accurately.

6.3.1 Probability of CTAP

The CTAP probability, P_{CTAP}, can be measured using the data with low LED intensity [49] like Fig. 6.1 and 6.2. It is assumed that the distribution of LED light at low light intensity follows a Poisson distribution. The probabilities for 0 photon (pedestal) and 1 photon at Poisson are written by:

$$P(0) = e^{-\mu} P(1) = \mu e^{-\mu} \tag{6.1}$$

The cross-talk and after-pulse don't affect the $P(0)$, but decrease the $P(1)$. The actual probability of 1 photon is:

$$P'(1) = (1 - P_{CTAP})\mu e^{-\mu} \tag{6.2}$$

Using these equations, the CTAP probability P_{CTAP} can be written by:

$$P_{CTAP} = 1 - \frac{P'(1)}{P(0)\log P(0)} \tag{6.3}$$

The ADC distribution at low LED intensity is fitted by the multi-gaussian, and the $P(0)$ and $P'(1)$ are calculated by the integral of the gaussian of 0 and 1 photon. Then, the P_{CTAP} calibration can be done by analyzing the LED data with low light intensity.

Fig. 6.11 shows the P_{CTAP} distributions with 15 μm-pitch and 10 μm-pitch SiPM. The measured P_{CTAP} of 25% at 15 μm-pitch SiPM and 12% at 10 μm-pitch SiPM is in agreement with the catalogue value of the cross-talk probability; 14% at 15 μm-pitch SiPM and 5% at 10 μm-pitch SiPM, and the typical after-pulse probability of less than 10%.

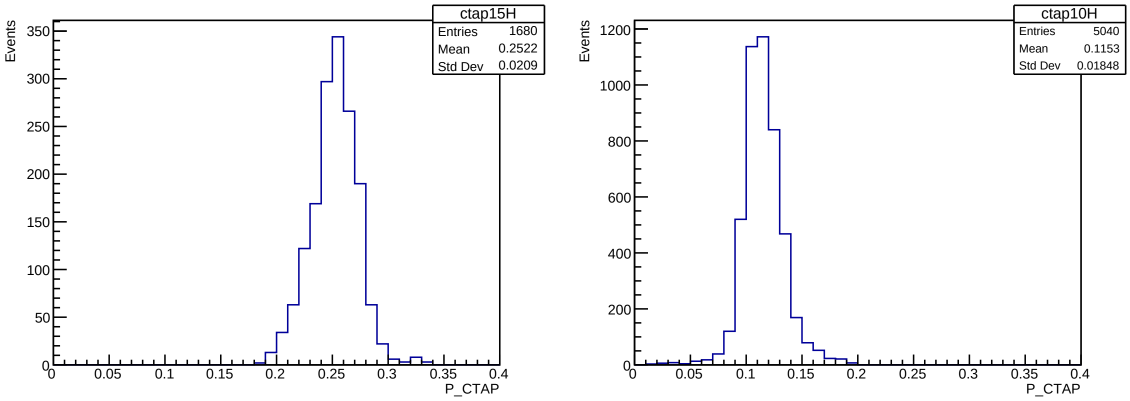

Figure6.11 Distribution of the probability of cross-talk and after-pulse for 15 μm-pitch (left) and 10 μm-pitch (right) SiPM.

6.4 Pedestal

The signal pedestals is calibrated because the ADC counts with the pedestals subtracted can be used to the MIP calibration and the analysis using the cosmic-ray. The cosmic-ray data contains no-hit channels because the data is taken per chip including the hit beyond the threshold and no-hit just belonging the chip.

6.4.1 Pedestal calibraiton

Fig. 6.12 gives the typical pedestal spectrum fitted by a gaussian. The peak value of the gaussian is set as the pedestal calibration factor, $c^{pedestal}$, and the sigma of the gaussian is set as the error of the pedestal. Fig. 6.13 and Fig. 6.14 shows the distributions of the mean and the sigma of the pedestal spectrum with 15 μm-pitch and 10 μm-pitch SiPMs respectively. There are no dependence on the types of SiPMs, and the typical pedestal value is 422 ADC with about 5% variance for all channels. The pedestals are subtracted from the signal per channel, so this variance has no problem after the subtraction. The typical sigma of the pedestal is quite small, about 3.3 ADC with about 16% variance, less than 1% of the pedestal value.

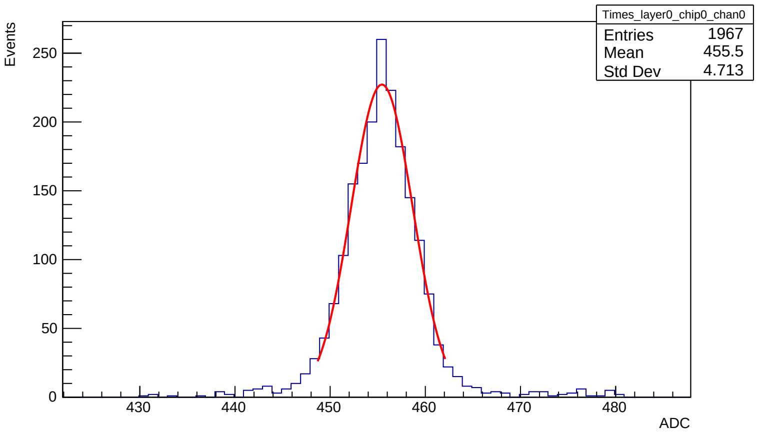

Figure6.12 ADC distribution of the signal pedestal

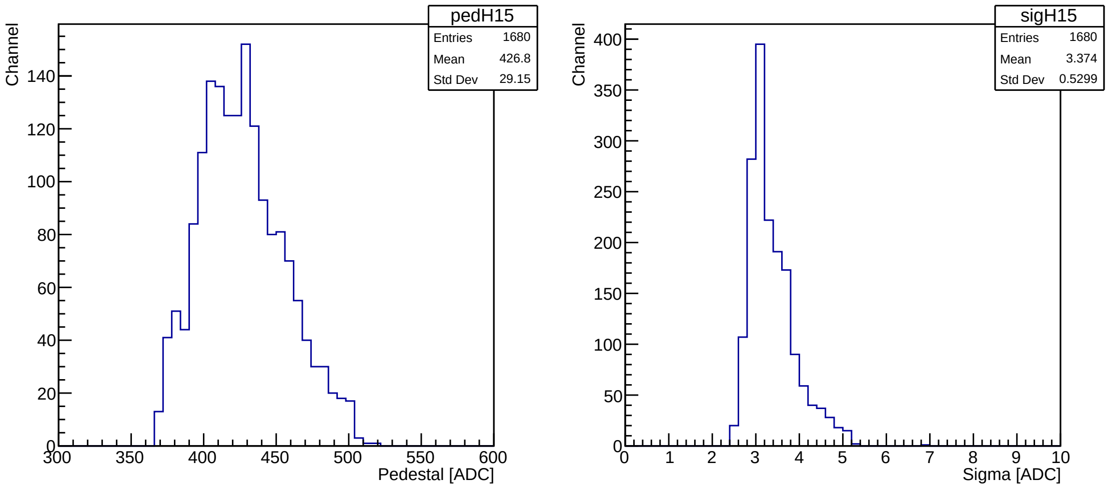

Figure6.13 Distribution of the pedestal (left) and the sigma of the ADC distribution (right) with 15 μm-pitch SiPM

6.5 MIP calibration

When a high-energy charged particle passes through a material, it loses a certain amount of energy due to the Coulomb interaction with the atoms in the material. Such a particle is called a Minimum Ionizing Particle (MIP). In the experiments using scintillators, the analogue signal for the detector is converted to the energy in units of the number of MIPs using the MIP calibration factor c^{MIP}.

This section gives the results of the MIP calibration.

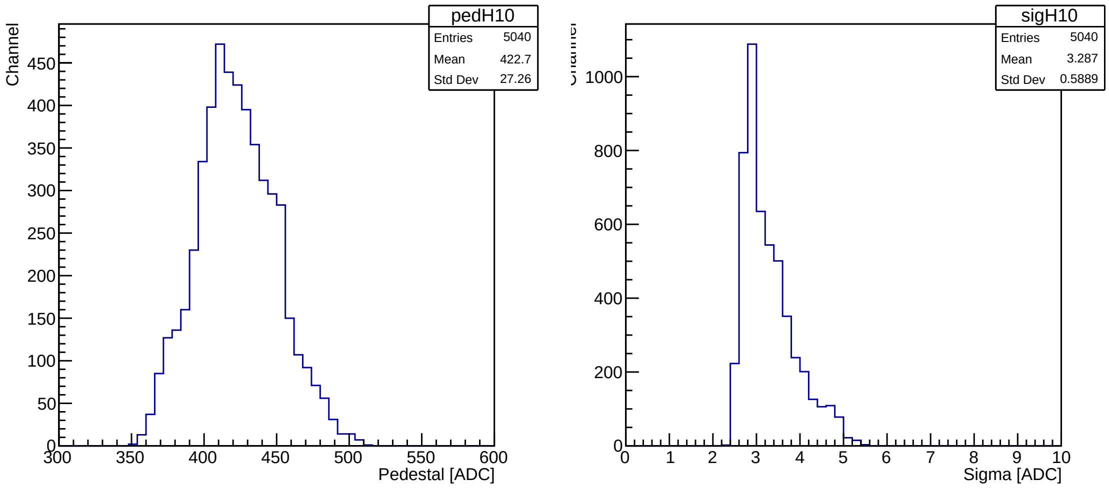

Figure6.14 Distribution of the pedestal (left) and the sigma of the ADC distribution (right) with 10 μm-pitch SiPM

6.5.1 MIP calibration

The c^{MIP} is obtained per channel using all the cosmic-ray events. The angular correction, discussed in Section 5.2.5, and the temperature correction as the reference temperature of 20 °, discussed in Section 6.6, are performed at each MIP hit. Fig. 6.15 and 6.16 show the typical ADC distributions of the MIP response with 15 μm-pitch and 10 μm-pitch SiPM respectively, fitted with a Gauss-convoluted Landau function. The most probable value (MPV) of the function is taken to be the MIP calibration factor, c^{MIP}.

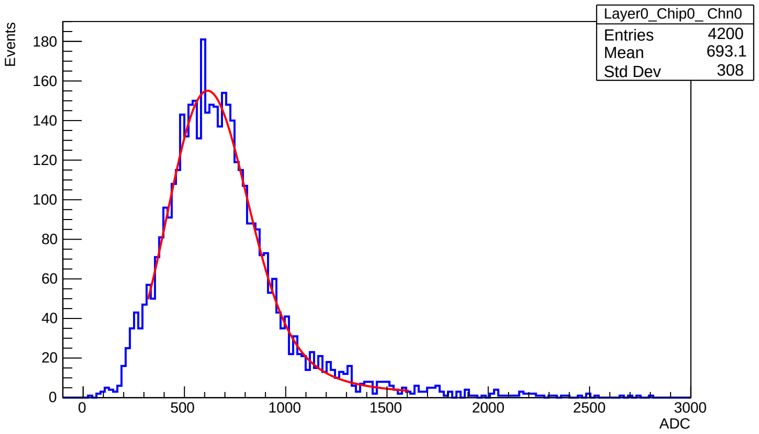

Figure6.15 ADC distribution for the MIP response with 15 μm-pitch SiPM

The Landau distribution of the MIP is obtained for all channels. Fig. 6.17 shows the distribution of the c^{MIP}. The signal ADC counts can be converted to the number of MIPs using this results.

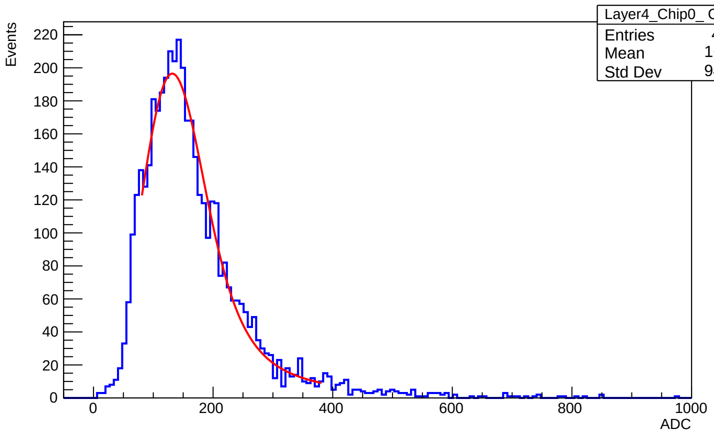

Figure6.16 ADC distribution for the MIP response with 10 μm-pitch SiPM

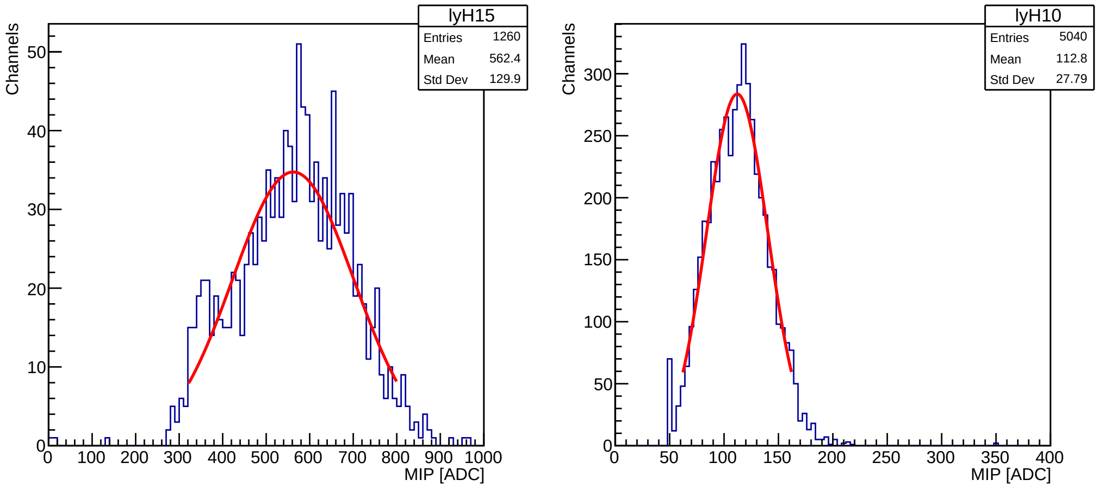

Figure6.17 Distribution of c^{MIP} for 15 μm-pitch (left) and 10 μm-pitch (right) SiPM

6.5.2 Light yield

The MIP light yield in units of the number of photoelectrons is calculated by dividing the c^{MIP} by the c^{gain}. Fig. 6.18 shows the distribution of the MIP light yields in units of the number of photoelectrons for 15 μm-pitch (left) and 10 μm-pitch (right) SiPM. The average light yield is 22.6 p.e. for 15 μm-pitch SiPM and 7.6 p.e. for 10 μm-pitch SiPM. The MIP light yield contains the effects of the cross-talk and after-pulse, The light yield after subtracting the effects of the cross-talk and after-pulse is about 18 p.e. for 15 μm-pitch SiPM and 7 p.e. for 10 μm-pitch SiPM. The difference of the light yield is caused by the difference of the photon detection efficiency (PDE). The PDE at the catalogue is 25% for 15 μm-pitch SiPM and 10% for 10 μm-pitch SiPM, so the difference of measured light yields replicate the difference of the PDE.

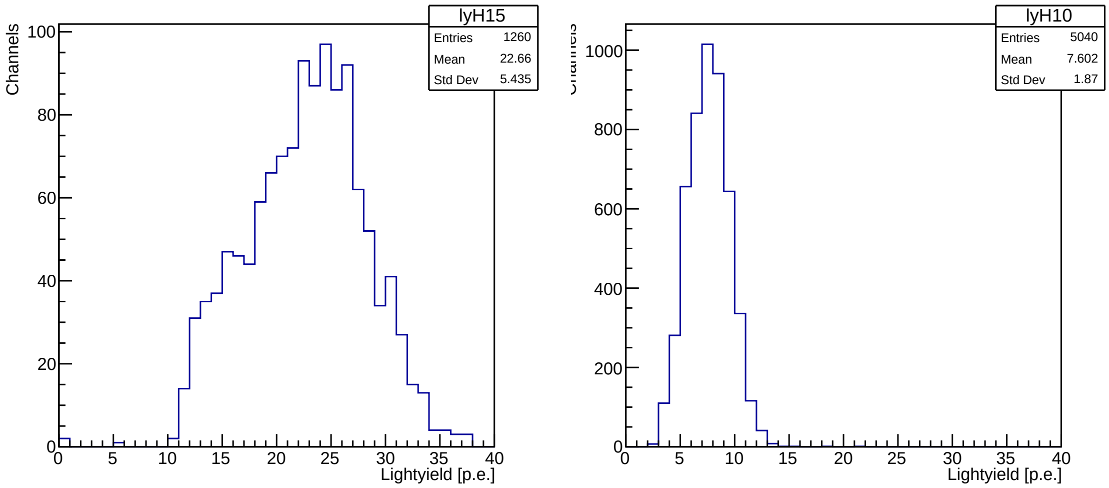

Figure6.18 Distribution of MIP light yields in units of p.e. for 15 μm-pitch (left) and 10 μm-pitch (right) SiPM

6.6 Temperature

The temperature is monitored during one month LED run and three months cosmic-ray run using the temperature sensors on the EBU. The temperature at each channel is reconstructed by the inverse distance weighting [50]. The temperature dependence of the gain and MIP can be obtained, and the temperature correction is performed using these results. This section describes the method of the temperature correction.

6.6.1 Temperature distribution

The temperature is monitored at each event during the LED run and the cosmic-ray run. Sixteen temperature sensors are equipped in one EBU. The temperature at each channel is reconstructed by the inverse distance weighting:

$$W(x,y) = \Sigma_{i=1}^{n} Q_i W_i Q_i = \frac{\frac{1}{L_i}}{\Sigma \frac{1}{L_i}} \tag{6.4}$$

where, $W(x,y)$ is the temperature at (x,y), Q_i is the weight, W_i is the temperature at each sensor, and L_i is the length form (x,y) to each sensor. Fig. 6.19 shows the temperature distribution before and after the reconstruction.

Fig. 6.20 shows the temperature variation during one month LED run at each layer. The temperature changes from 19 $°C$ to 22 $°C$. Fig. 6.21 shows the temperature transition during three months cosmic-ray run at each layer. The temperature changes from 16 $°C$ to 25 $°C$. The temperature variation in the cosmic-ray run is larger than that in the LED run, because the air conditioning doesn't work properly sometimes and the outside temperature changes during the long run.

6.6.2 Temperature dependence

The SiPM has a high temperature dependence. If the temperature increases, the crystal lattice in the SiPM pixel vibrates more heavily. The accelerated carriers may collide with the lattice before reaching an energy threshold,

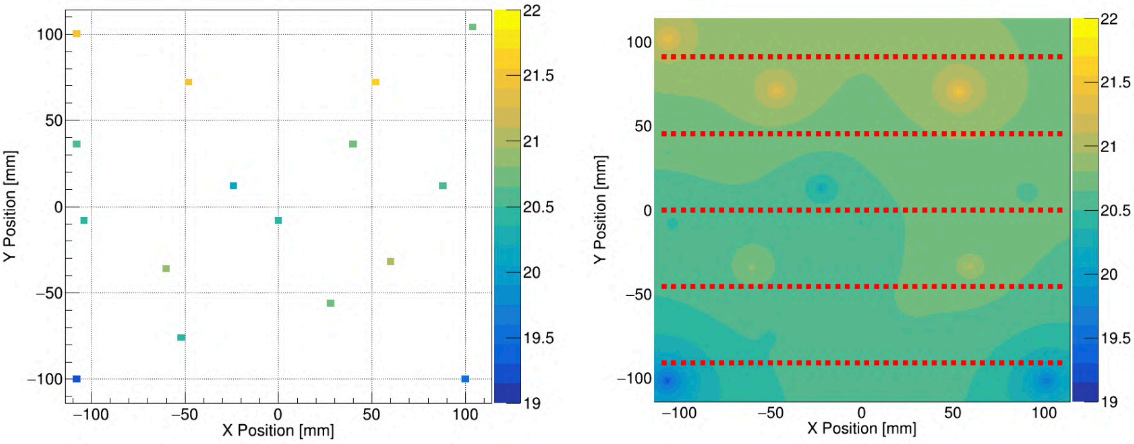

Figure6.19 The left shows the temperatures measured at the temperature sensors, and the right shows the temperature distribution reconstructed by the inverse distance weighting.

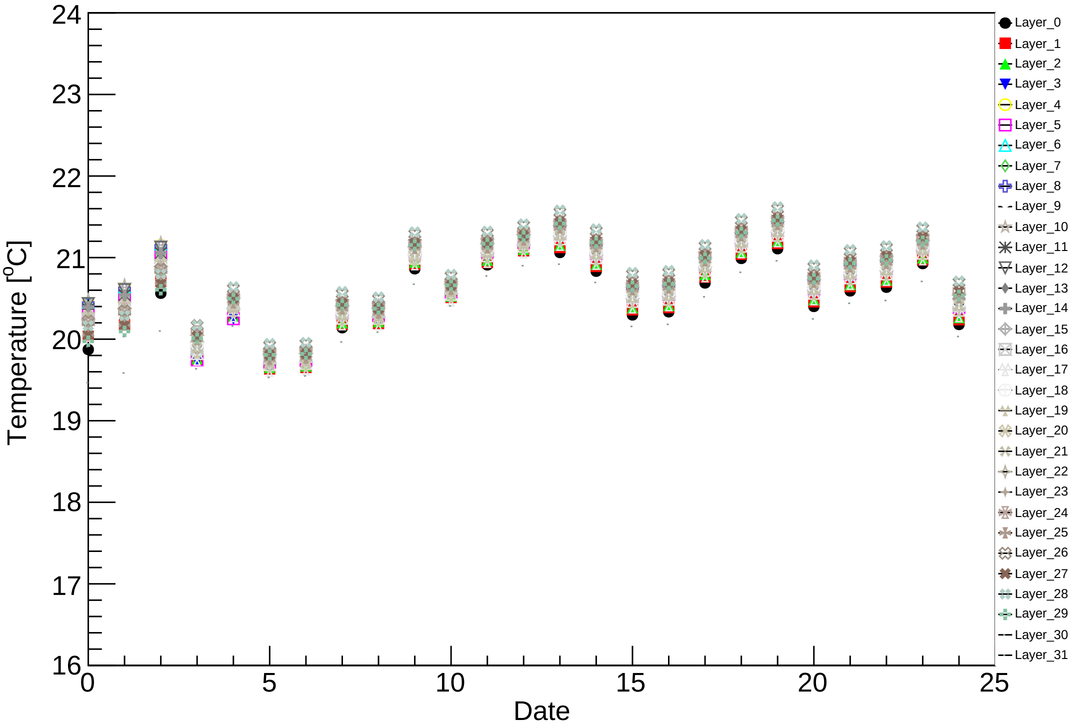

Figure6.20 Temperature variation during one month LED run at each layer. Each plot shows the average temperature reconstructed by the inverse distance weighting at each layer.

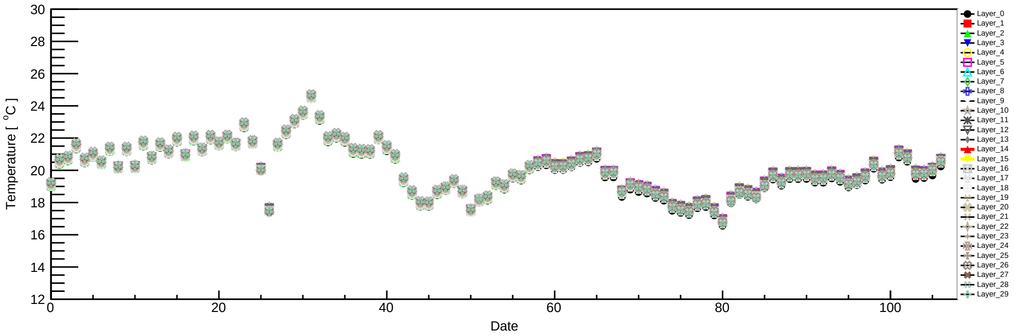

Figure6.21 Temperature variation during three months cosmic-ray run at each layer. Each plot shows the average temperature reconstructed by the inverse distance weighting at each layer.

and the ionization is difficult to happen. Then the breakdown voltage increases. If the operation voltage is constant, the over voltage decrease. This temperature dependence affects some properties of the SiPM such as the gain, PDE, cross-talk and after-pulse. In the temperature range from $\sim -20°C$ to $\sim 80°C$, the gain, PDE, CTAP is almost proportional to the breakdown voltage.

The temperature dependence needs to be corrected at the reconstruction. Especially the gain and MIP ADC counts are affected by the temperature dependence, so they should be corrected at each hit in order to calibrate correctly. The temperature dependence for some calibration parameters is measured.

Fig. 6.22 shows the correlation between the average temperature and the gain. The temperature dependence is determined by the slopes of the fitted linear function. Fig. 6.23 shows the results of the temperature dependence at each layer. The average temperature dependence is estimated to be $-1.22\%/°C$ for 15 μm-pitch SiPM and $-0.73\%/°C$ for 10 μm-pitch SiPM.

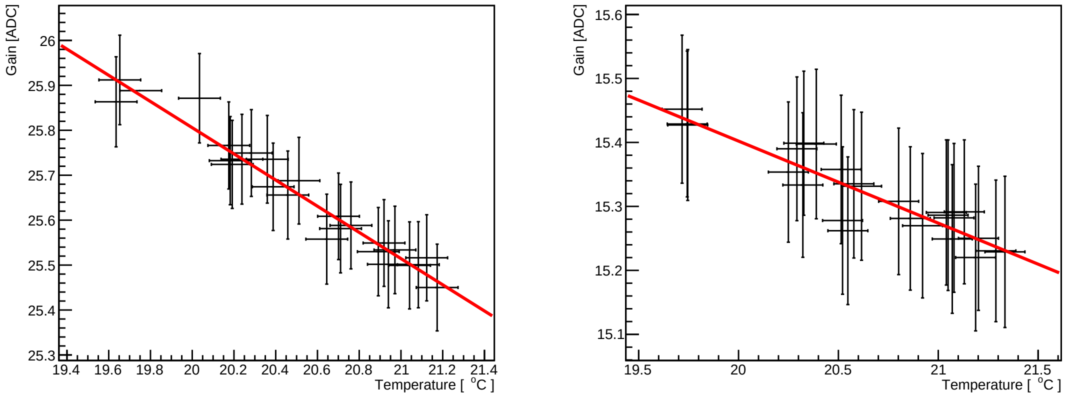

Figure6.22 Correlation between the temperature and gain.

The MIP ADC counts are calculated per layer and per day. Fig. 6.24 shows the sum distribution over all the channels in each layer, fitted with a Gaussian-convoluted Landau function. The most probable value (MPV) of the function is taken to be the MIP calibration factor. The 6 belts shown in Fig. 6.25 have the large temperature difference in short periods during the cosmic-ray run, these short 6 periods are selected for the calculation of the temperature dependence of the MIP response. The reason for setting short periods is to avoid the effect of the

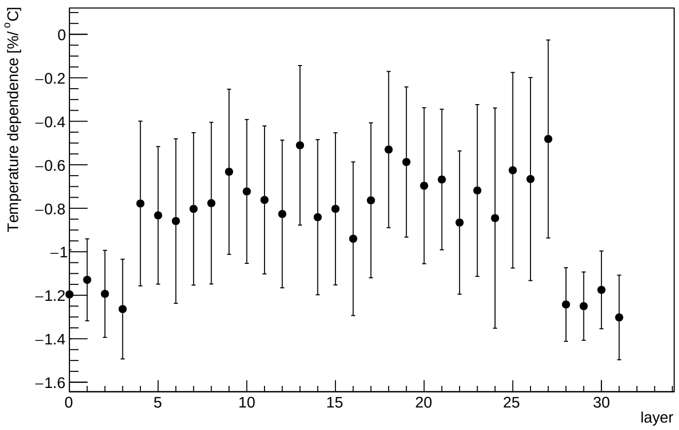

Figure6.23 Temperature dependence for the gain at each layer.

decrease in MIP response described in section 7.1.

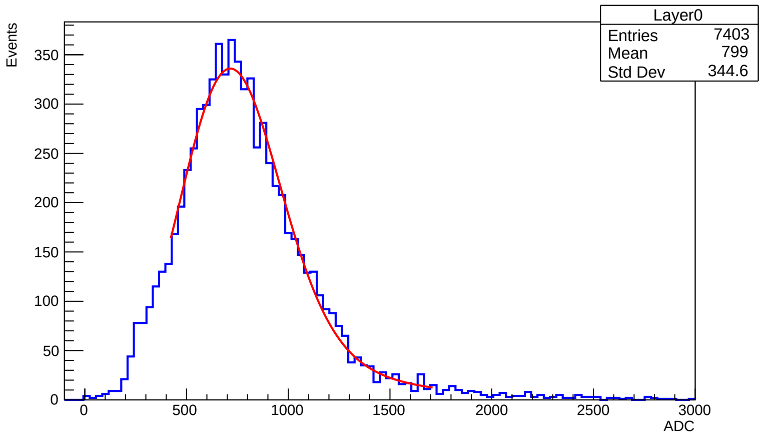

Figure6.24 The sum distribution over all the channels in each layer. The red line shows the fitted Gaussian-convoluted Landau function.

Fig. 6.26 shows the correlation between the average temperature and the Landau MPV. The temperature dependence of the MIP response is determined by the mean value of the slopes of the fitted linear functions at 6 periods. Fig. 6.27 shows the results of the temperature dependence at each layer. The average temperature dependence is estimated to be $-3.23\%^{\circ}C$ for 15 $\mu\mathrm{m}$-pitch SiPM and $-3.70\%^{\circ}C$ for 10 $\mu\mathrm{m}$-pitch SiPM.

The difference of the temperature dependence between the gain and MIP response is caused by the difference in SiPM properties that each contains. The temperature difference of the gain is caused only by the gain variation, while the temperature difference of the MIP response is caused by the variations such as the gain, PDE, cross-talk and after-pulse. Therefore, the temperature dependence of the MIP response is larger than that of the gain.

6.6.3 Temperature correction

The typical MIP calibration factor c^{MIP} is obtained by the cosmic-ray muon. The cosmic-ray test is performed during the 3 months to accumulate the statistics and check the stability, but the temperature changes during the test.

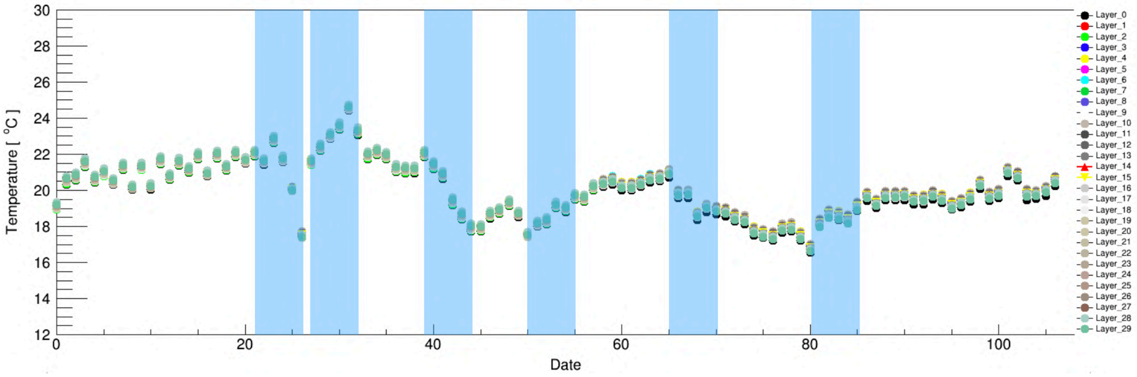

Figure6.25 Six short periods during the cosmic-ray run. Each period contain 6 data points which have large temperature difference.

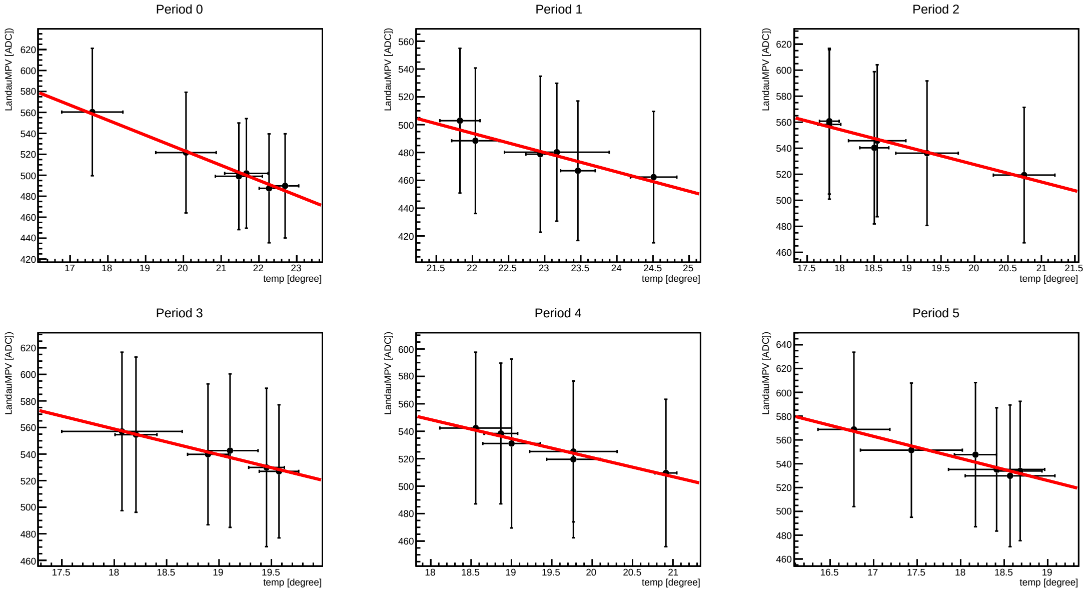

Figure6.26 Correlation between the temperature and MPV value.

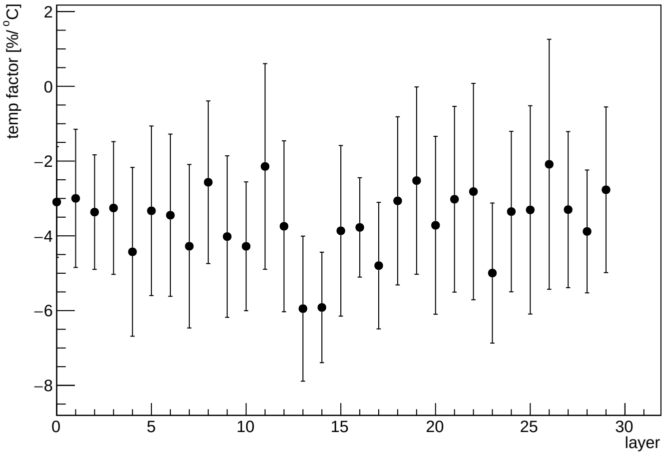

Figure6.27 Temperature dependence for the MIP response at each layer.

The temperature correction is performed at each MIP hit using the monitoring temperature and the temperature dependence. After the temperature correction, the typical c^{MIP} at the reference temperature can be obtained.

The temperature correction for the signal ADC counts is performed by:

$$A_i^{temp\ corr}[\mathrm{ADC}] = (1 + (T_i - T_{ref})d^{MIP})A_i^{no\ corr}[\mathrm{ADC}](T) \tag{6.5}$$

where, $A_i^{temp\ corr}[\mathrm{ADC}]$ and $A_i^{no\ corr}[\mathrm{ADC}](T)$ is the signal ADC count at each hit after the temperature correction and without correction respectively. T_i is the temperature at each hit, and T_{ref} is the reference temperature, which is set as 20 °C. d^{MIP} is the temperature dependence for the MIP response.

Fig. 6.28 shows the ADC distributions before and after the temperature correction. The ADC distributions for the two periods with large temperature difference (average temperature is 17 °C and 22 °C) have large deviation without the correction. After the correction, the distributions match well.

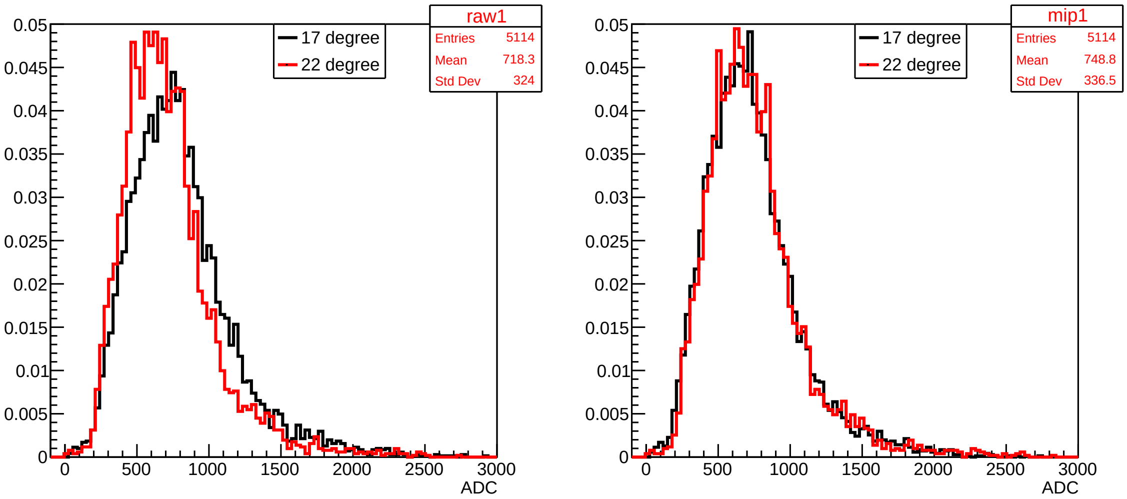

Figure6.28 ADC distributions without the temperature correction (left) and after the temperature correction (right). The two days with large temperature difference are selected. The temperature in the legend is the mean value of all hits, but the temperature correction is performed at each hit.

The temperature dependence is evaluated and the method of the temperature correction is established, then the temperature correction is applied to the measurement using the actual detector. This makes it possible for the first time to evaluate the performance on the actual detector.

Chapter 7

Performance

The performance of the Sc-ECAL is evaluated using the technological prototype in the following methods:

- Stability of the calibration parameters
- Performance evaluation using the cosmic-ray tracks
- Performance evaluation using the showers induced by the cosmic-ray

The stability of the key parameters is measured to verify that the detector is operating stably. As a performance evaluation using the cosmic-ray tracks, the efficiency and the position resolution is evaluated to check the requirements of the Sc-ECAL, and compared with the Monte Carlo simulation. The performance of the Sc-ECAL for the electromagnetic showers is evaluated by comparing the showers induced by the cosmic-ray and simulation. This chapter gives the results of the performance evaluation.

7.1 Stability

Since the actual detector is required to operate stably over a long period of time, the stabilities of key parameters are evaluated during long-term commissioning runs. The stabilities for the gain, inter-calibration factor, and CTAP probability are evaluated using one-month long LED run. The stabilities for the pedestal and MIP response are evaluated using three-months long cosmic-ray run. This section gives the measured stabilities of the key calibration parameters.

7.1.1 Gain stability

Fig. 7.1 shows the c^{gain} stability of one channel at each layer. The c^{gain} is found to be quite stable at per-channel level, although a weak correlation with the temperature variation is seen. In order to store the statistics to reduce the error and to check the correlated time-dependence in the performance between channels in a certain layer or ASIC, which shares services such as power supply, the stability per layer is checked. Fig. 7.2 shows the stability of the c^{gain} averaged over all the channels at each layer. The average c^{gain} at each layer is found to be quite stable and no layer correlation is seen, although a weak correlation with the temperature variation is still seen.

Fig. 7.3 shows the c^{gain} stability after the temperature correction. The stability is found to be even further improved by the temperature correction. An excellent long-term stability of the c^{gain} is achieved.

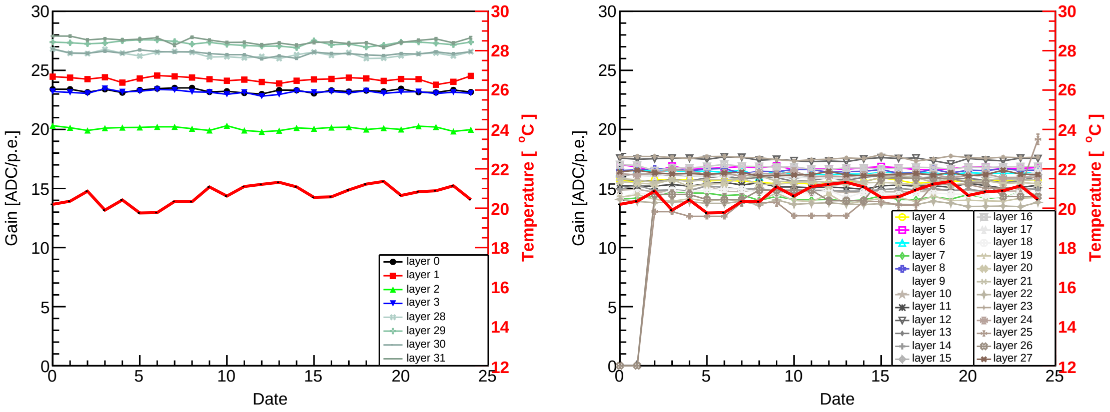

Figure7.1 Stability of one-channel gain at each layer for 15 μm-pitch (left) and 10 μm-pitch (right) SiPM. The red line shows the temperature during the LED run.

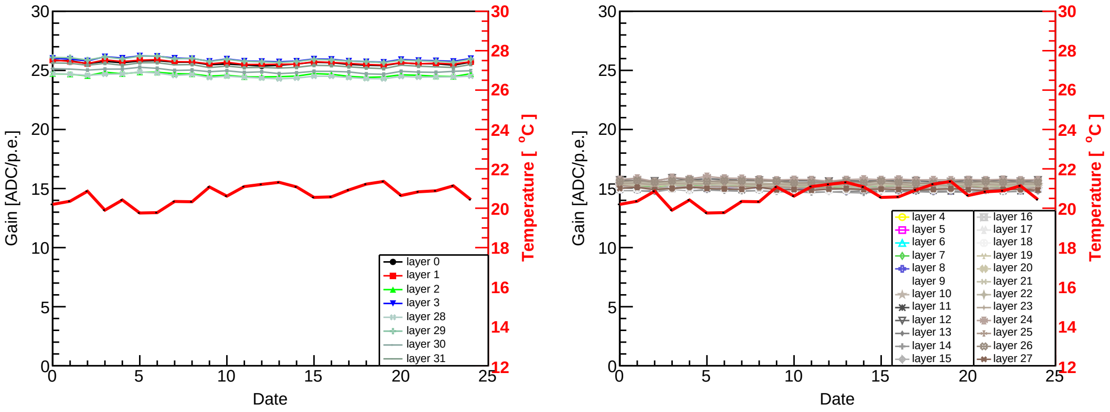

Figure7.2 Stability of the gain averaged over all the channels at each layer for 15 μm-pitch (left) and 10 μm-pitch (right) SiPM. The red line shows the temperature during the LED run.

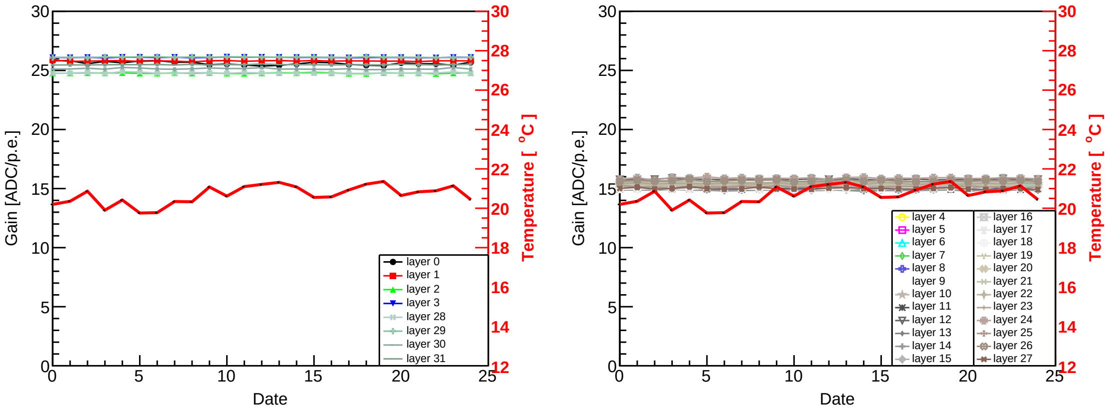

Figure7.3 Stability of the average gain at each layer after temperature correction for 15 μm-pitch (left) and 10 μm-pitch (right) SiPM.

7.1.2 Inter-calibration stability

Fig. 7.4 shows the c^{inter} stability of one channel at each layer. the per-channel c^{inter} is almost stable, but some floundering can be seen on some days due to the rough pitch of the LED intensities. In order to store the statistics to reduce the error and to check the correlated time-dependence in the performance in a certain layer or ASIC, the stability per layer is also checked. Fig. 7.5 shows the stability of the c^{inter} averaged over all the channels at each layer. The average c^{inter} at each layer is found to be quite stable during one month LED run and no layer correlation is seen. The temperature dependence is not seen because the dependence is cancelled by taking the ratio.

There is a limit to the measurement precision at the per-channel level due to the rough pitch of the LED light. The LED data is taken by the finest pitch of the LED intensity, but the fitting plots are sometimes too few to measure the c^{inter}. However, the precision becomes higher at the per-layer level due to the error reduction by the large statistics. The c^{inter} is set as the mean of all runs in the current setup. The update of the LED system with the fine pitch of the LED intensities makes the inter-calibration more precise.

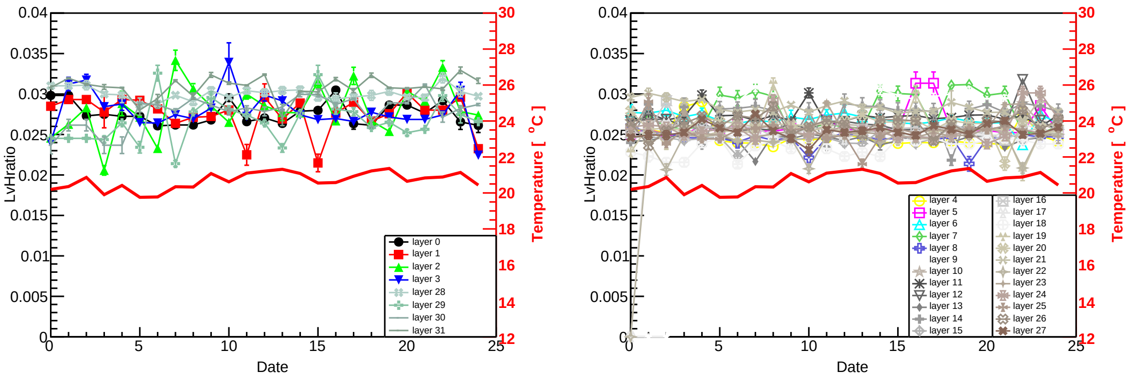

Figure7.4 Stability of one-channel c^{inter} at each layer for 15 μm-pitch (left) and 10 μm-pitch (right) SiPM. The red line shows the temperature during the LED run.

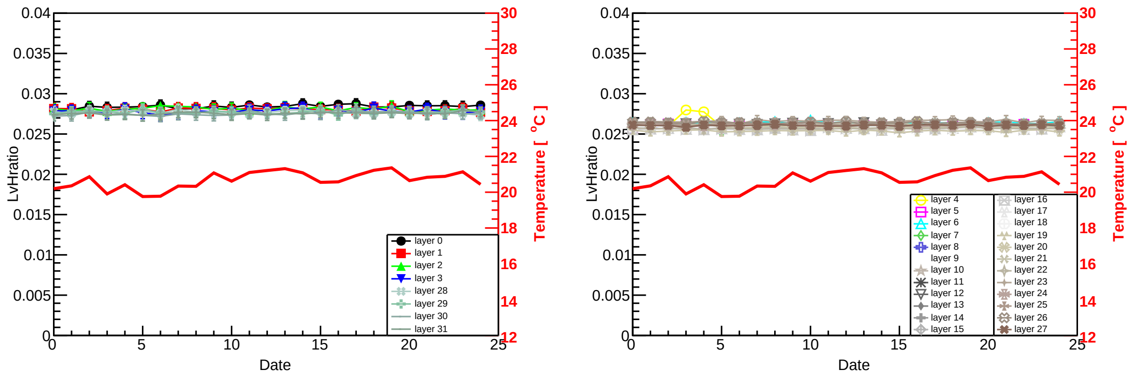

Figure7.5 Stability of the c^{inter} averaged over all the channels at each layer for 15 μm-pitch (left) and 10 μm-pitch (right) SiPM. The red line shows the temperature during the LED run.

7.1.3 CTAP stability

Fig. 7.6 shows the P_{CTAP} stability of one channel at each layer. The per-channel P_{CTAP} is almost stable, but some floundering can be seen on some days. In order to store the statistics to reduce the error and to check the correlated time-dependence in the performance in a certain layer or ASIC, the stability per layer is also checked. Fig. 7.7 shows the stability of the P_{CTAP} averaged over all the channels at each layer. The average P_{CTAP} at each layer is found to be quite stable during one month LED run, and no layer correlation is seen.

The measurement precision of this method become worse due to the fluctuation of the LED especially at the per-channel level. This method uses the LED data with low light intensity which has rather larger fluctuation of the LED intensity. Moreover, if the separation of 0 and 1 photon distribution is difficult due to the low single photoelectron gain especially in 10 μm-pitch SiPM, the calculations of $P(0)$ and $P(1)$ have large uncertainties and the P_{CTAP} is wrongly calculated. It is not a problem by taking the average of all runs to suppress the effects of the measurement precision. The P_{CTAP} is set as the mean of all runs in the current setup. The update of the LED system with the more stable LED or the SiPM with more high gain makes the CTAP calibration more precise.

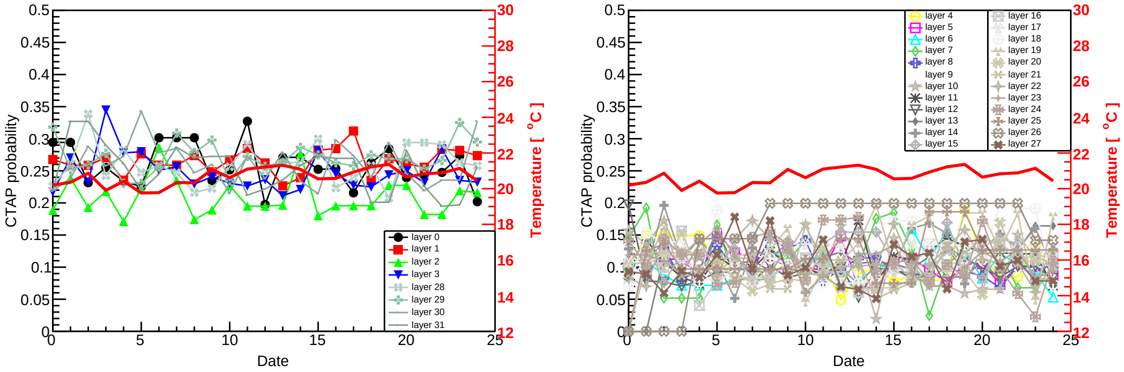

Figure7.6 Stability of one-channel P_{CTAP} at each layer for 15 μm-pitch (left) and 10 μm-pitch (right) SiPM. The red line shows the temperature during the LED run.

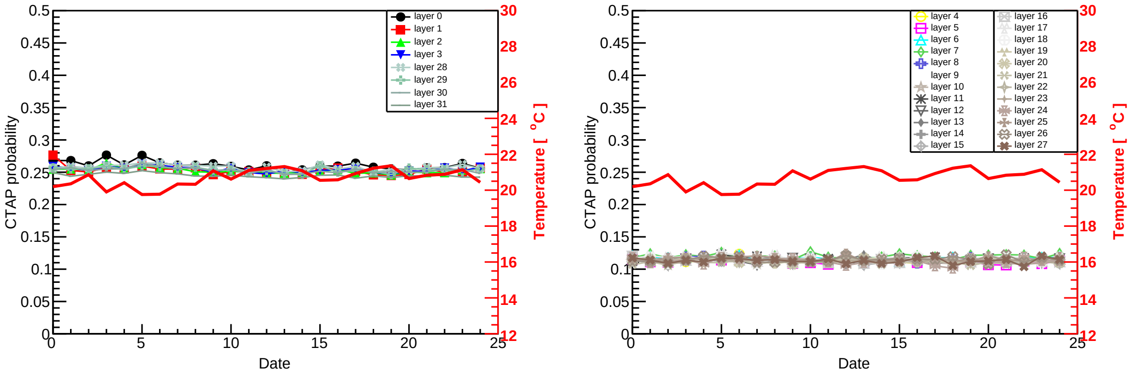

Figure7.7 Stability of the P_{CTAP} averaged over all the channels at each layer for 15 μm-pitch (left) and 10 μm-pitch (right) SiPM. The red line shows the temperature during the LED run.

7.1.4 Pedestal stability

Fig. 7.8 shows the $c^{pedestal}$ stability of one channel at each layer. The $c^{pedestal}$ can be obtained per channel with less than 1% variance, and the $c^{pedestal}$ is found to be quite stable at per-channel level. In order to check the correlated time-dependence in the performance in a certain layer or ASIC and confirm the pedestal stability at the per-layer level , the stability per layer is checked. Fig. 7.9 shows the stability of the $c^{pedestal}$ averaged over all the channels at each layer. The $c^{pedestal}$ is found to be quite stable during three months run at all layers, and no layer correlation is seen

When performing test beam experiments or extending the system to the actual detector, $c^{pedestal}$ can be calibrated for each channel by acquiring pedestals from channels with no hits or by acquiring data with random triggers for pedestals.

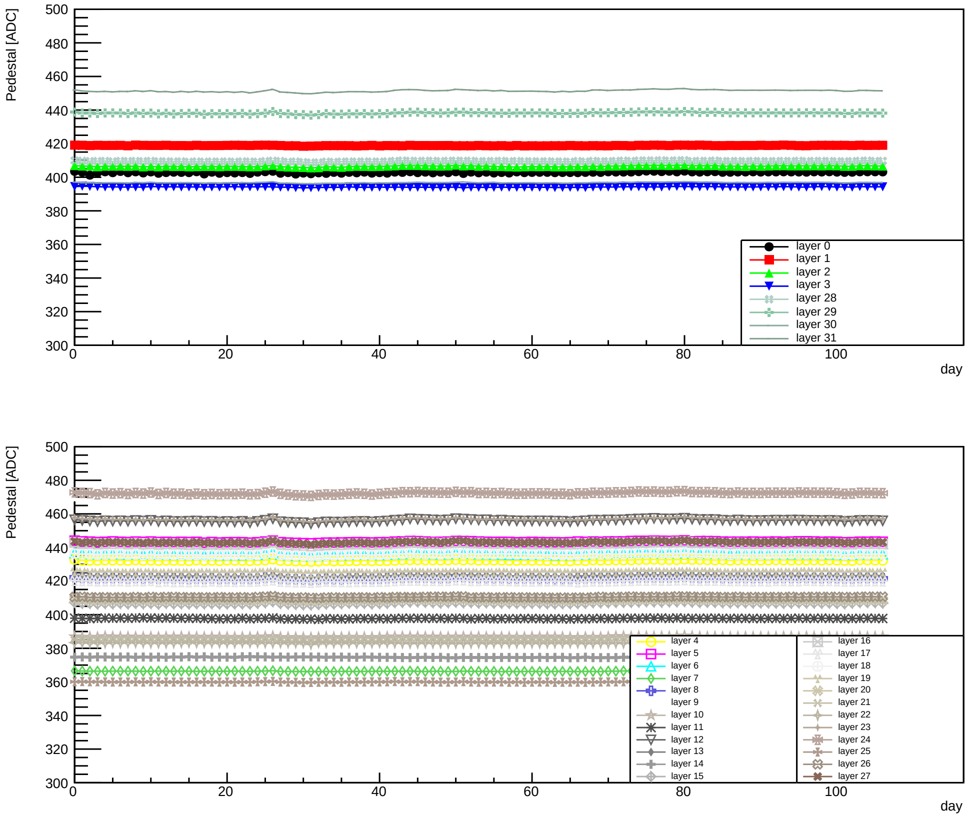

Figure7.8 Stability of one-channel pedestal at each layer with 15 μm-pitch (top) and 10 μm-pitch (bottom) SiPM.

7.1.5 MIP stability

The c^{MIP} stability of one channel cannot be evaluated per day due to the poor statistics, although it is necessary to calibrate and check the stability of each channel and make corrections if necessary. In the operation of the actual detector, the statistics can be stored from the charged particle track events and the per-channel calibration and stability check can be done, which allows the correction per channel.

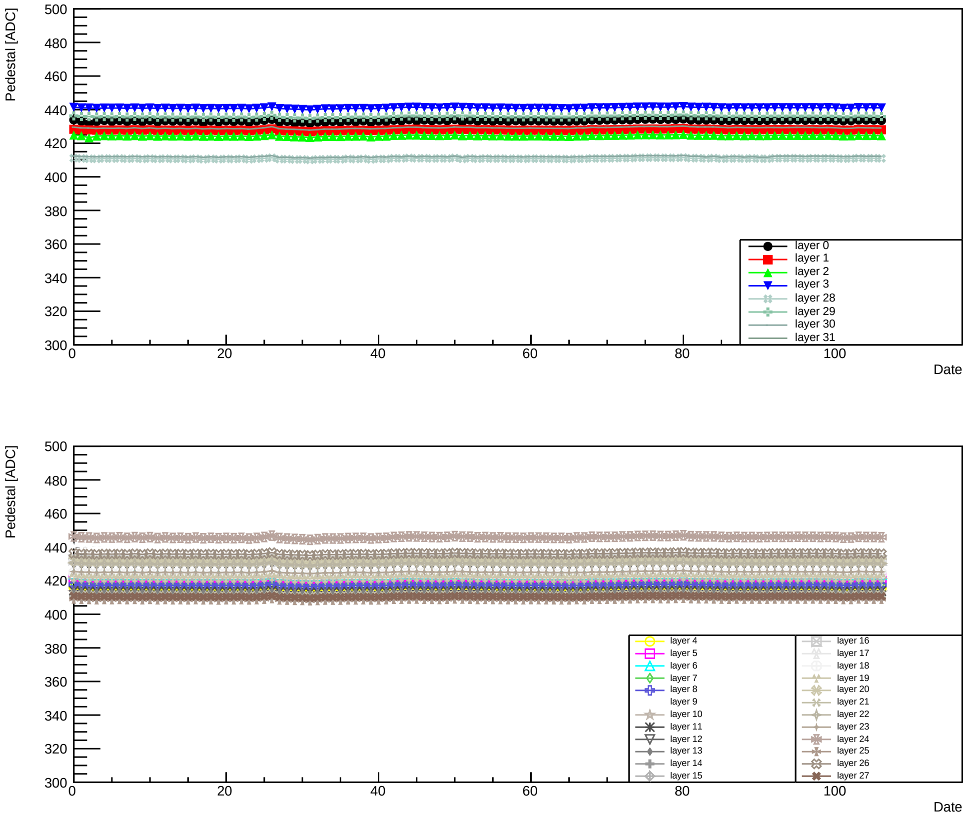

Figure7.9 Stability of the pedestal averaged over all the channels for each layer with 15 μm-pitch (top) and 10 μm-pitch (bottom) SiPM.

For a discussion of the stability, the c^{MIP} stability is checked using the per-layer calibration. Fig. 7.10 shows the stability of the c^{MIP} which is calibrated by fitting the sum distribution of all the channels at each layer before the temperature correction, discussed in Section 6.6.2. A weak correlation between the c^{MIP} and the temperature can be seen. Fig. 7.11 shows the stability after the temperature correction. The temperature dependence is not seen, and the c^{MIP} is almost constant day by day. However, some decrease of the c^{MIP} is seen, and the decrease rate varies between 5–13% over 3 months depending on layer.

The temperature correction is successfully done at the MIP calibration. The 5–10% accuracy is required for the determination of the c^{MIP}, and the larger variation than this requirement affects the calorimeter and physics performance such as the energy linearity and jet energy resolution. The temperature variation causes at most the 10% variation of the MIP response, but the temperature correction turns off this effect and almost no variation is seen day by day. The temperature correction allows the accurate calibration of the MIP response so that the performance is not affected.

The reason of this decrease of the c^{MIP} is under investigation, but it could be due to the aging of the scintillation light emission or the instability of the electronics or SiPMs. It is found in the one-month long LED run that the SiPM gain is quite stable, but the LED run isn't taken during three months cosmic-ray run, so the decrease of the SiPM gain during the cosmic-ray run is not known. A cosmic ray test with frequent LED calibration should be performed to better understand this instability of the c^{MIP}. The possible approaches to solve this problem are the

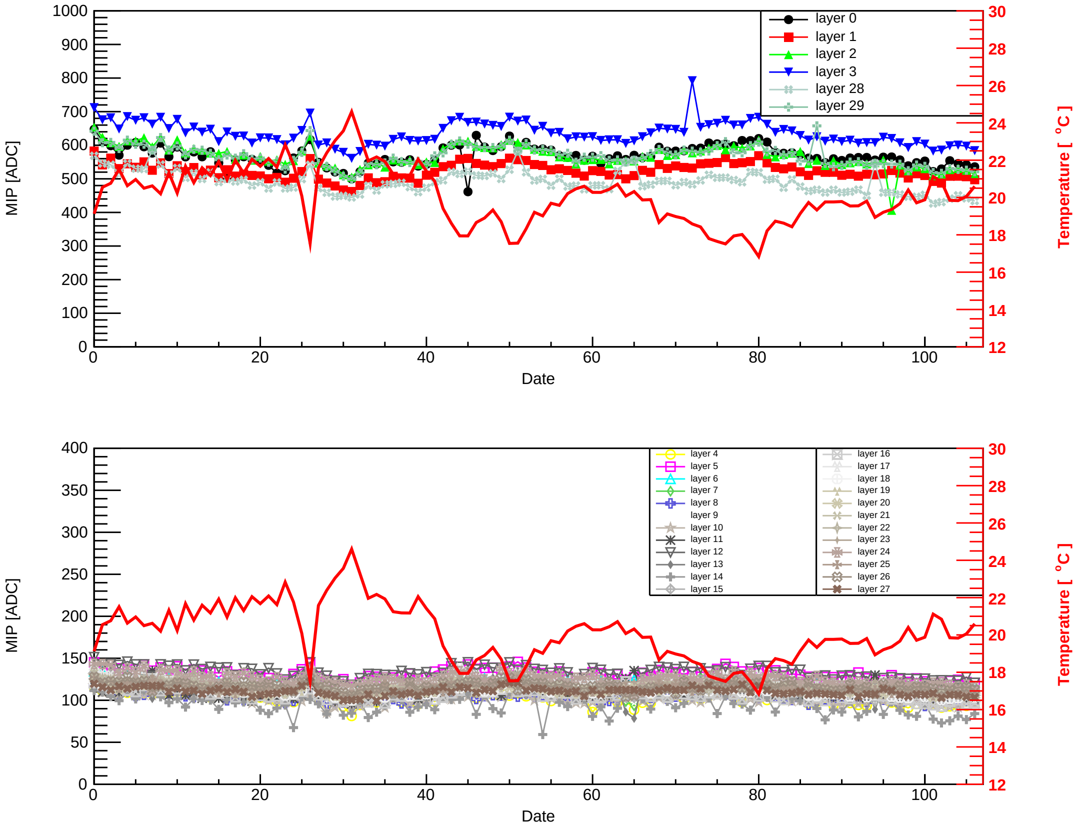

Figure7.10 Stability for the c^{MIP} with the calibration per layer before the temperature correction with 15 μm-pitch (top) and 10 μm-pitch (bottom) SiPM

frequent MIP calibration and the voltage adjustment of SiPMs.

7.2 Simulation of cosmic-ray

The cosmic-ray test using the technological prototype is simulated using a GEANT4 [51]. A reference physics list of QGSP_BERT is selected in the Geant4 version 4.10.06 p03. The Sc-ECAL simulation model consists of 30 layers of the absorbers, detection layers, and readout PCBs. The detection layers are aligned in the same way as the prototype.

The cosmic-ray shower library (CRY) [52] is used to simulate the cosmic-ray. The CRY software library generates the cosmic-ray particle shower. Fig. 7.12 shows the distribution of the energy and the zenith angle for each particle type generated by the CRY. The cosmic-ray particles generated by the CRY have wide range of energies of 1 MeV to 100 TeV, and several particles such as muons, electrons, gamma, and hadrons are generated. The CRY can disable a certain particle, but in this setup, all the particle types are used to simulate. The CRY has the setups of three elevations, and the sea level is set at this time. The CRY also sets the latitude of 32 degree in China. The discontinuity of the energy distribution is a specification of the CRY. The cosmic rays produced by CRY are injected from the top of the prototype randomly within the angles detectable by the prototype, where the cut of the zenith angle of 60 degree is applied. The cosmic-ray test is conducted indoors, so a material that replicates a building around the prototype is placed on the top of the prototype. The building material is replaced

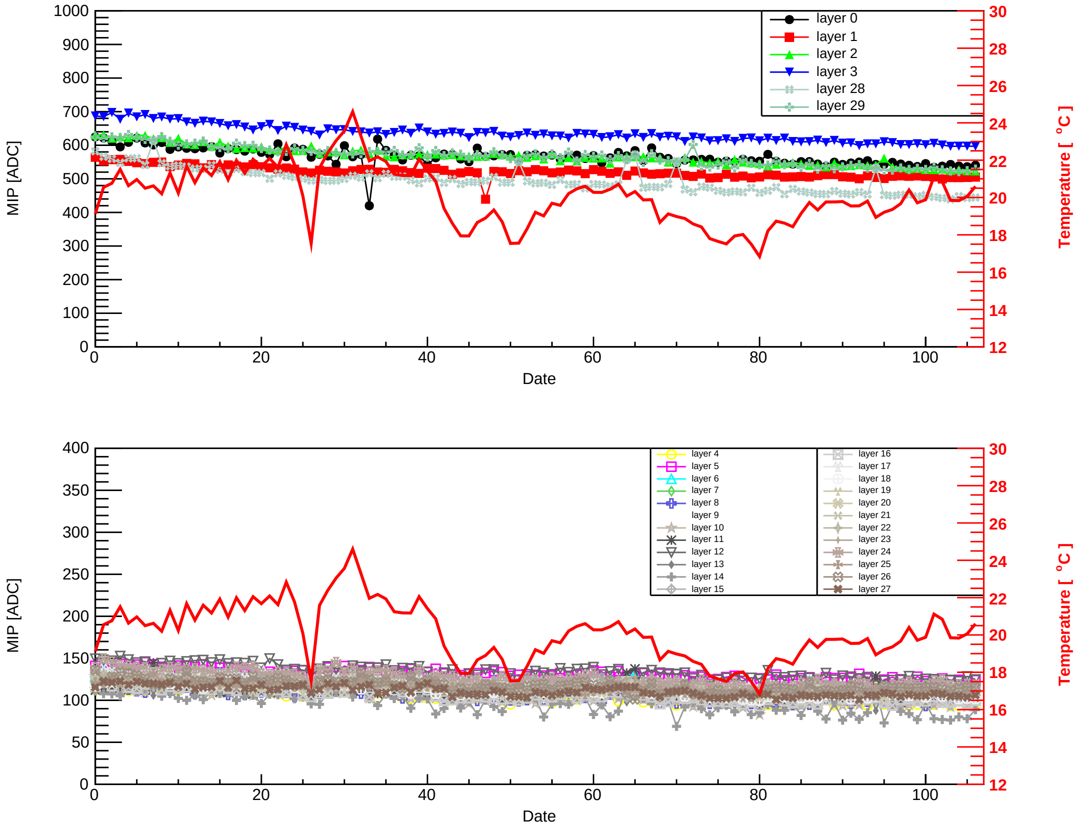

Figure7.11 Stability for the c^{MIP} with the calibration per layer after the temperature correction with 15 μm-pitch (top) and 10 μm-pitch (bottom) SiPM

by the SiO_2, and 15 pieces of 12 cm thickness plates are placed with 4.2 m pitch, which reproduces the situation of the cosmic-ray test with 15 floors above the prototype.

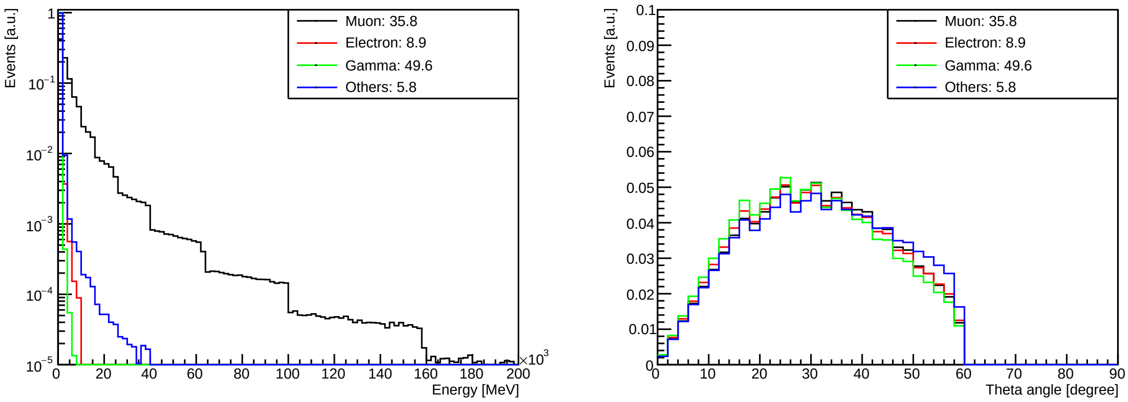

Figure7.12 Distribution of the primary energy at each particle type (left) and the zenith angle (right) The number next to the particle type means the content of the particle.

251 million cosmic-rays are generated by the CRY, and injected to the simulation setup. Only muons reach the setup for the straight track events, while some types of particles cause the showers. The same tracking algorithms

as in the cosmic-ray analysis are applied to the simulation data. However, at the first step of the track finding, the channel characteristics obtained in the prototype calibration such as the c^{MIP}, decline of c^{MIP}, and threshold are applied to each channel in the simulation. Assuming that the c^{MIP} decrease linearly, the rate of the decrease for each layer calculated in the prototype is also applied to each layer at the simulation. The average threshold of the signal is set to the 0.5 MIP, but the threshold is different from each ASIC same as the prototype.

7.3 Performance evaluation using the cosmic-ray straight track

This section gives the performance such as the efficiency and position resolution measured with the straight track of the cosmic-ray, and the comparison with the simulation.

7.3.1 Efficiency

The detection efficiency is measured as the ratio of events that have hits in a layer to all cosmic-ray events. The denominator of the ratio (all cosmic-ray events) only contains the events whose cosmic-ray track can be reconstructed, and the numerator only contains the hits in the reconstructed cosmic-ray track. The blue plots in Fig. 7.13 show the detection efficiency at each layer using all the cosmic-ray data. The efficiency is measured to be 84% on average.

The red plots in Fig. 7.13 show the detection efficiency per layer using the simulation. The both results in the data and simulation show a good agreement with each other. The efficiency in the simulation is a slightly larger than that in the cosmic-ray data. This is considered because the simulation doesn't contain the efficiency variation by the temperature change, found in the cosmic-ray data and discussed as below.

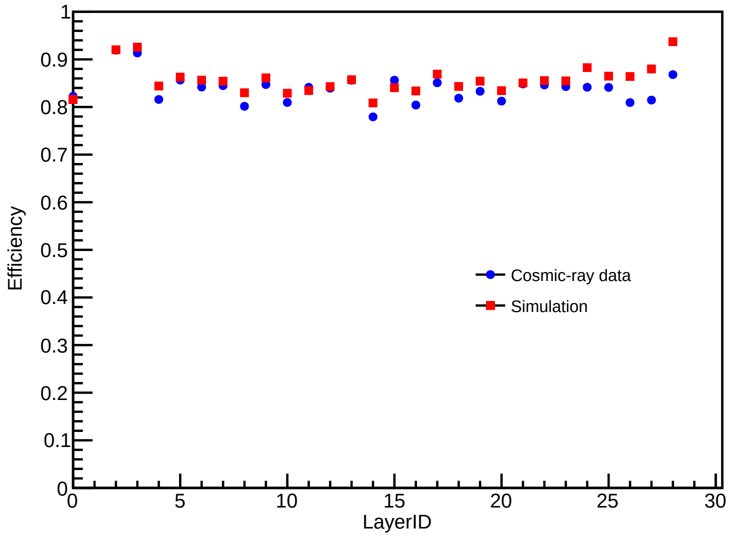

Figure7.13 Detection efficiency at each layer with the cosmic-ray data (blue) and simulation (red).

The inefficiency comes from the threshold of 0.5 MIP and dead space between the strips. The cosmic-rays that pass across the two strips lose energy as they split into their respective channels and also pass through dead areas. Such events are not detected because they have less energy deposit than the threshold of 0.5 MIP, and thus cause the inefficiency. The fraction of the dead channel is less than 1% (66 out of 6,300 channels). The effect of the dead channel is, therefore, negligible.

The stability of the detection efficiency is evaluated in the cosmic-ray data. Fig. 7.14 and Fig. 7.15 shows the stability of the efficiency at each layer with 15 μm-pitch SiPM and 10 μm-pitch SiPM respectively. It can be seen that the efficiency changes in response to temperature changes. The temperature dependence of the SiPM affects the efficiency. The increase of the temperature leads to the increase of the breakdown voltage of the SiPM, while the operation voltage is constant, so the over voltage decrease and the SiPM gain decrease. The gain decrease leads to more events below the threshold. The efficiency gradually decrease as time goes on, because the decline of the c^{MIP} causes the decline of the efficiency. However, the all layers still have reasonably high efficiency of about 80%.

The decline of the efficiency and the MIP response have no significant effect on the detector performance. If they are caused by a fluctuation in the electronics, the gain can be adjusted in online. For the test beam experiments and actual detector operations, the MIP calibration is taken at the time and the threshold is set as lower by taking the external trigger.

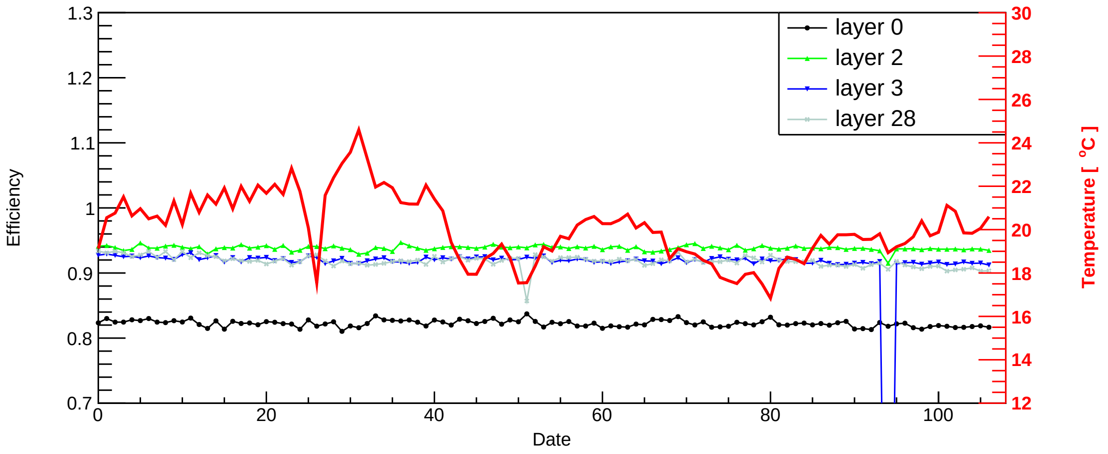

Figure7.14 Stability of the detection efficiency for each layer with 15 μm-pitch SiPM. Red line shows the average temperature.

7.3.2 Position resolution

The position resolution is estimated at each layer in the following way. The track fitting is performed using the hits reconstructed by the SSA in all the layers except the target layer. The distance between the intersection of the reconstructed track on the target layer and the SSA hit in the target layer is calculated. Fig. 7.16 shows the distance distribution. The position resolution is calculated by the RMS of the distribution of the distance.

As described in Section 4.2, the SSA can give multiple hits along the long side of the strip. The position resolution can, therefore, be a little worse in the long-side (45 mm length) direction than in the short-side (5 mm width) direction. The position resolution is evaluated in x-axis and y-axis, which are the axes parallel to the detection layer. The long side and short side of the strips are aligned orthogonally in each axis. The blue plots in Fig. 7.17 show the results of the position resolution at each layer in x-axis (left) and y-axis (right). In x-axis, the results in odd layers correspond to the short-side (5 mm width) direction of the strip, the results in even layers correspond to the long-side (45 mm length) direction of the strip. In y-axis, the results in even layers correspond to the short-side direction of the strip, the results in odd layers correspond to the long-side direction of the strip.

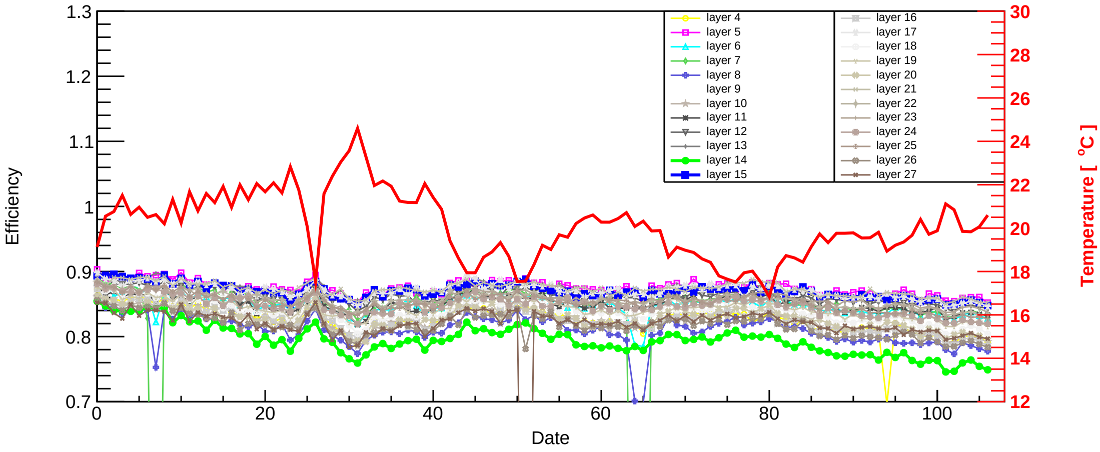

Figure7.15 Stability of the detection efficiency for each layer with 10 μm-pitch SiPM. Red line shows the average temperature.

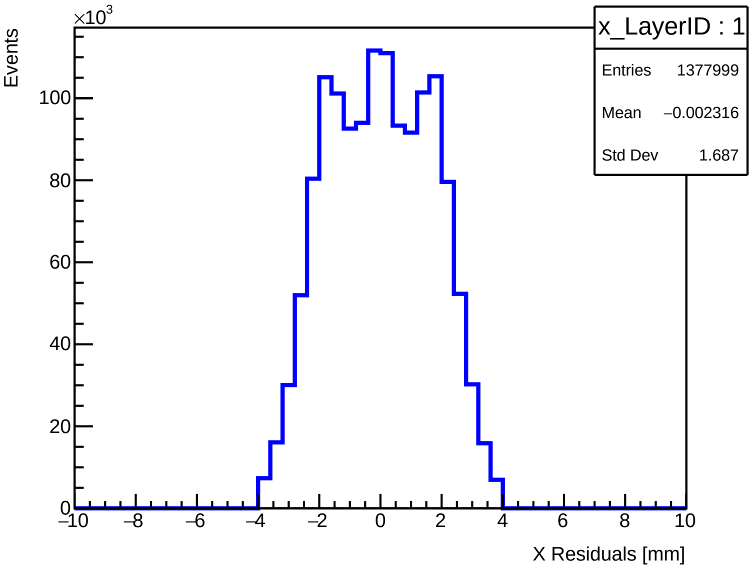

Figure7.16 Distribution of the residual at a single layer in short-handed (5 mm width) direction of the strip.

The red plots in Fig. 7.17 show the position resolution measured by the simulation in x-axis (left) and y-axis (right). The both results in the data and simulation show a good agreement with each other.

The position resolution in the short-side direction is estimated to be 1.5–1.8 mm, which is more or less consistent with the strip pitch width of 5.3 mm, where the variance of the uniform distribution of 5.3 mm is $5.3\ \mathrm{mm}/\sqrt{12} = 1.53\ \mathrm{mm}$. The position resolutions at the central layers are around 1.53 mm, so the prototype realizes the cell segmentation of 5.3 mm in the short-side direction. The position resolution at outer layers is worse than the inner layers. This is because the fit track has some extensional errors, i.e. the error in inner layers are smaller than the error in outer layers. However, the position resolution of 1.8 mm at the outer layer is equivalent to the strip pitch width of 6 mm, which doesn't have a large effects on the granularity of the whole detector.

The position resolution in the long-side direction is estimated to be 2.3 mm, which is equivalent to the strip pitch width of 8 mm. The worse resolution compared to the short-side direction is due to the SSA. The SSA splits the

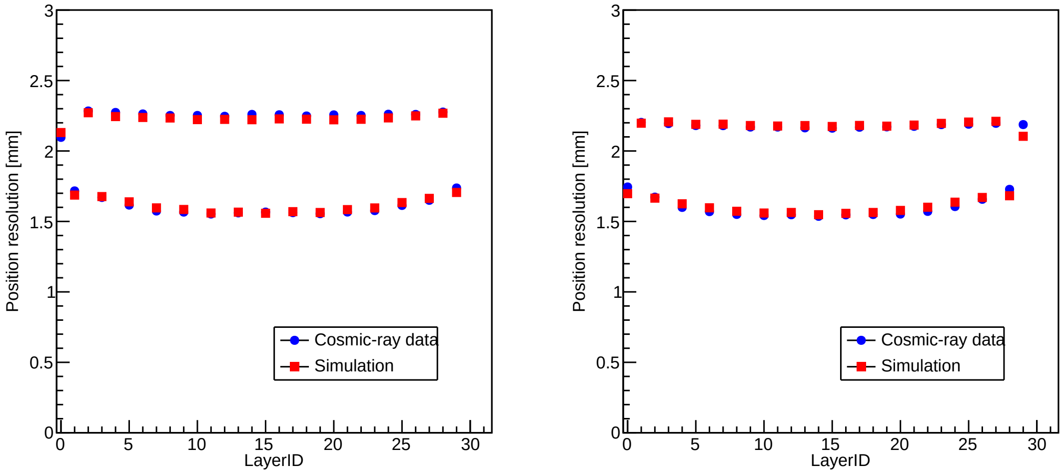

Figure7.17 Position resolution at each layer with the cosmic-ray data (blue) and simulation (red) in x-axis (left) and y-axis (right).

strip based on the hit information of the previous and next layers, and if the hit positions are different in the upper and lower layers, two cells are formed. Since the track is likely to be reconstructed to pass between two cells, the residual between the track and the cell becomes large. Although there are events across the strips in the short-side direction as well, the resolution is worse in the long-side direction because there are more such events.

7.3.3 Sum of hits and energies

The sum of the number of hits and the energy in the cosmic-ray track are compared between cosmic-ray data and simulation. Fig. 7.18 shows the distribution of the sum of the number of hits (left) and the energy (right). The both results show a good agreement with each other. The slight difference is caused by the slightly higher efficiency in the simulation as shown in Fig. 7.13 because the simulation doesn't have the effect of the temperature variation. Fig. 7.19 shows the distribution of the total energy divided by total hits, that is, the average energy deposit in a single cell. The both results also show a good agreement with each other. The energy deposit in a cell is the same as the cosmic-ray data and simulation.

7.4 Performance evaluation using the cosmic-ray shower

The detailed study of the calorimeter using the electromagnetic showers is usually taken by the test beam experiment, but unfortunately the test beam experiment is cancelled due to the COVID-19 pandemic. The performance of the Sc-ECAL is evaluated by looking for shower events induced by the cosmic-ray and comparing the shower properties with the simulation. A few examples of the event displays of the shower events from the cosmic-rays are shown in Fig. 5.10 and 5.11 This section gives the shower study using the cosmic-ray and the comparison with the simulation.

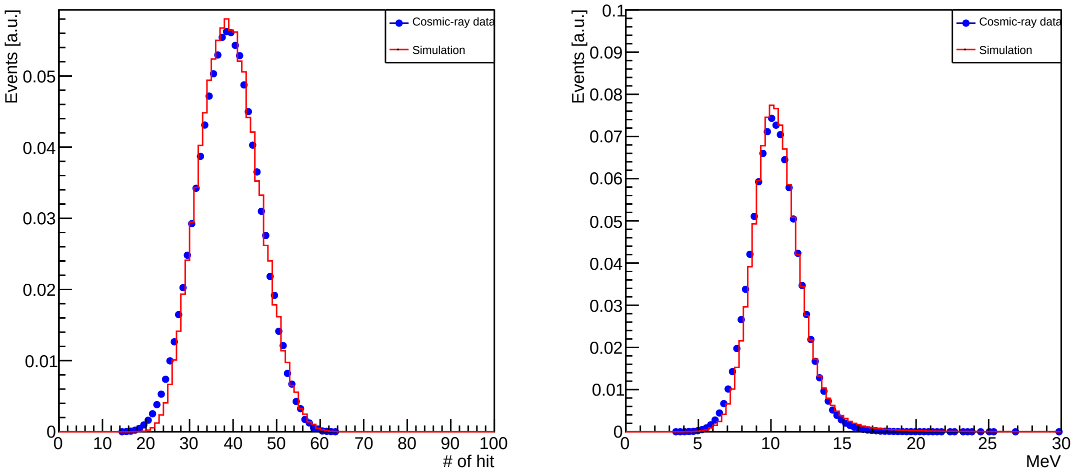

Figure7.18 Comparison of sum of hit cells (left) and energies (right) in the cosmic-ray track. The distribution shows the sum of hits and energies for all the cosmic-ray events.

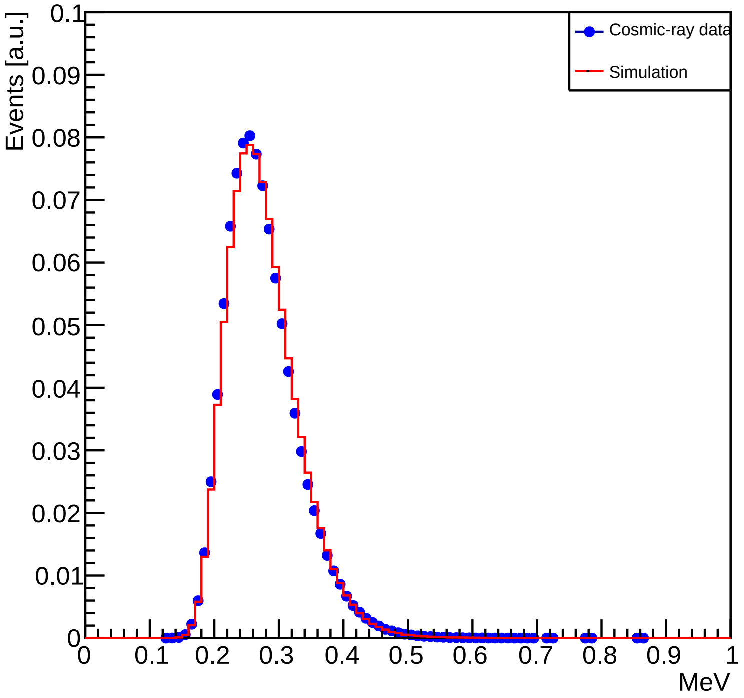

Figure7.19 The comparison of the average energy deposit in a single cell.

7.4.1 Comparison with data and simulation

Fig. 7.20 shows the energy distribution at each type of the cosmic-ray particle in the simulation. The showers induced by the cosmic-ray are electromagnetic showers caused mainly by the muon with various energies, but some electrons and gamma-rays inject to the prototype through the building and cause the EM shower. A few hadrons also inject to the prototype through the building and cause the hadronic showers.

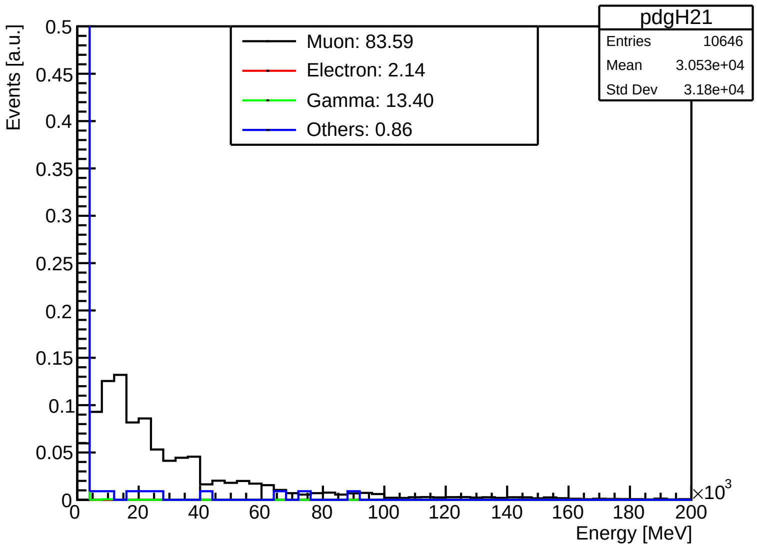

Figure7.20 Distribution of the energy at each type of injected cosmic-ray particle in the simulation. The number next to the particle in the legend means the ratio of each particle.

Fig. 7.21 shows the distributions of the shower start layer for cosmic-ray data and simulation. Both the distributions for cosmic-ray data and simulation match well. The first 5 layers are used for the linear fit to determine the injection angle, so the shower events are not found. The shower events are searched for by taking the cut of the many hits in consecutive 3 layers, so that it is difficult to find the shower events in last 3–4 layers.

Fig. 7.22 shows the distribution of the injection angle at x-axis (left) and y-axis (right). Both the distributions for cosmic-ray data and simulation match well, although some fluctuations can be seen due to the small statistics.

Fig. 7.23 shows the longitudinal shower profile for the number of hits and the energy at each layer. The simulation almost agrees with the cosmic-ray data, but a slight deviation is observed especially after the shower maximum. Fig. 7.24 and 7.25 show the transverse shower profiles for the number of hits and the energy respectively. All the profiles almost match with the data and simulation, but a slight deviation is also observed. Fig 7.26 shows the distribution of the sum of the number of hits and the energy at each event. The simulation also agrees with the data, but the simulation has less low-energy events compared to the data. To understand the deviation in more detail, the comparison using the events with fully contained shower and with shower escape is performed in the following sections.

7.4.2 Fully contained shower

The prototype may not contain the full shower depending on the shower start position and the energy of the incident particle. The comparison between the data and the simulation is performed for the fully contained showers.

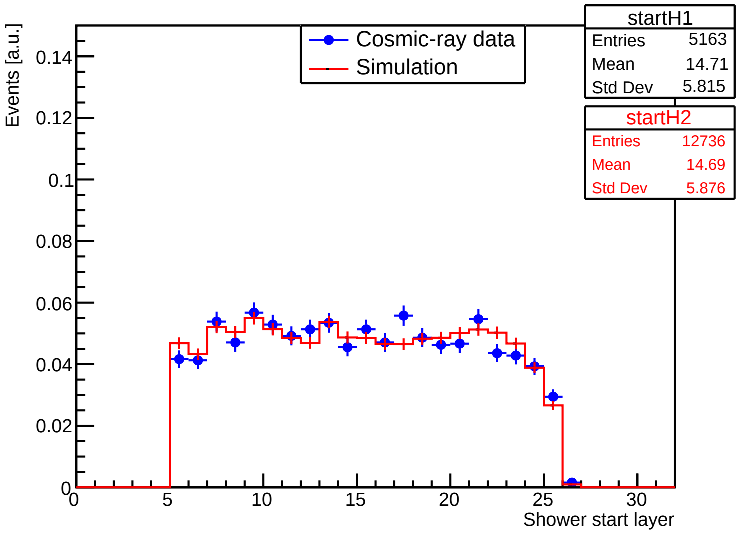

Figure7.21 Distribution of the shower start layer.

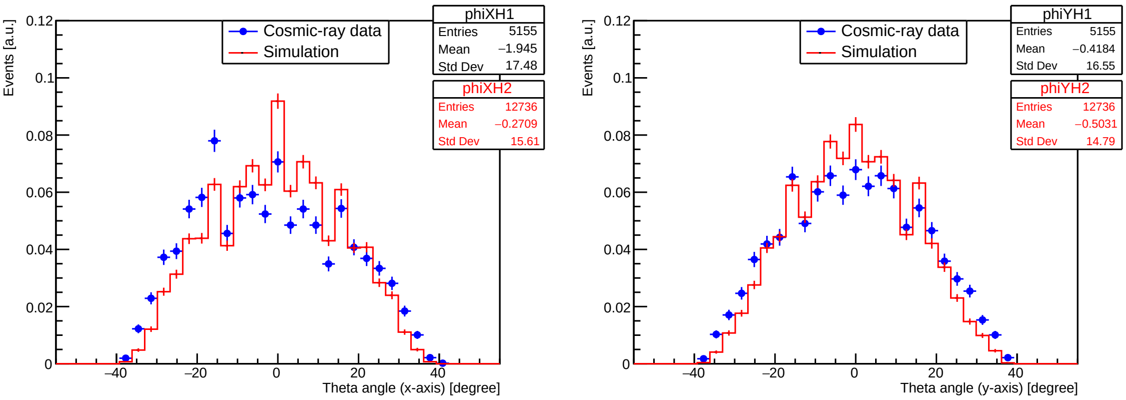

Figure7.22 Distribution of the injection angles at x-axis (left) and y-axis (right)

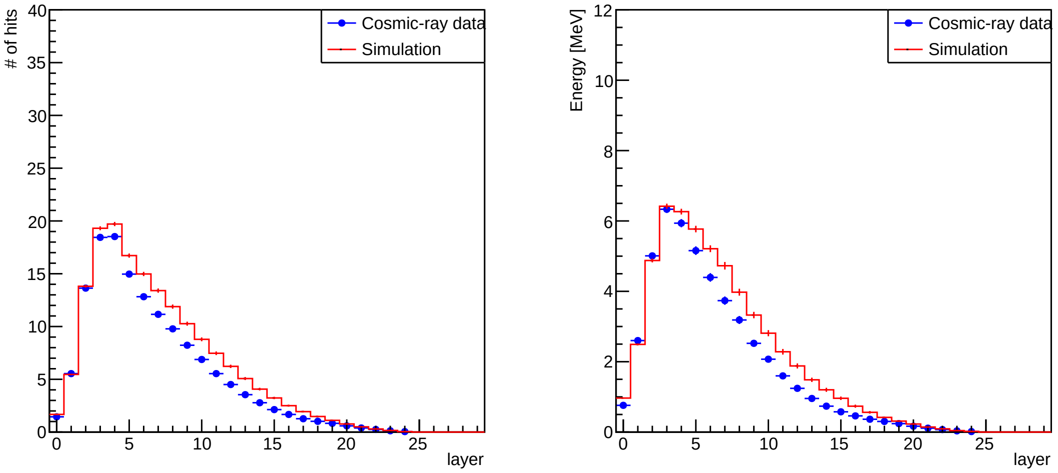

Figure7.23 Longitudinal shower profile of the number of hits (left) and the energy (right) from the shower start layer.

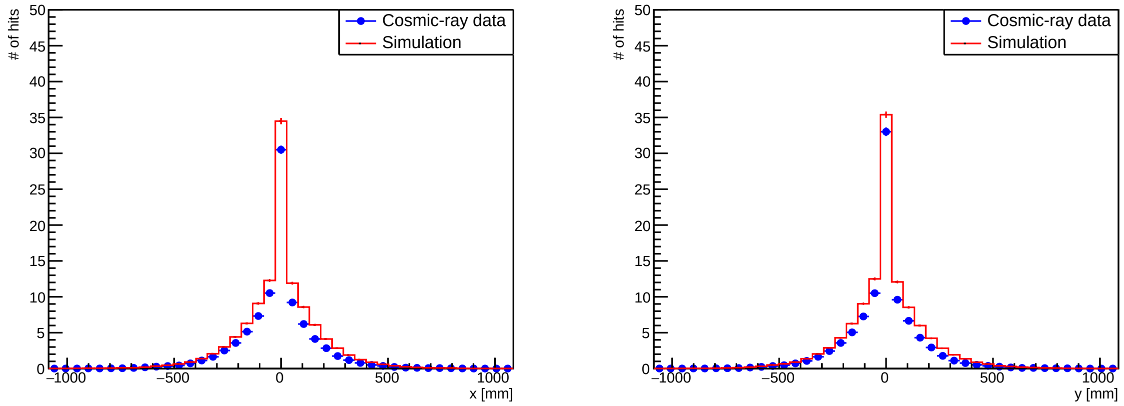

Figure7.24 Transverse hit profile for x-axis (left) and y-axis (right). The origin is set as the shower start point.

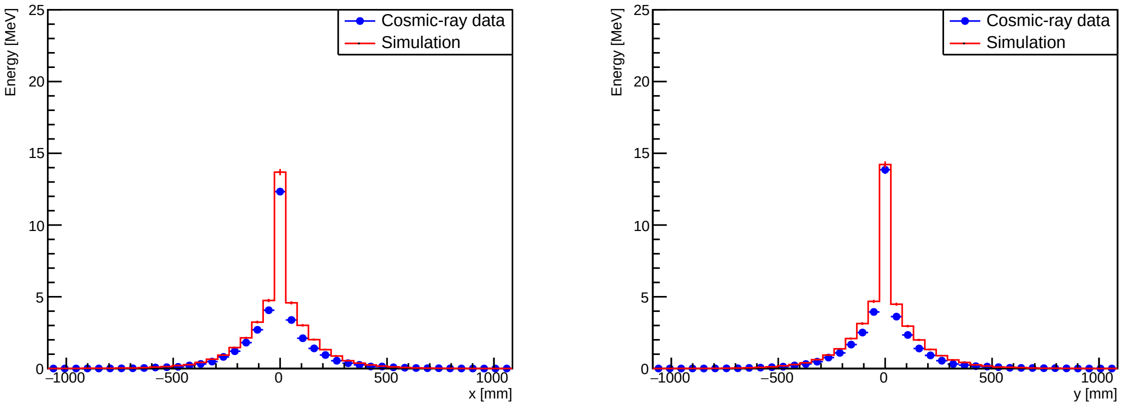

Figure7.25 Transverse energy profile for x-axis (left) and y-axis (right). The origin is set as the shower start point.

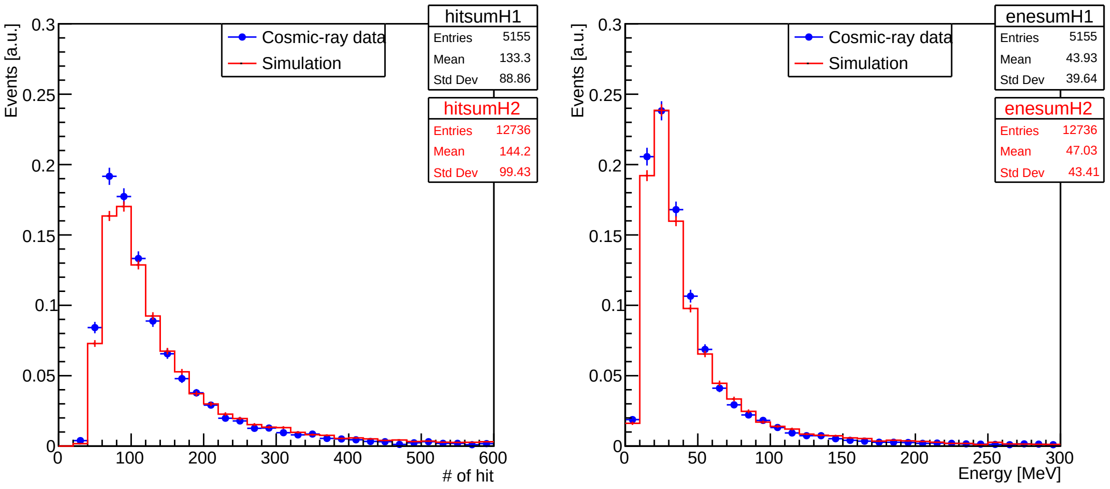

Figure7.26 Distribution of the sum of the number of hits (left) and energies (right)

The track and converged shower are within 4 hits (2 strips × 2 strips), but the non-converging shower has more hits. The fully contained shower events are selected by taking a selection that the sum of hits at the last layer (Layer 29) is less than 4. Fig. 7.27 and 7.28 shows the event displays after the selection using the cosmic-ray data and simulation respectively. Fig. 7.29 shows the distributions of the shower start layers after the selection. The shower events at latter layers decrease, and only the shower events fully contained in the prototype are selected.

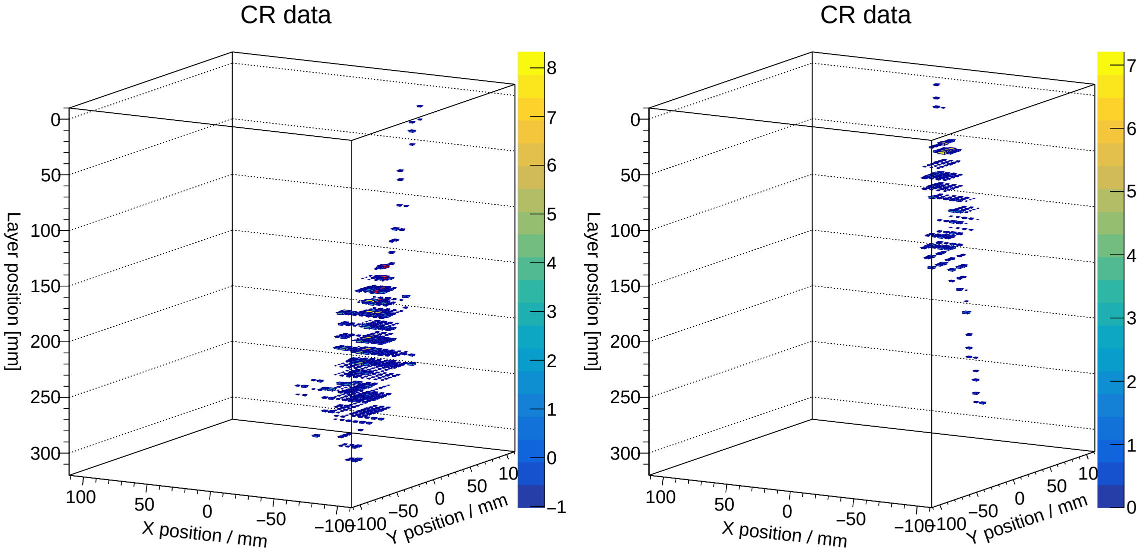

Figure7.27 Event displays of the fully contained shower events in the cosmic-ray data. The color bar shows the number of MIPs, and the hit above 10 MIPs is colored red to make it easier to see the difference in color.

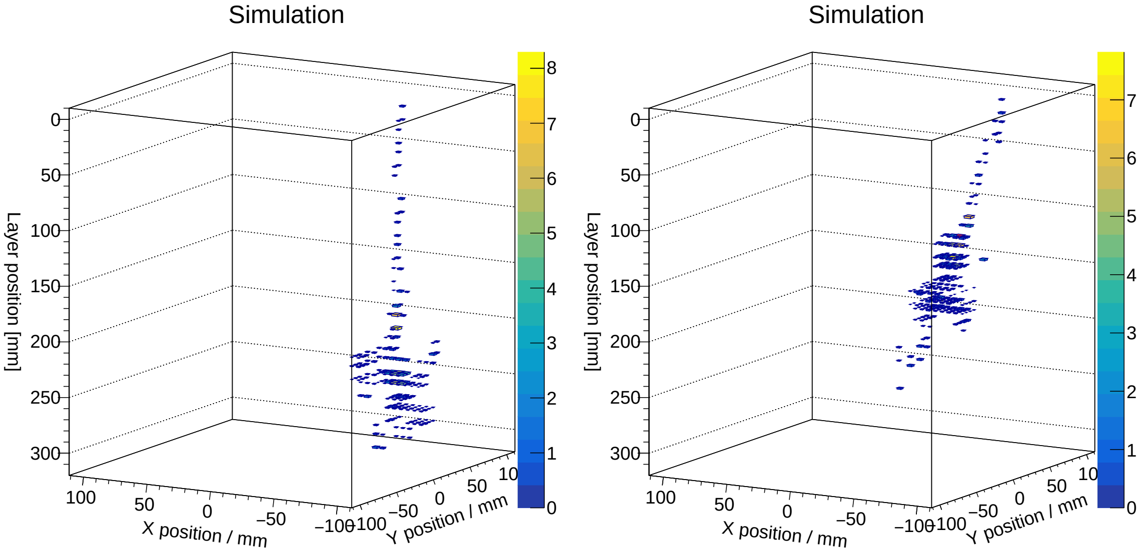

Figure7.28 Event displays of the fully contained shower events in the simulation. The color bar shows the number of MIPs, and the hit above 10 MIPs is colored red to make it easier to see the difference in color.

Fig. 7.30 shows the distribution of the injection angle at x-axis (left) and y-axis (right). Both the distributions for cosmic-ray data and simulation match well, although some fluctuations can be seen due to the small statistics.

Fig. 7.31 shows the longitudinal shower profile for the number of hits and the energy at each layer. The simulation agrees with the cosmic-ray data much better without the selection. The profiles for the simulation have a bit higher

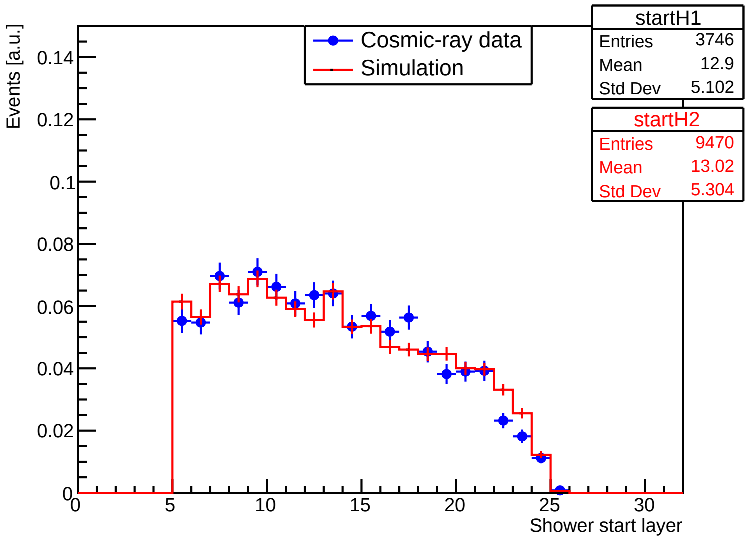

Figure7.29 Distribution of the shower start layers for fully contained showers.

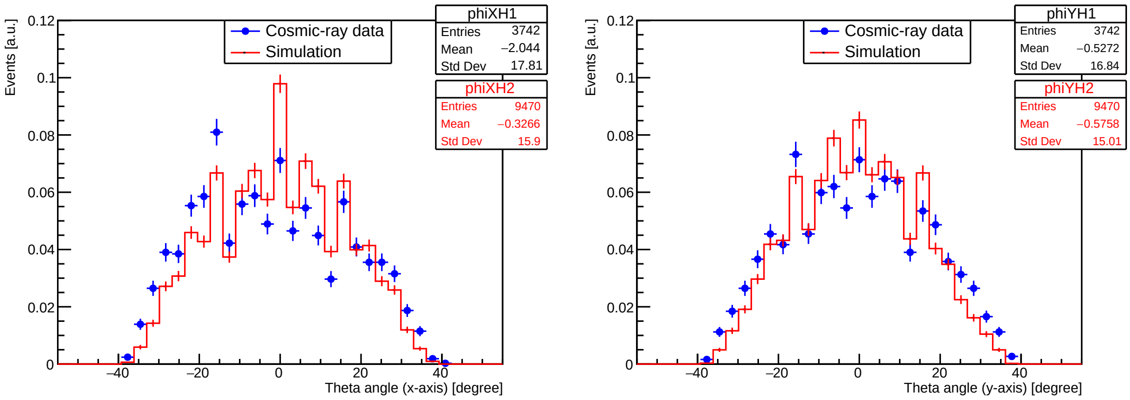

Figure7.30 Distribution of the injection angles for fully contained showers at x-axis (left) and y-axis (right)

at the central layers than the cosmic-ray data. This is because the low energy particles can not be detected by the prototype due to the threshold and decline of the MIP response. The transverse profiles for hits and energies and sum of the number of hits and the energy for the fully contained showers also match with the data and simulation as shown in Fig. 7.32, 7.33, and 7.34. In summary, the simulation reproduces the behavior of the prototype very well for the fully contained showers.

7.4.3 Shower escape

Studies with the cosmic-ray shower event are performed also for the event with a shower escape where a part of the shower tail escapes from the prototype. The selection that the sum of hits at the last layer (Layer 29) is more than 4 is applied. Fig. 7.35 and 7.36 show the examples of the event displays for the selected events using the cosmic-ray data and simulation respectively. Fig. 7.37 shows the distribution of the shower start layer for shower escape events. It can be seen that the shower tends to start at later layers for the shower escape events.

Fig. 7.38 shows the distribution of the injection angle at x-axis (left) and y-axis (right) for midway showers. Both the distributions for cosmic-ray data and simulation match well, although some fluctuations can be seen due

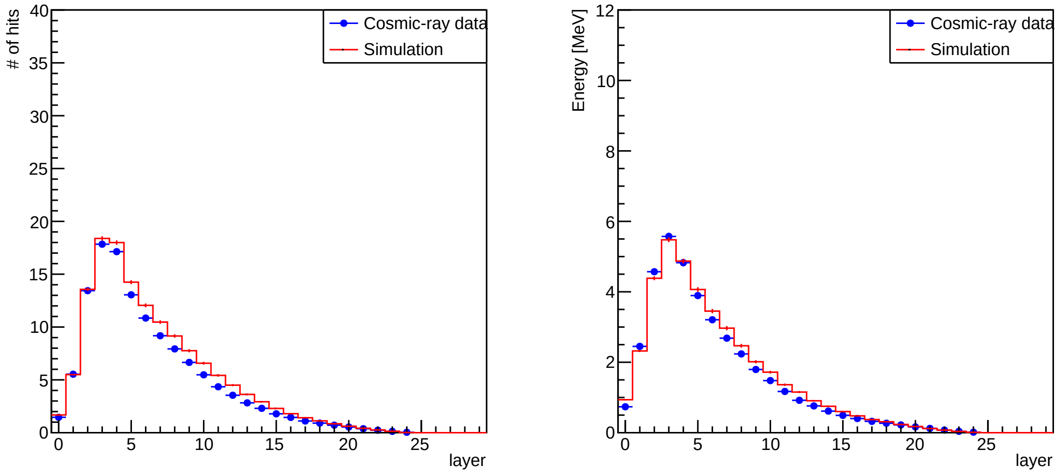

Figure7.31 Longitudinal shower profile for fully contained showers of the number of hits (left) and the energy (right)

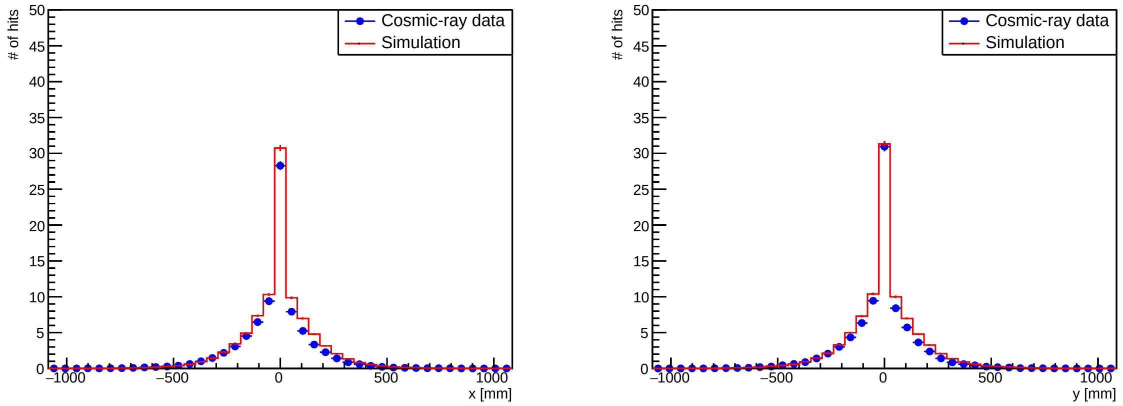

Figure7.32 Transverse hit profile for fully contained showers for x-axis (left) and y-axis (right). The origin is set as the shower start point.

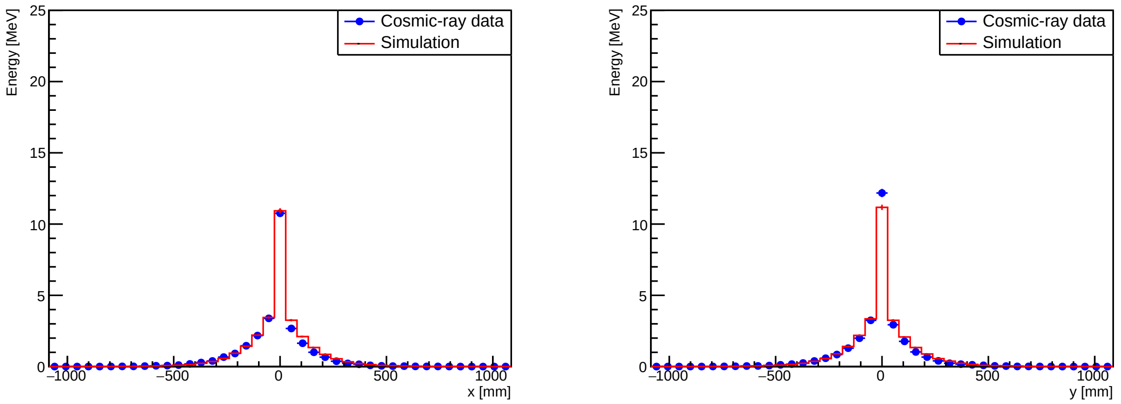

Figure7.33 Transverse energy profile for fully contained showers for x-axis (left) and y-axis (right). The origin is set as the shower start point.

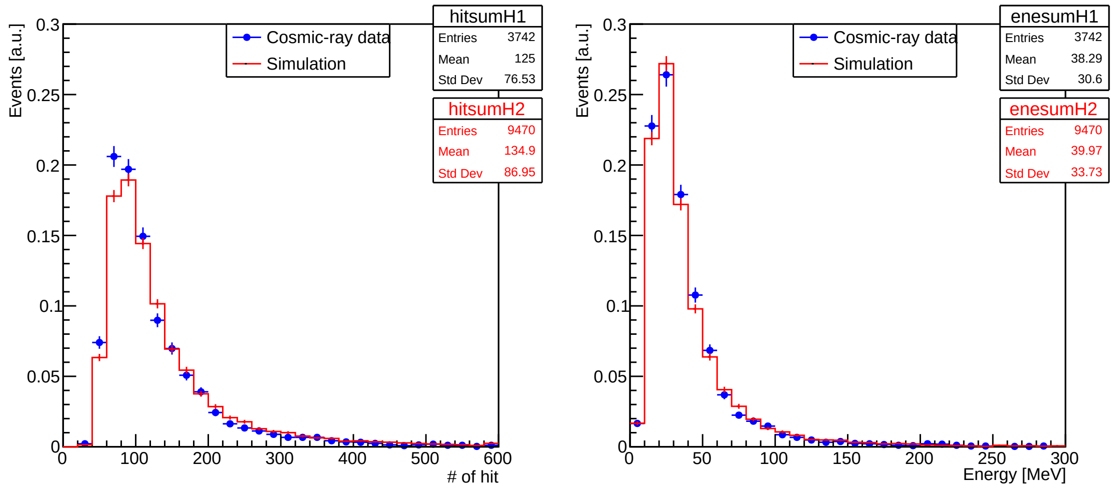

Figure7.34 Distribution of the sum of the number of hits (left) and the energy (right) for fully contained showers.

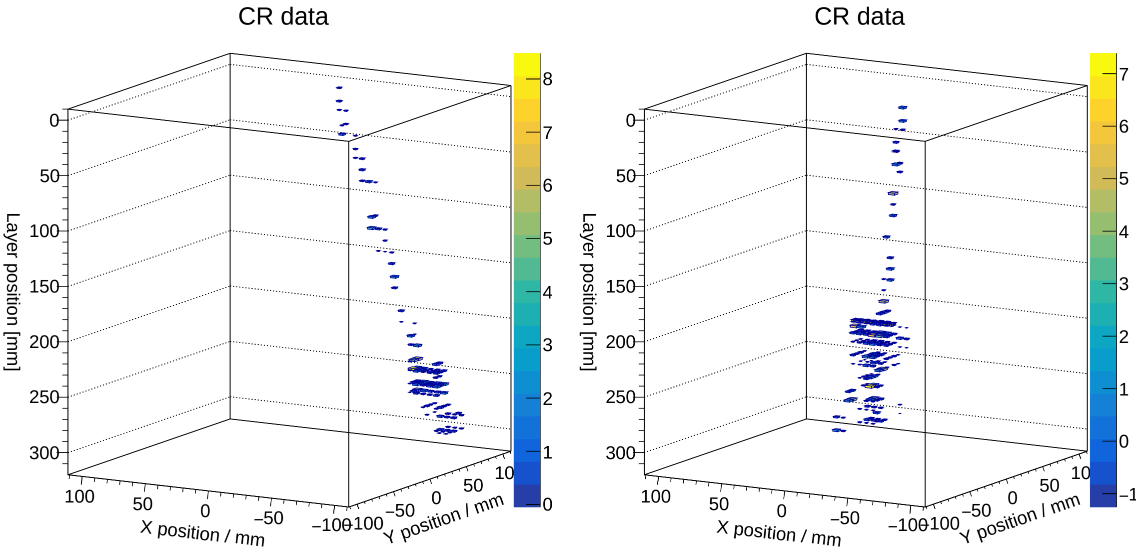

Figure7.35 Event displays of the shower escape events in the cosmic-ray data. The color bar shows the number of MIPs, and the hit above 10 MIPs is colored red to make it easier to see the difference in color.

to the small statistics.

Fig. 7.39 shows the longitudinal shower profiles for the shower escape events, and Fig. 7.40 and 7.41 show the transverse profiles for the shower escape events. A much larger deviation between the data and the simulation for the profiles of the shower escape events is observed. This is discussed in the next section.

Fig. 7.42 shows the distribution of the sum of the number of hits and the energy for the shower escape events. The simulation also agrees with the data, but the simulation has less low-energy events compared to the data. To understand the deviation in more detail, the comparison with the primary energy in the simulation is performed in the next section.

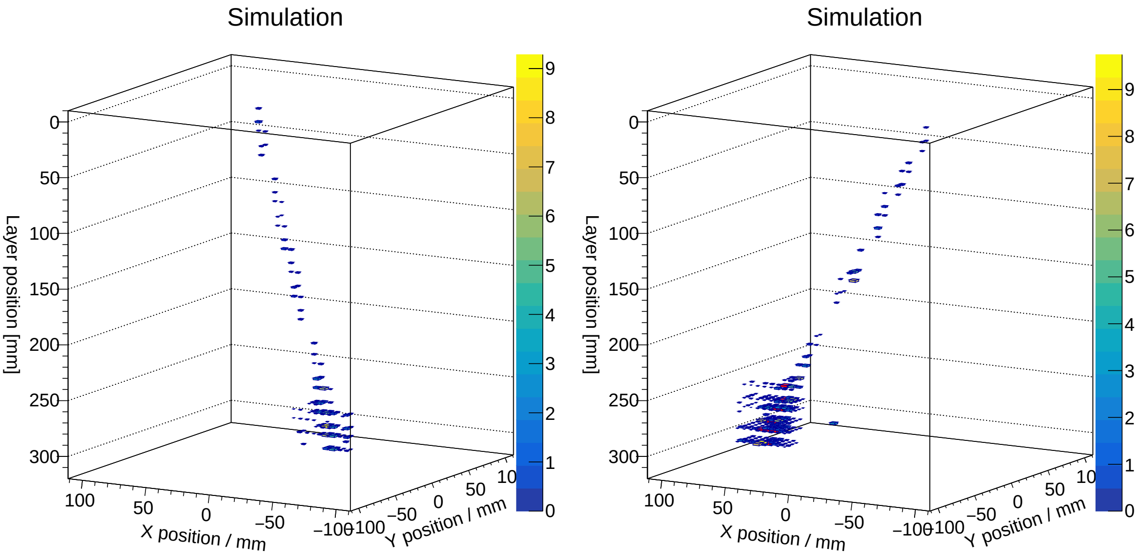

Figure7.36 Event displays of the shower escape events in the simulation. The color bar shows the number of MIPs, and the hit above 10 MIPs is colored red to make it easier to see the difference in color.

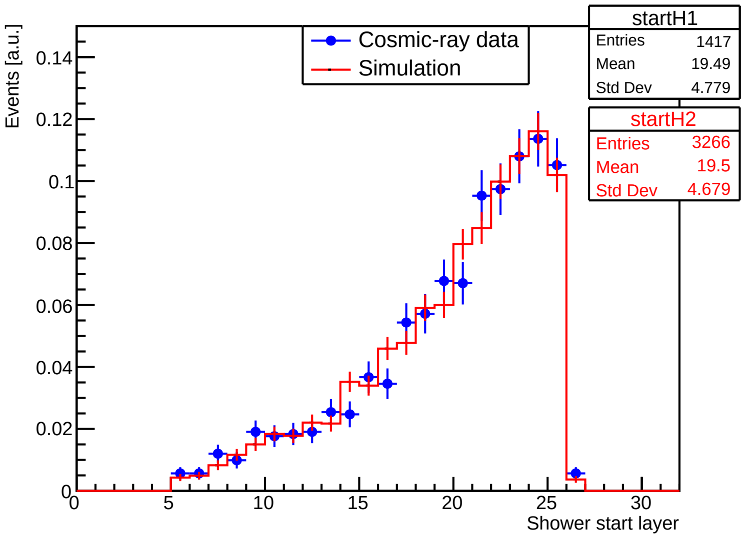

Figure7.37 Distribution of the shower start layers for shower escape events.

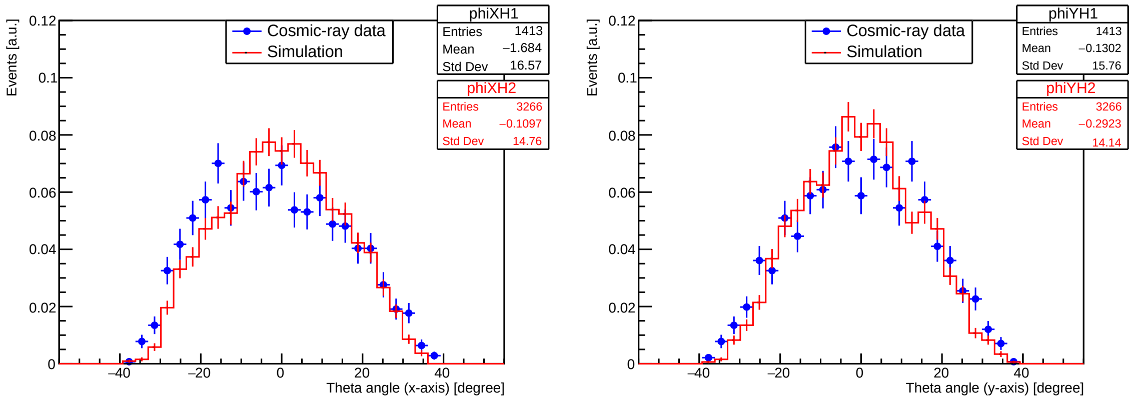

Figure7.38 Distribution of the injection angles for midway showers at x-axis (left) and y-axis (right)

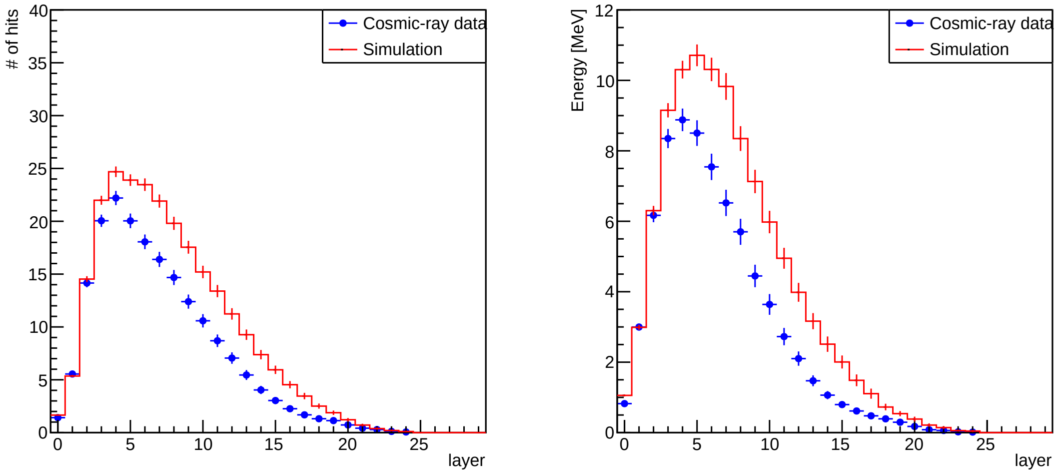

Figure7.39 Longitudinal shower profile for shower escape events of the number of hits (left) and the energy (right)

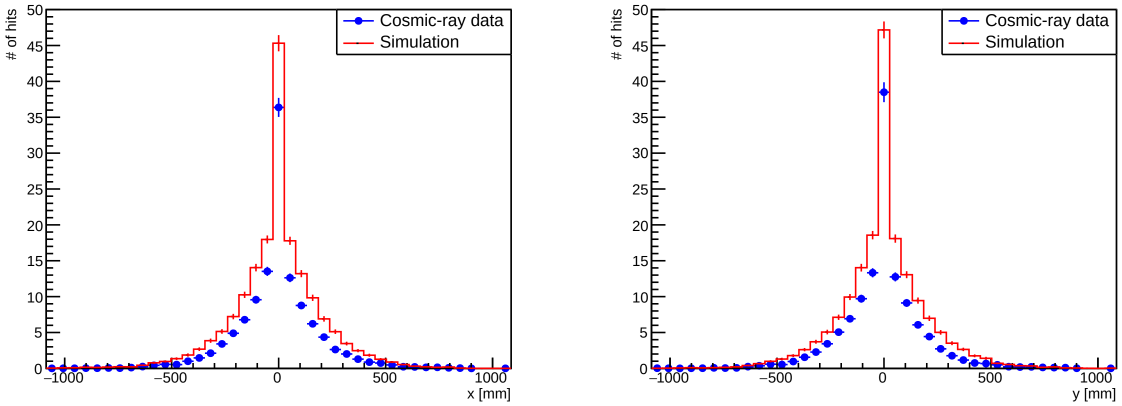

Figure7.40 Transverse hit profile for shower escape events for x-axis (left) and y-axis (right). The origin is set as the shower start point.

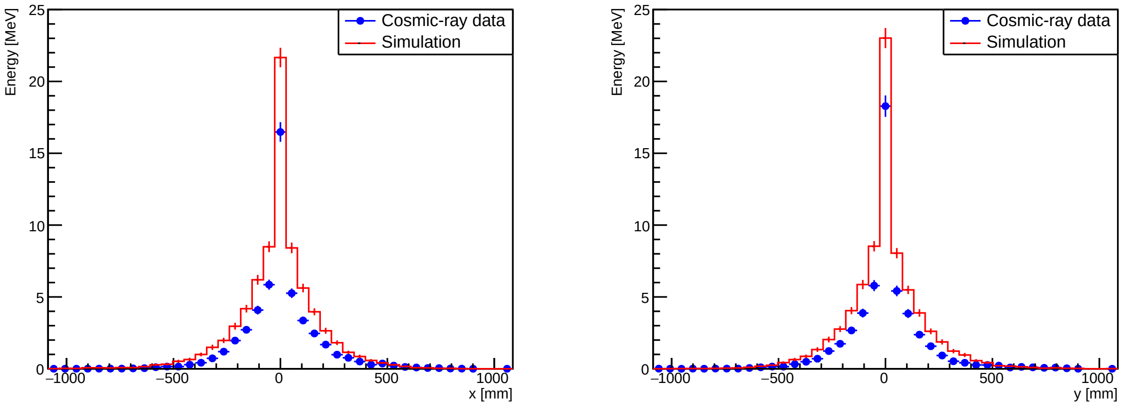

Figure7.41 Transverse energy profile for shower escape events for x-axis (left) and y-axis (right). The origin is set as the shower start point.

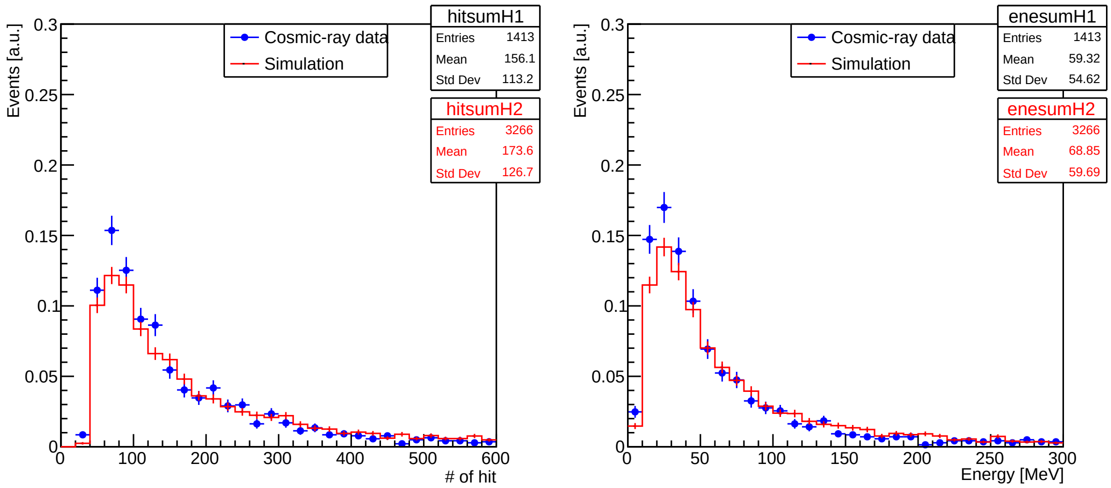

Figure7.42 Distribution of the sum of the number of hits (left) and energies (right) for shower escape events

7.4.4 Comparison of primary energy in simulation

Fig. 7.43 shows the comparison of the primary energy for the fully contained showers and the shower escape events. The shower escape events have more high energy events. The difference between the fully contained showers and shower escape events may be due to this difference in primary energy of the incident particle.

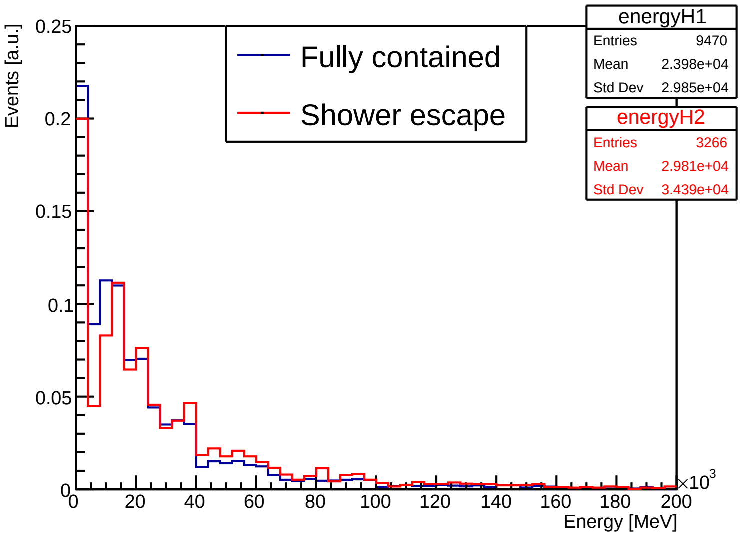

Figure7.43 Distribution of the primary energy for the fully contained shower (blue) and shower escape events (red)

Fig. 7.44 shows examples of the event displays in the simulation with the lower primary energies, and Fig. 7.45 shows the events with the higher primary energies. The shower events from the high-energy particles create larger showers and have more high-energy hits compared to the events from the low-energy particles.

The distribution of the primary energy in the simulation is adjusted by hand for better agreement with the shower profiles in data. Fig. 7.46 shows the distribution of the primary energy after the energy suppression (green) and

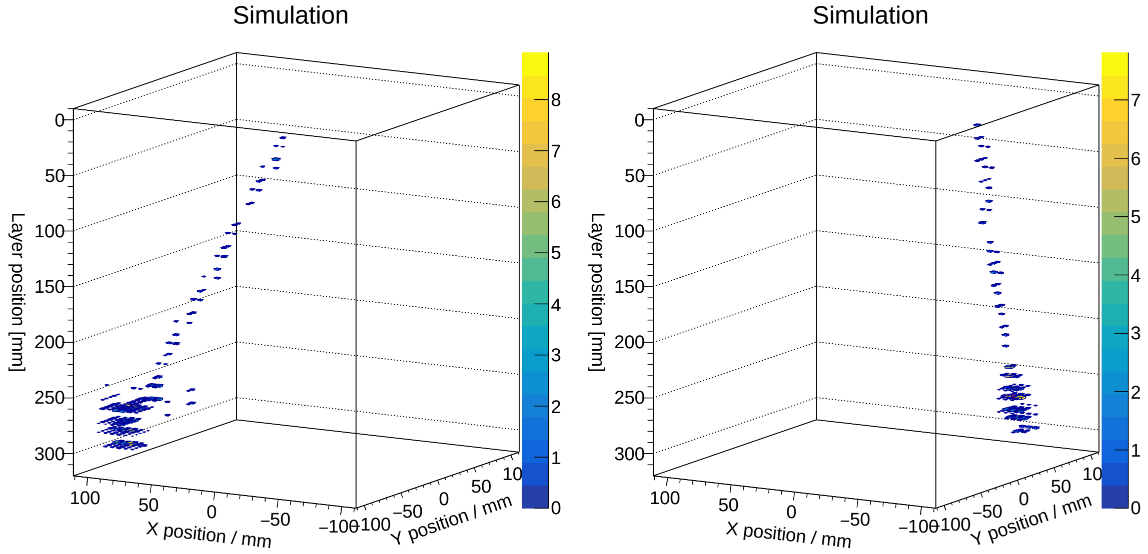

Figure7.44 Event displays of the shower escape events in the simulation with the energy of 1 GeV (left) and 9 GeV (right).

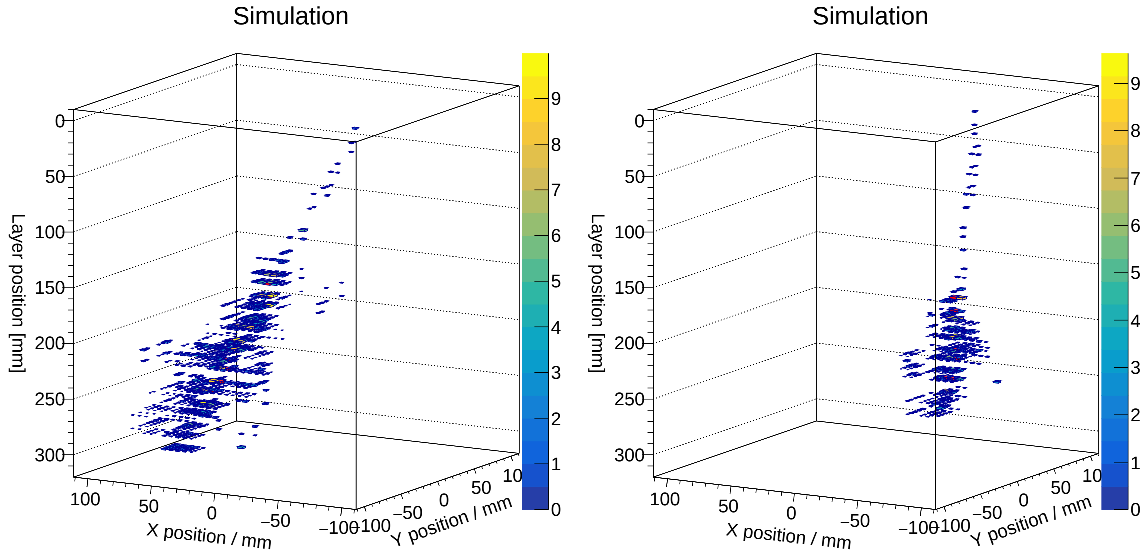

Figure7.45 Event displays of the shower escape events in the simulation with the energy of 89 GeV (left) and 112 GeV (right).

for all shower escape events for comparison (red). The shower escape events are suppressed linearly depending on the primary energy, i.e., suppressed by $3 \times (\mathrm{energy})\%$.

Fig. 7.47, 7.48, and 7.49 shows the shower profiles after the energy suppression in the simulation, where all the shower escape events are used in the cosmic-ray data. Fig. 7.50 shows the distributions of the sum of the number of hits and the energy after the suppression in the simulation. All the distributions in the simulations show a much better agreement with the cosmic-ray data.

In summary, the observed deviation in the shower distributions between the simulation and the data is likely due to a problem of the energy distribution in the high energy region in the simulation. The discontinuous distribution of the cosmic-ray energy shown in Fig. 7.12 may not reproduce the actual cosmic-ray energy spectrum, and this may cause the deviation between the data and simulation. However, in the adjusted environment such as the fully

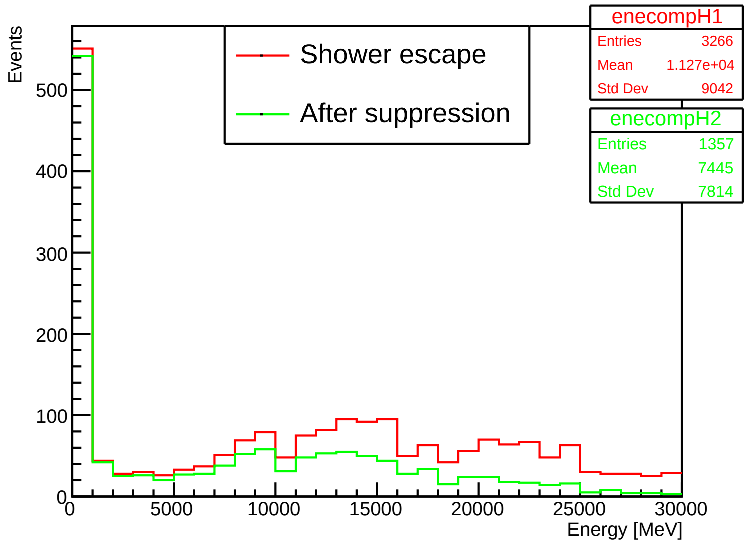

Figure7.46 Distribution of the primary energy after the suppression (green) and all shower escape events (red)

contained shower and the shower escape with the energy suppression, the data and simulation match well. At least in such an environment, the Sc-ECAL can measure the showers successfully.

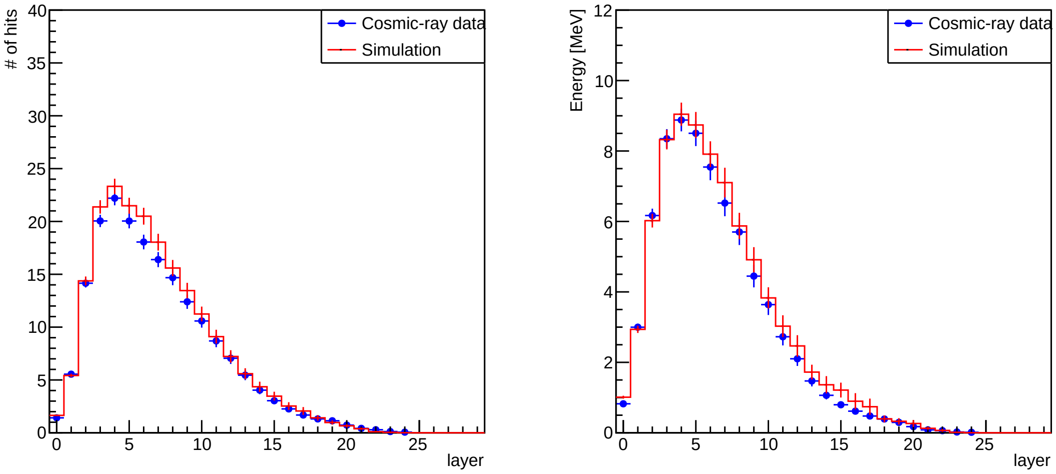

Figure7.47 Longitudinal shower profile for midway showers of hits (left) and energies (right) after the selection.

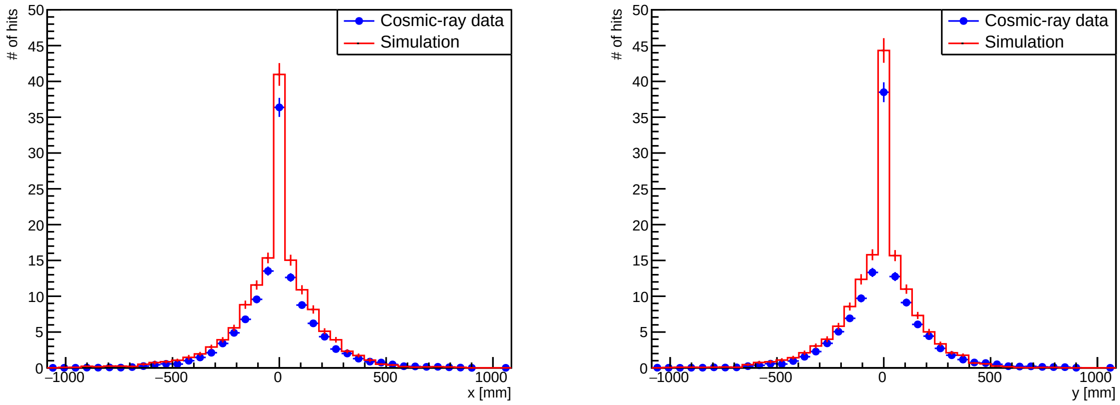

Figure7.48 Transverse hit profile for midway showers for x-axis (left) and y-axis (right) after the selection.

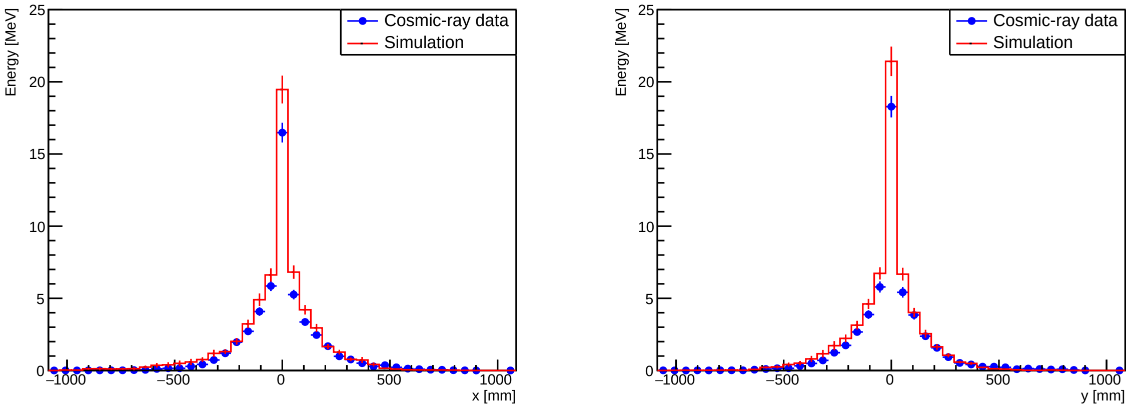

Figure7.49 Transverse energy profile for midway showers for x-axis (left) and y-axis (right) after the selection.

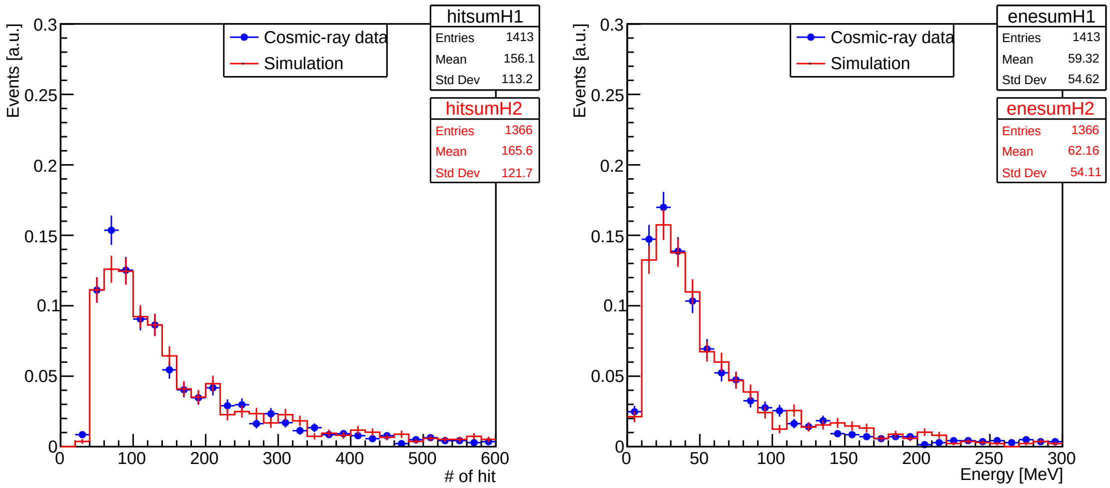

Figure7.50 Distribution of the sum of the number of hits (left) and energies (right) after the selection.

Chapter 8

New method for the saturation correction

A new method for the measurement and correction of the saturation of the SiPM is developed. The saturation is an issue for the detector using SiPMs involving the Sc-ECAL, which have many pile-up hits. The saturation curve is usually measured by directly injecting fast visible light pulse to SiPM [53][54], but this method doesn't consider the crucial effects of the time constant of the emission of the scintillation light. New idea is to measure the SiPM saturation with the scintillation light excited by the UV light pulse. This allows to measure the saturation in the real situation including the effect of the time constant of the scintillation emission. A new modeling of the SiPM saturation containing the effect of the new method is developed, and the model is validated by comparing the results with measurements.

This chapter describes the new method and the modeling of the SiPM saturation.

8.1 Saturation

The SiPM is widely used in high energy experiments. The SiPM has many advantages such as the high gain with a bias voltage lower than 100 V, small size and so on. One disadvantage is the non-linear response at high input light intensities. When a large number of photons are injected to a SiPM, the output of the SiPM can be saturated due to the limited number of pixels. The saturation of the SiPM can be an issue for calorimeters using SiPMs, especially for the electromagnetic calorimeter involving the Sc-ECAL, because the narrow and dense EM shower creates many pile-up hits.

The non-linear response of the SiPM, called saturation curve, is usually measured by directly injecting fast visible light pulse ($\sim$400 nm) to a SiPM. However, this conventional method doesn't include the effect of the time constant of the emission of the scintillation light (few ns), which is not negligible compared to the recovery time of the SiPM pixel (dozens ns). New idea is to measure the SiPM saturation with the scintillation light excited by the UV light pulse. The saturation curve measured by this method includes the effect of the pixel recovery during the scintillation emission, and can directly be used for the saturation correction in calorimeters using scintillators and SiPMs.

8.2 Saturation measurement

The saturation curve is measured using the UV light. This section gives the experimental setup, analysis process, calibration, the results of the saturation measurement.

8.2.1 Setup

A sub-nanosecond UV pulse LED with a wavelength of 255 nm, PLS-255 produced by PicoQuant [55], is used to excite the scintillation light. Fig. 8.1 shows the wavelength spectrum of the PLS-255. Scintillation can be excited in the typical plastic scintillator by injecting the UV light with the wavelength below 300 nm, while the SiPM is not sensitive to the UV light below 300 nm as shown in Fig. 8.2.

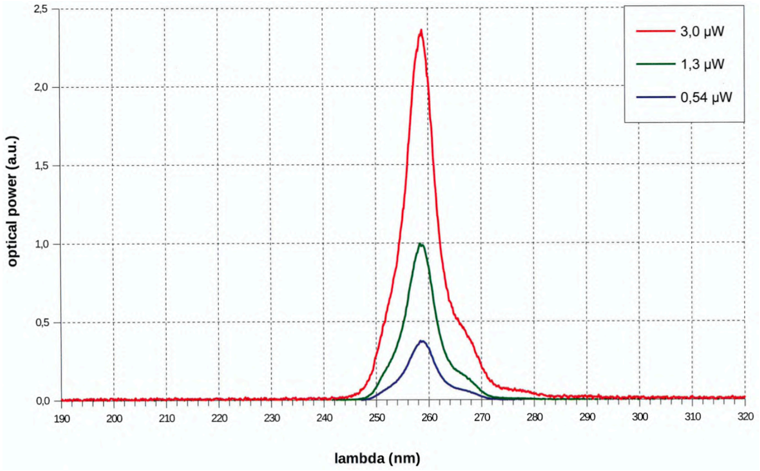

Figure8.1 Wavelength spectrum of the PLS-255 [55]

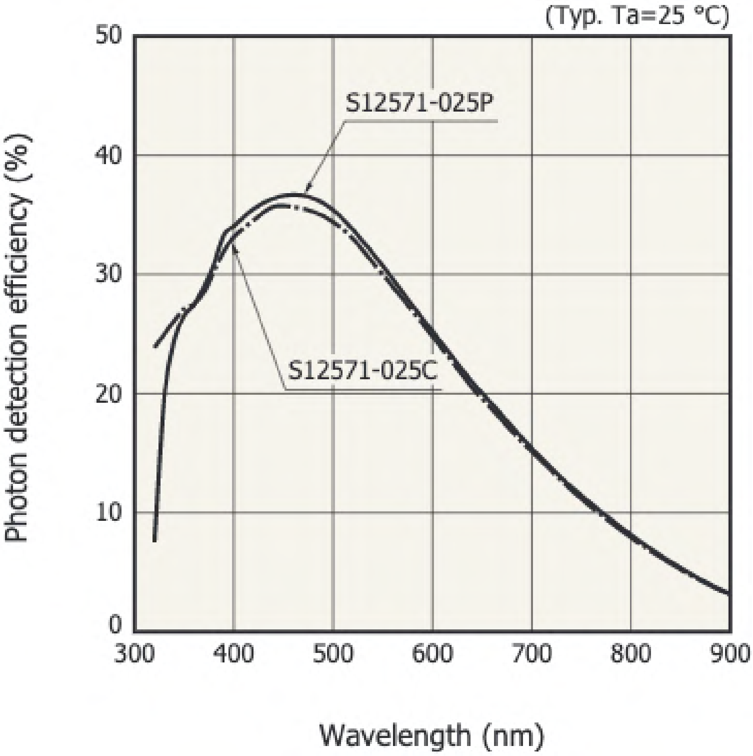

Figure8.2 Photon detection efficiency against wavelength for S12571-025P [37]

A scintillator, EJ-200 produced by Eljen [56], of $2\ \mathrm{mm} \times 2\ \mathrm{mm} \times 2\ \mathrm{mm}$ coupled to a SiPM is used. The EJ-200 is a commercial PVT scintillator, which is equivalent to the BC-408 used for the Sc-ECAL prototype, as shown in Table 8.1. The SiPM used in the measurement is Hamamatsu S12571-025P. The S12571-025P is the same series as the SiPMs used in the prototype (S12571-010P and S12571-015P), but with a large pixel (25 $\mu\mathrm{m}$-pitch) because the light intensity of the PLS-255 is too low for the saturation measurement with the SiPM of the prototype with the small pixel (10 $\mu\mathrm{m}$-pitch and 15um $\mu\mathrm{m}$-pitch).

Table8.1 Performance parameters of BC-408 and EJ-200

Parameter	BC-408	EJ-200
Light output	64%	64%
Rise time	0.9 ns	0.9 ns
Decay time	2.1 ns	2.1 ns
Wavelength of maximum emission	425 nm	425 nm
Light Attenuation length	210 cm	380 cm

Fig. 8.3 shows the experimental setup for the saturation measurement. The UV light is focused by a convex lens, passes through a variable ND filter and a band-pass filter, and then enters the scintillator. The variable ND filter controls the light intensity, and the band-pass filter allows only the wavelength from 250 nm to 270 nm to pass through. The scintillator is excited by the injected UV light, and the SiPM detects the scintillation light. The operating voltage of the SiPM is the recommended voltage by Hamamatsu Photonics. The photomultiplier tube (PMT), which has a much wider dynamic range, is used to confirm that the linear relationship between the excited scintillation light and the incident light intensity. The temperature of the SiPM is monitored by a Pt-100 temperature sensor placed behind the SiPM.

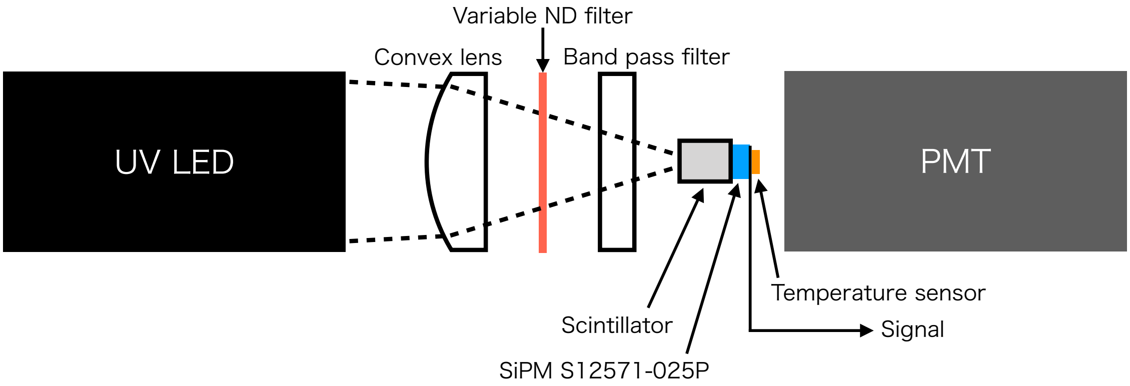

Figure8.3 Experimental setup for the saturation measurement using the UV light

8.2.2 Measurement

Fig. 8.4 shows the typical saturation curve measured by the visible light pulse. N_{seed} is the expected number of photoelectrons when assuming no saturation, and N_{det} is the number of photoelectrons detected by the SiPM. The saturation curve can be obtained by scanning the light intensities. In this measurement, the N_{seed} is measured by the photodiode, and the N_{det} is measured by the SiPM. They are usually expressed in units of the number of photoelectrons, but in this measurement, they are measured as current because it is not possible to analyze the whole range in units of the number of photoelectrons. The current is converted to the number of photoelectrons by simultaneously measuring the number of photoelectrons at the low light intensities, as explained in the next section.

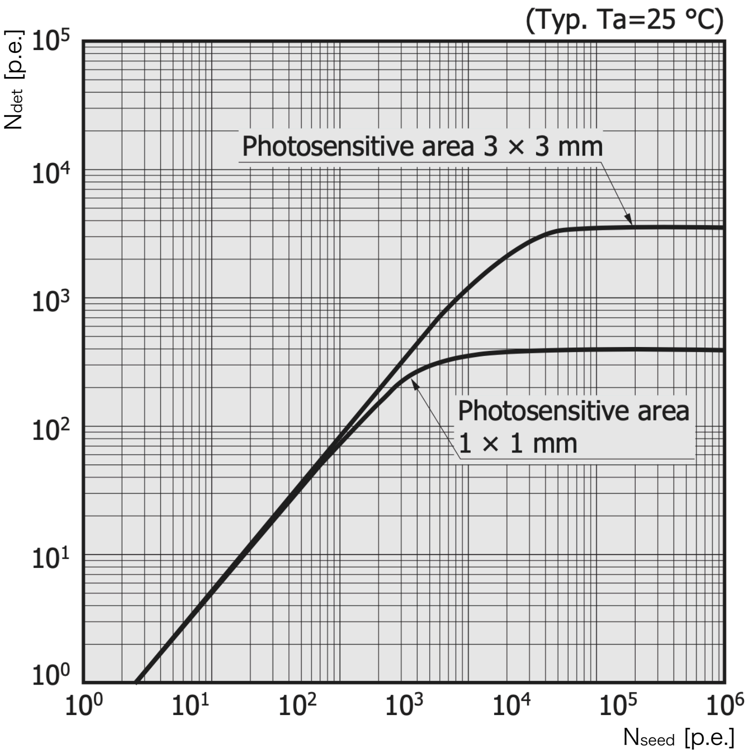

Figure8.4 Saturation curve measured by the visible light pulse [40]

The new method is composed of three types of measurements as shown in Fig. 8.5;

- The signal from the SiPM is monitored at low light intensity in units of the number of photoelectrons by a waveform digitizer. (The signal from the PMT is also monitored by the waveform digitizer)
- The signal from the SiPM is read by a picoammeter over the whole light intensity range
- The light intensity is monitored by a photodiode

The saturation curve is measured by performing the three sets of the measurements at each light intensity.

At the first measurement, the signal from the SiPM is measured in units of the number of photoelectrons. The waveform digitizer, DRS4 produced by the Paul Scherrer Institute [57], is used. The charge by integrating the signal waveform is converted to the number of photoelectrons using the single photoelectron charge measured by the dark noise spectrum. However, the dynamic range of the DRS4 is limited, so this measurement using the DRS4 is performed only in the region of low light intensity. The signal from the PMT is also measured by the DRS4 to confirm the linearity of the scintillation emission. The scintillation light which injects to the PMT is very small due to the material between the scintillator and PMT, so the signal from the PMT can be measured by the DRS4 at the whole range of the light intensities.

At the second measurement, the signal from the SiPM is measured by the picoammeter in the whole range of the light intensities. The model 6487 picoammeter, produced by the Tektronix [58], onboards the feedback ammeter and double-Integrating analogue-to-digital converter. The signal from the SiPM is integrated and converted to the

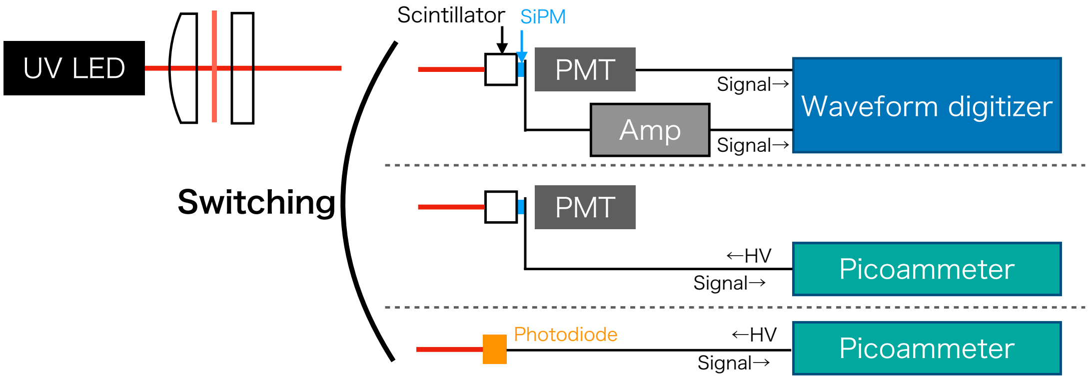

Figure8.5 Readout method for the saturation measurement

current. The dynamic range of the DRS4 is too small to measure the saturation curve at the whole range, but the picoammeter has enough dynamic range.

At the third measurement, the UV light intensity is monitored by the photodiode. The photodiode, S12689-02 produced by Hamamatsu Photonics is used. The S12689-02 is a UV-sensitive photodiode and has large dynamic range enough to monitor the whole range of the light intensities. The signal from the photodiode is measured as current by the picoammeter.

8.2.3 Calibration

The current of the SiPM and photodiode is converted to the number of photoelectrons using the linearity of the SiPM response at the low light intensity. Fig. 8.6 shows the correlation between the current and the number of photoelectrons. The signal from the SiPM is monitored in units of the number of photoelectrons at low light intensity by dividing the measured charge by the single photoelectron gain. The signal is linear against the injected light intensity at low light intensity. The current of the SiPM signal is converted to the N_{det} by multiplying the slope of the correlation by the current. The current of the photodiode is also converted to the N_{seed}.

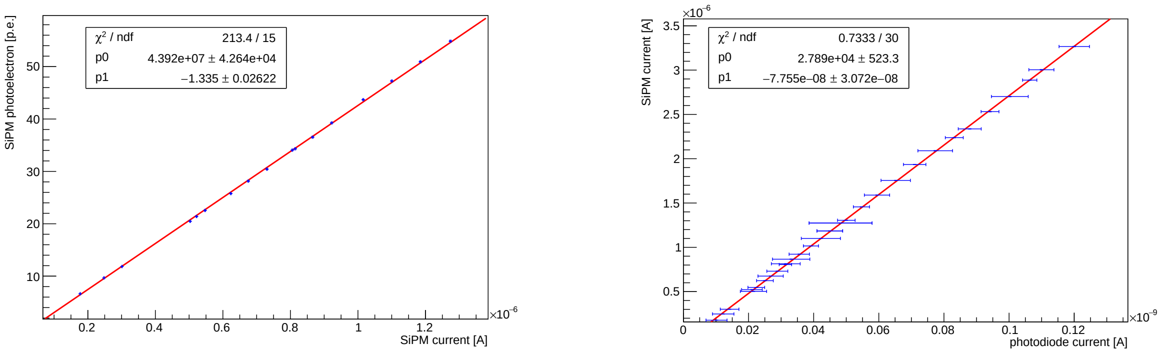

Figure8.6 Correlation between the SiPM current and the number of photoelectrons (left), and correlation between the photodiode current and SiPM current (right).

Fig. 8.7 shows the results of the linearity of the scintillation light emission. The signal from the PMT increases linearly as the intensity of the UV light increases. Then, the linearity of the scintillation light emission is confirmed.

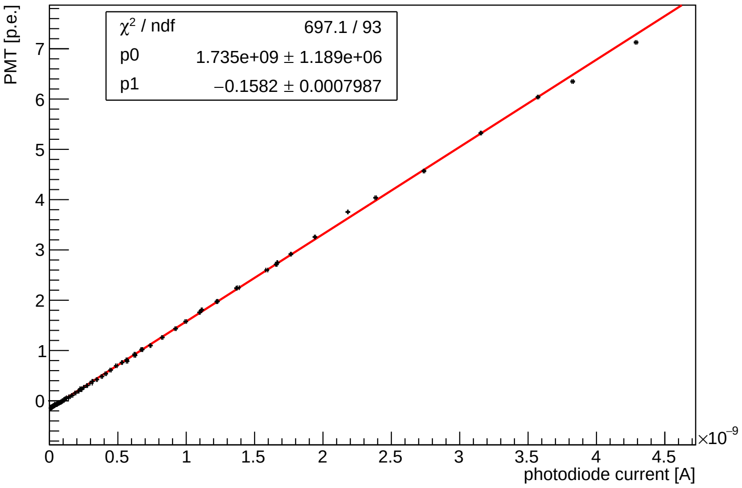

Figure8.7 Linearity of the scintillation light emission measured by the PMT as a function of the photodiode current.

Fig. 8.8 shows the stability of the temperature of the SiPM. The temperature is quite stable during the measurement.

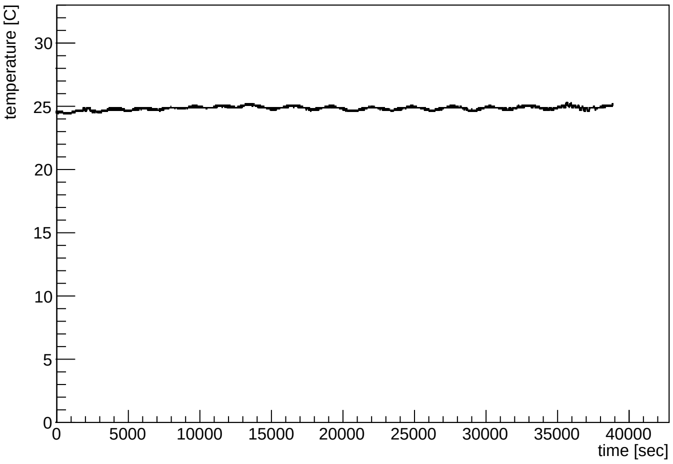

Figure8.8 Stability of the temperature of the SiPM during the measurement.

Fig. 8.9 shows the comparison of the signal waveform derived by the UV light, visible light, β-ray from ^{90}Sr. The waveform with the UV light and β-ray matches well because both the UV and β-ray excite the scintillation light. The waveform with the visible light is different from the others, because the visible light directly injects to the SiPM and makes the waveform sharp. This results show that the UV light excites the scintillation light.

8.2.4 Results

The black plots in Fig. 8.10 show the measured saturation curve using the UV light. A large over-saturation is observed. For comparison, the same measurement is performed with the conventional method using the visible light pulse, as shown in the red plots in Fig. 8.10. There is the significant difference between the saturation curves with the UV light and visible light, and the saturation recovery can be seen at the new method. This shows that the

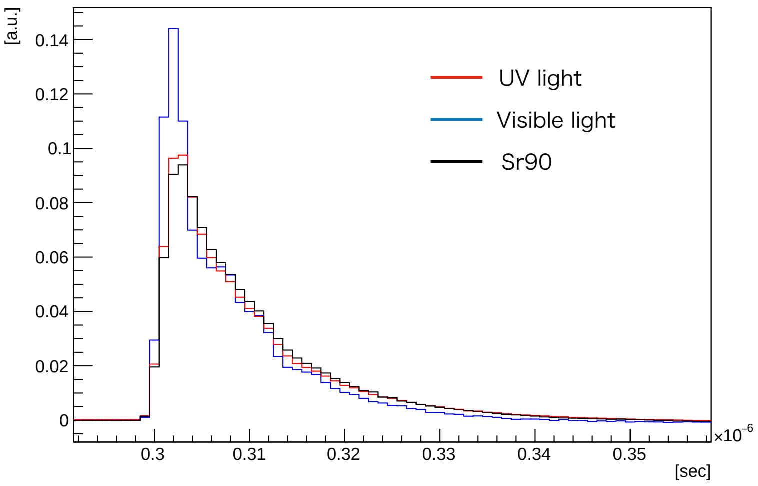

Figure8.9 Comparison of the signal waveform with the UV light (red), visible light (blue), and β-ray from ^{90}Sr.

effect of the time constant of the scintillation light emission has a big effect on the saturation curve.

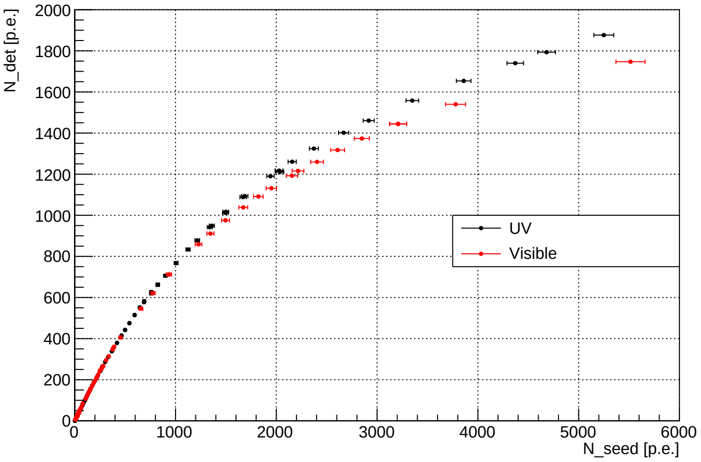

Figure8.10 Saturation curves measured with the UV light (black) and the visible light (red). The number of pixels of the S12571-025P is 1600.

A PLS-500, a similar LED to the PLS-255 with the wavelength of around 500 nm, is used in the conventional method. The pulse widths of the PLS-255 and PLS-500 are about 0.4 ns and 0.9 ns respectively. The effect of the pulse width is not crucial for the new method using the PLS-255, because the pulse width of 0.4 ns is smaller than the recovery time of the SiPM pixel (dozens ns) and the time constant of the scintillation light emission (few ns), and the effect of the pulse width can be convoluted by the scintillation light emission. On the other hand, the effect of the pulse width is crucial to the conventional method using the PLS-500. The pulse width of 0.9 ns is rather larger than the fast laser pulse used in the previous studies [53][54] with the pulse width of few ps to dozens ps. The effect of the pulse width may affect the saturation curve, and is one of the causes of the over-saturation at the conventional method using the PLS-500. However, the difference between the saturation curves with the new method and conventional method is clearly seen, so it's not a problem.

This results can be a big impact on the saturation correction for the detectors using the scintillators and SiPMs.

The conventional method using the visible light pulse doesn't consider the time constant of the scintillation light emission. It doesn't measure the accurate saturation curve, and the saturation correction is not perfect. The new method can provide the saturation curve in the same way in a real situation, and the measured saturation curve can be directly applied to the saturation correction of the Sc-ECAL. This new method can be applied to the other detectors using the scintillators and SiPMs.

The actual saturation curve contains the effect of the time constant of the scintillation light emission, but in usual, the modeling of the saturation including this effect is not sufficiently validated, and the saturation is not corrected accurately. The effect of the scintillation light emission is rather big, so the modeling and correction of the saturation should be validated thoroughly.

8.3 Modeling

A new modeling of the saturation curve is needed for the validation of the new method and for the simplification of the saturation correction. The accurate modeling of the saturation makes it easy to apply to the other detectors using the scintillators and SiPMs. The modeling of the saturation involving the effect of the time constant of the scintillation light emission is not validated. The modeling with the cross-talk and after-pulse and the modeling the response of a recovering SiPM was suggested [53] [59]. However, there is no model that includes all the effects such as the time constant of the scintillation light emission, recovery time of the SiPM, and cross-talk and after-pulse.

A new modeling of the saturation, involving all the effects of the time constant of the scintillation light emission, recovery time of the SiPM, and cross-talk and after-pulse, is developed. Since it is difficult to include time information in statistical methods, the analytical method is used for the modeling. The number of detected photons relative to the number of incident photons is calculated at each event, and the saturation curve is obtained by scanning the number of incident photons. The calculation procedure in the new model is summarized as follows:

- Divide the time periods at 1 event
- Calculate the number of incident photons ΔI at each period
- Calculate the number of detected photons N_{det} at each period
- Sum the N_{det} at all the time periods

8.3.1 Scintillation light emission

The scintillation light emission has the time constant. In case of the EJ-200, the rise time is $\tau_{rise} = 0.9\ ns$ and the decay time is $\tau_{decay} = 2.1\ ns$. The time-dependent function of the scintillation light emission is described as:

$$I(t) = I_0(t) \times \int_t (e^{-u/\tau_{decay}} - e^{-u/\tau_{rise}})du \tag{8.1}$$

where, $I(t)$ is the number of incident photons as a function of the time, and $I_0(t)$ is the initial value depending on time due to the time-dependent function of the UV-LED. The full width at half maximum of the light pulse (FWHM) of the UV-LED is about 0.5 ns as shown in Fig. 8.11. The light pulse is approximated by the Gause function with the FWHM of 0.5 ns:

$$I_0(t) = I_0 e^{-\frac{(t-1.5[\mathrm{ns}])^2}{2(0.5/2.35)^2}} \tag{8.2}$$

where the Gause function is shifted by 1.5 ns to start the analysis from the beginning of the pulse. Then, the time dependent function of the incident photons are described like the convolution of the latter exponential term of Function 8.1 and Function 8.2.

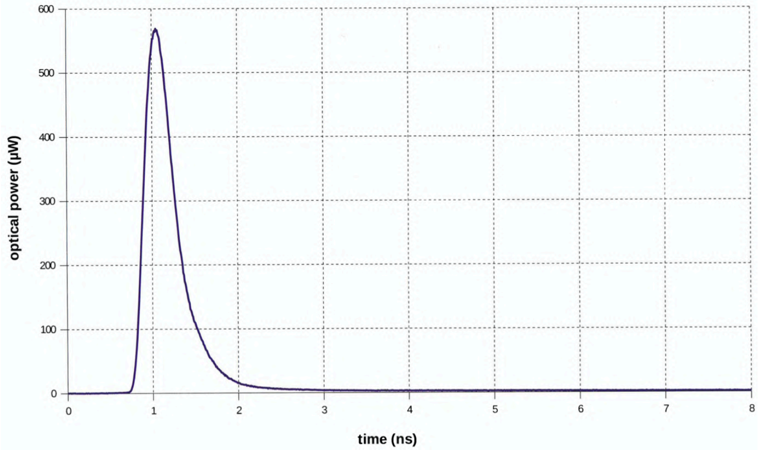

Figure8.11 Light pulse of the UV-LED [55].

The time range for the calculation of the incident photons and detected photons is set from 0 to 100 ns. The time range is divided by 0.1 ns pitch. The number of incident photons is calculated at this time period, and the function at the time of t is written by:

$$\Delta I(t) = \sum_{t_i=0}^{t_i=t} I_0 e^{-\frac{(t_i-1.5[\mathrm{ns}])^2}{2(FWHM/2.35)^2}} \Delta t \times \int_t^{t+\Delta t} (e^{-(u-t_i)/\tau_{decay}} - e^{-(u-t_i)/\tau_{rise}}) du \tag{8.3}$$

where Δt is the pitch of the time period (0.1 ns).

8.3.2 Recovery time for SiPM pixel

When the incident light has a time constant, there is a possibility that a photon will be injected again while the fired pixel is recovering, and this effect must be considered. In that case, an avalanche occurs at a reduced gain. The over-voltage V_{over} of the fired pixel drops to zero, and recovers exponentially with a time constant:

$$V_{over}(t) = V_0(1 - e^{-t/\tau_{rec}}) \tag{8.4}$$

where t is the time from the first pixel trigger, τ_{rec} is the recovery time of the pixel, and V_0 is the initial over-voltage with no photon injection. While the pixel is recovering, the PDE $\varepsilon_{rec}(t)$ and gain $q_{rec}(t)$ depend on the $V_{over}(t)$ almost linearly:

$$\varepsilon_{rec}(t) = \varepsilon_0 \frac{V_{over}(t)}{V_0} \tag{8.5}$$

$$q_{rec}(t) = q_0 \frac{V_{over}(t)}{V_0} \tag{8.6}$$

where ε_0 and q_0 are the PDE and gain with the over-voltage of V_0.

In this model, $\varepsilon_0 = 1$ and $q_0 = 1$. The number of incident photons at a short time period, $\Delta I(t)$, are incident on the SiPM at all, so $\varepsilon_0 = 1$. If a photon injects to the pixel with the over-voltage of V_0, the pixel detects just one photon, so $q_0 = 1$. Then, the number of photons injected to the SiPM, $N_{in}(t)$, and the number of photons detected by the SiPM, $N_{det}(t)$, can be written by:

$$N_{in}(t) = \Delta I(t) \times \varepsilon_{rec}(t) = \Delta I(t) \times (1 - e^{-t/\tau_{rec}}) \tag{8.7}$$

$$N_{det}(t) = \Delta I(t) \times \varepsilon_{rec}(t) \times q_{rec}(t) = \Delta I(t) \times (1 - e^{-t/\tau_{rec}})^2 \tag{8.8}$$

8.3.3 Calculation of number of detected photons

The calculation of $N_{det}(t)$ is performed for each time period. The number of incident photons, $\Delta I(t)$, is calculated at each period, and the number of detected photons are calculated using the $\Delta I(t)$. The pixels which detect photons at t, N_t, and the pixels with no photon injection until t, N_{empty}, is stored at each period. For example, at the first time period of $t = t_0 = 0$ ns,

$$N_{in}(t_0) = \Delta I(t_0) \tag{8.9}$$

$$N_{det}(t_0) = \Delta I(t_0) \tag{8.10}$$

$$N_{empty}(t_0) = N_{pixel} - \Delta I(t_0) \tag{8.11}$$

$$N_{t_0}(t_0) = \Delta I(t_0) \tag{8.12}$$

where N_{pixel} is the number of pixels of the SiPM.

At the second time period of $t = t_1 = 0.1$ ns, the $\Delta I(t_1)$ injects to the SiPM, and the empty pixels (N_{empty}) can detect the injected photons, but the fired pixel (N_{t_0}) must consider the effect of the pixel recovery. The pixels which detect photons at t_1, N_{t_1}, is stored apart from N_{t_0}. The N_{empty} and N_{t_0} are updated by subtracting the number of photons injected at t_1. Then, at $t = t_1 = 0.1$ ns,

$$N_{in}(t_1) = \Delta I(t_1) \times \frac{N_{empty}}{N_{pixel}} + \Delta I(t_1) \times \frac{N_{t_0}(t_0)}{N_{pixel}} \times (1 - e^{-(t_1 - t_0)/\tau_{rec}}) \tag{8.13}$$

$$N_{det}(t_1) = \Delta I(t_1) \times \frac{N_{empty}}{N_{pixel}} + \Delta I(t_1) \times \frac{N_{t_0}(t_0)}{N_{pixel}} \times (1 - e^{-(t_1 - t_0)/\tau_{rec}})^2 \tag{8.14}$$

$$N_{empty}(t_1) = N_{empty}(t_0) - \Delta I(t_1) \times \frac{N_{empty}}{N_{pixel}} \tag{8.15}$$

$$N_{t_0}(t_1) = N_{t_0}(t_0) - \Delta I(t_1) \times \frac{N_{t_0}(t_0)}{N_{pixel}} \times (1 - e^{-(t_1 - t_0)/\tau_{rec}}) \tag{8.16}$$

$$N_{t_1}(t_1) = N_{in}(t_1) \tag{8.17}$$

where $\frac{N_{empty}}{N_{pixel}}$ is the probability that $\Delta I(t_1)$ injects to the empty pixels, and $\frac{N_{t_0}}{N_{pixel}}$ is the probability that $\Delta I(t_1)$ injects to the pixels fired at t_0.

The gradual expression at the time period t, where t' is the time period just before t, $t' = t - 0.1$, is described as:

$$\Delta I(t) = \sum_{t_i=0}^{t_i=t} I_0 e^{-\frac{(t_i-1.5[\mathrm{ns}])^2}{2(FWHM/2.35)^2}} \Delta t \times \int_t^{t+\Delta t} (e^{-(u-t_i)/\tau_{decay}} - e^{-(u-t_i)/\tau_{rise}}) du \tag{8.18}$$

$$N_{in}(t) = \Delta I(t) \times \frac{N_{empty}}{N_{pixel}} + \sum_{t_i=0}^{t_i=t'} \Delta I(t) \times \frac{N_{t_i}(t')}{N_{pixel}} \times (1 - e^{-(t-t_i)/\tau_{rec}}) \tag{8.19}$$

$$N_{det}(t) = \Delta I(t) \times \frac{N_{empty}}{N_{pixel}} + \sum_{t_i=0}^{t_i=t'} \Delta I(t) \times \frac{N_{t_i}(t')}{N_{pixel}} \times (1 - e^{-(t-t_i)/\tau_{rec}})^2 \tag{8.20}$$

$$N_{empty}(t) = N_{empty}(t') - \Delta I(t) \times \frac{N_{empty}}{N_{pixel}} \times (1 - e^{-(t-t_i)/\tau_{rec}}) \tag{8.21}$$

$$N_{t_i}(t) = N_{t_i}(t') - \Delta I(t) \times \frac{N_{t_i}(t')}{N_{pixel}} \times (1 - e^{-(t-t_i)/\tau_{rec}}) \tag{8.22}$$

$$N_t(t) = N_{in}(t) \tag{8.23}$$

These steps are repeated to calculate $N_{det}(t)$ at each time period. As a result, the total number of incident photons and detected photons are written by:

$$N_{int} = \sum_{t_i=0}^{t_i=100\ \mathrm{ns}} \Delta I(t_i) \tag{8.24}$$

$$N_{det} = \sum_{t_i=0}^{t_i=100\ \mathrm{ns}} N_{det}(t_i) \tag{8.25}$$

The saturation curve is obtained by scanning the initial value of the incident photons, I_0. The saturation curve considering the effect of the time constant of the scintillation light emission and the SiPM recovery can be obtained by this method.

8.3.4 Cross-talk

The effect of the cross-talk is implemented to this model. The SiPM causes a crosstalk with a certain probability, P_{CT}, resulting in a state where infrared photons are detected in surrounding pixels. The number of infrared photons caused by the cross-talk depend on the number of photons injected by the scintillation emission. The detected photons by the scintillation emission and those by the cross-talk are calculated separately and summed up. For example, at $t = t_0 = 0$ ns,

$$N_{in}(t_0) = \Delta I(t_0) \tag{8.26}$$

$$\Delta I_{CT}(t_0) = N_{in}(t_0) \times (P_{CT} + P_{CT}^2 + \cdots + P_{CT}^9) \tag{8.27}$$

$$N_{det}(t_0) = (N_{det}\ \text{Calculation using}\ \Delta I(t_0)) + (N_{det}\ \text{Calculation using}\ \Delta I_{CT}(t_0)) \tag{8.28}$$

where $\Delta I_{CT}(t_0)$ is the number of incident photons caused by the cross-talk, and $(P_{CT} + P_{CT}^2 + \cdots)$ considers the second-, third-, $\cdots$, ninth-order effects of the cross-talk.

At $t = t_1 = 0.1$ ns,

$$N_{in}(t_1) = \Delta I(t_1) \times \frac{N_{empty}}{N_{pixel}} + \Delta I(t_1) \times \frac{N_{t_0}(t_0)}{N_{pixel}} \times (1 - e^{-(t_1-t_0)/\tau_{rec}}) \tag{8.29}$$

$$\Delta I_{CT}(t_1) = N_{in}(t_1) \times (P_{CT} + P_{CT}^2 + \cdots) \tag{8.30}$$

$$N_{det}(t_2) = (N_{det}\ \text{Calculation using}\ \Delta I(t_1)) + (N_{det}\ \text{Calculation using}\ \Delta I_{CT}(t_1)) \tag{8.31}$$

The gradual expression of the model at the time period t, where t' is the time period just before t, $t' = t - 0.1$, is described as:

$$N_{in}(t) = \Delta I(t) \times \frac{N_{empty}}{N_{pixel}} + \sum_{t_i=0}^{t_i=t'} \Delta I(t) \times \frac{N_{t_i}(t')}{N_{pixel}} \times (1 - e^{-(t-t_i)/\tau_{rec}}) \tag{8.32}$$

$$N_{det}(t) = \Delta I(t) \times \frac{N_{empty}}{N_{pixel}} + \sum_{t_i=0}^{t_i=t'} \Delta I(t) \times \frac{N_{t_i}(t')}{N_{pixel}} \times (1 - e^{-(t-t_i)/\tau_{rec}})^2 \tag{8.33}$$

$$N_{empty}(t) = N_{empty}(t') - \Delta I(t) \times \frac{N_{empty}}{N_{pixel}} \times (1 - e^{-(t-t_i)/\tau_{rec}}) \tag{8.34}$$

$$N_{t_i}(t) = N_{t_i}(t') - \Delta I(t) \times \frac{N_{t_i}(t')}{N_{pixel}} \times (1 - e^{-(t-t_i)/\tau_{rec}}) \tag{8.35}$$

$$\Delta I_{CT}(t) = N_{in}(t) \times (P_{CT} + P_{CT}^2 + \cdots) \tag{8.36}$$

$$N_{in}(t) = N_{in}(t) + \Delta I_{CT}(t) \times \frac{N_{empty}}{N_{pixel}} + \sum_{t_i=0}^{t_i=t'} \Delta I_{CT}(t) \times \frac{N_{t_i}(t)}{N_{pixel}} \times (1 - e^{-(t-t_i)/\tau_{rec}}) \tag{8.37}$$

$$N_{det}(t) = N_{det}(t) + \Delta I_{CT}(t) \times \frac{N_{empty}}{N_{pixel}} + \sum_{t_i=0}^{t_i=t'} \Delta I_{CT}(t) \times \frac{N_{t_i}(t)}{N_{pixel}} \times (1 - e^{-(t-t_i)/\tau_{rec}})^2 \tag{8.38}$$

$$N_{empty}(t) = N_{empty}(t) - \Delta I_{CT}(t) \times \frac{N_{empty}}{N_{pixel}} \times (1 - e^{-(t-t_i)/\tau_{rec}}) \tag{8.39}$$

$$N_{t_i}(t) = N_{t_i}(t) - \Delta I_{CT}(t) \times \frac{N_{t_i}(t)}{N_{pixel}} \times (1 - e^{-(t-t_i)/\tau_{rec}}) \tag{8.40}$$

$$N_t(t) = N_{in}(t) \tag{8.41}$$

In this way, the effect of the cross-talk is implemented to the model by adding the N_{det} calculation at each time period using the number of infrared photons caused by the cross-talk.

8.3.5 After-pulse

The effect of the after-pulse is also implemented. The after-pulse occurs with a certain probability P_{AP} and time period τ_{AP}:

$$N_{AP}(t) = P_{AP} \frac{1}{\tau_{AP}} e^{-t/\tau_{AP}} \tag{8.42}$$

where $N_{AP}(t)$ is the number of photons (avalanches) caused by the after-pulse. The number of photons caused by the after-pulse depend on the number of fired photons and the time difference from the first photon injection. For example, at $t = t_0 = 0$ ns, there is no after-pulse. At $t = t_1 = 0.1$ ns,

$$N_{AP}(t_1) = N_{t_0} \times P_{AP} \frac{1}{\tau_{AP}} e^{-(t_1-t_0)/\tau_{AP}} \tag{8.43}$$

$$N_{t_0}(t_1) = N_{t_0}(t_0) - N_{t_0}(t_0) \times P_{AP} \frac{1}{t_{AP}} e^{-(t_1-t_0)/\tau_{AP}} \tag{8.44}$$

$$N_{det}(t_1) = (N_{det} \text{ Calculation using } \Delta I(t_1) \& N_{t_0}(t_1)) + N_{AP}(t_1) \times (1 - e^{-(t_1-t_0)/\tau_{rec}})^2 \tag{8.45}$$

Since $N_{AP}(t_1)$ is treated as pixels fired at t_1, N_{t_0} is updated by subtracting $N_{AP}(t_1)$. The number of detected photons by after-pulse is also affected by the pixel recovery, so the PDE and gain dependence is considered. Then the total number of detected photons at t_1 is sum of the N_{det} calculated by the $\Delta I(t_1)$ using updated N_{t_0}, and the N_{det} calculated by the $N_{AP}(t_1)$.

The gradual expression of the model at the time period t, where t' is the time period just before t, $t' = t - 0.1$, is described as:

$$N_{AP}(t) = \sum_{t_i=0}^{t_i=t'} N_{t_i} \times P_{AP} \frac{1}{\tau_{AP}} e^{-(t-t_i)/\tau_{AP}} \tag{8.46}$$

$$N_{empty}(t) = N_{empty}(t') \tag{8.47}$$

$$N_{t_i}(t) = N_{t_i}(t') - N_{t_i}(t') \times P_{AP} \frac{1}{t_{AP}} e^{-(t-t_i)/\tau_{AP}} \tag{8.48}$$

$$N_{in}(t) = \Delta I(t) \times \frac{N_{empty}}{N_{pixel}} + \sum_{t_i=0}^{t_i=t'} \Delta I(t) \times \frac{N_{t_i}(t)}{N_{pixel}} \times (1 - e^{-(t-t_i)/\tau_{rec}}) + \sum_{t_i=0}^{t_i=t'} N_{AP}(t_i) \times (1 - e^{-(t-t_i)/\tau_{rec}}) \tag{8.49}$$

$$N_{det}(t) = \Delta I(t) \times \frac{N_{empty}}{N_{pixel}} + \sum_{t_i=0}^{t_i=t'} \Delta I(t) \times \frac{N_{t_i}(t)}{N_{pixel}} \times (1 - e^{-(t-t_i)/\tau_{rec}})^2 + \sum_{t_i=0}^{t_i=t'} N_{AP}(t_i) \times (1 - e^{-(t-t_i)/\tau_{rec}})^2 \tag{8.50}$$

$$N_{empty}(t) = N_{empty}(t) - \Delta I(t) \times \frac{N_{empty}}{N_{pixel}} \tag{8.51}$$

$$N_{t_i}(t) = N_{t_i}(t) - \Delta I(t) \times \frac{N_{t_i}(t)}{N_{pixel}} \times (1 - e^{-(t-t_i)/\tau_{rec}}) \tag{8.52}$$

$$N_t(t) = N_{in}(t) \tag{8.53}$$

In this way, the effect of the after-pulse is implemented to the model by adding the N_{det} calculation at each time period using the number of photons caused by the after-pulse.

8.3.6 Model

The new saturation model is completed combining all the effects described in the previous sections. The time period for the calculation can be adjusted according to the SiPM types. In case of the comparison with the measurement using the S12571-015P, it is set as 100 ns divided by 0.1 ns pitch. The gradual expression of the model at the time period t, where t' is the time period just before t, $t' = t - 0.1$, is described as:

$$\Delta I(t) = \sum_{t_i=0}^{t_i=t} I_0 e^{-\frac{(t_i-1.5[\mathrm{ns}])^2}{2(FWHM/2.35)^2}} \Delta t \times \int_t^{t+\Delta t} (e^{-(u-t_i)/\tau_{decay}} - e^{-(u-t_i)/\tau_{rise}}) du \tag{8.54}$$

$$N_{AP}(t) = \sum_{t_i=0}^{t_i=t'} N_{t_i} \times P_{AP} \frac{1}{t_{AP}} e^{-(t-t_i)/\tau_{AP}} \tag{8.55}$$

$$N_{empty}(t) = N_{empty}(t') \tag{8.56}$$

$$N_{t_i}(t) = N_{t_i}(t') - N_{t_i}(t') \times P_{AP} \frac{1}{t_{AP}} e^{-(t-t_i)/\tau_{AP}} \tag{8.57}$$

$$N_{in}(t) = \Delta I(t) \times \frac{N_{empty}}{N_{pixel}} + \sum_{t_i=0}^{t_i=t'} \Delta I(t) \times \frac{N_{t_i}(t)}{N_{pixel}} \times (1 - e^{-(t-t_i)/\tau_{rec}}) + \sum_{t_i=0}^{t_i=t'} N_{AP}(t_i) \times (1 - e^{-(t-t_i)/\tau_{rec}}) \tag{8.58}$$

$$N_{det}(t) = \Delta I(t) \times \frac{N_{empty}}{N_{pixel}} + \sum_{t_i=0}^{t_i=t'} \Delta I(t) \times \frac{N_{t_i}(t)}{N_{pixel}} \times (1 - e^{-(t-t_i)/\tau_{rec}})^2 + \sum_{t_i=0}^{t_i=t'} N_{AP}(t_i) \times (1 - e^{-(t-t_i)/\tau_{rec}})^2 \tag{8.59}$$

$$N_{empty}(t) = N_{empty}(t) - \Delta I(t) \times \frac{N_{empty}}{N_{pixel}} \tag{8.60}$$

$$N_{t_i}(t) = N_{t_i}(t) - \Delta I(t) \times \frac{N_{t_i}(t)}{N_{pixel}} \times (1 - e^{-(t-t_i)/\tau_{rec}}) \tag{8.61}$$

$$\Delta I_{CT}(t) = N_{in}(t) \times (P_{CT} + P_{CT}^2 + \cdots) \tag{8.62}$$

$$N_{in}(t) = N_{in}(t) + \Delta I_{CT}(t) \times \frac{N_{empty}}{N_{pixel}} + \sum_{t_i=0}^{t_i=t'} \Delta I_{CT}(t) \times \frac{N_{t_i}(t)}{N_{pixel}} \times (1 - e^{-(t-t_i)/\tau_{rec}}) \tag{8.63}$$

$$N_{det}(t) = N_{det}(t) + \Delta I_{CT}(t) \times \frac{N_{empty}}{N_{pixel}} + \sum_{t_i=0}^{t_i=t'} \Delta I_{CT}(t) \times \frac{N_{t_i}(t)}{N_{pixel}} \times (1 - e^{-(t-t_i)/\tau_{rec}})^2 \tag{8.64}$$

$$N_{empty}(t) = N_{empty}(t) - \Delta I_{CT}(t) \times \frac{N_{empty}}{N_{pixel}} \tag{8.65}$$

$$N_{t_i}(t) = N_{t_i}(t) - \Delta I_{CT}(t) \times \frac{N_{t_i}(t)}{N_{pixel}} \times (1 - e^{-(t-t_i)/\tau_{rec}}) \tag{8.66}$$

$$N_t(t) = N_{in}(t) \tag{8.67}$$

Then, the total number of incident photons by the scintillation emission I and detected photons by the SiPM N_{det} are described as:

$$I = \sum_{t_i=0}^{t_i=100} \Delta I(t) \tag{8.68}$$

$$N_{det} = \sum_{t_i=0}^{t_i=100} N_{det}(t) \tag{8.69}$$

The saturation curve can be obtained by scanning the initial value of the scintillation emission I_0. The new saturation model including all the effects of the time constant of the scintillation emission, recovery time, cross-talk and after-pulse is developed.

8.4 Comparison between measurement and model

The comparison between the measurement and the model is performed to confirm the validity of the new method for the saturation measurement. The key parameters of the model are obtained by separate measurements for the accurate comparison. This section gives the measurements of the parameters of the SiPM, and the results of the comparison.

8.4.1 Measurements of the cross-talk, after-pulse, and recovery time

In order to complete the saturation model, the properties of the SiPM used in the measurement should be measured and applied to the model. The parameters of the SiPM used in the saturation measurement are measured using dark noise events. The measurement uses the waveform digitizer, and Fig. 8.12 shows a typical waveform of a dark noise as the first pulse, and an after-pulse as the second pulse. The probability of the cross-talk is measured by the height distribution of the first pulse where the height is calculated in the range of the fast component of the first signal as represented by the red arrow. The after-pulse and recovery time is calculated using the height of the after-pulse and the time difference between the first pulse and the after-pulse, so the slow component of the first pulse as represented by the blue arrow is also analyzed.

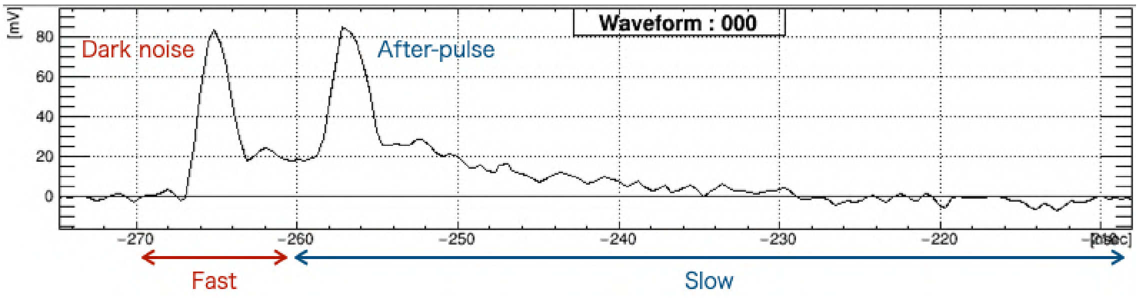

Figure8.12 Waveform of a dark noise of the SiPM with an after-pulse.

Fig. 8.13 shows the distribution of the height of the first pulse. The probability of the cross-talk P_{CT} is calculated by:

$$P_{CT} = \frac{N_{>1.5\ \mathrm{p.e.}}}{N_{>0.5\ \mathrm{p.e.}}} \tag{8.70}$$

where $N_{>0.5\ \mathrm{p.e.}}$ and $N_{>1.5\ \mathrm{p.e.}}$ is the number of events more than 0.5 p.e. and 1.5 p.e. respectively. The probability of the cross-talk of the SiPM used in the saturation measurement is $P_CT = 33.7 \pm 1.7\%$.

Fig. 8.14 shows the distribution of the time difference between the first pulse and after-pulse. The time difference is calculated by the peak times for each pulse. The after-pulse probability P_{AP} and time constant τ_{AP} are calculated by:

$$N_{AP} = P_{AP}\frac{1}{\tau_{AP}}e^{-t/\tau_{AP}} * N_{event} * t_{bin} \tag{8.71}$$

where the total number of events N_{event} and bin width t_{bin} is multiplied by the function of the after-pulse. There is effect of the dark noise, but it can be ignored because it is small enough compared to the after-pulse. The distribution of the time difference is fitted by this function. The probability of the after-pulse is $P_{AP} = 4.0 \pm 0.4\%$, and the time constant of the after-pulse is $\tau_{AP} = 10.3 \pm 1.0$ ns.

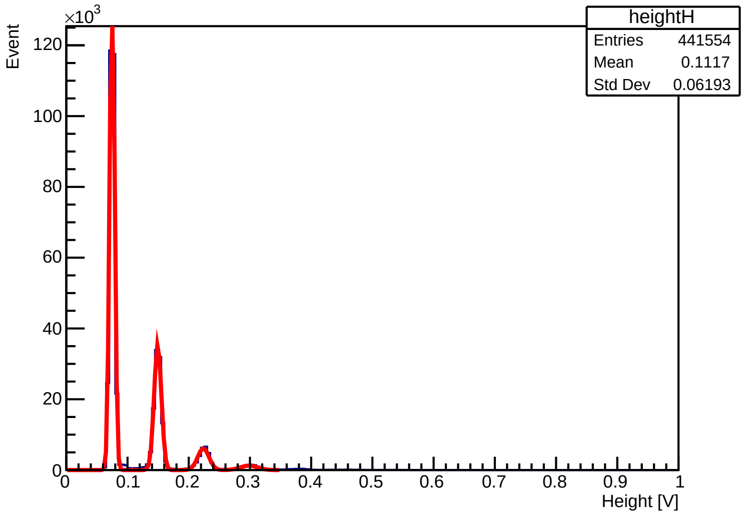

Figure8.13 Distribution of the height of the first pulse by the dark noise. The spectrums of 1 p.e., 2 p.e., etc are clearly separated, and fitted by the multi-gaussian.

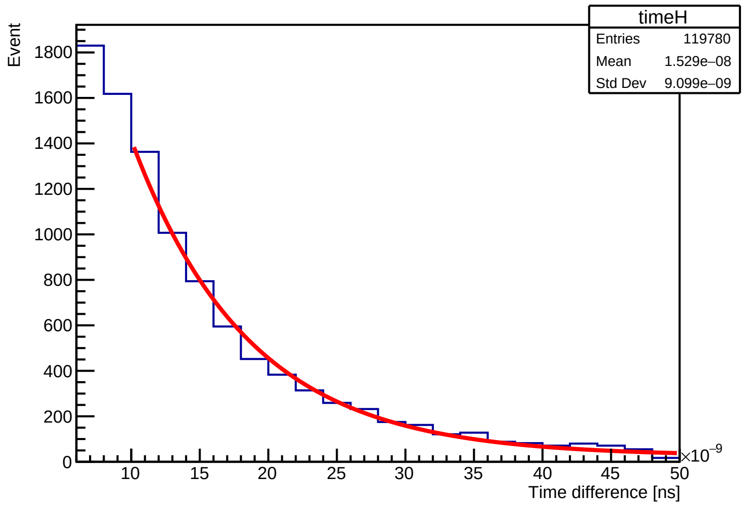

Figure8.14 Distribution of the difference of the peak time between the first pulse and after-pulse. The distribution is fitted by the function for the after-pulse.

Fig. 8.15 shows the 2D scatter plot of the time difference and the height of the after-pulse. The recovery time is calculated by:

$$h_{1\ \mathrm{p.e.}}(1 - e^{-t/\tau_{rec}}) \tag{8.72}$$

where $h_{1\ \mathrm{p.e.}}$ is the height of the 1 p.e. spectrum. The scatter plot is fitted by this function using the $h_{1\ p.e.}$ obtained by Fig. 8.13. The recovery time is $\tau_{rec} = 7.38 \pm 0.05$ ns.

8.4.2 Comparison with measured saturation curve

A comparison between the saturation curve measured in Section 8.2 and the new model is performed. The time constants of the scintillator is used as the catalogue value, the rise time is $\tau_{rise} = 0.9\ ns$, and the decay time is

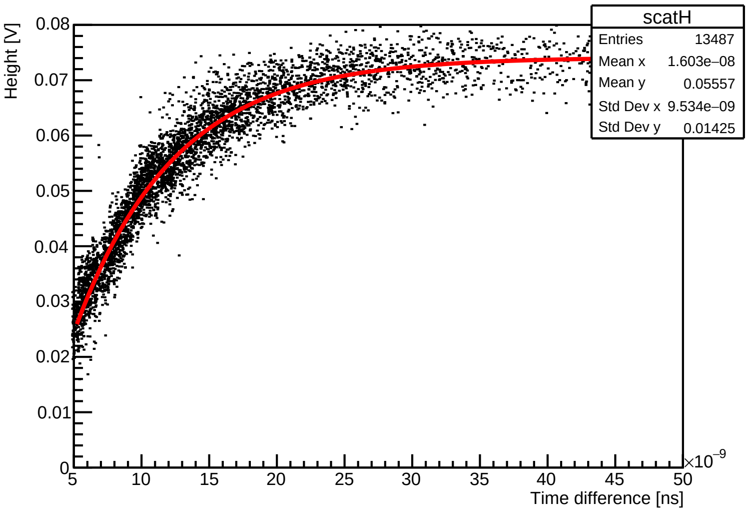

Figure8.15 Scatter plot of the peak time difference between the first pulse and after-pulse vs. the height of the after-pulse.

$\tau_{decay} = 2.1\ ns$. Fig. 8.16 shows the comparison with the measurement and model. A slight deviation can be seen, so the time constants are adjusted since the time constants can change due to the characteristics of the scintillator. The time constants are optimized by taking the minimum of the sum of the chi square at each measurement point. Fig. 8.17 shows the saturation model with the optimized time constants with $\tau_{rise} = 1.3\ ns$ and $\tau_{decay} = 2.6\ ns$. The saturation model match well with the measured saturation curve. Therefore, taking into account the possible uncertainty of the time constant of the scintillation emission, the new saturation model describes very well the measured saturation curve.

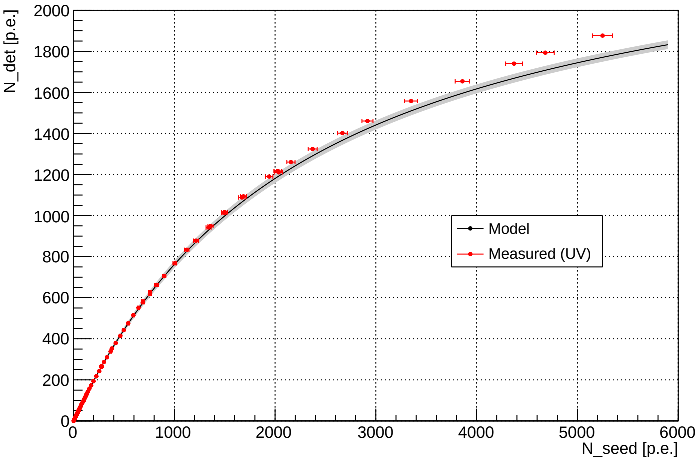

Figure8.16 Saturation curves measured with the UV light (red) and the model (black) using the catalogue value as the time constants of the scintillator. The gray belt shows the effects of the errors of the SiPM parameters

The same comparison is performed with the saturation curve using the visible light. The new saturation model can describe the saturation curve measured by the visible light by turning off the effect of the scintillation light emission. In order to check the validity of the new method for the saturation measurement and modeling in more detail, the comparison of the saturation curve with visible light between the measurement and model is performed.

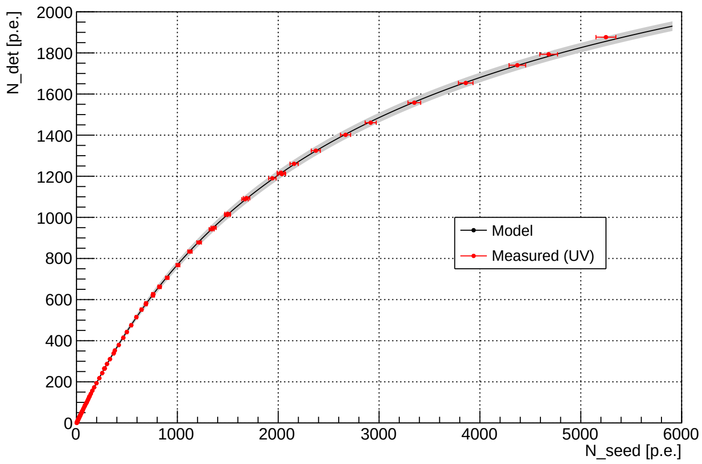

Figure8.17 Saturation curves measured with the UV light (red) and the model (black) using the optimized time constants of the scintillator.

In case of visible light, the time constant of the scintillation emission is not considered, but the visible light from the PLS-500 has the pulse width with the FWHM of the 0.9 ns. Fig. 8.18 shows the comparison with measurement and model using the visible light. The model matches with the measured saturation curve at low light intensities, but doesn't match at high intensities. The pulse width is adjusted to search for the reason of this unmatched result. Fig. 8.19 shows the saturation model with the optimized pulse width of 2.0 ns. The saturation model match with the measured saturation curve, so the pulse width of the visible light may cause the over-saturation and mismatch with the model.

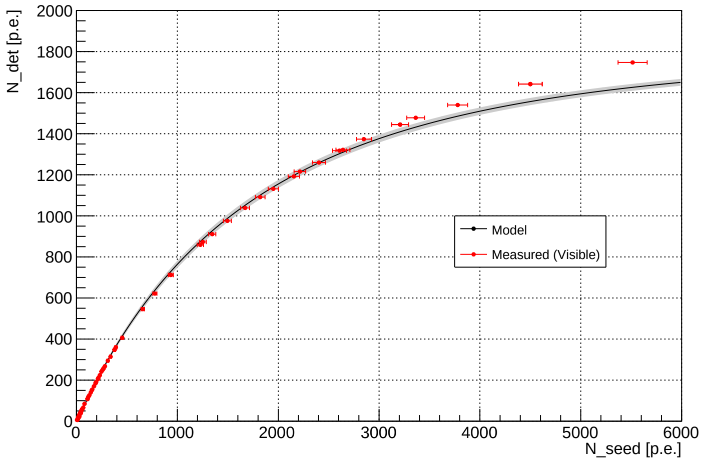

Figure8.18 Saturation curves measured with the visible light (red) and the model (black) using the catalogue value as the pulse width.

Fig. 8.20 shows the comparison of the saturation curves between the UV light, visible light, and the conventional method. The saturation curve with the conventional method is obtained by the model without the pulse width of the visible light assuming the fast visible light. There is the significant difference between the saturation curves

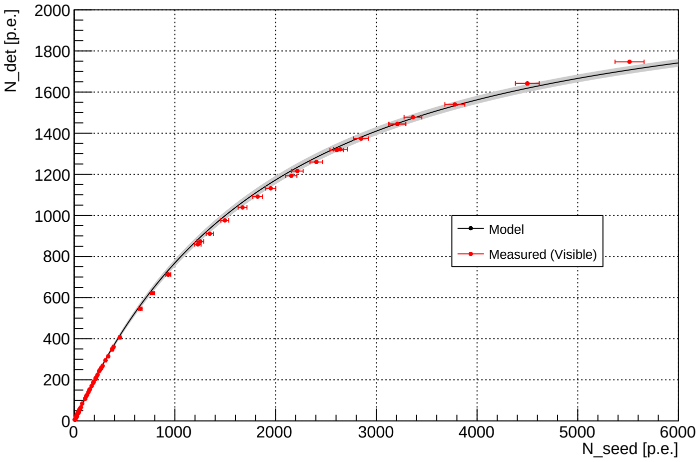

Figure8.19 Saturation curves measured with the visible light (red) and the model (black) using the optimized pulse width.

with the new method using the UV light and with the conventional method, and the larger saturation recovery can be seen at the new method, compared to the comparison between the saturation curves using the UV light and the visible light from the PLS-500.

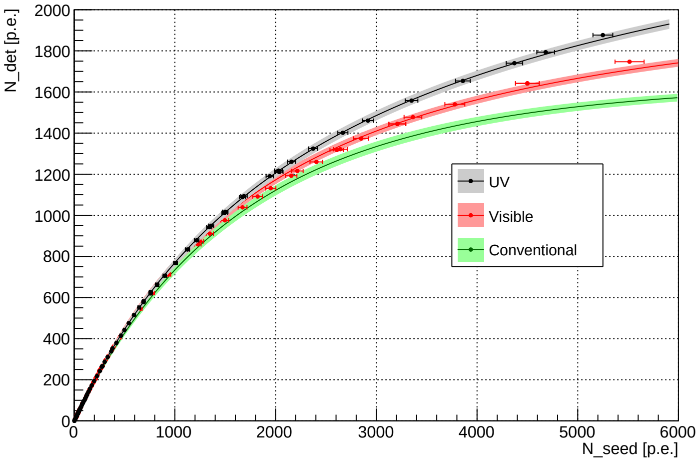

Figure8.20 Saturation curves in the measurement and model with the UV light (black), the visible (red), and the conventional method.

In summary, the new saturation model describes the measured saturation curve very well. It can correct accurately the saturation curve at the detector using the SiPM and scintillator, and be possible to develop a new calibration method, such as directly measuring the saturation curve by injecting the UV light to the actual system. The model reproduces the actual saturation curve including the time constant of the scintillation emission, recovery time, cross-talk and after-pulse, and turn these effects on and off. By changing the model parameters for the SiPM and scintillator, the model can be easily applied to various systems with scintillator and SiPM. It has a big impact on the calibration and saturation correction for the SiPM and scintillator techniques involving the Sc-ECAL.

Chapter 9

Evaluation of jet energy resolution

The jet energy resolution is revisited using the full simulation model for the ILD, based on the performance of the Sc-ECAL studied in this work. The reasonable jet energy resolution is obtained based on the results of this work. In addition, the effects of the saturation model and the pixel pitch of the SiPM on the jet energy resolution are evaluated. This chapter gives the results of the evaluation of the jet energy resolution using the full detector simulation.

9.1 iLCSoft [60]

The iLCSoft is a widely used software suitable for the simulation and analysis of the linear colliders. It is used to prepare for the future linear collider projects such as the ILC. The iLCSoft is used for the performance evaluation of the detector models and physics studies. Based on the actual layout of the detectors, detailed simulations of all the components and their reactions can be performed using Geant4 and reconstruction algorithms. The full MC simulation samples can be used to study the performance of the detectors and physics.

The main components of iLCSoft can be divided into the event data model LCIO, the toolkit DD4hep for describing detector geometry, and the application framework Marlin, as shown in Fig. 9.1. This section gives an overview of each component and the central algorithm PandoraPFA.

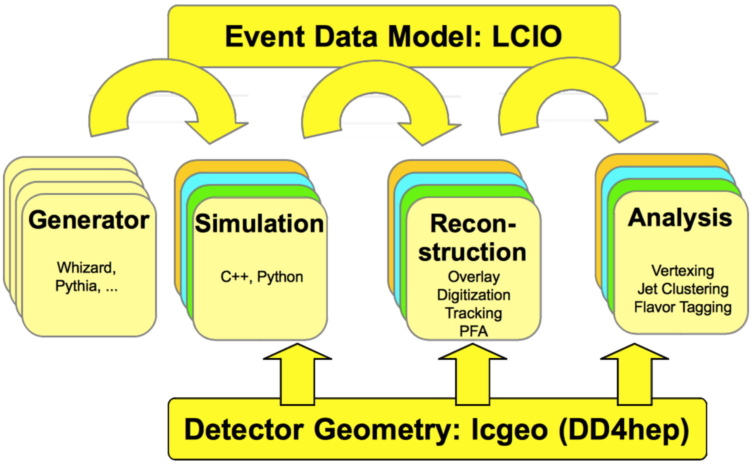

Figure9.1 The main components of the iLCSoft and their flow [60]

9.1.1 Linear Collider I/O (LCIO)

Fig. 9.2 shows the overview of the LCIO data model. The LCIO is a hierarchical data model, from Monte Carlo information to tracker and calorimeter hits, and from reconstructed particle information to tracks, clusters, and vertexes. The LCIO event data model is in a common data format that can be used throughout the linear collider community and in detector test beam experiments.

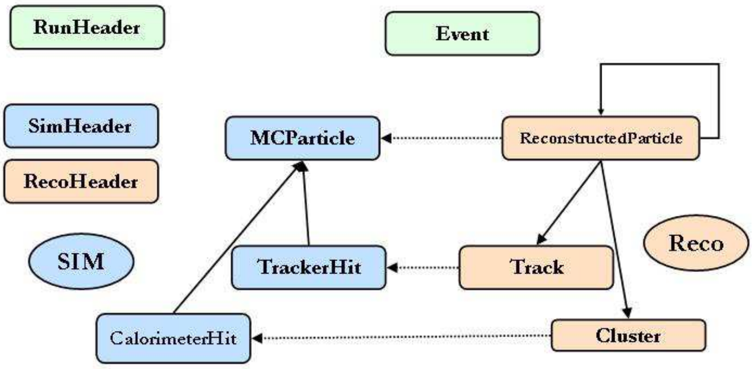

Figure9.2 Overview of the data model as defined by LCIO [61]. Each square corresponds to a different data entry or class, and the arrows correspond to the relationships between them.

9.1.2 Detector Description toolkit for high energy physics (DD4hep)

In high-energy physics experiments, it is essential to describe the geometry of the detector and the properties of its materials in a detailed and realistic manner. This is evident in Monte Carlo simulations, where information about the location, shape, and composition of each detector component is necessary to accurately understand the response of the detector and the underlying physics. For digitization and reconstruction processes, it is equally important to accurately describe the detector geometry, which should ideally be generated from the same source to avoid inconsistencies.

The DD4hep is developed to meet these requirements, and uses the same detector model with the same geometry for all simulation, digitization, reconstruction, and analysis. Fig. 9.3 shows the components of the DD4hep. The detector is described through a C++ constructor, and detailed parameters can be set in xml. The package also includes the lcgeo, a sub-package of the detector model for linear colliders, and the ddsim, a python program to run the full simulation.

The DD4hep is a general geometry toolkit based on the ROOT and Geant4, which are widely used in high energy experiments. The DD4hep is developed primarily for linear accelerator projects, but is designed to support experiments from start to finish. This means that it is applicable from the preparation stage of an experiment to the running experiment.

9.1.3 Modular Analysis and Reconstruction for LINear Collider (Marlin)

The Marlin is an application framework that uses C++ as the reference language and is used throughout the iLCSoft. Fig. 9.4 shows the components of the DD4hep. The process of the digitization, reconstruction, and

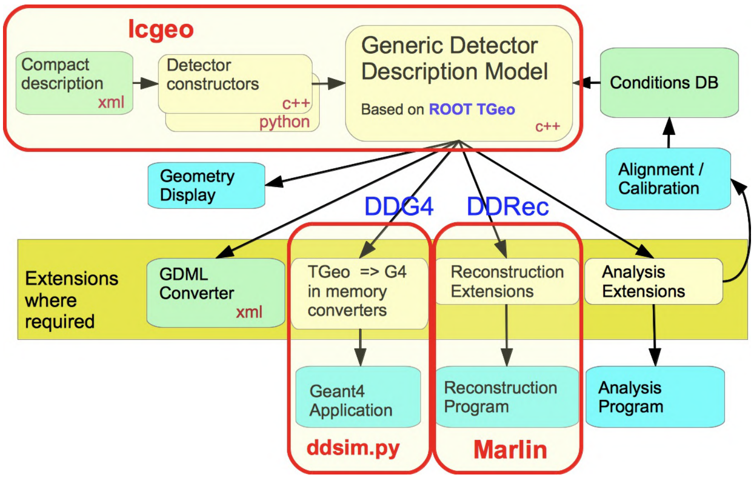

Figure9.3 Components of DD4hep and their flow [60]

analysis is implemented as a processor, and can be executed in an integrated manner.

Digitization

The hit information obtained from the DD4hep is given in the form of an energy deposit that each particle drops into its respective detector. The digitization is the process of digitizing the hit information into signals from the detectors, which are output in the same format as the experimental data, including the effects of noise and saturation. Then, the simulation and the experimental data are compatible and can be compared and verified. In the digitization of the calorimeter, there are parameters such as the energy fraction in the detection layer among the total energy deposit and the MIP response of the detector, which are calibrated using gamma-rays, K_L^0, and muons of specific energy.

Reconstruction

The reconstruction is to reconstruct the events from the hit information of the experimental data or the simulation data after digitization. In the calorimeter, the energy dropped by the particle is reconstructed from the magnitude of the signal, and these are reconstructed using the pandoraPFA.

PandoraPFA [24]

The PandoraPFA is an event reconstruction algorithm based on the PFA. It makes clustering from tracks and calorimeter hits to create a list of reconstructed particles called Particle Flow Objects (PFOs). The parameters of PandoraPFA include "correlation between the detected energy and the number of MIPs", and "correlation between MIPs and GeV". These parameters are also calibrated using gamma-rays, K_L^0, and muons of specific energy.

9.2 Simulation

The jet energy resolution of the ILD is evaluated using the configuration of the calorimeter option with the Sc-ECAL and the AHCAL. The impacts of the saturation model and the SiPM types are also evaluated. This section gives the setup of the simulation, the results of the evaluation of the jet energy resolution.

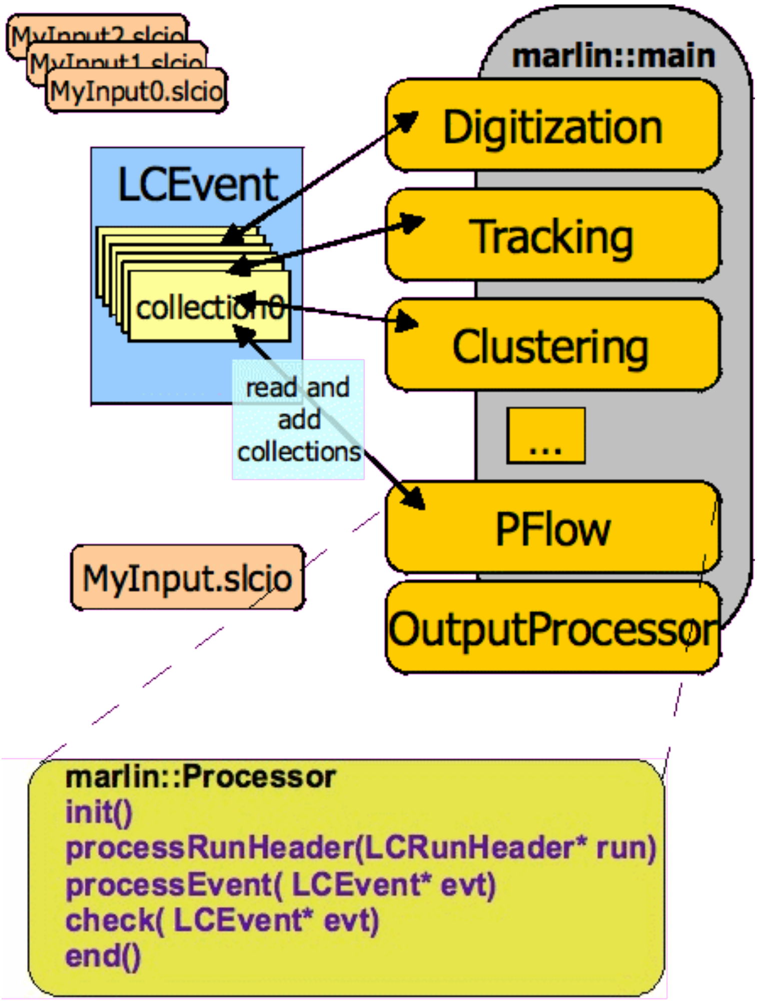

Figure9.4 Components of Marlin [60]

9.2.1 Setup

The version of the ILD model at the DD4hep is ILD_l5_o3_v02, which is based on the Sc-ECAL and scintillator-based analogue HCAL (AHCAL). The configuration of the Sc-ECAL is basically the same as the technological prototype, but the only difference is the strip geometry of 5 mm × 45 mm × 1.5 mm. This is because the ILD model includes both the scintillator and silicon sensors for the Sc-ECAl and Si-ECAL respectively to compare two models, so the sensor thickness is set to be a bit smaller due to the space limit. The energy is corrected to calibrate the thickness from 1.5 mm to 2.0 mm.

Some parameters at the digitization and PandoraPFA are calibrated using the gamma-rays, K_L^0, and muons. Then, using the ddsim, quark pairs (u, d, s) of 91 GeV, 200 GeV, 360 GeV, and 500 GeV are generated from the collision point and injected into the ILD model. The events are reconstructed to evaluate the energy resolution of the jet. Since they are two-jet events, the energy of one jet is half the energy of quark pairs. The resolution is evaluated using the RMS90 method. This method evaluates the resolution by calculating the standard deviation using only 90% of the total events around the core of the distribution to exclude the extra tail events.

9.2.2 Jet energy resolution

The saturation curve is applied to the simulation in the digitization step, and the correction of the saturation is applied in the reconstruction step. The new model of the saturation curve involving the effects of the time constant of the scintillation emission, recovery time, and cross-talk and after-pulse, discussed in 8.3, is applied to the digitization and reconstruction step of the simulation. The S12571-010P is used as the SiPM, and the CTAP probability is based on the measurements of the technological prototype. The light yield for MIP is set to 7 p.e. based on the prototype results. The black plots in Fig. 9.5 shows the saturation curve based on the new model in this setup.

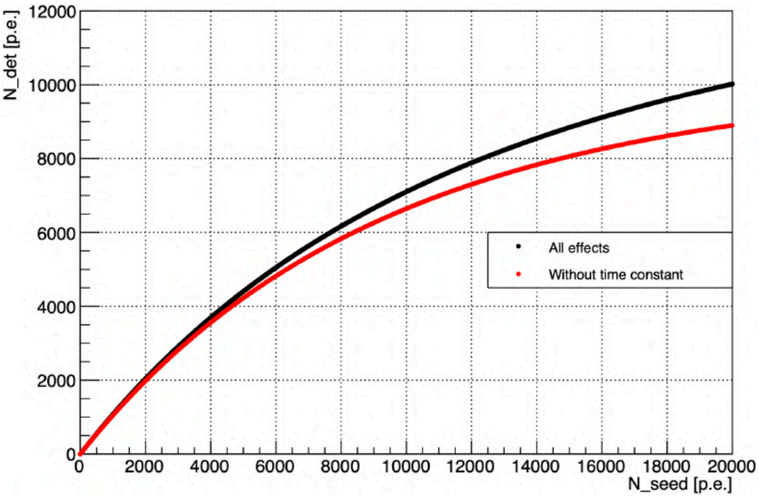

Figure9.5 Saturation curve with all effects (black), and without the time constant of the scintillation emission (red)

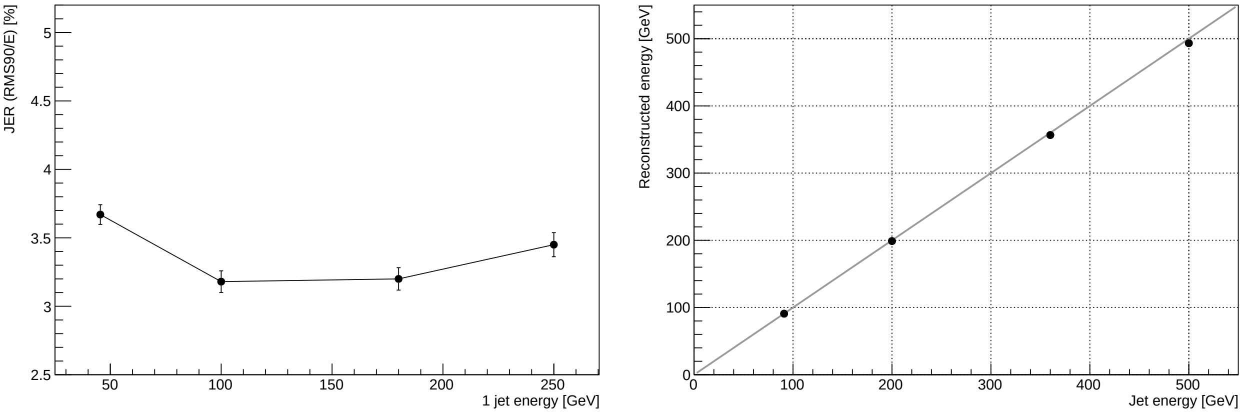

Figure9.6 Jet energy resolution (left) and linearity (right) with S12571-010P using the new saturation model.

Fig. 9.6 shows the jet energy resolution (JER) and linearity using the S12571-010P and the new saturation model. The JER is less than 3.7% at the whole energy range, which meets the requirement of 3–4% for the PFA. The reconstructed jet energy is linearly proportional to the injected energy. This result is reasonable and consistent with previous studies in [25][33]. The quite good resolution and linearity can be achieved using the Sc-ECAL as the PFA ECAL, and the Sc-ECAL is capable of realizing the precise physics at the ILC.

9.2.3 Effect of saturation correction

For comparison, the JER based on the saturation correction with the conventional method is evaluated. The SiPM saturation occurs based on the new model including the time constant of the scintillation emission, but the saturation correction is made with the conventional method where the saturation curve is measured without taking into account the time constant of the scintillation light emission. The new model is applied to the digitization, and the model without the scintillation emission is applied to the reconstruction. The saturation curve with the conventional method is also shown as the red plots in Fig. 9.5.

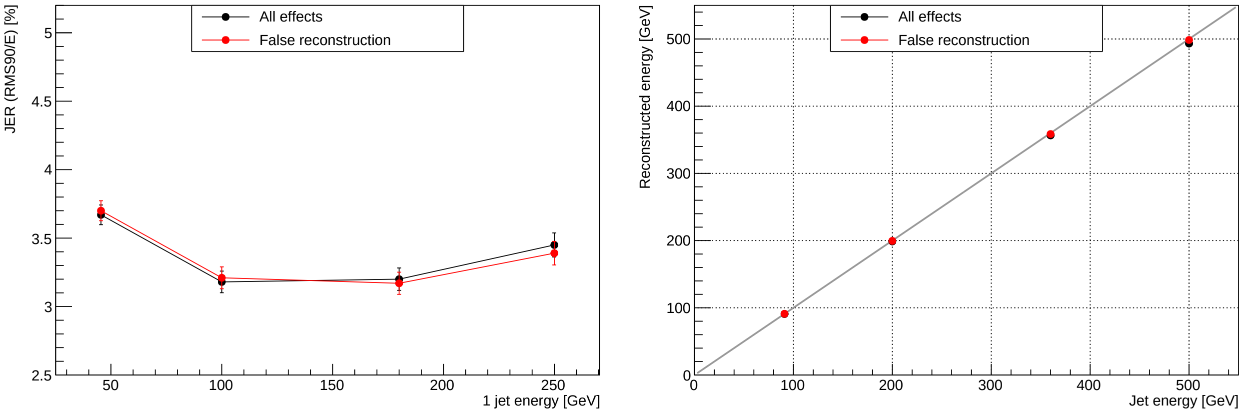

Figure9.7 Jet energy resolution (left) and linearity (right) with S12571-010P using the new saturation model (black) and the conventional method (red). The red uses the saturation correction with the conventional method at the reconstruction step.

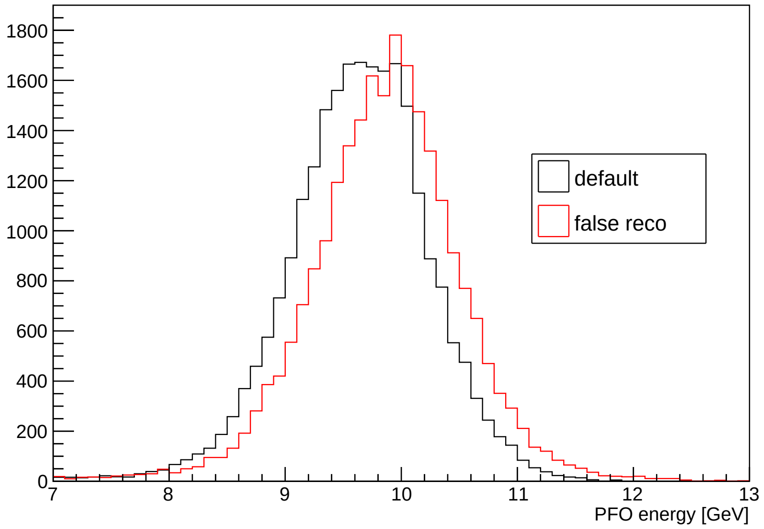

Figure9.8 Distribution of the reconstructed energy at 10 GeV gamma with all effects (black) and without the time constant (red).

The red plots in Fig. 9.7 show the results of the jet energy resolution and linearity based on the saturation correction with the conventional method at the reconstruction. Both the JER and linearity have no significant difference from the new model, because the effect of the false reconstruction is normalized at the calibration step. Fig. 9.8 shows the energy distributions at 10 GeV gamma. The energy scale of the Sc-ECAL is calibrated by taking a factor to adjust the mean of the energy distribution to 10 GeV. The calibration factors for the energy scale is 1.0374 with all effects, and 1.0158 without the time constant. The difference of the saturation curve can disappear at the calibration step for the energy scale.

The SiPM characteristics for the CTAP probability is applied to the JER simulation. The CTAP probability has about 10% variation from sensor to sensor according to the measurement at the prototype, and the 10% variation of the CTAP probability corresponds to the 2% variation of the N_{det} at the new saturation model. The effect of the uncertainty is included in the simulation by smearing the N_{det} using a Gause function with a variance of 2%.

The green plots in Fig. 9.9 show the JER and linearity with the variation of the SiPM characteristics for the CTAP probability. Compared to the results with no variation, the JER is slightly worse at the high energy region, but the linearity is the same. The deteriorated JER can be restored by per-channel CTAP calibration the same way as described in Section 6.3. The saturation model can be calculated channel by channel using the measured CTAP probabilities, and the SiPM characteristics for the CTAP can be corrected.

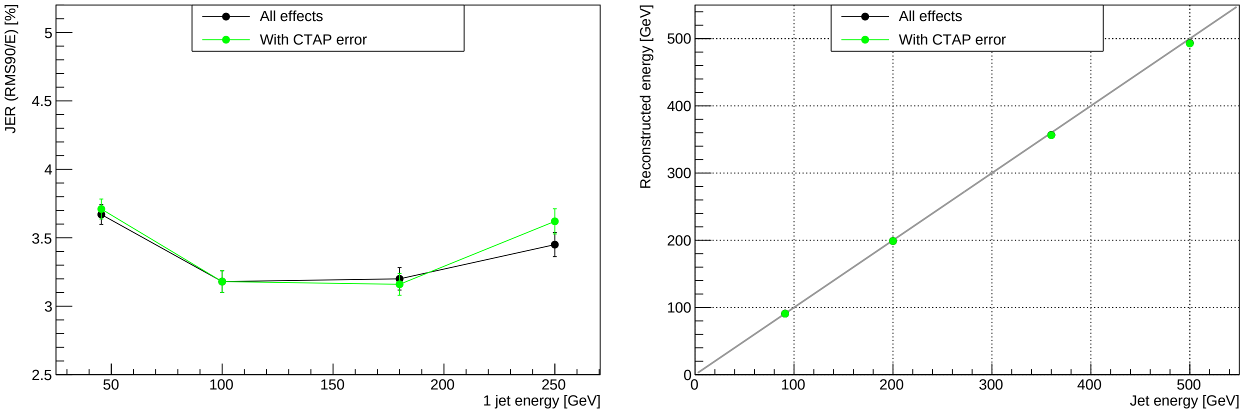

Figure9.9 Jet energy resolution and linearity including the variation of the N_{det} caused by the SiPM characteristics of the CTAP (green), and the new saturation model (black) for comparison.

9.2.4 Effect of SiPM types

There are some candidates of SiPMs for the Sc-ECAL discussed in Section 4.5.6, but the detailed comparison between the SiPM types has not been done. Using the new saturation model and results of the prototype, the JER with the different SiPM types is evaluated. According to the measurements of the prototype, the light yield for MIP is set as 7 p.e. for the S12571-010P and 18 p.e. for S12571-015P respectively. The light yield for the S14160 series, which are not used in the prototype, is calculated according to the difference of PDE and sensitive area, then set as 21 p.e. for the S14160-1310PS and 38 p.e. for S14160-1315PS respectively.

Fig. 9.10 shows the results of the JER and linearity with different SiPMs. The results with all types of SiPMs have similar resolution below 3.7% and meets the requirement of 3–4% for the PFA. The linearity is also good at all types. In terms of the jet energy resolution, all candidates of the SiPMs for the Sc-ECAL can achieve the quite good resolution and realize the precision physics at the ILC. The decision of SiPM type will be determined by examining the effect of the Bhabha scattering, where a large number of particles are incident.

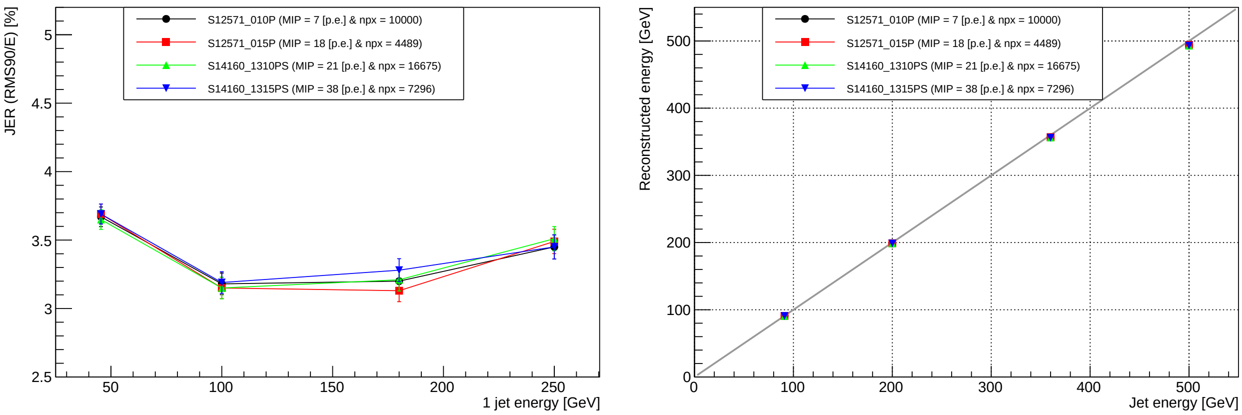

Figure9.10 Comparison of the jet energy resolution (left) and linearity (right) between different types of SiPMs. In the legend, MIP means the MIP light yield in units of p.e., and npx is the number of pixels.

Chapter 10

Conclusion

Conclusion

Future Higgs factories based on the electron-positron collider are planned for the precision Higgs physics. The precise measurements of the mass and coupling for the Higgs boson would be a key portal to the new physics beyond the Standard Model. One of the most important advantages for the future Higgs factories such as the ILC and CEPC is the model-independent measurement of the Higgs coupling constant. Especially the precise measurement of the Higgs hadronic decay $H \to WW^*/ZZ^*/q\bar{q}$ is important, because it is difficult in the LHC because of the huge backgrounds. It requires a precise jet measurement with the jet energy resolution of of 3–4% at the whole jet energy range. The PFA is a central concept of the detectors at the Higgs factories, which requires high-granularity calorimeters. Especially the high granularity of the cell size of the 5 mm × 5 mm is required for the PFA ECAL.

The Sc-ECAL is one of the technology options for the PFA ECAL. It is based on a scintillator strip readout by a SiPM to realize the 5 mm × 5 mm cell size by aligning the strips orthogonally in x-y configuration. The number of readout channels can be greatly reduced compared to the genuine 5 mm × 5 mm segmentation without the degradation of the calorimeter performance. In order to demonstrate the performance of the Sc-ECAL and to prepare for the construction of the actual detector, a full-layer technological prototype with all the technologies integrated is constructed. This is the first ever demonstration with a full technological prototype for the PFA-ECAL.

By calibrating the key parameters of the prototype and checking their stabilities, It is verified that the Sc-ECAL can be operated stably. By demonstrating the good performance such as the position resolution, efficiency, shower measurement, and jet energy resolution by simulation, it is confirmed that the Sc-ECAL meets the requirements as the PFA ECAL for the precision physics at the future Higgs factories. The commissioning of the technological prototype is based on long-term tests with LED and cosmic-ray. The calibration scheme and reconstruction algorithm such as the SSA and cone clustering are developed, which can be applied to the actual detector.

The per-channel calibrations are successfully done for the key parameters of the Sc-ECAL. The gain, inter-calibration factor, and probability of the cross-talk and after-pulse are obtained by the LED run. The pedestal and MIP response are calibrated using the cosmic-ray run. The temperature dependence is evaluated and the method of the temperature correction is established, then the temperature correction is applied to the measurement using the prototype. This makes it possible for the first time to evaluate the performance on the prototype. It is found that the Sc-ECAL can be properly calibrated and operated.

The performance of the Sc-ECAL is evaluated using the long-term commissioning runs. The key parameters are successfully monitored and it is found that most of the parameters show excellent stability over a long period. The temperature correction eliminates the effect of the temperature dependence, and allows the accurate calibration of the MIP response so that the performance is not affected. A slight degradation of the MIP gain is observed. It is still under investigation, but it can basically be corrected by the calibration. The detection efficiency of $\sim 84\%$ is achieved and found to be consistent with the Monte Carlo simulation. The position resolution of 1.5–1.7 mm is achieved and corresponds to the ~ 5 mm uniform distribution, which meets the granularity requirement for the PFA ECAL. The position resolution is also found to be consistent with the simulation. The shower analysis is performed using the cosmic-ray instead of the test beam experiment. The shower properties with the data and simulation match well especially in the fully contained shower and the shower escape with the energy suppression. The showers induced by the cosmic-ray are successfully measured as expected in the simulation. Although more detailed evaluation of the performance of the Sc-ECAL will require the planned test beam experiments, the basic performance is successfully demonstrated in this work.

A new method for the measurement and correction of the saturation of the SiPM is developed. The saturation is a crucial issue for the detectors based on the scintillator with the SiPM readout. The new method is to measure the SiPM saturation with the scintillation light excited by the UV light pulse, then the measured saturation curve contains the effects of the time constant of the scintillation emission. In the saturation measurement based on the new method, a large recovery of the saturation is observed at the new method compared to the conventional method. The new method gives a big impact on the saturation correction for the detectors using the scintillators and SiPMs. In addition, a new saturation model for the first time contains the effects of the time constant of the scintillation emission, recovery time of the SiPM, cross-talk and after-pulse, is developed. The measurement and model are found to be consistent. The new method of the saturation measurement and the new saturation model can be useful to the accurate saturation correction for the Sc-ECAL, and can also be applied to various detectors and experiments based on the scintillator with the SiPM readout.

The jet energy resolution is evaluated using the current configuration of the Sc-ECAL. Based on the performance measured by the prototype and the new saturation model, the jet energy resolution of less than 3.7% over a wide energy range is found to be achievable, meeting the requirements for the PFA. A comparison of the jet energy resolution for different types of the SiPMs is performed, and it turns out that all types of SiPMs have similar resolution of less than 3.7% over a wide energy range, meeting the requirement.

In conclusion, the Sc-ECAL is found to be a promising and mature technology for the highly granular calorimeter to achieve the precision physics at the future Higgs factories.

Prospect

The Sc-ECAL is planned to be tested in beam. The possibility is the electron beam at the Beijing Synchrotron Radiation Facilities (BSRF) [47]. The BSRF provides the 1–2.5 GeV electron beam with about 50 $\mathrm{Hz/cm^2}$. It is possible to conduct operational tests in an environment similar to that of the actual detector, and the detailed performance such as the energy scale, linearity, resolution can be demonstrated. We are now preparing a front-end detector for the calibration of the beam energy and a support structure for the prototype towards the test beam experiment. Moreover, there is a possibility of a test beam experiment combined with the Sc-ECAL and HCAL. Detailed performance study such as the shower study and the cluster tagging can be evaluated. Through these test beam experiments, we will be able to demonstrate the performance of the scintillator-based PFA calorimeter in more detail.

The ILC is scheduled to begin the construction within the next 5 years and to begin the physical runs within the next 15 years, to discover the precision Higgs physics. Remaining challenges toward the detector construction will include the engineering design, which would require R&D for large scale production such as scintillator production (injection moulding) and automated assembly system.

Appendix

A SiPM double-side readout

The Sc-ECAL technological prototype includes the additional two layers with the SiPM double-side readout. This appendix shows the principle of the double-side readout and the construction of the detection layers

A.1 Principle

The SiPM double-side readout method is a newly invented method for the Sc-ECAL, in which two SiPMs are mounted at both ends of the strip to readout the signals, as shown in Fig. A.1. To keep the total number of readout channels, a strip with a length of 90 mm is used instead of a strip with 45 mm length. The possible advantages of the double-side readout method are as follows:

- Eliminating a noise by taking coincidence of 2 SiPMs
- Higher light yield by summing the signals from 2 SiPMs
- Even lower light yield for each SiPM
- Position reconstruction by charge and/or timing difference between 2 SiPM readouts

The lower light yield for each SiPM compared to the single readout can suppress the saturation. The position reconstruction can reduce the ghost hits.

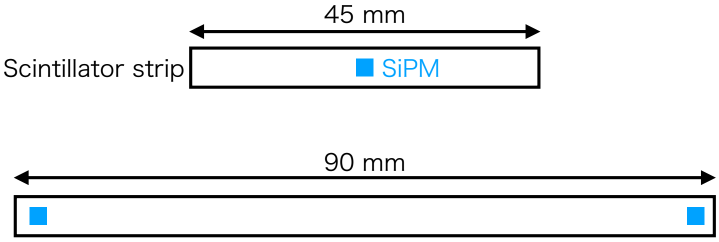

FigureA.1 Scematic of the SiPM double-side readout.

A.2 Performance test

Two types of strips are produced as shown in Fig. A.2. The position dependence of the light yield is measured by using the β-ray from ^{90}Sr and scanning the incident position, as shown in Fig A.3. The strip is coupled to the Hamamatsu MPPC S12571-015P with the recommended operation voltage (68 V).

Fig. A.4 and A.5 shows the results of the light yield measurements with SiPM single readout and double-side readout respectively. The sum of the light yields from two SiPMs is about 35 p.e., which is a larger light yield

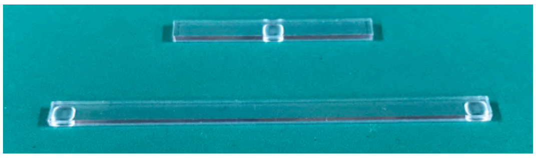

FigureA.2 Scintillator strip with SiPM single readout (top) and SiPM double-side readout (bottom).

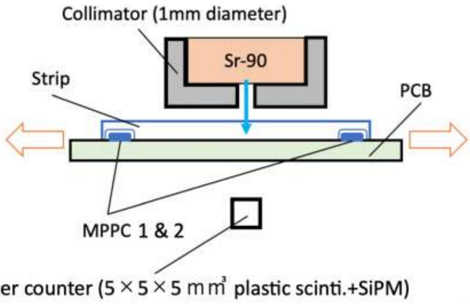

FigureA.3 Setup for the measurement of the position dependence of the light yield [62].

than that of the single readout over the entire strip. The light yield with one MPPC is smaller than that of the single readout, which results in the less SiPM saturation. By taking the geometric mean, the position dependence becomes flat.

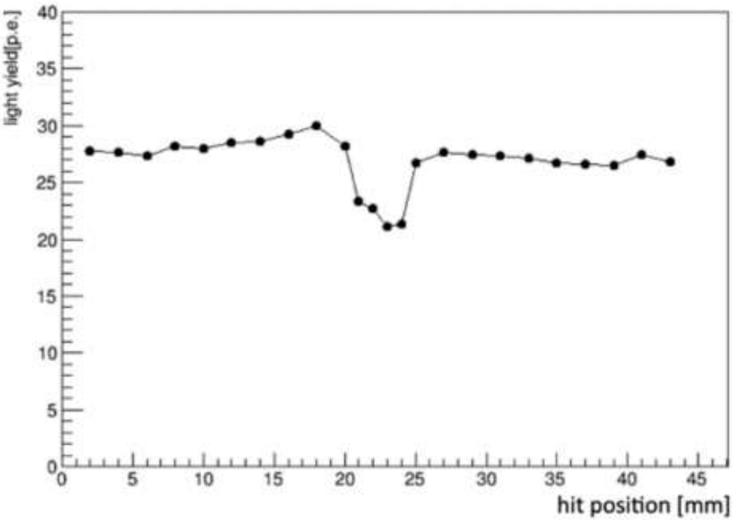

FigureA.4 Position dependence of the light yield with single readout [62].

Fig. A.6 shows the position resolution at each incident position. The position resolution is calculated by the difference of the light yield and timing between 2 SiPMs. The average position resolution is 32 mm using only the time difference, 27 mm using only the light yield difference, and 22 mm for the weighted average of the differences of the time and light yield. The results show that the SiPM double-side readout can reduce ghost hits discussed in Section 3.2.2.

Fig. A.7 shows the distribution of the light yield with and without the coincidence of 2 SiPMs. The data is taken by the self-trigger of 2 SiPMs with the low threshold. The noise (pedestal) events like the blue histogram can be extracted, and the MIP spectrum like the red histogram can clearly be seen. By lowering the threshold and removing the noise events with the coincidence, it is possible to acquire the events with a lower energy.

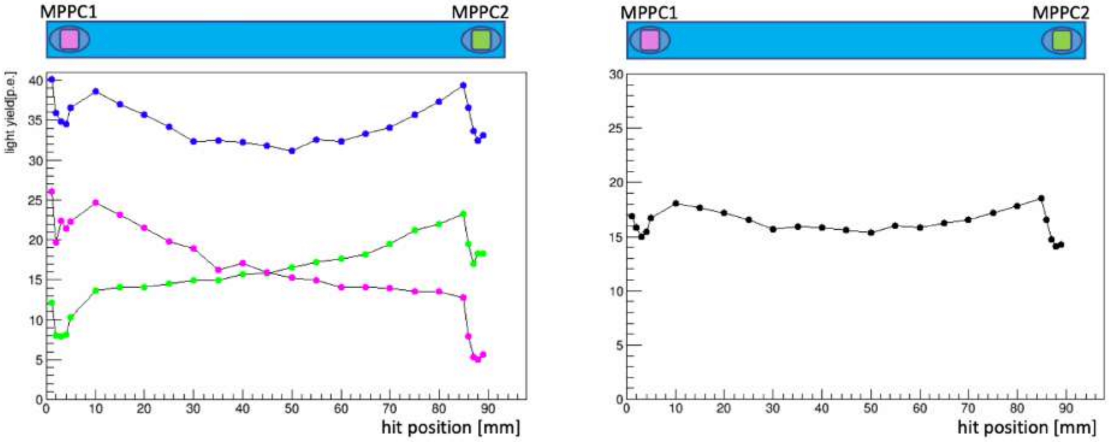

FigureA.5 Position dependence of the light yield with double-side readout [62]. The Magenta and green plots in the left figure show the light yield with each SiPM, and blue plots show the light yield summed by 2 SiPMs. The black plots in the right figure show the geometric mean of the light yields.

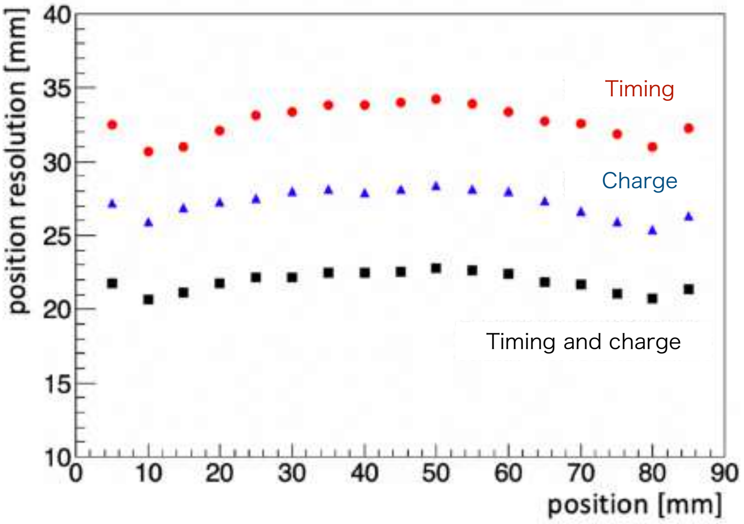

FigureA.6 Position resolution with the double-side readout at each position [62].

A.3 Detection layer

Two detection layers with the SiPM double-side readout are produced for the Sc-ECAL technological prototype. Fig. A.8 shows two options of the strip design; 2 SiPMs in the middle of the strips, and 2 SiPMs at strip ends. In order to implement the double-side readout with minimal modifications using the standard EBU, the option 1 with the 2 SiPMs in the middle of the strips is adapted in the detection layers for the technological prototype. The option 2 will be adapted if the configuration of the SiPM position on the EBU can be modified. One line contains 5 rows of 45 mm strips at the standard EBU configuration, while one line at the double-side readout layers is set as 90 mm strip + 90 mm strip + 45 mm strip.

The design of the strips and reflector (ESR) films are based on the standard configuration of the prototype, as shown in Fig. A.9. 200 pieces of 90 mm strips and 100 pieces of 45 mm strips are produced for two detection

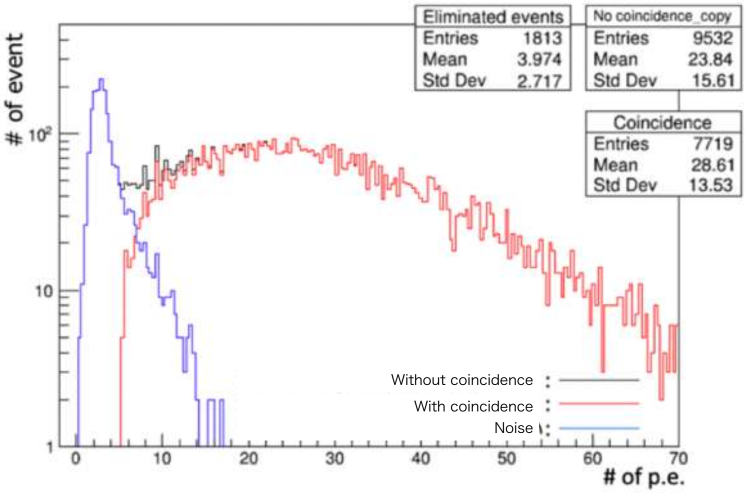

FigureA.7 Distribution of the sum of light yields of 2 SiPMs with or without the coincidence of 2 SiPMs [62].

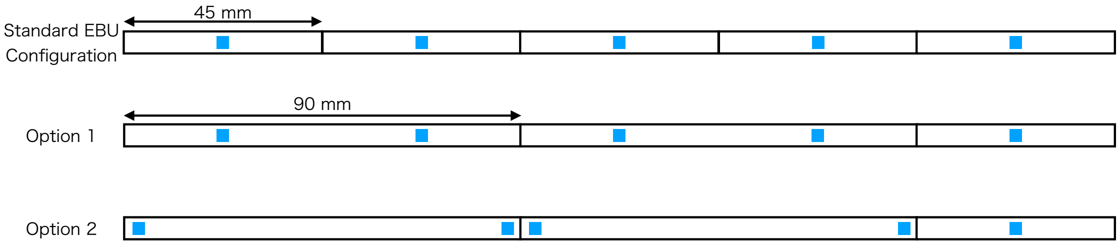

FigureA.8 Two options of the 90 mm strip design for the SiPM double-side readout.

layers. All the strips are wrapped with the reflector films by hand as shown in Fig. A.10. The wrapped strips are sent to China, and the assembly on the EBU is performed in the same way as the standard detection layers with single readout. Then, one super-layer with two EBUs with the double-side readout is completed, and installed into the back end of the technological prototype.

FigureA.9 Scintillator strip (left) and reflector film (right) for the double-side readout layer.

FigureA.10 Scintillator strip wrapped with the reflector film by hand.

A.4 Scintillator material

The scintillator strips for the double-side readout are produced by the injection moulding. The injection moulding is suitable for a large scale production, but the light yield is smaller than that of the cast moulding, as discussed in 4.4.1. A dedicated mould for the strip is not ready, so a large plate with 2 mm thickness is produced by the injection moulding, and the strip shape and dimple for the SiPM are machined.

Fig. A.11 shows the comparison of the light yield between the 45 mm strips produced by the cast moulding (BC408) and injection moulding. The light yield with the injection moulding is lower by ~20% compared to the cast moulding. However, the scintillator strip produced by the injection moulding has still sufficient light yield for the prototype.

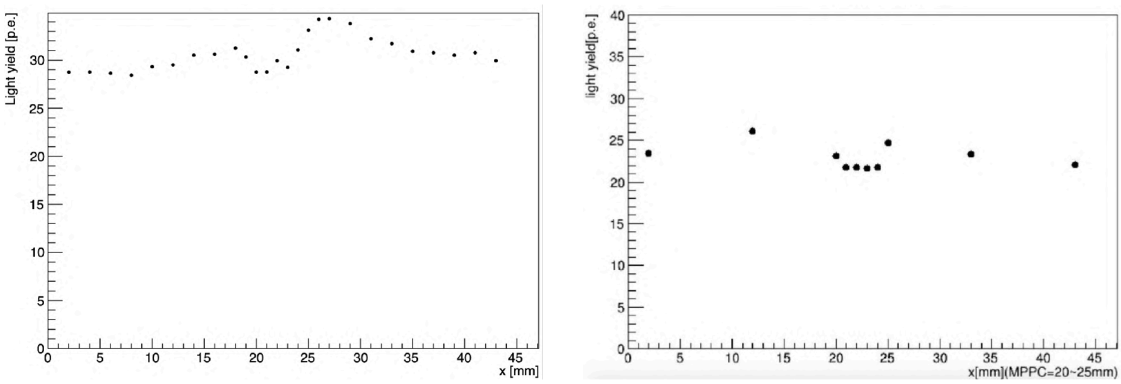

FigureA.11 Light yield of the standard 45 mm strip for the prototype (left) and the 45 mm strip produced by the injection moulding (right).

The dedicated moulds for the scintillator strips with single readout and double-side readout are produced after the construction of the detection layers, as shown in FIg. A.12. The light yield test is in preparation.

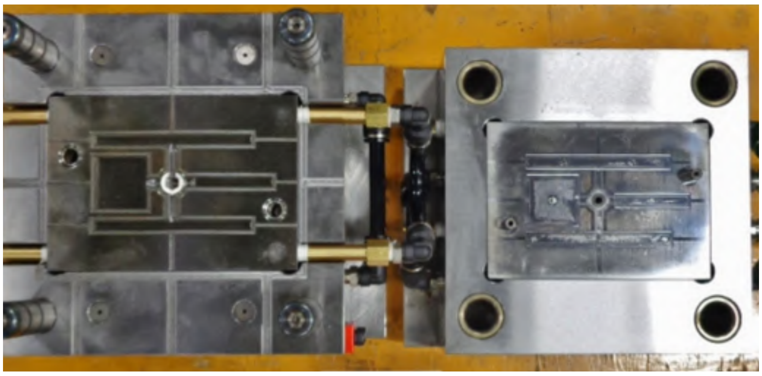

FigureA.12 Dedicated mould for the scintillator strips with single readout and double-side readout (and scintillator tile for the AHCAL).

A.5 Analysis plan for double readout layers

The additional analysis of the technological prototype is planned using the detection layers with double-side readout (DR layers). One is the noise reduction with the coincidence of 2 SiPMs. It needs the dedicated run with the low threshold at the DR layers and with the trigger of the DR layers. The noise reduction can be evaluated by taking the offline coincidence of 2 SiPMs, because the online coincidence between 2 SiPMs is not possible in the current DAQ system.

The other is the evaluation of the position reconstruction. The hit position of the cosmic-ray can be reconstructed using the difference of the light yield between 2 SiPMs. The position resolution can be evaluated by the deviation between the reconstructed position and the cosmic-ray track obtained by the track fit.

The dedicated run and the performance evaluation of the DR layers are in preparation.

Acknowledgements

First of all, I would like to thank Prof. Wataru Ootani who supervised me and gave me an opportunity to join the project of the future Higgs factories, and whose rigorous research attitude and broad knowledge greatly helped me in the studies and became a lifelong asset.

I would like to thank all members of the ILD Sc-ECAL group and the CEPC Sc-ECAL group: Prof. Tohru Takeshita, Dr. Yazhou Niu, Prof. Jianbei Liu, Prof. Yunlong Zhang, Prof. Mingyi Dong, Dr. Zhigang Wang, Dr. Yong Liu. I am heartily thankful for the supports and advises of Prof. Toshinori Mori, Dr. Toshiyuki Iwamoto, Dr. Yusuke Uchiyama, and Dr. Kei Ieki. I would like to express my special thanks to my colleagues especially in the ILD group: Linghui Liu, Tatsuro Torimaru, Ryunosuke Masuda, Tatsuki Murata, and Yuki Ueda. This research was supported by JSR Fellowship, the University of Tokyo.

Last but not least, I would like to express my deepest gratitude and appreciation to my family and everyone who has supported and guided me.

Bibliography

[1] ATLAS Collaboration, "Observation of a new particle in the search for the Standard Model Higgs boson with the ATLAS detector at the LHC," Phys. Lett. B, 716, 1, 2012.

[2] CMS Collaboration, "Observation of a new boson at a mass of 125 GeV with the CMS experiment at the LHC," Phys. Lett. B, 716, 30, 2013.

[3] J. Woithe et al, "Let's have a coffee with the Standard Model of particle physics!," Phys. Educ., 52, 034001, 2017.

[4] P. W. Higgs, "Broken Symmetries and the Masses of Gauge Bosons," Phys. Rev. Lett., 13, 508–509, 1964.

[5] S. L. Glashow, "Partial Symmetries of Weak Interactions," Phys. Rev. Lett., 19, 579–588, 1961.

[6] S. Weinberg, "A Model of Leptons," Phys. Rev. Lett., 19, 1264–1266, 1967.

[7] A. Salam, "Weak and Electromagnetic Interactions," NuovoCim, 11, 568–577, 1959.

[8] J. Ellis, "Higgs Physics," arXiv:1312.5672v1, 2013.

[9] G. Aad et al., "Combined Measurement of the Higgs Boson Mass in pp Collisions at $\sqrt{s} = 7$ and 8 TeV with the ATLAS and CMS Experiments," Phys. Rev. Lett., 114, 191803, 2015.

[10] Linear Collider Collaboration, "The International Linear Collider Technical Design Report - Volume 2: Physics," arXiv:1306.6352, 2013a.

[11] ACFA Linear Collider Working Group, "Particle Physics Experiments at JLC," arXiv:hep-ph/0109166, 2001.

[12] Linear Collider Collaboration, "The International Linear Collider Technical Design Report - Volume 1: Executive Summary," arXiv:1306.6327, 2013b.

[13] CEPC Study Group, "CEPC Conceptual Design Report: Volume 1 - Accelerator," arXiv:1809.00285, 2018.

[14] T. Barklow et al., "Improved Formalism for Precision Higgs Coupling Fits," Phys. Rev. D, 97, 053003, 2018a.

[15] T. Barklow et al., "Model-Independent Determination of the Triple Higgs Coupling at e^+e^- Colliders," Phys. Rev. D, 97, 053004, 2018b.

[16] LCC Physics Working Group, "Physics Case for the 250 GeV Stage of the International Linear Collider," arXiv:1710.07621, 2017.

[17] L. G. Almeida et al., "Study of the 125 GeV Standard Model Higgs Boson Partial Widths and Branching Fractions," Phys. Rev. D, 89, 033006, 2014.

[18] J. Yan et al., "Measurement of the Higgs boson mass and $e^+e^- \to ZH$ cross section using $Z \to \mu^+\mu^-$ and $Z \to e^+e^-$ at the ILC," Phys. Rev. D, 94, 113002, 2016.

[19] Linear Collider Collaboration, "The International Linear Collider Technical Design Report - Volume 3.II: Accelerator Baseline Design," arXiv:1306.6328, 2013c.

[20] Linear Collider Collaboration, "The International Linear Collider Technical Design Report - Volume 3.I:

Accelerator R&D," arXiv:1306.6353, 2013d.

[21] Linear Collider Collaboration, "The International Linear Collider Technical Design Report - Volume 4: Detectors," arXiv:1306.6329, 2013e.

[22] M. Kobayashi et al., "Cosmic ray tests of a GEM-based TPC prototype operated in Ar-CF4-isobutane gas mixtures," Nucl. Instrum. Meth. A, A641, 37–47, 2011.

[23] J.S. Marshall et al., "Pandora Particle Flow Algorithm," arXiv1308.4357, 2013.

[24] M.A. Thomson, "Particle Flow Calorimetry and the PandoraPFA Algorithm," Nucl. Instrum. Meth. A, 611, 25–40, 2009.

[25] ILD Collaboration, "International Large Detector: Interim Design Report," arXiv:2003.01116, 2020.

[26] J. Repond et al., "Construction and response of a highly granular scintillator–based electromagnetic calorimeter," Nucl. Instrum. Meth. A, 887, 150–168, 2018.

[27] Kuraray Co., URL: `https://www.kuraray.com/`.

[28] KIMOTO Co., URL: `https://www.kimoto.co.jp/en`.

[29] Hamamatsu Photonics K.K., URL: `https://www.hamamatsu.com/jp/en/index.html`.

[30] E. Garutti, "Dedicated front-end electronics for an ILC prototype hadronic calorimeter with SiPM readout," IEEE Nuclear Science Symposium Conference Record, 3, 1499–1502, 2005.

[31] Omega Microelectronics center, URL: `https://portail.polytechnique.edu/omega/`.

[32] N. Yazhou et al., "Design of Sc-ECAL Prototype for CEPC and Performance of First Two Layers," JINST, 15, C05036, 2020.

[33] K. Kotera et al., "A novel strip energy splitting algorithm for the fine granular readout of a scintillator strip electromagnetic calorimeter," Nucl. Instrum. Meth. in A, 789, 158–164, 2015a.

[34] Saint-Goabin Co., "BC-408, BC-412, BC-416," URL: `https://www.crystals.saint-gobain.com/products/bc-408-bc-412-bc-416`.

[35] 3M Co., "ESR series," URL: `http://www.mmm.co.jp/display/spec/`.

[36] T. Mogi, "Study of a segmented electromagnetic calorimeter using Pixelated Photon Detector for next–generation electron-positron collider experiments," Master thesis, 2019.

[37] Hamamatsu Photonics K.K., "MPPC S12571 series," .

[38] M. Yokoyama et al., "R&D of Multi Pixel Photon Counter," High Energy News, 26-3, 216, 2007.

[39] A. Ghassemi et al, "MPPC / Technical note," 2017.

[40] Hamamatsu Photonics K.K., "Handbook Vol.03 Si APD, MPPC," .

[41] H. Otono, "Study of MPPC at liquid nitrogen temperatures," PoS, PD07, 007, 2008.

[42] Hamamatsu Photonics K.K., "MPPC S14160 series," .

[43] S. Zhao et al, "The Readout Electronics Research Design and Development for CEPC Scintillators Electromagnetic Calorimeter Prototype," IEEE Transactions on Nuclear Science, 66, 1107–1114, 2019a.

[44] S. Conforti et al., "SPIROC: design and performances of a dedicated very front-end electronics for an ILC Analog Hadronic CALorimeter (AHCAL) prototype with SiPM read-out," JINST, 8, C01027, 2013.

[45] A. Zhou et al, "Study on the FPGA-based Temperature Compensation for the SiPM of CEPC ECAL prototype," JINST, 15, C10008, 2020.

[46] A. Zhou et al, "FELIX: a High–Throughput Network Approach for Interfacing to Front End Electronics for ATLAS Upgrades," J. Phys.: Conf. Ser., 664, 082050, 2015.

[47] Beijing Synchrotron Radiation Facilities, URL: `http://english.bsrf.ihep.cas.cn/`.

[48] T. H. Tran, "Pandora PFA - a brief introduction," Pattern recognition meeting at LLR, 2012.

[49] S. Gomi et al, “Development and study of the multi pixel photon counter,” Nucl. Instrum. Meth. A, 581, 427–432, 2007.

[50] S. Zhao et al, “The Readout Electronics Research Design and Development for CEPC Scintillators Electromagnetic Calorimeter Prototype,” IEEE Transactions on Nuclear Science, 66, 1107-1114, 2019b.

[51] S. Agostinelli et al, “GEANT4 - a simulation toolkit,” Nucl. Instrum. Meth. A, 506, 250–303, 2003.

[52] C. Hagmann et al, “Cosmic-ray shower generator (CRY) for Monte Carlo transport codes,” 2007 IEEE Nuclear Science Symposium Conference Record, 2, 1143–1146, 2007.

[53] K. Kotera et al, “Describing the response of saturated SiPMs,” arXiv:1510.01102, 2015b.

[54] S. Krause et al, “Measurement of saturation functions,” AHCAL main meeting, 2017.

[55] PicoQuant Co., URL: `https://www.picoquant.com/`.

[56] Eljen Technology Co., URL: `https://eljentechnology.com/`.

[57] Paul Scherrer Institute, URL: `https://www.psi.ch/en`.

[58] Tektronix, URL: `https://jp.tek.com/keithley`.

[59] D. Jeans, “Modeling the response of a recovering SiPM,” arXiv:1511.06528, 2015.

[60] F. Gaede, Presentation at ILD SW Meeting, iLCSoft Tutorial, 2017.

[61] F. Gaede, “LCIO - A persistency framework for linear collider simulation studies,” arXiv:physics/0306114, 2003.

[62] R. Masuda, “Study on SiPM readout method for scintillator-based electromagnetic calorimeter for future electron-positron colliders,” Master thesis, 2019.